ON THE GLOBAL STABILITY OF MAGNETIZED ACCRETION DISKS

by

Charles L. Curry, B.Sc., M.Sc.

A Thesis
Submitted to the School of Graduate Studies
in Partial Fulfilment of the Requirements for the Degree
Doctor of Philosophy

McMaster University
September 1995

DOCTOR OF PHILOSOPHY (1995) (ASTROPHYSICS)	MCMASTER UNIVERSITY Department of Physics and Astronomy Hamilton, Ontario
TITLE:	On The Global Stability of Magnetized Accretion Disks
AUTHOR:	Charles L. Curry B.Sc. (Saint Mary's University) M.Sc. (Queen's University)
SUPERVISORS:	Professor Ralph E. Pudritz Professor Peter G. Sutherland
PAGES:	xx, 228

ON THE GLOBAL STABILITY OF MAGNETIZED ACCRETION DISKS

Acknowledgements

Although it occurred more or less by accident, the relatively rare situation of having two supervisors instead of one has been a great boon. And I could not have encountered two more different scientists in style. I'd like to thank Ralph Pudritz for always having an open door, and mind, when it came to science. He never let up trying to get my pure theoretician's hands dirty, and I'm sure I'm the better for it. I also thank him for steering me to a "hot" topic and for making possible a trip to France in November 1992, ostensibly for scientific reasons, that couldn't have come at a better time. Peter Sutherland is a born educator who has a deep understanding of how science is done; he continues to surprise me with his insights and perception. I thank Peter and Ralph both for their patience and much-needed financial support while I completed the final stages of this thesis at my customary plodding pace.

I benefitted tremendously from the dissertations of two other sometime Ph.D.s, Omer Blaes and George Schramkowski, both of whom allowed me to reproduce parts of their theses. I extend special thanks to Omer for allowing me to xerox his thesis and entertaining frequent discussions in person and by email. Fred Kus at CIS supplied numerical expertise from time to time. The third member of my committee, Anthony Peirce, taught a great course in asymptotics and opened my eyes to myriad alternatives to "just computing it." Carrie Klatt proofread several chapters, and provided some expert cutting and pasting. Jeff Secker, Jennifer Rendell, and Pat Coté saved me heaps of time by sending me their various LaTex tricks, and inevitably explaining them to me.

There were times when, if Mac weren't buried deep in Southern Ontario, I'd have sworn I was back in God's Country: legions of Maritimers just keep flowing through this place. Thus I was spoiled with one lively gathering after another during my days here, and the fault is my own, not theirs, for still not knowing every line of every verse to Barrett's Privateers.

Thanks to Hamish J., Mohammed M., and no doubt countless other revered coffee club managers for, among other things, maintaining the Dabrowski Memorial Sugar Bowl. Thank you Dave B., for showing me why NEVER to pull an all-nighter. Grad school would not have been the same without the students from other countries I argued with, learned

from, and laughed with. There were many and I hope it will always be that way. Thanks to Bill A. for introducing me to Al Purdy, Neil S. for *introducing* me to Al Purdy, and Hamish J. for spicing up the lunch hours with his FRANK gossip. Karen Z. and Vicky S. were (are) good friends who tolerated (nay, indulged) my frequent lapses into artsie mode. Karen also shared some very difficult experiences with me which I shall never forget. Thanks to Bill A., Hamish J., Peter M., and Rachid O. for staying here as long as I did and sharing in so many ridiculous, yet profound life experiences. I've had many good friends here; you only really know when it's finally time to leave. My friends and family back home have stuck with me all the way, and continue to be an anchor for my thoughts and views. I thank my parents especially for never doubting that what I do is important, no matter
what ...

Thank you Carrie for knowing what's important, loving me so dearly, and giving me so much to look forward to.

Finally, I would be remiss not to mention our absurdly helpful and cheery Department secretaries Jackie, Wendy, Marg, Rosemary, and Cheryl, especially since a copy of this thesis will make its way into their office and if they ever looked ...

To the memory of William MacDonald Curry,
1960 – 1992

Death destroys Man, but the thought of it saves Him.

All day I follow
Watching the swift dark furrow
That curls away before me,
And care not for skies or upturned flowers,
And at the end of the field
Look backward
Ever with discontent.
A stone, a root, a strayed thought
Has warped the line of that furrow -
And urge my horses 'round again.

Sometimes even before the row is finished
I must look backward;
To find, when I come to the end
That there I swerved.

Unappeased I leave the field,
Expectant, return.

The horses are very patient.
When I tell myself
This time
The ultimate unflawed turning
Is before my share,
They must give up their rest.

Someday, someday, be sure
I shall turn the furrow of all my hopes
But I shall not, doing it, look backward.

RAYMOND KNISTER

Contents

Abstract

We investigate the global stability of a differentially rotating fluid shell threaded by magnetic fields to linear perturbations. This system models an accretion disk far from its vertical boundaries. To focus on the direct interaction between the magnetic field and differential rotation, the stability analysis employs an equilibrium model of homogeneous and incompressible fluid which allows these phenomena to be studied in isolation. Depending on the degree of internal pressure support, disks may be either "thick" or "thin" and both possibilities are considered here. The magnetic field exterior to the fluid has an effect on the radial boundary motion, and we derive the appropriate boundary conditions.

The first interaction of interest is the axisymmetric instability of Velikhov and Chandrasekhar. It has both local and global manifestations, the latter of which can be stabilized for all perturbations if and only if the equilibrium magnetic field strength is above a certain threshold value, which we calculate in our model for a wide range of equilibrium parameters. The growth rates of the unstable modes are always less than, but comparable to, the corresponding local growth rates. The former are also considerably higher for free boundaries than for the rigid configurations considered by other authors. The connection between the global and local characters of the instability is fully elucidated.

These results are generalized from a purely vertical field to the case when an azimuthal magnetic field is present. In most cases, the azimuthal field tends to stabilize the VC instability, although strong fields (Alfvén speed of order the characteristic rotational speed) are required for complete stabilization. We find an additional strong field instability that arises when the azimuthal Alfvén speed exceeds the characteristic rotational speed. For freely-bounded configurations, this instability resembles the sausage instability for interpenetrating fields in plasma physics.

Other interesting interactions appear in the presence of nonaxisymmetric perturbations. The global, dynamical instability of Papaloizou and Pringle, previously known to exist only in non-magnetized models of thick disks, is shown to have a magnetic counterpart. Indeed, this instability grows much more rapidly than in the corresponding hydrodynamic case. There also exist two additional types of unstable modes not present in hydrodynamic disks. The basic instability mechanism for these modes appears to be wave over-reflection between the boundaries and one or more of the singular Alfvén radii that can lie within the shell. These Alfvén resonances have a similar role to the corotation resonance in the purely hydrodynamic disk. We find, as in the axisymmetric case, that highly localized modes are fastest growing; however, they do not exceed the axisymmetric growth rates for any of the system parameters examined.

Although all of the instabilities we found grow on the dynamical timescale, they may not be catastrophic to accretion disks. Indeed, the highly localized nature of the fastest growing modes suggests that these modes do not lead to large-scale breakup, but rather serve to "stir up" the fluid locally. Thus our results support the oft-mentioned conjecture that these magnetic instabilities could lead to turbulence. The globally unstable modes we found have quite different implications, among them the possibility that large-scale magnetic field generation (which we demonstrate in the linear growth regime) could obviate the need for the α-effect in standard dynamo theory.

List of Figures

List of Tables

List of Symbols

a	power-law index of differential rotation
b	power-law index of azimuthal magnetic field
B	z-component of magnetic field (Ch. 3)
$\mathbf{B}$	magnetic field
c	speed of light
c	power-law index of vertical magnetic field (Ch. 4)
c_s	sound speed
$\mathbf{E}$	electric field
$\mathbf{g}$	effective gravitational acceleration
g_{eff}	effective gravity (r-component only)
G	gravitational constant
h	enthalpy
H	half-thickness of disk
$\mathbf{J}$	electric current density
k_B	Boltzmann's constant
$\mathbf{k}$	spatial wavevector
ℓ	specific angular momentum
m	azimuthal wavenumber
M	central mass
$\mathbf{n}$	normal vector
N	Brunt-Väisälä frequency
p	pressure
p_T	$p + \lvert\mathbf{B}\rvert^2/8\pi$
Q^+, Q^-	volumetric heating, cooling functions
r	distance from rotation axis
r_0	$(GM/\Omega_0^2)^{1/3}$ = pressure maximum radius
r_1	inner radius

r_2	outer radius
r_{CR}	corotation radius
$r_{A,1}$	inner Alfven radius
$r_{A,2}$	outer Alfven radius
s	specific entropy
t	time
$\mathbf{u}$	fluid velocity
v_A	$B/(4\pi\rho)^{1/2}$ = Alfven velocity (Ch. 3)
$\mathbf{V}$	$\mathbf{B}/(4\pi\rho)^{1/2}$ = Alfven velocity
W	$\delta p/\rho\sigma$
$\mathcal{W}$	$i\sigma\delta p_T/\rho\tilde{\sigma}^2$ (Ch. 2)
z	height above equatorial plane
α	Shakura-Sunyaev viscosity parameter
γ	adiabatic index
Γ	$mB_\phi/r + k_z B_z$
$\overline{\Gamma}$	$\Gamma/(4\pi\rho)^{1/2}$
δ	Eulerian perturbation
Δ	$\delta + \xi \cdot \nabla$ = Lagrangian perturbation
η	electrical resistivity
κ	epicyclic frequency
λ	$k/2\pi$ = wavelength
μ	thickness parameter
μ_{min}	minimum thickness for instability
ν	frequency
ν_t	turbulent viscosity
ν_m	magnetic diffusivity
ξ	Lagrangian displacement
π	3.14159...
Π_{ij}	stress tensor

ϖ	$k_z r$
ρ	density
ρ_e	electric charge density
σ	Doppler-shifted eigenfrequency
$\tilde{\sigma}^2$	$\sigma^2 - \Omega_A^2$
ϕ	azimuthal angle
ω	eigenfrequency
$\tilde{\omega}^2$	$\omega^2 - \Omega_A^2$
Ψ, Ψ_{ext}	external gravitational potential
Ψ_{int}	self-gravitational potential
Ψ_{rot}	centrifugal potential
Ψ_{mag}	magnetic potential
χ	scalar magnetic potential
ζ	$(r^2k_z^2 + m^2)^{1/2}$
Ω	rotational frequency
Ω_A	$k_z V_z$ = vertical Alfven frequency
Ω_p	$-\omega_R/m$ = pattern speed (azimuthal phase velocity of mode)

Chapter 1

INTRODUCTION

The significance of accretion as an astrophysical process can hardly be overemphasized. That planets and stars owe it their very existence is indisputable, although many details of the formation process still elude theorists. Furthermore, for the most massive bound astronomical objects such as supermassive black holes, accretion is *the* most efficient mechanism of energy release. It is therefore surprising that while most energy production processes of importance in the cosmos were known by the middle of this century, e.g. nuclear fusion, radioactivity, etc., accretion was not promoted to such status until quite late (Hoyle & Lyttleton 1939; Bondi 1952). The ubiquity and significance of disks in astronomy, on the other hand, has long been recognized (Laplace 1802). But the best known disk systems, galaxies and our own solar system among them, often show no evidence for accretion. The concept of an *accretion disk* arose only when consideration was given to material flows in the vicinity of rotating, massive objects. It is now believed that such situations are common in the universe on almost all scales from planetary rings to the nuclei of galaxies.

Direct signatures of accretion are exceedingly hard to observe. This is because the process only occurs in regions with a significant reservoir of surrounding material which, unfortunately, often obscures the central object of interest from view. It is therefore appropriate to begin by reviewing the observational evidence for accretion disks, before undertaking a description of the processes believed to occur in these objects.

1.1 Observational Evidence for Accretion Disks

1.1.1 Close binary systems

The best observational evidence for accretion disks to date comes from accreting binary systems. In these, one of the components (the "primary") is an evolved compact object (white dwarf, neutron star, or black hole) while the other (the "secondary") is a post-main-sequence giant star. In the course of its evolution, the secondary can overfill its Roche lobe and, as a consequence, have its outer layers gravitationally stripped by the primary. As both components are rotating about their common centre of mass, the stripped gas has considerable angular momentum, and so cannot fall onto the primary purely radially. This leads to the formation of an accretion disk, a structure in which gas spirals slowly inwards toward the primary through a series of roughly circular orbits. In the absence of external torques, the gas falling in transfers angular momentum outward through the disc by internal torques, the exact nature of which are still very uncertain (see §1.2 below).

Systems in which the primary is a white dwarf are called cataclysmic variables (CVs). Of particular interest are the so-called short-period cataclysmic variables, or "dwarf novae" (DNs). These number around 300 and are characterized by frequent, small (2 - 5 mag brighter in outburst than in quiescence), short-period (days - weeks) outbursts of radiation. Their orbital periods are often correlated with the time they take to return to quiescence after an eruption. This is thought to imply the presence of an accretion disk since a longer orbital period allows a larger disk, which in turn has a longer intrinsic decay timescale (Bath & Pringle 1985). Since DNs are the best-studied system thought to contain an accretion disk, I confine my attention mainly to them in this subsection.

In order to interpret observations of accreting binaries, it is useful to have some idea of the energies liberated in the accretion process. A simple order-of-magnitude estimate of the gravitational potential energy released by the accretion of a mass Δm onto a star of mass M and radius r_* is

$$\Delta E_{acc} = GM\Delta m/r_*.$$

Assuming ΔE_{acc} is subsequently released in the form of electromagnetic radiation, this can be expressed as a luminosity

$$L_{acc} = GM\dot{\mathcal{M}}/r_*, \tag{1.1}$$

where $\dot{\mathcal{M}}$ is the accretion rate. This is the total energy available via accretion. For a white dwarf (Frank, King, & Raine 1985, hereafter FKR),

$$L_{acc} = 1.3 \times 10^{33} \dot{\mathcal{M}}_{16}(M/M_\odot)(10^9 \text{ cm}/r_*) \quad \text{erg s}^{-1},$$

where the formula has been expressed in factors of order unity for a typical white dwarf. $\dot{\mathcal{M}}_{16}$ is the accretion rate in units of 10^{16} g s^{-1} ($1.6 \times 10^{-10} M_\odot$ yr^{-1}), and is expected to be of order unity. The predicted luminosity, 10^{33} erg s^{-1}, is within an order of magnitude of the values observed in such systems (Wade & Ward 1985). Actually, the expected contribution to the accretion luminosity from the disk *alone* is $L_{acc}/2$; the other half is believed to emerge from the thin boundary layer between the disk and star (FKR).

One can similarly estimate the expected spectral ranges of emission for CVs. Fairly simple arguments lead to (FKR)

$$6 \text{ eV} \lesssim h\overline{\nu} \lesssim 100 \text{ keV},$$

where $h\overline{\nu}$ is the energy of a typical emitted photon. This suggests that most white dwarf systems are likely to be optical, ultraviolet, and possibly X-ray sources. The prediction agrees with observations of CVs, the most luminous of which were found by the Copernicus and IUE satellites to have strong ultraviolet continua.

The expected spectral energy distribution (SED) of a typical DN system is shown in Figure 1.1. The main contribution to the luminosity comes from the accretion disk. The expected contributions from the boundary layer and red giant companion are also shown. The smooth disk curve is obtained by summing the spectra of unit surface area contributions all over the disk, assuming that the latter is geometrically thin, optically thick, and radiates locally like a blackbody. For $r \gg r_*$, the effective temperature of such a disk varies with radius as $T \sim r^{-3/4}$, while the spectrum (flux F_ν vs. frequency ν) obeys $F_\nu \sim \nu^{1/3}$ (Lynden-Bell & Pringle 1974). This simple picture is for *steady* disks only, and therefore would be

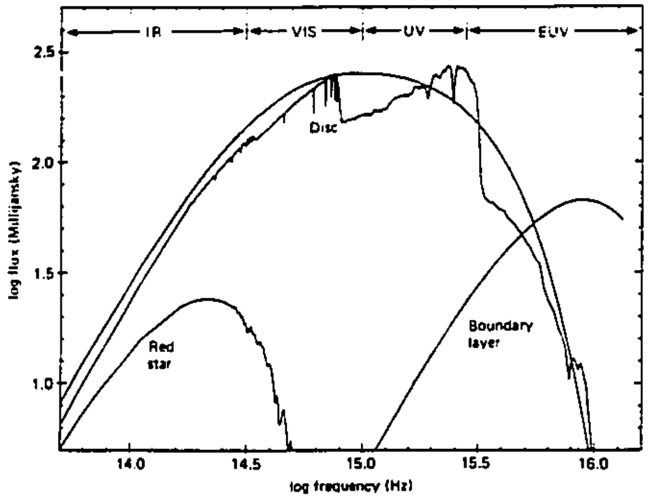

Figure 1.1: Various components that might contribute to the spectrum of a DN. The smooth disc curve is obtained if each disk element radiates like a blackbody and the other if each element radiates like a stellar atmosphere. The visible data for the red star are taken from observations of single stars, and the infrared is a blackbody extrapolation of the last observed point (Bath & Pringle 1985).

expected to hold only in the DN's quiescent state.[1]

It is generally agreed that DN outbursts are caused by variations in the accretion rate onto the white dwarf, but the cause of these changes is still unknown. Two commonly suggested possibilities are: (1) Variations in the mass transfer rate onto the outer disk edge by the secondary. This would not require any gross changes in the disk internal structure, e.g. in the viscosity. (2) The viscosity, which governs the mass transfer rate through the disk, varies as a result of some instability germane to the disk, while the transfer rate from the secondary remains unchanged. The latter interpretation suggests a way of measuring the viscous timescale: it should be correlated with the outburst decay time. At present, this is the only known method of estimating the magnitude of the viscosity. Further discussion of these issues can be found in Bath & Pringle (1985). In sum, DN are amongst the very few astronomical systems in which accretion disks can be studied in temporal and spatial detail. The only other area offering such promise for detailed modelling is star formation,

---

[1] In fact, it may not hold even then. This depends on the value of the viscosity in quiescence. Longer-period CVs, however, such as UX UMa and Z Cam stars which show little variation on timescales of months to years, should represent steady disks (Bath & Pringle 1985).

and then only quite recently.

1.1.2 Protostellar systems

Due largely to advances in instrumentation, it is only in the past decade or so that direct, optical evidence for disks around nearby stars has become available. β Pictoris, a main sequence star possessing a dusty disk a few hundred astronomical units (AU) in radius, is a rare and stunning example of a completely unambiguous detection (Smith & Terrile 1984). Presumably, β Pic's disk was formed early in its evolution, as a natural outcome of the initial pre-stellar collapse (Tscharnuter & Boss 1993). The frequency of stars with disks should therefore increase as younger and younger sources are observed.

The arena of star formation, however, is well veiled. Copious amounts of dust and gas lead to large visual extinctions ($A_V \gtrsim 10$ mag), calling for a cadre of observing techniques in multiple wavebands. Different methods probe different spatial scales, and it is therefore useful to discuss the current observational evidence for disks in terms of these scales separately as has been done, e.g., by Beckwith (1994). Several of the most compelling pieces of evidence supporting the presence of disks in young stellar objects (YSOs) are summarized below.

(1) On large scales (100 - 5000 AU), several YSOs (e.g., HL Tau) are surrounded by cold ($T \simeq 30$ K) molecular gas with the flattened appearance of an edge-on disk (Sargent & Beckwith 1991). The line-of-sight velocities decrease with distance from the star, although a distinctly Keplerian falloff has yet to be detected.

(2) On somewhat smaller scales (1 - 100 AU), the far-infrared continuum optical depths in many *visually* identified stars imply visual optical depths of 100 or more for the circumstellar material (Strom et al. 1989). Since the source would be entirely obscured were this material to lie along the line of sight, it is more plausible that it lies in a thin disk orbiting the star.

(3) The extended winds observed in many YSOs generate visual lines possessing only blue-shifted components. It has been suggested that the "missing" red-shifted components are hidden behind the opaque plane of a circumstellar disk (Edwards et al. 1987).

(4) On small scales (0.1 - 100 AU), excess infrared contributions to the SEDs of several YSOs have been observed. These are well-modelled by disks, although other distributions, e.g. spherical shells of circumstellar dust, have not been ruled out (Adams, Lada, & Shu 1988; also, see below).
(5) On the smallest observable scales ($\sim$ 0.01 AU), comparison of velocity widths of optical and infrared spectral lines in FU Orionis objects indicates that the infrared rotational velocity is smaller than that of the optical. This is consistent with a decreasing rotation curve with radius, since the optical lines are believed to originate in the hot region closer in to the star (Hartmann & Kenyon 1987).

I will focus now on the SED ((4) above) as a diagnostic of protostellar disks. Of all the above data it presently offers the greatest potential for deriving physical quantities of interest to disk theorists. The best modelled YSOs in this respect are the T-Tauri stars, the optical and ultraviolet spectra of which feature prominent emission lines and high variability. These low mass ($0.2- \sim 3M_\odot$) stars also display strong mass loss and magnetically active atmospheres, both believed to be signs of their extreme youth.

Given the SED, one can define a spectral index n by

$$n \equiv -\frac{d\,\log(\nu F_\nu)}{d\,\log\nu} = \frac{d\,\log(\lambda F_\lambda)}{d\,\log\lambda}.$$

This index is useful in characterizing the excess flux observed in the near- and mid-infrared, where the slopes tend to be almost linear (i.e. the Rayleigh-Jeans limit). A stellar blackbody, e.g., has $n = 3$. It is widely accepted that the infrared excess is due to starlight absorbed by circumstellar dust grains and reradiated at longer wavelengths. There are those, however, who question the disk interpretation for the dominant distribution of the dust. It has been suggested, e.g., that the dust could be distributed roughly spherically or be largely contained within the gaseous outflows frequently observed in YSOs (see, e.g., Rowan-Robinson et al. 1986).

In a survey of 86 YSOs, Beckwith et al. (1990) found that 42% have detectable far-infrared (1.3 mm) emission from small particles. The measured visual extinctions are generally quite small ($\lesssim$ 7 mag), arguing for a disk interpretation. The authors used far-infrared and millimeter-wave spectra of these sources to estimate both the mass and temperature distribution of the presumed disks.[2] These estimates are only weakly dependent on the assumed outer radius of the disk, R_d, a fortunate occurrence since the latter is only loosely constrained by spectral fits to the data. Typically, one finds $R_d \approx 50-100$ AU. Disk masses ranged from 0.001 to 0.5 $M_\odot$, with a mean of $\sim 0.02 M_\odot$. A more recent study (Osterloh & Beckwith 1995) found more low-mass disks, bringing the mean value down to $\sim 0.01 M_\odot$. In any case, these results show that *most disks are much less massive than their central stars*, implying that the common theoretical bias toward Keplerian disks is probably justified for most sources (see ff. §1.2). A very recent study (McCaughrean et al. 1995) shows that the frequency of circumstellar disks in dense clusters such as the Trapezium may be even higher ($\sim 50-80$ %) than in previous samples.

With a typical extent of $\sim 10^2$ AU , the disk is likely to be optically thick provided its mass $M \gtrsim 10^{-2}\ M_\odot$ (Adams, Lada, & Shu 1987; Kenyon & Hartmann 1987). Such disks can be expected to fall into two general categories: those that have appreciable radiation arising from intrinsic processes within the disk ("active" disks), and those that do not ("passive" disks). Clearly, these two types may have different spectral indices. If the equilibrium temperature distribution of the disk is well-represented by $T \sim r^{-l}$, then the emergent spectrum will have a spectral index $n = 2/l - 4$ (Lynden-Bell & Pringle 1974). The standard viscous accretion disk (§1.2), which has $l = 3/4$, then gives $n = -4/3$. Friedjung (1985) and Adams & Shu (1986) showed that a passive, *non-accreting*, spatially thin, optically thick disk would intercept 25% of the starlight and reradiate it in the near- and far-infrared. Remarkably, they showed that such a disk also has $l = 3/4$. This means that if the accretion rate is so low that the luminosity from accretion is less than a quarter of the stellar luminosity, then simple reprocessing will dominate over viscous accretion. For example, in models of the minimum-mass solar nebula (Ruden & Lin 1986), $\dot{\mathcal{M}} \sim 5 \times 10^{-8} M_\odot\ \mathrm{yr}^{-1}$, producing a total disk luminosity of $L_d \sim GM_* \dot{\mathcal{M}}/2R_* \simeq 0.39(M_*/M_\odot)/(R_*/R_\odot)\ L_\odot$, which for typical T Tauri parameters can easily be smaller than the corresponding repro-

---

[2] Note that while the authors' temperature estimates rest on relatively few assumptions (they fit the observed SEDs to a blackbody distribution in a low-frequency (far-infrared), optically thin limit), their mass estimates are quite sensitive to their choice of an opacity law, which depends strongly on the largely unknown emissive properties of grains (cf. Hildebrand 1983).

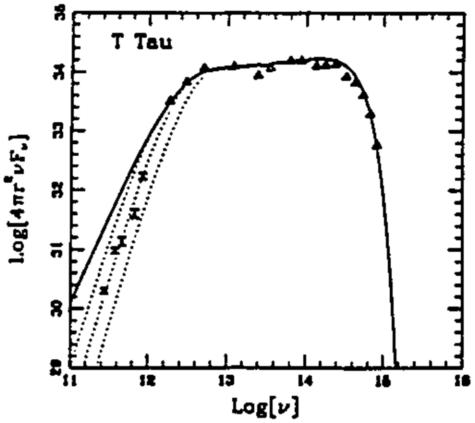

Figure 1.2: A flat-spectrum source, T Tau. The curves are models of a star plus a spatially flat disk. The solid curve is for a disk of infinite mass which is optically thick at all ν; the dotted curves have disk masses of (from left to right) 1, 0.1 and $0.01 M_\odot$. The triangles are infrared data, while the data points with error bars are measurements at mm and sub-mm frequencies (Adams, Emerson, & Fuller 1990).

cessing luminosity of $L_*/4$. Accretion will therefore only be observable if the star radiates additional luminosity from a viscous boundary layer.

While the spectra of a few T Tauri stars (e.g. SR 9) appear to follow $l = 3/4$, most display a somewhat flatter law, somewhere in the range $-4/3 \lesssim n \lesssim 0$ ($3/4 \gtrsim l \gtrsim 1/2$) (Beckwith et al. 1990). A source with an $n = 0$ SED is referred to, appropriately enough, as a *flat-spectrum* source. A good example of this is the star T Tauri itself (Figure 1.2). One possible explanation for the flattened SEDs of these sources is disk "flaring" (Kenyon & Hartmann 1987). In this picture the disk, while geometrically thin in its inner parts, possesses a substantial circumstellar layer of gas and dust at larger radii. The additional extinction due to this material flattens the SED. While this scenario can reconcile the passive disk idea with observed SEDs, it has been criticized (e.g. Shu 1991) on the grounds that: (i) If flared disks are common (which they need to be) then, statistically speaking, obscured T Tauri stars should be just as common. In fact, the latter are about ten times as scarce as visible T Tauris. (ii) Reprocessing of starlight in a passive, flared disk is not likely to produce a *single* power law SED from near- to far-infrared. Natta (1993) showed that the addition of a tenuous, dusty envelope to the disk-star system could reproduce the entire observed range of spectral indices in the interval 5 - 100 μm. Her three-component model of T Tauri systems then overcomes the difficulty (ii), but is equally prone to (i).

A distinct possibility is that the disk is not passive but *active*, in the sense that significant energy and momentum transport due to hydrodynamic or hydromagnetic instabilities (see ff., §1.3 - 1.5) takes place in the disk. An example of such a mechanism is a one-armed spiral-density wave, which may be generated whenever the disk mass is $\gtrsim 25\%$ of the total mass (star plus disk) (Adams, Ruden, & Shu 1989; Shu at al., 1990). Interestingly, the resulting dissipation leads to a *nonuniform* accretion rate in the disk with $\dot{\mathcal{M}} \propto r$ for a flat-spectrum source. Standard viscous disk models, on the other hand, feature $\dot{\mathcal{M}}$ = constant (see ff., §1.2). The resulting "pile-up" of matter due to this nonuniform accretion could lead to ancillary phenomena such as FU Orionis outbursts (Hartmann & Kenyon 1987; Hartmann 1994). More importantly, however, Shu (1991) pointed out that other global instabilities are in general inconsistent with $\dot{\mathcal{M}}$ = constant, suggesting that the standard model may be too limited to account for many phenomena of interest in the protostellar regime.

1.1.3 Active galactic nuclei (AGN)

In this class, I include Seyfert galaxies, quasars, and related systems such as BL Lac objects, liners and radiogalaxies. Taken as a group, there is perhaps no other class of system which argues so strongly for the presence of accretion power from purely *energetic* considerations. AGN have a range in luminosity extending from 10^{43} erg s^{-1} (Seyferts) to 10^{48} erg s^{-1} (quasars). The quoted luminosities have been known to vary on timescales of weeks or less, suggesting a very compact accreting mass. In addition, if these luminosities occur at or below the Eddington limit[3] 1.3×10^{38} $(M/M_\odot)$ erg s^{-1}, then this suggests masses of order 10^5 to 10^{10} $M_\odot$. Hence the widespread belief that only massive black holes could be powering these systems.

Despite these convincing arguments on energetic grounds, AGN are still poorly understood objects as far as the details of the accretion process are concerned. Ongoing herculean attempts to unify observations that span more than a dozen orders of magnitude in both

---

[3] The Eddington limit, $L_E = 4\pi G M m_p c/\sigma_T$ (where σ_T is the Thomson cross-section), is the critical luminosity at which the outward radiation pressure on an electron-proton pair just balances the inward gravitational force. For steady, spherically-symmetric flows, accretion stops when $L > L_E$.

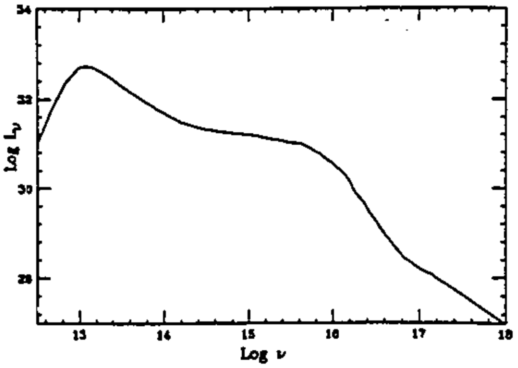

Figure 1.3: A characteristic AGN continuum. (Netzer 1990).

spatial scale and frequency often betray the difficulty of such a task (Woltjer 1990; Antonucci 1993; Blandford 1990). Consequently, the evidence for *disk* accretion in AGN is on much shakier ground than for either CVs or YSOs, and the comparative brevity of the present section will reflect this fact.

The emission (Netzer 1990) and absorption (Woltjer 1990) line spectra of AGN have been studied in great detail, but I will restrict discussion here to a "typical" continuum spectrum such as that shown in Figure 1.3. Between 10 and 0.1 μm, the spectrum can be decomposed into a power-law component $F_\nu \sim \nu^{-\gamma}$ (with $\gamma \approx 1$) plus a superposed "bump" at blue and near-ultraviolet frequencies. At higher frequencies, one typically finds an X-ray tail, with a cutoff in the vicinity of 20 keV. After subtraction of the nonthermal power-law component, the blue-UV bump can be fit by a single blackbody spectrum with $T \simeq 3 \times 10^4$ K (Shields 1978; Malkan & Sargent 1982). A standard thin accretion disk (§1.2) radiating at sub-Eddington luminosity ($L/L_E \approx 0.1$) and orbiting around a $\sim 10^8 M_\odot$ black hole can achieve this temperature, and furthermore, its spectrum peaks in the near-UV (Shields 1978). Unfortunately, this interpretation is not unique. In the well-studied quasar 3C 273, e.g., the bump may also be attributed to synchrotron radiation (FKR).

It is in fact the X-ray excesses of AGN continua that pose the biggest difficulty for thin accretion disk models. If thermal in origin, these excesses require much higher temperatures ($\sim 10^7$ K), and therefore luminosities ($L \gg L_E$) than are consistent with thin disk theory (§1.4). Thick disks, supported primarily by radiation pressure and accreting at super-Eddington rates, are more successful in describing these properties (Jaroszyński,

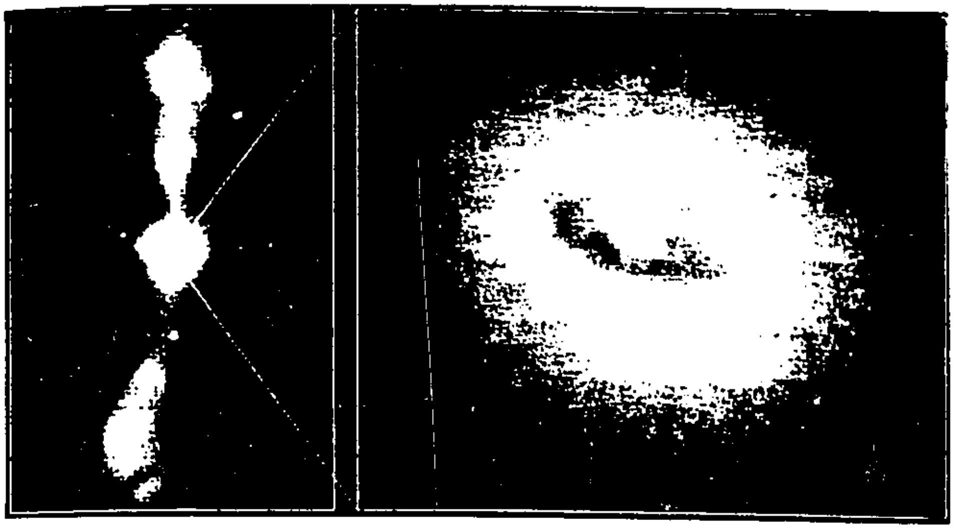

Figure 1.4: (a) Ground-based, composite image of the radio jets and optical galaxy NGC 4261. (b) High-resolution, HST optical image of the galaxy core, showing a dusty torus oriented perpendicular to the radio jets (Jaffe et al. 1993).

Abramowicz, & Paczyński 1980; Madau 1988). In addition, they may be able to better explain certain inclination effects known to be important in these distant and poorly-resolved systems (Netzer 1990).

Finally, I draw attention to the recent high-resolution optical images of the liner galaxy NGC 4261, which appear to have resolved a dusty torus perpendicular to the (previously known) bipolar jet (Figure 1.4; Jaffe et al. 1993). Previous dust continuum and broad-line emission observations had suggested the existence of such objects on much larger scales ($\sim$ 100 pc) than the radiation pressure supported disk mentioned above (Antonucci 1993). Models of the Seyfert 2 galaxy NGC 1068 have also incorporated such dusty tori (Krolik & Begelman 1988; Pier & Krolik 1992).

1.2 Thin Disk Theory: Basics

Much of the literature on steady accretion disks utilizes a particular model: that of the "standard" thin disk.[4] In this, the disk is geometrically thin in the sense that, at some radius $r = R$, the scale height (or half-thickness) $H \ll R$. Physical quantities inside the

---

[4] Much of the material in this section is gleaned from the excellent reviews of Pringle (1981) and FKR.

disk are then well-approximated by their values averaged over the thickness. Choosing cylindrical polar coordinates (r, ϕ, z), the components of the fluid velocity $\mathbf{u}$ are assumed to obey the following ordering:

$$u_\phi \gg u_r \gg u_z \approx 0. \tag{1.2}$$

That is, the disk is rotationally-dominated, with a small accretion rate, and vertical motions are essentially negligible. The latter implies that the vertical pressure gradient is balanced by the z-component of gravity:

$$\frac{\partial p}{\partial z} = \rho \frac{\partial}{\partial z}\left[\frac{GM}{(R^2+z^2)^{1/2}}\right] \approx -\rho\Omega_K^2 z, \tag{1.3}$$

where $\Omega_K \equiv \sqrt{GM/R^3}$ is the local Keplerian rotation frequency. To order of magnitude, $\partial p/\partial z \sim p/H$, $z \sim H$, and taking $p \sim \rho c_s^2$ where c_s is the isothermal sound speed, this equation then becomes

$$\frac{H}{R} \simeq c_s \left(\frac{R}{GM}\right)^{1/2} = \frac{c_s}{u_K}, \tag{1.4}$$

where $u_K \equiv R\Omega_K$ is the Keplerian circular speed. The thin disk assumption $H \ll R$ then amounts to

$$c_s \ll u_K.$$

That is, the local Kepler velocity should be highly supersonic.

Where does accretion fit in? In a differentially rotating fluid, viscous friction between shearing layers will extract energy from the gas, some of which goes into heat, resulting in a steady infall of material toward the central object. It has long been known that ordinary molecular viscosity is too weak to have a significant effect on the mean flow: under typical conditions expected to hold in disks, the Reynolds number Re (the dimensionless ratio of inertial to viscous forces) has been estimated as (FKR)

$$\mathrm{Re} \gtrsim 10^{14}. \tag{1.5}$$

The sheer magnitude of this number, as compared with typical laboratory values at which viscous liquids undergo the transition from laminar to turbulent flow ($\mathrm{Re} \sim 10^2 - 10^3$), has led to the frequent conjecture that accretion disk flow is likely to be turbulent. That this argument rests upon a misapplication of the laboratory results is perhaps not as widely known as it should be (cf. Shu 1992), but in any event it has led to a plethora of interesting proposals for the elusive viscosity mechanism. Nominally, the "viscosity" due to turbulence, ν_t, can be estimated on dimensional grounds given the length scale L and velocity $\overline{u}$ of the largest turbulent eddies, since $[\nu_t] = \mathrm{cm}^2\ \mathrm{s}^{-1}$. One can be reasonably certain that $\overline{u} \lesssim c_s$, since supersonic motions would be subject to additional dissipation via shocks (however, this need not be true in magnetized disks, which are considered in §1.5). In addition, $L \lesssim H$ in a thin disk. One can therefore write

$$\nu_t = \alpha c_s H, \tag{1.6}$$

where $\alpha \lesssim 1$ is, as FKR put it, "a useful parameterization of our ignorance," and contains the unknown physics behind the turbulence.[5]

On dimensional grounds, one also has $u_r \sim \nu_t/R$; this implies

$$u_r \sim \alpha c_s H/R \ll c_s. \tag{1.7}$$

That is, the inflow velocity is highly subsonic. This is entirely consistent with the original assumption (1.2).

The above "α-prescription" was first introduced by Shakura & Sunyaev (1973), and allowed significant progress toward a phenomenological theory of accretion disks. In addition to modelling the disk fluid flow, viscosity, and accretion, these authors introduced relations for radiative balance and opacity, assuming that the disk was optically thick. In all, they obtained 20 equations in 24 unknown physical quantities, leaving 4 independent quantities. One usually chooses these as: M, $\dot{\mathcal{M}}$, R, and α. Note that due to the local nature of the thin disk model, the system of equations to be solved is *algebraic*, not differential; i.e. R is a fiducial radius in the thin disk. The radial structure only enters the calculation insofar as

---

[5] Even if the real mechanism which facilitates angular momentum transport in accretion disks is not turbulent in nature, α is still an acceptable parameterization for modelling purposes. In that case it represents a constant of proportionality between the viscous shear stress and the pressure (see ff. §1.3).

it fixes the local energy generation rate (FKR).

In the two extremes where either the gas pressure p_{gas} or radiation pressure p_{rad} dominate, one can obtain analytic solutions of the thin disk structure equations. These, along with the numerical solution of the $p_{gas} \sim p_{rad}$ case, led to the identification of three qualitatively distinguishable regions. In the context of compact binaries and AGN, these can be characterized as follows (Shakura & Sunyaev 1973):

- the inner region, where radiation pressure dominates gas pressure and Thompson scattering is the dominant opacity mechanism;
- the middle region, where gas pressure dominates but Thompson scattering is still the most important contribution to the opacity; and
- the outer region, which is gas pressure dominated, but where the dominant opacity mechanism is free-free absorption.

The bulk of the observed X-ray luminosity is expected to originate from the radiation-dominated inner disk. Note that this is also likely to be the most highly ionized and magnetically active region. In protostellar disks, where dust is likely to be the dominant source of opacity, the inner radiation-dominated region is probably not present. Such disks are expected to be optically thick out to many AU (Strom et al. 1993).

1.3 Hydrodynamic Instabilities in Disks

The theory outlined above is for *steady* disks, and does not allow for the possibility that either external (e.g. a sudden change in the external mass supply) or internal (e.g. spontaneous fluid instabilities) factors could lead to alterations in the overall disk structure in time. Of particular concern are changes which might occur over a dynamical timescale, i.e.

$$t_{dyn} \sim \Omega_K^{-1},$$

since this is crucial to the postulation of equilibrium. Two other timescales of interest are the thermal (the time required for heat to be viscously generated) and the viscous (the time required for a fluid element to be viscously transported through the disk):

$$t_{th} \sim \alpha^{-1} t_{dyn}, \qquad t_{visc} \sim \alpha^{-1} \left(\frac{H}{r}\right)^{-2} t_{dyn}.$$

Note that $t_{visc} \gg t_{th} \gg t_{dyn}$. For the standard α-disk,

$$\begin{aligned} t_{dyn} &\sim \alpha t_{th} \sim 100 (M/M_{\odot})^{-1/2} (R/10^{10}\mathrm{cm})^{3/2} \quad \mathrm{sec}, \\ t_{visc} &\sim 3 \times 10^{5} \alpha^{-4/5} \dot{\mathcal{M}}_{16}^{-3/10} (M/M_{\odot})^{1/4} (R/10^{10}\mathrm{cm})^{5/4} \quad \mathrm{sec}. \end{aligned}$$

Thus the dynamical and thermal timescales are on the order of minutes, the viscous timescale on the order of days to weeks for typical parameters.

The Shakura & Sunyaev solution, while a self-consistent equilibrium configuration, does not necessarily represent a *stable* equilibrium. That is, one should still check that the supposed steady state remains so when subjected to arbitrary infinitesimal perturbations. If such perturbations begin to grow then the putative equilibrium is in fact unstable. The disparity of the above timescales allows us to distinguish between different types of instability. For example, assuming axisymmetric perturbations of wavelength λ such that $H \ll \lambda \ll r$, only the equations of radial viscous diffusion and thermal energy balance need to be considered (i.e. choosing this lengthscale singles out the thermal and viscous timescales; see Shakura & Sunyaev 1976). It can then be shown that such perturbations will be spontaneously unstable if

$$\left.\frac{d \ln Q^{+}}{d \ln T_c}\right|_{\Sigma} > \left.\frac{d \ln Q^{-}}{d \ln T_c}\right|_{\Sigma} \quad \text{(thermal instability)},$$

or

$$\left.\frac{\partial}{\partial \Sigma}(\nu_t \Sigma)\right|_{Q^{+}=Q^{-}} < 0 \quad \text{(viscous instability)},$$

where Q^{+} and Q^{-} are the local heating and cooling rates, T_c is the temperature at a given radius, and Σ is the local surface density. The former condition states that a small increase (decrease) in T_c causes Q^{+} to increase faster (slower) than Q^{-}, causing an even larger increase (decrease) in T_c (Pringle, Rees, & Pacholczyk 1973; Shakura & Sunyaev 1976). The latter condition states that unless the mass diffusion coefficient $\nu_t\Sigma$ is positive, material will be fed into regions of high density and removed from areas of low density, causing the disk to break up into rings (Lightman & Eardley 1974; Lightman 1974). Piran (1978) showed that both of these instabilities have their origin in the variation of the accretion rate $\dot{\mathcal{M}}$ with Σ. In particular, $d\ \ln\dot{\mathcal{M}}/d\ \ln\Sigma < 0$ is a necessary and sufficient criterion for instability. For the standard model, it can be shown that an equivalent condition is $p_{rad} > 3p_{gas}/2$ (Treves, Maraschi, & Abramowicz 1988). Thus these instabilities are most likely to occur in the inner region of the disk, where $p_{rad} \gg p_{gas}$.

Due to the rough agreement of t_{visc} with the outburst timescale in DNs, the above instabilities have been studied extensively in the hope that they might aid in the explanation of the outbursts (see FKR for further details). The discussion of §1.1.2 might also lead one to speculate that FU Orionis outbursts may be caused by the piling up of matter due to viscous instability, rather than the eccentric gravitational instabilities found by Adams, Ruden & Shu (1989) (ARS). This hypothesis could be tested in two ways: (1) The ARS instability, since it is dynamical, should have a much shorter timescale than t_{visc}, which one would expect to be correlated with the outburst timescale; (2) If FU Ori systems have low mass disks ($\lesssim$ 25% of the total mass), the ARS instability will not occur, but the viscous instability could. The possible role of thermal instabilities in FU Ori events has recently been investigated by Bell & Lin (1994), and a review of the subject may be found in Hartmann (1994).

The thermal instability discussed above was initially considered a serious blow to the standard disk model, since it implied changes in the *global* structure of the disk; the thermal runaway would inflate the inner region, invalidating the thin disk assumption. The breakup of the disk into rings via the viscous instability is a similarly disasterous occurence (although it occurs on the timescale $t_{visc} \gg t_{th}$). Note, however, that the mere presence of an instability need not have such drastic consequences. Most instabilities are discovered via the technique of *linear* stability analysis, in which perturbations of fluid quantities (δX) are always assumed small as compared with their corresponding equilibrium values (X). For perturbations which are found to be unstable in the linear regime, the only way to determine their ultimate effect on the disk is to follow their development into the *nonlinear* realm, where $\delta X \sim X$. Numerical calculations are usually required for this task.

It is sometimes the case that the ultimate effect of a given instability is not to disrupt the global equilibrium, but rather to stay quite localized in its effects. An example of this is gravitational (Jeans) instability in the gaseous component of galaxies which, due to the competing effect of differential rotation, can only form gravitationally-bound structures of limited extent.[6] Another example is hydrodynamic turbulence, which dissipates energy from large scales down to the smallest scales, where molecular viscosity takes over. It is now known that several instabilities to which accretion disks may be vulnerable find their ultimate resolution in turbulence, rather than in global disruption. Thus, one can clearly distinguish between the two types of instability in terms of their nonlinear resolution.

A sufficiently *generic* instability that can lead to turbulence would remove the phenomenological character of α-disk theory by providing a means of calculating α. There is no agreement that such a mechanism has been found, but two promising candidates are the following. First, it has long been hoped that the strong differential rotation of disks would lead to shear turbulence (§1.2). Since the Rayleigh criterion, $d(r^2\Omega)^2/dr \geq 0$, which governs stability to linear, axisymmetric perturbations should always be satisfied in thin disks, this has led to the study of finite-amplitude, *nonlinear* perturbations in differentially rotating flows (Zahn 1990; Dubrulle & Knobloch 1992). These perturbations are unstable, but one is left with the question of their origin. Second, to balance the local heating and cooling rates Q^+ and Q^-, a steep vertical temperature gradient is required in the disk (FKR). If the gradient is superadiabatic (e.g. as a result of heating due to strong differential rotation), then the fluid is unstable to convection (Schwarzschild 1958). Convective turbulence in disks has been studied by Livio & Shaviv (1977) and Tayler (1980). It is likely to be a major source of viscosity only in cooler, high opacity environments, such as protostellar or solar nebula disks (Cameron 1978; Lin & Papaloizou 1980).

Frequently one characterizes the viscosity by a stress tensor, Π_{ij}, defined in terms of an

---

[6] Since gravity is a long-range force, however, other instabilities of a nonlocal nature, e.g. spiral density waves, may also occur.

individual velocity fluctuation δu_i by

$$\Pi_{ij} = -\rho < \delta u_i \delta u_j >, \tag{1.8}$$

where $< \cdot >$ denotes the ensemble average of a fluctuating quantity. Π_{ij}, as defined in equation (1.8), is often referred to as the Reynolds stress. In an accretion disk the turbulent viscosity is determined by the component

$$\Pi_{r\phi} = -\rho < u_r u_\phi >= -\frac{3}{2}\alpha(p_{gas} + p_{rad}) \tag{1.9}$$

in the α-prescription (Shakura & Sunyaev 1973). Note that α scales with the total (gas plus radiation) pressure.

1.4 Thick Disk Theory and the Papaloizou-Pringle Instability

1.4.1 Thick disks

Aside from the ad hoc nature of the α-viscosity prescription, most would agree that the phenomenological theory of thin accretion disks is reasonably complete. This is reflected in the high proportion of the literature on accreting binaries which addresses specific issues of modelling (e.g. Horne 1994). However, it has also been clear for some time that conditions should exist where the thin disk assumption, $H \ll r$, no longer holds. In the standard thin disk solution, the inner radiation-dominated region can exist only in neutron star or black hole systems (e.g. X-ray binaries; FKR). The disk scale height in this region is given by (Jaroszyński, Abramowicz, & Paczyński 1980; FKR)

$$H \simeq \frac{3r_*}{4\eta}\frac{\dot{\mathcal{M}}}{\dot{\mathcal{M}}_E}\left[1 - \left(\frac{r_*}{r}\right)^{1/2}\right],$$

where $\dot{\mathcal{M}}_E \equiv L_E\, r_*/2\eta GM \sim 10^{18}$ g s^{-1} $\sim 10^{-8} M_\odot$ yr^{-1} is the critical accretion rate based on the Eddington luminosity, η is an efficiency factor $\simeq 0.1$ for neutron stars and black holes,

Parameter	Rotating Stellar Atmosphere	Thin Disk	Thick Disk
Shape	Spheroidal	Disklike	Toroidal
Rotation	Slow: $v_\phi \ll v_K$, $v_\phi \ll v_s$	Fast: $v_\phi = v_K$, $v_\phi \gg v_s$	Fast: $v_\phi \approx v_K$, $v_\phi \approx v_s$
Pressure	Important: $v_s \approx v_K$	Unimportant: $v_s \ll v_K$, $v_s \ll v_\phi$	Important: $v_s \approx v_\phi$, $v_s \approx v_K$
Viscosity	Unimportant: $\alpha v_\phi \ll v_s$	Large: $\alpha \approx 1$	Small: $\alpha \ll 1$
Non-azimuthal flow	Unimportant: $v \ll v_s$, $v \ll v_\phi$, $v \ll v_K$	Unimportant in central and outer parts: $v \ll v_\phi$ Important in innermost parts: $v \approx v_s$	Unimportant in central and outer parts: $v \ll v_\phi$ Important in innermost parts: $v \approx v_s$
Horizontal and vertical structure	Similar: $H_r \approx H_z$	Very different: $H_r \gg H_z$	Similar: $H_r \approx H_z$

Table 1.1: Comparison of equilibrium parameters for rotating fluids. In this table only, v_ϕ, v_K, and v_s are the azimuthal, Keplerian, and sound speeds, respectively, and v is the velocity of non-Keplerian flow. H_r and H_z are the pressure scale heights in the r and z directions (Abramowicz et al. 1984b).

and r_* marks the location of the stellar surface (or $r_* = 2GM/c^2$ for a black hole). For $\dot{\mathcal{M}} = \dot{\mathcal{M}}_E$ and $r = 2r_*$, this equation gives $H/r \simeq 1$, showing that *if the accretion rate is too high, the thin disk approximation breaks down near the central object.* This result is independent of viscosity. Radiation pressure inflates the inner region, causing it to become quasi-spherical.

Due to the large inferred accretion rates of AGN ($\dot{\mathcal{M}}_{AGN} \sim 20 M_\odot \text{ yr}^{-1} \gg \dot{\mathcal{M}}_E$), the above argument implies that even larger regions of the surrounding disk are likely to be "thick", i.e. to have $H/r \sim 1$. By the general hydrostatic equilibrium equation (1.4), $H/r \sim 1$ implies $c_s \sim u_K$; i.e., *pressure gradients are now dynamically important in the equilibrium.* From equation (1.7), it follows that $\alpha \ll 1$ is required for hydrostatic equilibrium in a thick disk. In these respects, a thick disk is intermediate in properties between a rotating stellar atmosphere and a thin disk; the three are compared in detail in Table 1.1. A schematic of a still favoured AGN disk model is shown in Figure 1.5. In the hollow "funnel" near the rotation axis and in the surrounding torus, centrifugal forces always exceed gravity, and equilibrium is maintained by a balance of radiative pressure gradients

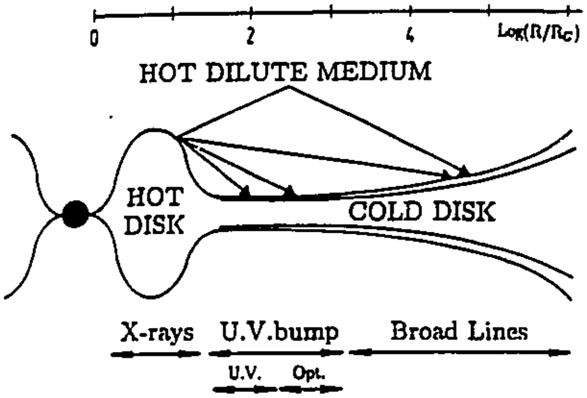

Figure 1.5: Schematic of the accretion disk component of AGN. R_G is the gravitational radius GM/c^2 (Collin-Souffrin 1992).

and rotation (§1.1.3). The radiative output from this region (much of which is observed in the form of highly collimated jets) therefore consists not only of the usual Eddington luminosity, but also contains contributions related to shear (always positive) and vorticity (always negative) (FKR). Such a picture nicely accounts for the observed super-Eddington luminosities and inferred supercritical accretion rates in AGN. The highest luminosities occur for vorticity-free configurations; in these, the angular momentum per unit mass is independent of radius. Many of the most elegant results of thick disk theory apply to such constant angular momentum tori.

The equilibrium theory of thick, perfect fluid tori is summarized in FKR and Blaes (1986), and I outline only salient aspects here. Ignoring relativistic processes, viscosity (shown to be small above), and accretion, the equation of hydrostatic equilibrium requires

$$\frac{1}{\rho}\nabla p = g_{eff} = -\nabla\Psi + \Omega^2 r\hat{\mathbf{r}}, \tag{1.10}$$

where g_{eff} is the effective acceleration due to both gravity and centrifugal forces. The adoption of a barotropic equation of state, $p = p(\rho)$ (see ff., Chapter 2), implies that the angular momentum, ℓ, is a function of r alone; i.e. $\ell = r^2\Omega(r)$. Despite the thickness of the disk, its mass is assumed small compared to that of the central body, so that the fluid's self-gravity can be neglected (however, see Abramowicz et al. 1984a). Specification

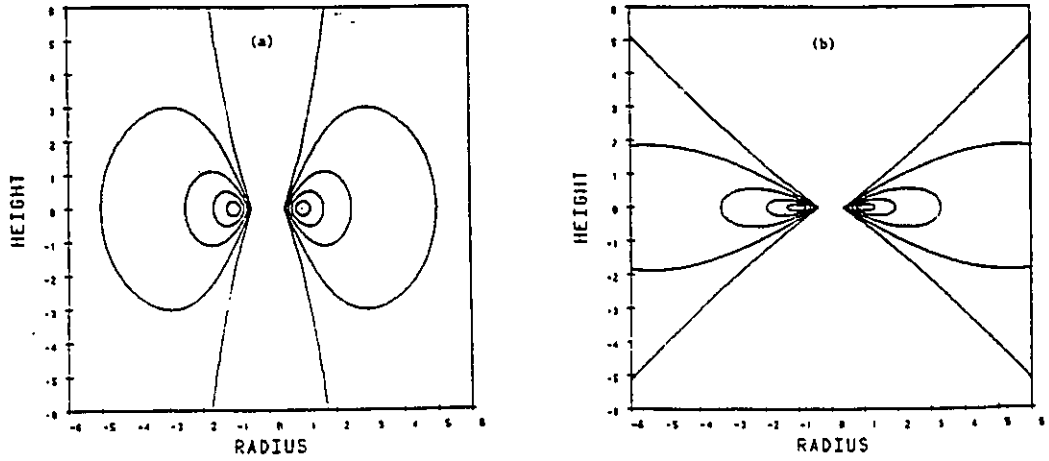

Figure 1.6: Equipotential surfaces for a Newtonian potential and specific angular momentum (a) $\ell = (GMr_0)^{1/2}$ and (b) $\ell = (GMr_0)^{1/2}(r/r_0)^{0.45}$. Distances are scaled with respect to the radius r_0 of the central, pressure maximum ring (Blaes 1986).

of the rotation law $\Omega(r)$ and gravitational field then allow one to solve for the shape of the isobaric, or "equipotential" surfaces. Sample equilibria, for a Newtonian potential $\Psi = -GM/(r^2+z^2)^{1/2}$ and two different rotation laws, are shown in Figure 1.6.

At $r = r_0$, $z = 0$, the *central pressure maximum* of the torus, the pressure gradient vanishes as fluid elements rotate with the Keplerian angular velocity. Inside r_0, $\ell > (GMr)^{1/2}$, so the radial pressure gradient must be directed inward to balance the excess centrifugal force. The opposite is true for $r > r_0$. Note from Fig. 1.6 that increasing the power-law exponent of ℓ flattens the equipotential surfaces in the r-direction. At $\ell = (GMr)^{1/2} \Rightarrow \Omega \sim r^{-3/2}$, the Keplerian distribution, one has the standard thin disk, as expected. Thus, the thin disk model is contained within the more general thick disk formalism. It is for this reason that I employ the latter (actually a simplified form thereof) for most of the calculations in this thesis.[7]

---

[7] It is worth noting that X-ray binaries and AGN are not the only systems for which pressure gradients should be important. To a lesser extent, protostellar disks are also expected to depart from strictly Keplerian rotation for this reason, and also because they are likely to be self-gravitating. However, these systems are clearly *gas*, not radiation, pressure dominated.

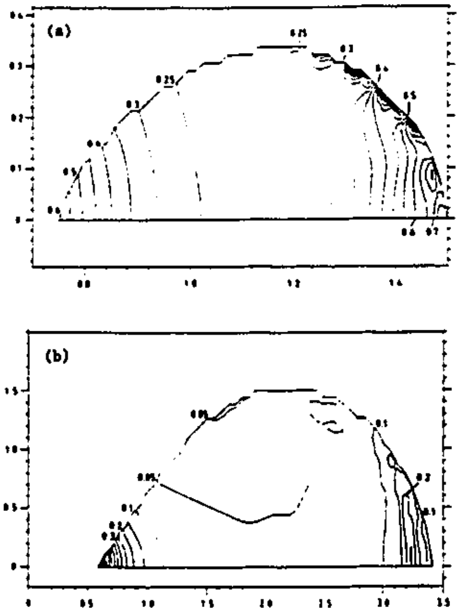

Figure 1.7: Structure of the fastest growing $m = 2$ modes in the (a) $\mu = 0.333$ and (b) $\mu = 0.707$ tori. The axes are in units of r_0, and the contours are the absolute value of the perturbed velocity potential normalized to its maximum value (Papaloizou & Pringle 1984).

1.4.2 The Papaloizou-Pringle instability

Due to the more complicated structure of thick tori, they are potentially susceptible to a much larger variety of fluid instabilities than are Keplerian disks. In particular, one might expect new effects to arise from two qualitatively different features of thick tori: (i) the presence of radial pressure gradients, which could lead to local buoyancy instabilities, e.g., and (ii) the presence of a finite boundary, leading to intrinsically global instabilities. In fact, both of these instabilities can occur, and many others as well. I refer the interested reader to Abramowicz et al. (1984b), who have provided an excellent review of the subject in two appendices.

Papaloizou & Pringle (1984) subjected axisymmetrically stable, non-self-gravitating, homentropic, constant ℓ tori to *nonaxisymmetric* perturbations. They demonstrated the existence of a global instability which operates on the dynamical timescale. A sample of their numerical results is shown in Figure 1.7. The contour plots show the spatial structure of the eigenfunctions for the most unstable growing mode. The parameter μ is a dimensionless measure of the radial dimension of the torus at $z = 0$; for constant ℓ, $r_{in} = 1/(1+\mu)$, $r_{out} =$

$1/(1-\mu)$, $0 \leq \mu \leq 1$ (see ff., Chapter 3). Three points are worth noting in Fig. 1.7: (i) for thinner tori, the eigenfunction lacks significant vertical structure; (ii) the magnitude of the perturbations is concentrated toward the inner and outer boundaries of the torus; (iii) thicker tori excite smaller amplitude perturbations (this results in a reduced growth rate). Subsequent work revealed several other interesting features of what has come to be known as the Papaloizou-Pringle (PP) instability.[8] Many of these will be reviewed in Chapter 5, and so will not be touched on here.

For now it is sufficient to state that for the problem under discussion, the unstable modes fall into two classes: (a) the principal branch, which occurs for all $\mu < 0.59$ ($\Rightarrow r_2/r_1 < 3.9$), and in which all unstable modes have corotation near r_0, the pressure maximum of the torus; and (b) higher-order branches, which occur at higher μ, have lower growth rates than the principal branch, and do not corotate near $r = r_0$ (Goldreich, Goodman, & Narayan 1986 (GGN)).

The key to understanding the principal mode mechanism is the fact that it occurs even in *incompressible* fluids (the higher-order modes do not). In such fluids wave motion can only be supported on the boundaries, which are assumed free in these models. For a given azimuthal wavenumber m, there exist four modes which represent surface gravity waves propagating upstream and downstream along the inner and outer edges (see also Chapter 5). According to Blaes (1986),

> As the boundaries are brought closer together, the faster outer mode catches up with the slower inner mode, their corotation points coincide, and they merge to form a single mode which has high amplitude at both edges and a corotation point in between - this mode is unstable.

The *radial* structure of the mode is therefore nodeless, since the amplitudes of the surface waves decay with depth away from the surfaces (cf. Drazin & Reid 1982). If either of the boundaries are fixed, or if the outer boundary is removed to infinity, then the principal mode is stabilized (Blaes & Glatzel 1986; GGN).

---

[8] The original paper, PP (1984), should be read with caution, as it was subsequently shown that many of the analytic results were in error, as were certain points addressing the underlying cause of the instability. See Blaes (1986) and Narayan & Goodman (1989) for the necessary clarification.

The higher-order modes have been attributed to the amplification of sound waves between a reflecting boundary (inner or outer) and the corotation resonance (Goldreich & Narayan 1985; GGN; Narayan & Goodman 1989); a mechanism akin to what is believed to maintain spiral density waves in galaxies. The interesting physics of this process has been examined further by Drury (1985) and Glatzel (1987a, b, 1988).

Two other features of the PP instability are worthy of note. First, in a numerical study, Blaes (1987) found that the inclusion of an accretion flow in the 2D, constant ℓ, compressible annulus *led to complete stabilization, provided that $\dot{\mathcal{M}}$ is large enough* (see also Gat & Livio 1992). It has been conjectured that a 3D torus may not be so easily stabilized, since only a fraction of the boundary (near the midplane) is involved in accretion; the remainder is available for wave propagation and reflection (Narayan & Goodman 1989; Hawley 1991). Second, sufficiently strong self-gravity in a non-accreting torus can have the same effect, although it is likely that the torus then becomes Jeans-unstable (Goodman & Narayan 1988; Christodoulou & Narayan 1992; Christodoulou 1993). Massive, self-gravitating thick disks may occur during star formation.[9]

What are the consequences of the PP instability for accretion disks? Due to the rapid growth of the principal mode, the equilibrium conditions under which it occurs are precisely those least likely to be found in nature. Studies of nonaccreting tori have shown that disks with an initially constant angular momentum evolve toward less steep angular velocity profiles ($\Omega \sim r^{-1.8}$; Zurek & Benz 1986; Hawley 1991), where the principal mode is damped and only the more slowly growing higher-order modes are left. This means that although thick tori may exist, they may not be able to provide the super-Eddington luminosities observed in AGN. The less virulent higher-order modes may then perform a different role, acting as an effective viscosity and aiding in angular momentum transport (Hawley 1991).

---

[9] Recent observational (Aitken et al. 1993) and theoretical (Galli & Shu 1993) results suggest that massive protostellar disks may form in which self-gravity is balanced by strong magnetic fields. This would then constitute a third category of thick disk.

1.5 Magnetic Processes in Disks

Observations of the three characteristic systems discussed in §1.1 lead one naturally to a consideration of magnetic fields in the accretion disk environment. *Dynamo theory* is dedicated to the study of the generation and maintenance of such fields in astronomical objects. In the present context, due to the predominantly azimuthal flow, only fields which are purely azimuthal could possibly constitute truly static configurations. However, due to diffusive effects, such a field decays in time, unless it is somehow constantly regenerated. More generally, magnetic fields will neither be aligned with the circular flow, nor confined to the disk plane. Thus, *the theory of magnetized disks is, at some level, intrinsically time-dependent*, a complication which is not encountered for purely hydrodynamic disks.

Due to the increased complexity of magnetized disks, there exists no widely accepted analogue of the hydrodynamic "standard model." Historically, the interest in magnetic fields sprouted not from an ambition to provide such an elaborate construct, but rather from the hope that certain magnetic effects might aid in the resolution of issues unsolved by the standard model.

By way of motivation, consider the following brief example. The magnetic equivalent of the Reynolds stress introduced in §1.3, the Maxwell stress, is given by

$$\Pi_{r\phi}^{(m)} = \frac{< B_r B_\phi >}{4\pi} = \alpha p_{gas}. \tag{1.11}$$

There is considerable uncertainty as to whether $\Pi_{r\phi}^{(m)}$ scales with the gas pressure only, or (like the Reynolds stress) with the total pressure. Those who argue in favour of the former point out that while the gas may be assumed "frozen" to the magnetic field (the magnetohydrodynamic (MHD) approximation; see ff. §2.1), the radiation may not (Lightman & Eardley 1974; Stella & Rosner 1984). An important consequence of this scaling is that the inner region of the standard disk model is rendered *stable* to both thermal and viscous instabilities (Shakura & Sunyaev 1976; Piran 1978). As we shall see, however, fluids threaded by magnetic fields are subject to a host of instabilities, not all of which threaten the integrity of the disk.

1.5.1 Hydromagnetic instabilities: a brief survey

In this subsection, I describe a few examples of the qualitatively new behavior which can occur in the presence of magnetic fields. The interested reader is referred to the monographs of Schmidt (1966), Bateman (1977), and Cap (1976) for further details.

In the MHD approximation, a magnetic field **B** threading a fluid of electrical conductivity σ_e moving at a velocity **u** can be characterized by a dimensionless quantity

$$\mathrm{Re}_m \equiv 4\pi\sigma_e uL \approx \frac{|\nabla \times (\mathbf{u} \times \mathbf{B})|}{\left|\frac{1}{4\pi\sigma_e}\nabla^2\mathbf{B}\right|}, \tag{1.12}$$

called the magnetic Reynolds number. If Re_m is large the field and fluid are frozen together, while if Re_m is small the field-fluid coupling is weak and **B** can diffuse out of the fluid on timescales $O(L/u)$.

Magnetic reconnection is likely to be the most important diffusive process in magnetized accretion disks (Lightman & Eardley 1974; Coroniti 1981). While not an "instability" in the usual sense, reconnection is nevertheless a process whereby a given configuration can lower its own magnetic energy, often with drastic consequences for the surrounding medium. A good example is provided by the solar photosphere, wherein lines of flux in a high Re_m region interact with the overlying coronal plasma and field (Figure 1.8). Since regions near the boundaries of accretion disks may be qualitatively similar to this region of our Sun, well-known solar phenomena such as flaring and ionic winds may also occur in disks. Heating via reconnection of coronal loops has in fact been suggested as a primary source of the hard X-ray component ($T \gtrsim 5 \times 10^8$ K) observed in the spectra of X-ray binaries (Galeev, Rosner, & Vaiana 1979).

Although of great importance, I have chosen to ignore diffusive processes in this thesis in order to isolate effects of more immediate interest which are not yet understood; namely, those involving differential rotation and frozen-in magnetic fields. Insofar as it will reduce the total magnetic energy available to high Re_m instabilities then, magnetic diffusion is of interest. Thus I briefly reconsider its effects when reviewing the Balbus-Hawley instability in the following section.

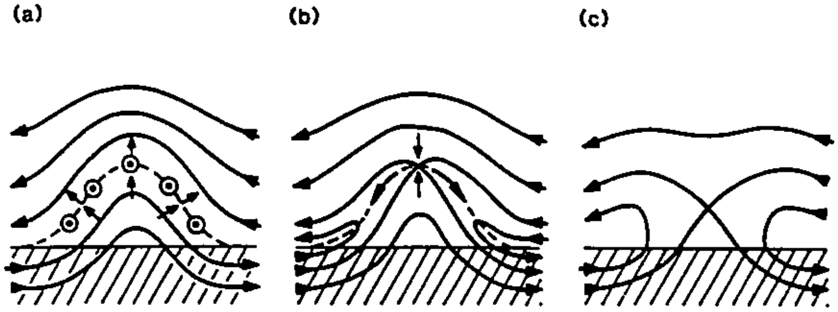

Figure 1.8: Flux emerges from the solar photosphere (hatched region) and interacts with overlying coronal plasma and field. (a) In the frozen-field limit the two plasmas remain distinct and a thin current sheet (dashed line) forms between them. (b) Reconnection results in field interconnection and plasma mixing across the boundary current sheet. (c) The end state is a potential field obeying the new photospheric boundary condition; the magnetic energy is reduced compared with (a), having been fed into the surrounding plasma (Cowley 1985).

To discuss non-diffusive magnetic instabilities one may distinguish between two main classes: those that result from bending the field lines, and those that do not. Beginning with the latter, a moment's thought shows that the only way to change a given magnetic field structure without bending field lines is to *interchange* them. The criterion for interchange instability has the rare distinction of being statable as a general theorem (Schmidt 1966):

> *Geometries in which the magnetic field lines curve toward the fluid along the entire fluid boundary are interchange-unstable, provided adjacent fieldlines in the direction of the pressure-gradient exist.*[10]

Interchange clearly requires rather special orientations of the magnetic field. Two well-known and astrophysically relevant examples are the cases of purely toroidal and vertical magnetic fields. The latter case has been shown in Figure 1.9, in the case where a magnetic field (directed into the page) lies outside an unmagnetized fluid and a perturbation is applied to the boundary in a direction perpendicular to the field. The protruding ripples (or "flutes") push against a weaker field, while the regions newly occupied by the field possess an increased magnetic pressure. The result is an exponential growth of the perturbation. Versions of this instability which could act in a strongly magnetized thin accretion disk have

---

[10] Unfortunately, the quoted source does not identify the original discoverer of this result.

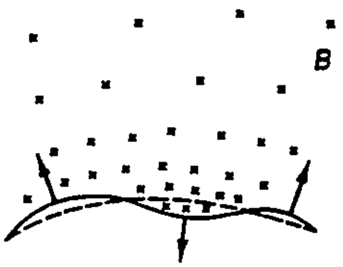

Figure 1.9: Top view of flute instability at a fluid (bottom) - vacuum (top) interface (Schmidt 1966).

been studied by Kaisig, Tajima, & Lovelace (1992) and more recently by Lubow & Spruit (1995) and Spruit, Stehle, & Papaloizou (1995).

There exists a large class of instabilities that result from bending the field lines. As the instabilities discussed in Chapters 3, 4, and 5 are all of this type, I will discuss only one further example here. The Parker (1966), or magnetic Rayleigh-Taylor instability, is thought to be important in a wide array of astrophysical contexts. By analogy with the classical Rayleigh-Taylor instability (Drazin & Reid 1982), the magnetic field plays the role of the light "fluid" in this picture, and an unstable configuration is one in which the horizontal magnetic field B_{horiz} decreases with height more rapidly than the corresponding density gradient. That is (Moffat 1978),

$$\frac{d}{dz}\left(\frac{B_{horiz}}{\rho}\right) < 0.$$

The Parker instability is slightly modified in the presence of differential rotation (Shu 1974; Foglizzo & Tagger 1994), and somewhat moreso in a self-gravitating fluid (Parker-Jeans instability; Elmegreen 1982). The combined effect has been examined by Elmegreen (1987), who considered the case of a (two-dimensional) galactic gas disk. Elmegreen found that when the magnetic field is in pressure equilibrium with turbulent motions in the surrounding gas, the linear instability growth time is similar to that for the nonmagnetic, nonrotating Jeans instability ($\approx 10^{7.5} - 10^{8}$ yr). The Parker-Jeans instability has important implications for the formation of structure in galaxies and, moreover, for the disk dynamo mechanism (see ff. §1.5.4). The buckling of magnetic field lines produced in the nonlinear stages of the

Figure 1.10: The Parker instability. Initially horizontal field lines rise in some places and fall in others, in such a way that matter loaded onto them slides off the peaks and sinks into the valleys, causing further distortion (Shu 1992).

instability (Figure 1.10) generates vertical field from horizontal, thus forming one link in the dynamo cycle.

1.5.2 The Balbus-Hawley and Velikhov-Chandrasekhar instabilities

Recently, Balbus & Hawley (1991) (BH) drew attention to an instability which should be quite generic to weakly-magnetized accretion disks. Velikhov (1959) and Chandrasekhar (1960, 1961) originally discovered the instability in models of Couette flow, where an incompressible fluid threaded by a uniform vertical magnetic field is placed between two rigid rotating cylinders.

The basic mechanism of the instability is as follows. Consider a conducting cylinder of fluid, rotating about the z-axis with a rotation law $\Omega = \Omega(r)$ which decreases with radius, and threaded by a uniform vertical magnetic field B_z. This is indeed an allowed equilibrium configuration (see ff., Chapter 2). Infinitesimal, axisymmetric perturbations to this equilibrium have two distinct and competing effects, both of which result from bending the field lines (Figure 1.11). First, the magnetic tension in the field tends to pull radially perturbed fluid elements back to their original radii. Second, the same tension forces an element to rotate at its *original* angular speed regardless of its *perturbed* radial location. The first effect is clearly stabilizing, but the second is the essence of the instability. Outwardly (inwardly) displaced fluid elements have local angular speeds which are larger (smaller) than that of the surrounding fluid, representing an excess (deficit) in centrifugal force that drives the element still further outward (inward).

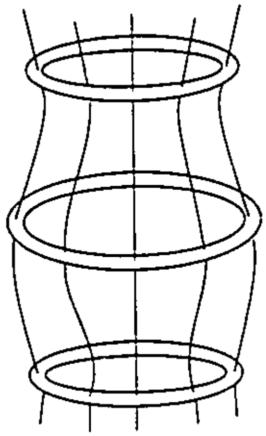

Figure 1.11: The Balbus-Hawley/Velikhov-Chandrasekhar instability. Rings of rotating gas expand and contract while conserving their angular velocity (Shu 1992).

Using a local stability analysis (see ff. Ch. 2), BH found that the instability grows on the dynamical timescale if and only if the Alfvén frequency, $\Omega_A \equiv kv_A < |d\Omega^2/d\ \ln r|^{1/2} \sim \Omega$ for power-law distributions of Ω, where k is the vertical wavenumber of the perturbation and $v_A \equiv B_z/(4\pi\rho)^{1/2}$ is the Alfvén speed. This result can be understood by defining the corresponding Alfvén timescale, $t_{mag} \sim \Omega_A^{-1}$, and noting that unless $t_{mag} \gtrsim t_{dyn}$, perturbations to the magnetic field will not have time to sample the shear, and will simply propagate away as torsional Alfvén waves (Shu 1992). Alternatively, since long wavelength (small k) perturbations do not bend the field lines as much as shorter wavelength (larger k) ones do, the radial return force loses out to the destabilizing centrifugal excess. This shows that there exists a critical wavelength longward of which the perturbation is stable; i.e. for instability,

$$\lambda < \lambda_{crit} \equiv \frac{\sqrt{3}}{2\pi}\frac{\Omega}{v_A}.$$

For a thin disk of scale height H, one might surmise that $\lambda_{crit} \lesssim 2H = 2\sqrt{2}c_s/\Omega$ (for an isothermal gas), from which BH derived $v_{A,crit}/c_s = \sqrt{6}/\pi \approx 0.8$ as a critical field strength above which the instability is no longer expected to occur. That is, *the local linear stability analysis suggests that the field may reach equipartition strength (with the thermal pressure) before the instability is quenched.* Physically, for $v_A > v_{A,crit}$ the restoring force on field lines dominates the resulting centrifugal excess, and the fluid element returns to its original location.

Since the instability relies only on the presence of a sufficiently weak B_z and a locally decreasing gradient of Ω, it is intrinsically *local* in nature. Thus although Velikhov and Chandrasekhar originally utilized a global model (i.e. Couette flow) the local analysis of BH, which assumes the wavelength of perturbations $\ll$ any characteristic disk length scale (e.g. H), is sufficient to establish the correct stability criterion. Other important properties of the instability, however, may be quite sensitive to global disk structure. As has been emphasized already, disks need not be thin, particularly magnetized disks which can develop significant coronae. Thus it is important to find the more general dependence of $v_{A,crit}$ on k_{crit} for disks of arbitrary vertical extent. This is a problem in *global*, as opposed to local, stability analysis, and will be undertaken in Chapter 3. There has also been some debate in the literature as to the influence of an azimuthal magnetic field B_ϕ on the BH instability (Knobloch 1992; Dubrulle & Knobloch 1993; Hawley & Balbus 1992; Kumar, Coleman, & Kley 1994). I address this question in Chapter 4. Throughout this thesis, I refer to the local version of the instability as the BH instability, and to its global counterpart as the VC instability. The necessity for this distinction is emphasized further in §2.7.

The original analysis of BH assumed a fluid of zero resistivity, ν_m. It is to this property that the following curious result can be traced. In the limit of vanishing B_z, one does *not* recover the linear stability criterion for nonmagnetic fluids, i.e. the Rayleigh criterion,

$$\frac{d(r^2\Omega)^2}{dr} \geq 0, \tag{1.13}$$

but rather,

$$\frac{d\Omega^2}{dr} \geq 0. \tag{1.14}$$

This result is obtained in both the local and global analyses, and is originally due to Chandrasekhar (1961), who offered the following explanation:

> ...in a fluid of zero resistivity the lines of magnetic force are permanently attached to the fluid ...and the permanency of this attachment is in no way

dependent on the strength of the magnetic field.

It may be, therefore, that (1.13) can be obtained from the magnetic model only in the limit $B_z \rightarrow 0$, ν_m *finite.*[11] Because it is a dissipative effect, finite resistivity is of greatest concern at short wavelengths/large wavenumbers. On dimensional grounds, one requires $\nu_m k_z^2/\Omega \ll 1$ for the resistivity to be negligible. Using the Spitzer (1962) resistivity for a hot ($\sim 10^4$ K) ionized gas, BH found that the latter requirement is equivalent to $\beta \equiv p_{mag}/p_{gas} \gg 10^{-10}$, which should be easily satisfied even in weakly magnetized disks. Dubrulle & Knobloch (1993) argued that even though a reasonable lower limit is obtained for the B_z field alone, including a strong equilibrium azimuthal field can lead to an unreasonably high lower limit on B_ϕ. These authors and Stepinski, Reyes-Ruiz & Vanhala (1993) also pointed out that the Spitzer resistivity is not likely to be applicable in cool protostellar disks, except perhaps on the upper and lower surfaces and near the inner radius, where the ionization fraction is fairly high.

With this in mind, Jin (1993) extended the analysis of BH to the $\nu_m \neq 0$ case, finding that when $k_z^2 \nu_m > 1.4\Omega$, the instability is damped. He went on to estimate the value of η for black hole, AGN, and CV disks, eventually concluding that resistivity would not damp the instability. However, adopting a model by Hayashi (1981) of the solar nebula, which accounts for recombination of H_2 on grains, the author was able to show that for the best-known grain abundances in protostellar regions, the instability *can* be damped outside of a small region $r \lesssim 0.1$ AU. Specifically, if f is the fractional grain abundance as compared with the interstellar value, then values of $f \simeq 1$ and $\beta \equiv 4\pi\rho c_s/|\mathbf{B}|^2 \gtrsim 10^4$ can lead to stabilization *throughout the remainder of the disk.* Smaller values of f and β allow the instability to persist, but only in the outer regions where cosmic ray ionization is effective.[12]

At a more fundamental level, finite resistivity effects are manifested by the degree of

---

[11] A formal proof of such seems to be lacking in the literature. Note also, in this connection, that the *unique* equilibrium rotation law for a *viscous* purely azimuthal flow is $\Omega(r) = A + B/r^2$, where A and B are constants (Chandrasekhar 1961). This form incorporates both of the limiting cases discussed here, seemingly indicating that the notion of "magnetic viscosity" is justified.

[12] Jin notes that it is likely that the instability is damped in the midplane even for small f and β, since grains tend to settle there, allowing effective recombination.

ionization in the disk gas. Magnetic fields couple only to the ions, which communicate with the neutrals via elastic collisions, collisional ionization, and recombinations. If the ionization ratio is low, as in protostellar disks, e.g., the coupling is weak and the BH instability will affect only a small portion of the fluid. Clearly, some minimum level of coupling is required for the BH instability to persist. To ascertain this level, Blaes & Balbus (1994) performed a linear stability analysis in a two-fluid disk of ions and neutrals. Their model also improved on BH by including compressibility and an equilibrium azimuthal field. They found: (1) If ionization and recombination can be neglected on an orbital timescale, adequate coupling is achieved when the collision frequency of a given neutral with the ions exceeds the local epicyclic frequency, $\kappa \equiv [rd\Omega^2/dr + 4\Omega^2]^{1/2}$. (2) If ionization equilibrium is maintained on t_{dyn}, sufficiently strong (but still subthermal) azimuthal fields can have a stabilizing effect. To avoid this, one requires potentially much higher collision frequencies between ions and neutrals. Although the analysis of Blaes & Balbus represents a significant improvement over both BH and Jin (1993), the authors caution that their results are not directly applicable to very dense, cool disks since dust grains are then expected to be the primary charge carriers and must be taken into account.

1.5.3 The issue of saturation

Dissipation due to finite resistivity and imperfect ion-neutral coupling is especially a concern in the context of turbulent viscosity, the application that BH originally had in mind. The issue of whether the BH instability can in fact lead to turbulence is fundamental, and can only be addressed by following the *nonlinear* evolution of the perturbations. While linear analysis suggests that the field may grow to equipartition strength with the thermal pressure (§1.5.2), dissipative processes could bring about saturation of the instability at more modest field strengths. The 2D numerical simulations conducted by Hawley & Balbus (1991, 1992) (HB), while displaying random motions and sustained field growth, are not decisive on this point because at late times the field strength and topology appear to be sensitive to the size of the computational domain. This makes the true impact of reconnection unclear (HB 1992; Goodman & Xu 1994). In addition, the simulations did not include vertical stratification and so were not sensitive to another important channel for removal of magnetic field, namely buoyancy.

The first noticable effect in the nonlinear simulations is the leveling off of the exponential growth of perturbations near equipartition. The system enters a more organized state consisting of radially inward and outward streaming velocities ("channel flow") in the initially purely circular flow (HB 1991, 1992; Goodman & Xu 1994; Stone & Norman 1994).[13] A second period of exponential growth then begins but at a reduced rate from the linear value. Stone & Norman (1994), using a global disk model with a magnetically-dominated corona, interpreted the inward component of the channel flow as indicative of radial disk collapse. For strong fields, the collapse is due to the action of magnetic braking, as the external coronal torque spins down the disk. For weak fields, the authors claim that only internal (magnetic) torques are responsible for collapse. However, as a significant amount of material in the disk midplane is still streaming *outward* in their simulations, the collapse interpretation seems somewhat premature. Moreover, Stone & Norman ignore resistive effects which can allow magnetic field to drift outward, dragging matter along with it (Lubow, Papaloizou, & Pringle 1994).

Fully three-dimensional (i.e. nonaxisymmetric) simulations of the BH instability were carried out by Hawley, Gammie, & Balbus (1995). These authors discovered that unless the magnetic field strength is made artificially large, the channel solution is not the ultimate saturated state of the BH instability. Rather, this solution breaks up into more random velocity structures at late times (Figure 1.12a). Calculation of the time-averaged Reynolds and Maxwell stress shows that the latter dominates and is correlated with the magnetic, not gas, pressure. Nevertheless, a naive estimate from equation (1.11) yields a time average of $\alpha \approx 0.4$ (Figure 1.12b), an encouraging figure from the point of view of a turbulent viscosity mechanism. The fact that the Maxwell stress dominates the Reynolds stress also has potential observational significance, if disk turbulent velocities can be successfully measured. For a fixed surface brightness disk, turbulent velocities in magnetized disks

---

[13] It is worth emphasizing that Goodman & Xu (1994), who utilize an *exact* nonlinear solution of the local incompressible MHD equations, find this channel flow. Thus, it cannot be an artifact of the ZEUS-2D numerical code used by both HB and Stone & Norman (1992).

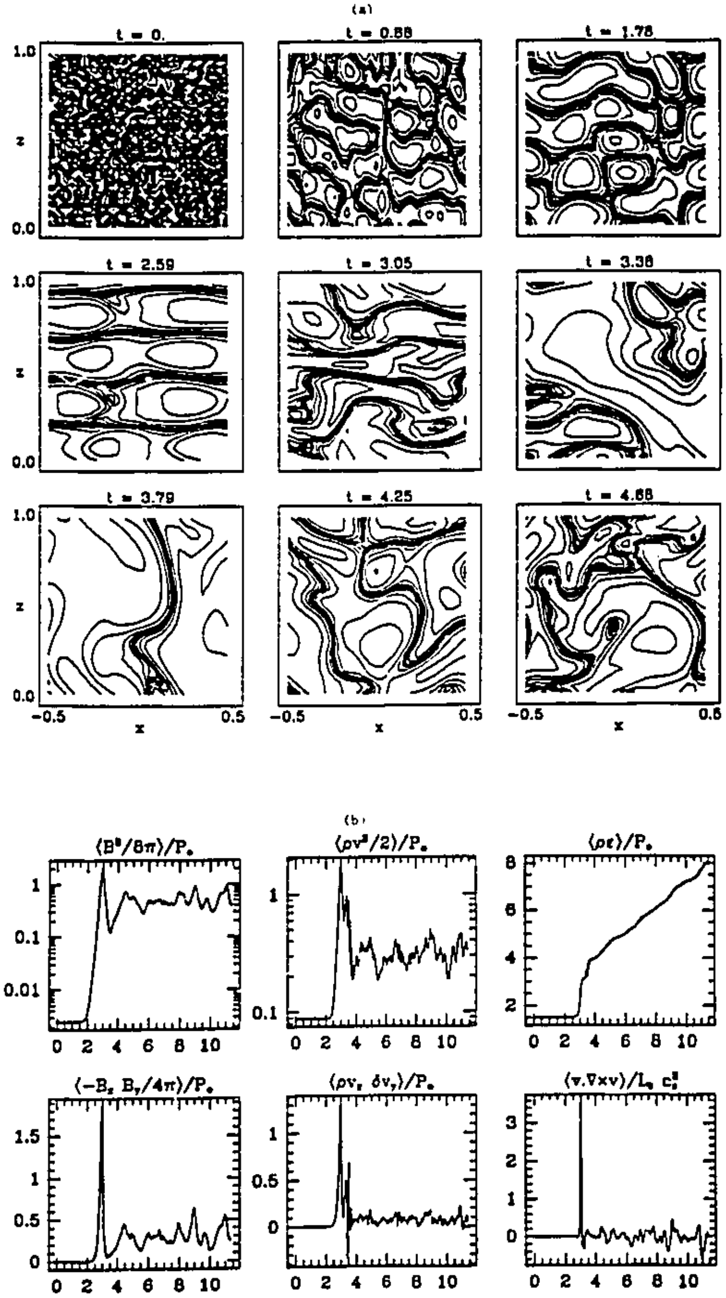

Figure 1.12: (a) Contour plots of perturbed azimuthal velocity δu_y in an (x, z) plane at a fixed value of y. The time in Keplerian orbits is indicated above each plot. The plots illustrate the development of a channel solution from small initial perturbations, and its eventual demise. (b) Time evolution of volume-averaged magnetic, kinetic, and thermal energies, Maxwell and Reynolds stress, and velocity field helicity for the model in (a). Time is given in orbits; P_0 is the initial pressure and L_x is the box size used in the simulation (Hawley, Gammie, & Balbus 1995).

should be smaller than those in purely hydrodynamic disks (Balbus, Gammie, & Hawley 1994). New techniques in Doppler tomography may make such observations possible in the near future (Horne 1995).

1.5.4 Instabilities, magnetic viscosity, and dynamos: a synthesis

As hinted in §1.5, dynamo theories of magnetic field generation are a study unto themselves. One has statistical dynamo theories which involve continuous magnetic fields, flux tube models which apply to intermittent magnetic structures, and MHD turbulence and magnetoconvection, which attempt to treat motions at a microscopic level. To review any one of these would take us far afield, nor is it needed for any of the work which follows. I refer the reader to the recent thesis of Schramkowski (1994) for an up to date discussion of these topics and extensive references.

What *would* be of value, however, is a concrete application of the instabilities described above; one which places their mere existence in context with the fundamental problems of accretion disk theory (e.g., the calculation of α from first principles). A recent paper by Tout & Pringle (1992) (TP) offers an ideal opportunity in this regard. These authors propose a simple disk dynamo model which relies on three fundamental, entirely hydromagnetic, processes: Parker instability, magnetic reconnection, and the BH instability.

Before going on it may be useful to briefly review the basic "$\alpha\omega$−dynamo" (Moffat 1978; see also Schramkowski 1994 for further references). The "ω-effect" signifies the generation of toroidal field from poloidal field via differential rotation, and is a process most agree will take place naturally in a disk environment. The poloidal field is generated from the toroidal by the "α-effect," which is really the crux of modern dynamo theory. Consider now the situation depicted in Figure 1.13. As mentioned in §1.5.1, a toroidal field which decreases sufficiently rapidly with height in a stratified medium is unstable to magnetic buoyancy. Assuming conditions are favourable for this to take place, a straight (frozen-in) field line can be distorted (Fig. 1.13a, b). Hence a vertical field component is generated. The problem now is to somehow produce the other poloidal component: the all-important radial field.

An important distinction between laminar and turbulent fluid flow can be made on the

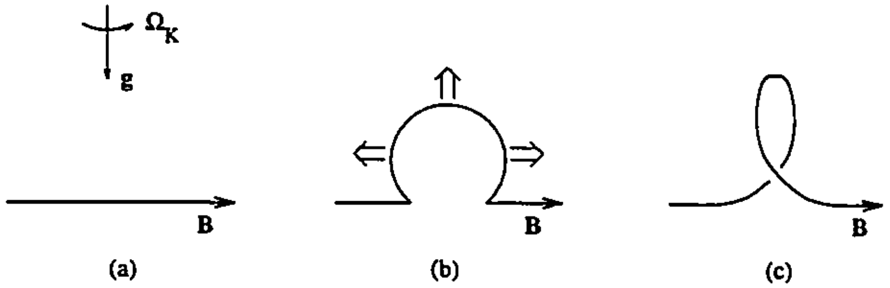

Figure 1.13: The α-effect. (Schramkowski 1994, after Takahara 1979).

basis of the quantity $I \equiv \int \mathbf{u}\cdot(\nabla \times \mathbf{u})dV$, the kinematic helicity. I gives an indication of how effective local Coriolis forces are in the fluid. A mean magnetic field immersed in a laminar fluid flow has $I = 0$. A turbulent magnetized flow can have $I > 0$; if the conditions appropriate for this are achieved, then the magnetic loop created in Fig. 1.13b can be twisted by the action of local Coriolis forces (Fig. 1.13c), and voilà: radial field has been created. This completes the dynamo cycle:

$$B_r,\ B_z \Rightarrow B_\phi \Rightarrow B_r,\ B_z.$$

A major problem in the above scheme is that there is widespread debate as regards the "appropriate conditions" for $I > 0$ (Moffat 1978; Parker 1979). I do not address the issue further, but simply explain the alternative suggested by TP which operates as follows. Consider an arbitrary magnetic field configuration in cylindrical geometry: (B_r, B_ϕ, B_z). Azimuthal field is generated by the shearing of radial field lines. Vertical field is generated via Parker instability of horizontal (radial and azimuthal) fields. The dynamo cycle is closed *not* by the α-effect, but by the BH instability, which generates radial from vertical field. Reconnection enters via the combined action of the Parker and BH instabilities; the excursions of field lines induced by the latter will sometimes cause adjacent lines of opposite polarity to overlap and reconnect. This leads to dissipation within the disk, as well as to flux loss in the exterior regions. TP retain only the essential details of each process, but model the time dependence explicitly, and follow the development of two characteristic equilibria (both of which are unstable) into the nonlinear regime.

The magnitude of all three magnetic field components is essentially controlled by that of B_z, which cannot exceed the maximum value $B_{z,max}/(\sqrt{4\pi\rho}c_s) \simeq \sqrt{6}/\pi \approx 0.8$ (§1.5.2). TP found that the ultimate solution shows oscillation in all three field components with a period $P \approx 2\Omega^{-1}$. The relative magnitude of the time averaged field components is:

$$B_r : B_\phi : B_z \approx 1 : 6 : 6.$$

The viscosity parameter α also oscillates in the TP solution, varying between 0.1 and 0.7, with a time average of $\alpha \approx 0.4$. About half of the energy released by the disk in their scheme (i.e. $\approx GM\dot{\mathcal{M}}/4r$) is the result of buoyant reconnection either near or beyond the upper and lower disk surfaces. This suggests the rather natural generation of an active disk corona or magnetic wind.

The TP model, while crude, is noteworthy insofar as it describes a self-sustaining dynamo using only (known) magnetic instabilities, and without recourse to processes such as hydrodynamic turbulence whose origin is considerably more obscure. The two traditional dynamo mechanisms that have been retained - buoyancy and reconnection - are not without their own problems, but these have always been much less serious than those associated with the α-effect. More detailed dynamo models which do not impose the latter are already under investigation (Brandenburg et al. 1994).

1.6 Scope and Outline of This Thesis

The above sections should have provided adequate motivation for a deeper study of magnetohydrodynamic instabilities in accretion disks. To proceed, I adopt as an equilibrium model not the standard thin disk of §1.2, but rather a *global* model which treats the radial structure of the disk explicitly. Such a model was originally motivated by two main stimuli: (1) the apparent controversy between local and global methods of stability analysis, as regards the Balbus-Hawley instability (Knobloch 1992; §2.7); and (2) the large body of work on global hydrodynamic instabilities in disks, which at the time I began this work, had not been extended to the magnetic context.

Chapter 2 provides a detailed overview of the equilibrium configurations and the techniques and known results of global stability analysis which apply to them. Some of the results in this chapter constitute original work on my part. The three chapters which follow examine different aspects of the linear stability of a particular global disk model from Chapter 2.

Chapter 3 is a reprint of the paper "On the Global Stability of Magnetized Accretion Disks. I. Axisymmetric Modes," published in the Astrophysical Journal:

> Curry, C., Pudritz, R. E., & Sutherland, P. G. 1994, ApJ, 434, 206-220.

To remedy typographical errors which appeared in the final published version, this paper has been included here in manuscript form. Chapter 4 is a preprint of the paper "On the Global Stability of Magnetized Accretion Disks. II. Vertical and Azimuthal Magnetic Fields," accepted for publication in the same journal:

> Curry, C., & Pudritz, R. E. 1995, ApJ, Nov 10 issue.

I carried out all of the analytical and numerical analysis, as well as the writing, in these two papers under the guidance of my supervisors Dr. Ralph Pudritz and Dr. Peter Sutherland.

Chapter 5 completes the programme initiated by the former two papers by examining nonaxisymmetric modes, and is presently being prepared for publication by myself and Dr. Pudritz. The analysis in this chapter, too, is my own. Finally, Chapter 6 discusses some applications of the current work, and mentions some possible future directions of fruitful research.

The material in Chapter 3 is reprinted with permission from the Astrophysical Journal; as principal author of material which originally appeared in the Astrophysical Journal, I hereby grant an irrevocable, non-exclusive license to McMaster University and the National Library of Canada to reproduce this material as part of the thesis.

Chapter 2

THEORY AND STABILITY OF THICK MHD DISKS: GENERAL RESULTS

2.1 The MHD Approximation: Fundamental Equations

The composition of an accretion disk is likely to be extremely varied. Although most of the material is expected to exist in the gas phase, ions, electrons, neutral atoms, molecules, dust grains, and electromagnetic fields are all believed present, each governed by its own unique physics. An exact, microscopic description of the situation is therefore prohibitive. In the low-energy limit, however, a macroscopic description will suffice. The theory of hydrodynamics, which allows one to define meaningful macroscopic quantities such as pressure, density, velocity, etc. and then to follow their evolution in space and time, has been quite successful in this regime. The basic equations of hydrodynamics are those expressing mass, momentum, and energy conservation. These are (Shu 1992; Landau & Lifshitz 1959)

$$\frac{D\rho}{\partial t} + \rho\nabla\cdot\mathbf{u} = 0, \tag{2.1}$$

$$\rho\frac{D\mathbf{u}}{Dt} = -\rho\nabla(\Psi_{int} + \Psi_{ext}) - \nabla p + \nabla_i\Pi_{ik} + \mathbf{f}_{rad}, \tag{2.2}$$

$$\rho T\frac{Ds}{Dt} = -\nabla\cdot\mathbf{F}_{cond} + Q^+ - Q^- + \Pi_{ik}\frac{\partial u_i}{\partial x_k}, \tag{2.3}$$

where $D/Dt \equiv \partial/\partial t + \mathbf{u} \cdot \nabla$ is the Lagrangian derivative, Ψ_{int} and Ψ_{ext} are the gravitational potentials due to the fluid itself and due to exterior sources (if any), and the remaining symbols are standard and may be found in the List of Symbols. These equations must be supplemented by the appropriate constitutive relations for the matter and radiation fields. Note that the latter are included in the hydrodynamic description, while other electromagnetic processes (e.g. electric and magnetic fields) are not. Before discussing how these can be brought into the fold, note that for self-gravitating fluids these relations are usually supplemented by Poisson's equation,

$$\nabla^2 \Psi_{int} = 4\pi G \rho. \tag{2.4}$$

Certain terms in these equations are not relevant to the goals of this thesis, as outlined in Ch. 1, and can be omitted at the outset. First, I ignore the terms which treat diffusive processes; namely, those proportional to Π_{ik} (viscous dissipation) and $\mathbf{F}_{cond}$ (heat conduction). Second, radiative interactions are neglected by setting $\mathbf{f}_{rad}$ (radiation force per unit volume) and $Q^+ - Q^-$ (volumetric heating and cooling functions) equal to zero. Finally, although self-gravity will not be included in the global stability analyses of the following chapters (due to the drastic increase in the complexity of global equilibria; cf. Fridman & Polyachenko 1984), I retain Ψ_{int} throughout most of this chapter, ignoring it only when absolutely necessary.

The presence of electric ($\mathbf{E}$) and magnetic ($\mathbf{B}$) fields necessitates the introduction of Maxwell's equations

$$\begin{aligned} \nabla \cdot \mathbf{E} &= 4\pi\rho_e, & (2.5)\\ \nabla \times \mathbf{E} &= -\frac{1}{c}\frac{\partial \mathbf{B}}{\partial t}, & (2.6)\\ \nabla \cdot \mathbf{B} &= 0, & (2.7)\\ \nabla \times \mathbf{B} &= \frac{4\pi}{c}\mathbf{J} + \frac{1}{c}\frac{\partial \mathbf{E}}{\partial t}, & (2.8) \end{aligned}$$

where ρ_e and $\mathbf{J}$ are the electric charge and current densities, respectively. Note that I employ Gaussian units throughout. In the *magnetohydrodynamic (MHD) approximation*, one supposes a high density of ions in the fluid, so that collisions of all species with the ions occur on a much shorter timescale than variations in $\mathbf{E}$ and $\mathbf{B}$ (cf. Jackson 1975). Such a highly conducting fluid contains little or no charge separation between ions and electrons, and so can be described by a *single* set of macroscopic fluid variables ρ, p, $s, \ldots$, etc. These considerations lead to two important simplifications of Maxwell's equations. First, the displacement current, $c^{-1}\partial \mathbf{E}/\partial t$, in equation (2.8) can be neglected in comparison with the conduction current $\mathbf{J}$. Second, accumulation of space charges inside the fluid can be neglected (i.e. the fluid is electrically neutral), meaning that Coulomb's law, equation (2.5), may be ignored. Then $\mathbf{E}$ is entirely determined by the two remaining Maxwell equations and Ohm's law,

$$\mathbf{J} = \sigma_e(\mathbf{E} + \frac{\mathbf{u}}{c} \times \mathbf{B}) = \sigma_e \mathbf{E}', \tag{2.9}$$

where σ_e is the electrical conductivity, and $\mathbf{E}'$ is the electric field measured by an observer in the rest frame of the fluid. These two approximations only introduce an error $O(|\mathbf{u}|^2/c^2)$ into the problem, and so are of little concern in most non-relativistic situations (Jackson 1975, Shu 1992).

In addition to equation (2.9), the fluid and magnetic field are coupled via the Lorentz force, $\mathbf{f}_L = c^{-1}(\mathbf{J} \times \mathbf{B})$, which enters the RHS of the Euler equation (2.2). Substituting equation (2.9) into (2.6) using (2.8) and (2.7) gives the *induction equation*:

$$\frac{\partial \mathbf{B}}{\partial t} = \nabla \times (\mathbf{u} \times \mathbf{B}) - \nabla \times (\eta \nabla \times \mathbf{B}), \tag{2.10}$$

where $\eta \equiv c^2/(4\pi\sigma_e)$ is the electrical resistivity. I shall in fact assume that the latter is zero, whence $\sigma_e \to \infty$, and (2.9) implies, for finite $\mathbf{J}$,

$$\mathbf{E} = -\frac{\mathbf{u}}{c} \times \mathbf{B},$$

showing quite clearly that $\mathbf{E}$ is indeed of secondary importance as compared with $\mathbf{B}$ in a non-relativistic, perfectly-conducting fluid. The resulting form of (2.10) is often referred to as the "flux-freezing" equation, since the field lines do not diffuse out of the fluid on any timescale.

The complete set of simplified equations now reads (in units such that $c = 1$):

$$\rho \frac{D\mathbf{u}}{Dt} = -\rho \nabla(\Psi_{int} + \Psi_{ext}) - \nabla p + \mathbf{J} \times \mathbf{B}, \tag{2.11}$$

$$\frac{Ds}{Dt} = 0, \tag{2.12}$$

$$\frac{\partial \mathbf{B}}{\partial t} = \nabla \times (\mathbf{u} \times \mathbf{B}), \tag{2.13}$$

with equations (2.1) and (2.4) unchanged. The energy equation (2.12) now describes isentropic flow, in which the entropy of each fluid particle remains constant along its path (Tassoul 1978), and allows one to write the equation of state as $p = p(\rho, s)$. For an ideal gas, $p = k_B \rho T/m$ and

$$s = c_v \ln\left(p\rho^{-\gamma}\right) + \text{constant}, \tag{2.14}$$

whence (2.12) reduces to

$$\frac{D}{Dt}\left(\frac{p}{\rho^\gamma}\right) = 0, \tag{2.15}$$

where $\gamma = c_p/c_v$ and c_p and c_v are the specific heats at constant pressure and volume, respectively. In passing, note that the terms *adiabatic* and *isentropic* are entirely equivalent when viscous dissipation is ignored, and that if one makes the further restriction $\nabla s = 0$, the flow is termed *homentropic*. In that case, equation (2.14) implies the *polytropic* relation,

$$p = A\rho^\gamma. \tag{2.16}$$

An isothermal fluid, e.g., has $\gamma = 0$, an adiabatic one $\gamma = 5/3$, and an incompressible one, $\gamma \to \infty$.

2.2 The Equilibria

Let us now seek stationary solutions of the above equations which describe a magnetized, thick disk in a state of pure rotation (i.e. non-accreting). Adopting cylindrical coordinates (r, ϕ, z), reasonable forms of the velocity and magnetic fields are

$$\mathbf{u} = [0, r\Omega(r,z), 0] \quad \text{and} \quad \mathbf{B} = [0, B_\phi(r,z), B_z(r,z)]. \tag{2.17}$$

In contrast to the stellar case (Tayler 1973), it is acceptable to ignore the radial component of $\mathbf{B}$, in the first approximation, when the accretion velocity, $u_r = 0$. This assumption is also necessary to maintain true stationarity; when $B_r \neq 0$, the ϕ-component of the induction equation reads

$$\frac{\partial B_\phi}{\partial t} = r\mathbf{B} \cdot \nabla\Omega = r\left(B_r \frac{\partial \Omega}{\partial r} + B_z \frac{\partial \Omega}{\partial z}\right). \tag{2.18}$$

For the bulk of this thesis I shall be concerned with the effect of an axial field, sometimes in concert with an azimuthal component, on a strong, differentially-rotating flow. From the above one therefore sees that B_ϕ *grows linearly with time unless*

$$B_r = 0 \quad \text{and} \quad \frac{\partial \Omega}{\partial z} = 0.$$

Equation (2.18) is key to understanding several effects of magnetic fields on shearing fluids, including the BH instability discussed in Ch. 1. The statement $\mathbf{B} \cdot \nabla \Omega = 0$, Ferraro's corotation theorem, states that to maintain stationarity, a magnetic field tends to enforce rigid rotation in the surrounding flow. Given that B_r vanishes, equation (2.7) and the ϕ-component of equation (2.11) imply

$$\frac{\partial B_z}{\partial z} = 0, \quad \text{and} \quad B_z \frac{\partial B_\phi}{\partial z} = 0.$$

Together, these results show that $\Omega = \Omega(r)$ and $\mathbf{B} = \mathbf{B}(r)$, while Ψ_{int}, Ψ_{ext}, ρ, p, and s are functions of both r and z in general.

Consider the equilibria permitted by these results. With Ω and $\mathbf{B}$ functions of r only, the Euler equation (2.11) becomes

$$r\Omega^2 \hat{\mathbf{r}} - \frac{\nabla p_T}{\rho} - \nabla(\Psi_{int} + \Psi_{ext}) - \frac{B_\phi^2}{4\pi \rho r} \hat{\mathbf{r}} = 0, \tag{2.19}$$

where $p_T \equiv p + |\mathbf{B}|^2/8\pi$ is the total (gas plus magnetic) pressure. It is convenient to introduce the "potentials"

$$\Psi_{rot} \equiv - \int r\Omega^2 dr, \quad \Psi_{mag} \equiv \frac{1}{8\pi} \int \frac{2B_\phi^2}{\rho r} dr, \tag{2.20}$$

and the enthalpy,

$$h \equiv - \int \frac{dp_T}{\rho}. \tag{2.21}$$

Then the r-component of equation (2.19) can be integrated, giving

$$h = h_0 + (\Psi_{int} + \Psi_{ext} - \Psi_0) + (\Psi_{rot} - \Psi_{rot\,0}) + (\Psi_{mag} - \Psi_{mag\,0}), \tag{2.22}$$

where the subscript '0' refers to a quantity's value at the pressure maximum of the configuration, $(r = r_0, z = 0)$.[1]

---

[1] One is free to *choose* the various arbitrary constants appearing in the equilibrium equations such that this is the case.

If $\Omega(r)$ is known, Ψ_{rot} can be easily calculated, but explicit forms of Ψ_{mag} and h await the specification of a definite relation between ρ and B. Note, however, that

$$-\frac{1}{\rho}\frac{\partial p_T}{\partial r} - \frac{B_\phi^2}{4\pi\rho r} = -\left\{\frac{1}{\rho}\frac{\partial p}{\partial r} + \frac{1}{8\pi\rho}\left[\frac{1}{r^2}\frac{d}{dr}(r^2 B_\phi^2) + \frac{dB_z^2}{dr}\right]\right\},$$

which shows that when $B_\phi \sim r^{-1}$,

$$h - \Psi_{mag} = -\int \frac{1}{\rho} d\left(p + \frac{B_z^2}{8\pi}\right) = -\int \frac{dp}{\rho}, \tag{2.23}$$

where the latter equality follows if B_z = constant. This configuration, i.e. $B_\phi \sim r^{-1}$, B_z = constant, happens to be *the unique zero current-density solution for this class of equilibria.* This property will be found useful in the section which follows.

2.2.1 Toroidal equilibria

The geometry of a torus is the most general axisymmetric one which includes both thick and (as a special case - see Ch. 1) thin disks. I employ the same formalism as in the hydrodynamic case, which can be found, e.g., in Papaloizou & Pringle (PP) (1984).

Due to the above-mentioned interdependence of ρ and B_ϕ, it is difficult to make further progress in general. However, when the zero-current situation examined above holds, equations (2.22) and (2.23) along with (2.16) yield

$$\frac{p}{\rho} = \frac{p_0}{\rho_0} - \frac{\gamma - 1}{\gamma}[(\Psi_{int} + \Psi_{ext} - \Psi_0) + (\Psi_{rot} - \Psi_{rot\,0})], \tag{2.24}$$

which is *identical* to the hydrodynamic expression (PP 1984). The appropriate external gravitational potential is that of a Newtonian point mass, i.e.

$$\Psi_{ext} = -\frac{GM}{(r^2 + z^2)^{1/2}}. \tag{2.25}$$

Also, one often assumes that the rotation follows a power-law, i.e.

$$\Omega = \Omega_0 (r/r_0)^{-a} \quad \Rightarrow \quad \Psi_{rot} = \frac{\Omega_0^2 r_0^2}{2(a-1)}\left(\frac{r}{r_0}\right)^{-2(a-1)}, \tag{2.26}$$

where Ω_0 and a are positive constants. Here equation (2.20) has been used, setting the additive constant of integration to zero to ensure that Ψ_{rot} vanishes as $r \rightarrow \infty$. If Ψ_{int} is specified, and all magnetic fields taken to be continuous across the boundaries, then solving equation (2.24) with $p = 0$ gives the equation of the fluid surface. For example, when $\Psi_{int} = 0$ one finds

$$\left[\left(\frac{r}{r_0}\right)^2 + \left(\frac{z}{z_0}\right)^2\right]^{-1/2} - 1 + \frac{1-(r/r_0)^{-2(a-1)}}{2(a-1)} + \frac{\mu^2}{2} = 0, \tag{2.27}$$

where $\mu^2 \equiv 2\gamma p_0 r_0/[GM\rho_0(\gamma-1)]$ is a constant equal to the ratio of thermal to kinetic energy at $r_0 \equiv (GM/\Omega_0^2)^{1/3}$, the pressure maximum of the torus. μ gives a measure of the torus' overall extent in the r-direction (Blaes 1986). Hence, for every a, there exists a continuum of toroidal equilibria, depending on the value of μ. These models can be distinguished by solving for the radial boundaries of the torus at its midplane, i.e. by setting $z = 0$ in equation (2.27) and solving for r. Consider a in the range $3/2 \leq a \leq 2$ (Ch. 3). When $a = 2$, one finds

$$\frac{r_\pm}{r_0} = \frac{1}{1\mp\mu},$$

where r_- and r_+ are the inner and outer radii of the torus at $z = 0$, respectively. For this a surfaces of constant density near the pressure maximum are concentric circles (see Fig. 1.6). For $a < 2$ these become ellipses, and for $a \to 3/2$ the eccentricity of these ellipses tends to ∞, $\mu^2 = 0$, and pressure support becomes negligible. This is the Keplerian case.

2.2.2 Homogeneous, non-self-gravitating, cylindrical equilibria

By considering the fluid to be homogeneous, one obviates the need to specify a precise relation between ρ and $\mathbf{B}$. For definiteness, I also adopt a power-law behavior for the magnetic fields; i.e.

$$B_\phi = B_{\phi 0}(r/r_0)^{-b+1}, \quad B_z = B_{z0}(r/r_0)^{-c+1}, \tag{2.28}$$

where $B_{\phi 0}$, B_{z0}, b and c are positive constants. Then equation (2.20) gives

$$\Psi_{mag} = \frac{B_{\phi 0}^2}{4\pi\rho}\frac{(r/r_0)^{-2(b-1)}}{2(1-b)}. \tag{2.29}$$

The equilibrium relation (2.22) now becomes

$$\begin{aligned} -\frac{p_T}{\rho} = -\frac{p_{T0}}{\rho} &+ GM\left(\frac{1}{r_0}-\frac{1}{r}\right) + \frac{\Omega_0^2 r_0^2}{2(a-1)}\left[\left(\frac{r}{r_0}\right)^{-2(a-1)} - 1\right] \\ &+ \frac{B_{\phi 0}^2}{8\pi\rho(1-b)}\left[\left(\frac{r}{r_0}\right)^{-2(b-1)} - 1\right], \end{aligned}$$

where I have assumed that

$$\Psi_{int} = 0 \quad \text{and} \quad \Psi_{ext} = -\frac{GM}{r}. \tag{2.30}$$

The purely radial dependence of the external potential is justified if, at every radius r, only heights such that $z \ll r$ are considered, so that there is little variation of Ψ_{ext} with z (cf. Blaes & Glatzel 1986; Jaroszyński 1988; Kumar, Coleman, & Kley 1994). The model therefore adequately describes the region near the midplane of a thick accretion disk.[2] Due to the removal of the z-dependence from the problem, the equilibrium is no longer toroidal, but rather infinite-cylindrical.

2.3 Exterior Fields and Boundary Conditions

At the fluid-vacuum interface, the boundary conditions (Tassoul 1978)

$$\left\langle -\left(p + \frac{|\mathbf{B}|^2}{8\pi}\right)\hat{\mathbf{n}} + \frac{\mathbf{B}}{4\pi}(\hat{\mathbf{n}}\cdot\mathbf{B})\right\rangle = 0, \tag{2.31}$$

$$\langle \hat{\mathbf{n}}\cdot\mathbf{B}\rangle = 0, \tag{2.32}$$

must be satisfied, where $\hat{\mathbf{n}}$ is the unit normal directed outward from the fluid at a boundary surface and the angle brackets denote a jump in the enclosed quantity across the surface, taken in the direction of $\hat{\mathbf{n}}$. The first condition (which follows from equation (2.11)) expresses the requirement that the normal component of the material and magnetic stresses be continuous across the surface, while the second (which follows from equation (2.7)) expresses conservation of magnetic flux. One sees from equations (2.31) and (2.32) that the magnetic field outside the shell must be specified and that, in particular, *the location of the boundaries depends not only on the magnetic field interior to the fluid, but also on that to its exterior.*

For definiteness, let us examine the form of the above boundary conditions in two specific fluid geometries. In the toroidal equilibria examined in §2.2.1, $\hat{\mathbf{n}}$ and B_ϕ are everywhere orthogonal. Thus equation (2.32) becomes simply $\langle \hat{\mathbf{n}}\cdot\mathbf{B}\rangle = \langle B_z \cos\theta\rangle = 0$, where θ is the

---

[2] As regards the stability of such a model, any instability occuring in the midplane should influence regions $z \gtrsim r$ on a dynamical timescale $t = z/c_s = r/u_K = t_{dyn}$ (equation (1.4)).

angle between $\hat{\mathbf{n}}$ and $\hat{\mathbf{z}}$. Taking the dot product of $\hat{\mathbf{z}}$ with equation (2.31) from the left, and denoting surface quantities with the subscript S, I obtain

$$p_S = \frac{< B_\phi^2 >}{8\pi} \cos\theta,$$

since the gas pressure vanishes in the exterior. Therefore, if B_ϕ is continuous across S, then $p_S = 0$, and useful hydrodynamic results like the hydrostatic balance condition, equation (2.24), can be employed. For the cylindrical equilibria examined in §2.2.2, $\hat{\mathbf{n}} = -\hat{\mathbf{r}}$ at $r = r_1$ and $+\hat{\mathbf{r}}$ at $r = r_2$, so $\hat{\mathbf{n}} \cdot \mathbf{B} = 0$ everywhere on S. Equation (2.31) becomes

$$p(r_{1,2}) = -\frac{1}{8\pi} \left\langle B_\phi^2(r_{1,2}) + B_z^2(r_{1,2}) \right\rangle.$$

In the work that follows, I will confine attention to a current-free external field, sometimes called a "potential field," for which

$$\mathbf{J}^{(V)} = \nabla \times \mathbf{B}^{(V)} = 0, \tag{2.33}$$

where the superscript V denotes a vacuum quantity. A more satisfactory approach would be to treat the exterior field as *force-free*, but this could be achieved only at the expense of a considerably more complex mathematical treatment.[3] A potential field might result if the Alfvén speed outside the disk is high enough that efficient reconnection takes place from a more complicated initial field structure; e.g., as in the solar corona (§1.5.1; Spruit et al. 1995).

In the cylindrical case equation (2.33) implies

$$B_\phi^{(V)}(r) = B_{\phi 0}^{(V)}(r/r_0)^{-1} \quad \text{and} \quad B_z^{(V)}(r) = B_{z0}^{(V)}. \tag{2.34}$$

Taking the fields to be continuous across r_1 and r_2 and adopting the power-law forms (2.28) then gives

$$B_{\phi 0,\text{in}}^{(V)} = B_{\phi 0}(r_1/r_0)^{-b+2}, \quad B_{\phi 0,\text{out}}^{(V)} = B_{\phi 0}(r_2/r_0)^{-b+2}, \quad \text{and} \quad B_{z0}^{(V)} = B_{z0},$$

where the subscripts "in" and "out" refer to the interior ($r < r_1$) and exterior ($r > r_2$) vacuum regions, respectively. Note that when $b \neq 2$ these conditions lead to a current discontinuity on S; for this reason, I shall usually take $b = 2$, whence $B_{\phi 0,\text{in}}^{(V)} = B_{\phi 0,\text{out}}^{(V)} = B_{\phi 0}$.

---

[3] This would best be carried out by transforming to coordinates centred on the pressure maximum of the torus; cf. Blaes (1986).

2.4 The Perturbations

2.4.1 The most general linearized perturbation equations: interior

Suppose that at $t = 0$ the equilibrium flow of §2.2 is everywhere perturbed by infinitesimal amounts; i.e. for any physical variable X, we write $X+\delta X$, $\delta X \ll X$. Here δX, the *Eulerian* change in a fluid variable X, is defined as the difference between X and its perturbed value evaluated at the same time and place. To first order in these small perturbations, equations (2.1), (2.4), and (2.11) - (2.13) become

$$
\begin{aligned}
\frac{\partial \delta\rho}{\partial t} + \Omega\frac{\partial \delta\rho}{\partial \phi} + \nabla\cdot(\rho\delta\mathbf{u}) &= 0, && (2.35)\\
\nabla^2\delta\Psi_{int} &= 4\pi G\delta\rho, && (2.36)
\end{aligned}
$$

$$
\begin{aligned}
&\frac{\partial \delta u_r}{\partial t} + \Omega\frac{\partial \delta u_r}{\partial \phi} - 2\Omega\delta u_\phi + \frac{1}{\rho}\frac{\partial \delta p_T}{\partial r} + \frac{\partial \delta\Psi_{int}}{\partial r} - \frac{\delta\rho}{\rho^2}\left(\frac{\partial p_T}{\partial r} + \frac{B_\phi^2}{4\pi r}\right)\\
&\qquad -\frac{1}{4\pi\rho}\left[\frac{B_\phi}{r}\frac{\partial \delta B_r}{\partial \phi} + B_z\frac{\partial \delta B_r}{\partial z} - \frac{2B_\phi\delta B_\phi}{r}\right] = 0, \qquad (2.37)
\end{aligned}
$$

$$
\begin{aligned}
&\frac{\partial \delta u_\phi}{\partial t} + \Omega\frac{\partial \delta u_\phi}{\partial \phi} + \frac{1}{r}\frac{d\ell}{dr}\delta u_r + \frac{1}{\rho r}\frac{\partial \delta p_T}{\partial \phi} + \frac{1}{r}\frac{\partial \delta\Psi_{int}}{\partial \phi}\\
&\qquad -\frac{1}{4\pi\rho}\left[\left(\frac{B_\phi}{r} + \frac{\partial B_\phi}{\partial r}\right)\delta B_r + \frac{B_\phi}{r}\frac{\partial \delta B_\phi}{\partial \phi} + B_z\frac{\partial \delta B_\phi}{\partial z}\right] = 0, \qquad (2.38)
\end{aligned}
$$

$$
\begin{aligned}
&\frac{\partial \delta u_z}{\partial t} + \Omega\frac{\partial \delta u_z}{\partial \phi} + \frac{1}{\rho}\frac{\partial \delta p_T}{\partial z} + \frac{\partial \delta\Psi_{int}}{\partial z} - \frac{\delta\rho}{\rho^2}\frac{\partial p_T}{\partial z}\\
&\qquad -\frac{1}{4\pi\rho}\left[\frac{\partial B_z}{\partial r}\delta B_r + \frac{B_\phi}{r}\frac{\partial \delta B_z}{\partial \phi} + B_z\frac{\partial \delta B_z}{\partial z}\right] = 0, \qquad (2.39)
\end{aligned}
$$

$$
\begin{aligned}
\frac{\partial \delta s}{\partial t} + \Omega\frac{\partial \delta s}{\partial \phi} + \delta\mathbf{u}\cdot\nabla s &= 0, && (2.40)\\
\delta p = \left(\frac{\partial p}{\partial \rho}\right)_s \delta\rho + \left(\frac{\delta p}{\delta s}\right)_\rho \delta s,& && (2.41)
\end{aligned}
$$

$$
\frac{\partial \delta B_r}{\partial t} + \Omega\frac{\partial \delta B_r}{\partial \phi} - \frac{B_\phi}{r}\frac{\partial \delta u_r}{\partial \phi} - B_z\frac{\partial \delta u_r}{\partial z} = 0, \qquad (2.42)
$$

$$
\frac{\partial \delta B_\phi}{\partial t} + \Omega\frac{\partial \delta B_\phi}{\partial \phi} - B_z\frac{\partial \delta u_\phi}{\partial z} + \frac{\partial (B_\phi\delta u_r)}{\partial r} + B_\phi\frac{\partial \delta u_z}{\partial z}
$$

$$+\left[\Omega - \frac{d(r\Omega)}{dr}\right]\delta B_r = 0, \tag{2.43}$$

$$\frac{\partial \delta B_z}{\delta t} + \Omega\frac{\partial \delta B_z}{\delta \phi} + \frac{\partial B_z}{\partial r}\delta u_r + \frac{B_z}{r}\left[\frac{\partial(r\delta u_r)}{\partial r} + \frac{\partial \delta u_\phi}{\partial \phi}\right] - \frac{B_\phi}{r}\frac{\partial \delta u_z}{\partial \phi} = 0, \tag{2.44}$$

where $p_T \equiv p + |\mathbf{B}|^2/8\pi$ is the total pressure and $\ell \equiv r^2\Omega$ is the specific angular momentum.

Both the toroidal and cylindrical equilibria described in this chapter possess symmetries which can be used to simplify the most general perturbation equations given above. The three most obvious of these symmetries are: (i) axisymmetry (i.e. independence of the equilibrium quantities on ϕ), (ii) time invariance, and (iii) equatorial symmetry (i.e. reflection about $z = 0$). The first allows us to Fourier analyze the perturbations as

$$\delta X \sim \exp(im\phi), \tag{2.45}$$

where m is an integer. The time-independence of the coefficients in the perturbation equations suggests the adoption of

$$\delta X \sim \exp(i\omega t), \tag{2.46}$$

i.e. "normal mode" perturbations. If Im $\omega < 0$ for any solution of the above equations, then one can say with certainty that the configuration is linearly unstable. However, even if Im $\omega \geq 0$ for all solutions of the form (2.46), one cannot be assured of linear stability to arbitrary initial perturbations unless the solutions form a complete set; the conditions for this completeness were discussed by Dyson & Shutz (1979).[4] Finally, equatorial symmetry permits expansion of the perturbations in terms of even and odd functions of z. While this simplification incurs no loss of generality, I shall not make use of it.

Adopting (2.16), (2.45) and (2.46), equations (2.35) - (2.44) become

$$i\sigma\delta\rho + \frac{1}{r}(r\rho\delta u_r)' + \frac{im\rho}{r}\delta u_\phi + (\rho\delta u_z)^\bullet = 0, \tag{2.47}$$

$$\frac{1}{r}(r\delta\Psi'_{int})' - \frac{m^2}{r^2}\delta\Psi_{int} + (\delta\Psi_{int})^\bullet = 4\pi G\delta\rho, \tag{2.48}$$

---

[4] In certain circumstances, the perturbations may grow as polynomials in time, instead of as exponentials (Case 1960).

$$
\begin{aligned}
i\sigma\delta u_r - 2\Omega\delta u_\phi + \frac{(\delta p_T)'}{\rho} + (\delta\Psi_{int})' - \frac{\delta\rho}{\rho^2}\left(p_T' + \frac{B_\phi^2}{4\pi r}\right) \\
-\frac{1}{4\pi\rho}\left[\frac{im}{r}B_\phi\delta B_r + B_z(\delta B_r)^\bullet - \frac{2B_\phi\delta B_\phi}{r}\right] &= 0, \qquad (2.49)
\end{aligned}
$$

$$
\begin{aligned}
i\sigma\delta u_\phi + \frac{\ell'}{r}\delta u_r + \frac{im}{r}\left(\frac{\delta p_T}{\rho} + \delta\Psi_{int}\right) \\
-\frac{1}{4\pi\rho}\left[\left(B_\phi' + \frac{B_\phi}{r}\right)\delta B_r + \frac{im}{r}B_\phi\delta B_\phi + B_z(\delta B_\phi)^\bullet\right] &= 0, \qquad (2.50)
\end{aligned}
$$

$$
\begin{aligned}
i\sigma\delta u_z + \frac{(\delta p_T)^\bullet}{\rho} + (\delta\Psi_{int})^\bullet - \frac{\delta\rho}{\rho^2}p_T^\bullet \\
-\frac{1}{4\pi\rho}\left[B_z'\delta B_r + \frac{im}{r}B_\phi\delta B_z + B_z(\delta B_z)^\bullet\right] &= 0, \qquad (2.51)
\end{aligned}
$$

$$
\delta p_T = \frac{\gamma p}{\rho}\delta\rho + \frac{1}{4\pi}(B_\phi\delta B_\phi + B_z\delta B_z), \qquad (2.52)
$$

$$
\begin{aligned}
i\sigma\delta B_r - \frac{im}{r}B_\phi\delta u_r - B_z(\delta u_r)^\bullet &= 0, \qquad (2.53)\\
i\sigma\delta B_\phi - B_z(\delta u_\phi)^\bullet + (B_\phi\delta u_r)' + B_\phi(\delta u_z)^\bullet - r\Omega'\delta B_r &= 0, \qquad (2.54)\\
i\sigma\delta B_z + B_z'\delta u_r + \frac{B_z}{r}[(r\delta u_r)' + im\delta u_\phi] - \frac{im}{r}B_\phi\delta u_z &= 0, \qquad (2.55)
\end{aligned}
$$

where $\sigma \equiv \omega + m\Omega$, and primes and dots denote $\partial/\partial r$ and $\partial/\partial z$, respectively.

The above is a system of nine equations in the nine unknowns $\delta\mathbf{u}$, $\delta\mathbf{B}$, δp_T, $\delta\rho$ and $\delta\Psi_{int}$, and thus is solvable in principle. One might proceed by: (i) solving equations (2.53) - (2.55) for the components of $\delta\mathbf{B}$ and substituting into the remaining equations, leaving six equations in six unknowns; (ii) eliminating $\delta\rho$ via equation (2.47) or (2.48); and (iii) substituting for δp_T from equation (2.52). This leaves four equations in the perturbed velocities and $\delta\Psi_{int}$. However, these perturbations are inextricably coupled via their z derivatives, and further reduction, e.g. to a single scalar equation in one of the perturbations, seems unlikely. When $\delta\Psi_{int} = 0$, one is left with a trio of equations in the components of $\delta\mathbf{u}$. Although in this case it would be possible to write down a single *vector* equation for the perturbations, a single *scalar* equation is not forthcoming. This has important consequences when one attempts to extend the proofs of certain general theorems from hydrodynamics into the MHD regime (see ff. §2.5.5).

Note that one often sees an alternate description of the perturbed flow in the form of the *Lagrangian* change Δ, defined in terms of the Eulerian change by

$$\Delta \equiv \delta + \xi \cdot \nabla, \tag{2.56}$$

where $\xi = \delta\mathbf{u}/(i\sigma) + r\Omega'\delta u_r\hat{\phi}$ is the Lagrangian displacement. The time derivative of ξ describes, at a given point, the velocity of a *single fluid element* as it varies in time. This is in contrast to $\delta\mathbf{u}$, which signifies the *velocity history* at the same point, as various fluid elements pass through it.

2.4.2 Perturbation equations: exterior

As mentioned in §2.3, the exterior region is supposed to be current-free. Assuming that this property carries over to the perturbations, one then has

$$\begin{aligned} \nabla \times \delta\mathbf{B}^{(V)} = 0, &\qquad \nabla \cdot \delta\mathbf{B}^{(V)} = 0, \\ \Rightarrow \quad \delta\mathbf{B}^{(V)} = \nabla\chi, &\qquad \nabla^2\chi = 0, \end{aligned}$$

where $\chi = \chi(r,z)e^{i(\omega t + m\phi)}$ is a scalar potential function. The exterior perturbations are therefore determined as solutions of Laplace's equation, which should be solved in the coordinates appropriate to the fluid geometry at hand. In the case of fluid tori, one could employ a coordinate system centred on the pressure maximum of the torus (Blaes 1986) or perhaps the flux coordinates often used in plasma confinement calculations (Bateman 1978).

In the considerably simpler case of an infinite cylinder (§2.2.2), there exist two topologically distinct exterior regions, one at $r < r_1$ and the other at $r > r_2$. Then one can take $\chi = \chi_{i,o}(r)e^{i(\omega t + m\phi + k_z z)}$, where k_z is the vertical wavenumber of the perturbation, and the interior and exterior potentials are found as

$$\chi_i(\varpi) = c_1 I_0(\varpi), \quad \chi_o(\varpi) = c_2 K_0(\varpi), \tag{2.57}$$

where $\varpi \equiv |k_z|r$, I_0 and K_0 are modified Bessel functions of order zero, c_1 and c_2 are arbitrary constants, and regularity conditions have been imposed on the solutions at $r = 0$ and $r \to \infty$.

2.4.3 Boundary conditions for the perturbations

Many of the results heretofore established in the theory of the flows considered here were done so in the context (mainly motivated by geophysical applications) of *Couette flow*, in which a perfectly conducting incompressible fluid rotates between two rigid cylinders (cf. Chandrasekhar 1961). In this situation, an appropriate boundary condition is that the radial component of the perturbed velocity should vanish at the boundary, i.e.

$$\delta u_r(r_1) = \delta u_r(r_2) = 0. \tag{2.58}$$

In a compressible gaseous disk, however, this is a highly unnatural requirement, since the boundaries are generally (a) free to move, and (b) not sharp. Moreover, the disk exterior is not expected to be field-free, so that the magnetic structure in the regions exterior to the fluid must be considered.

A more natural requirement is the continuity of *Lagrangian* perturbations of the total pressure and magnetic flux across the boundaries (Tassoul 1978, Goossens, Smeyers, & Denis 1976). This is equivalent to the requirement that Maxwell's equations and the equation of motion be satisfied in a reference frame moving with the perturbed surface, given by $S = S_0 + S_1(r,z)e^{i(\omega t + m\phi)}$. It then follows from equations (2.31) and (2.32) that the appropriate conditions to be satisfied on the fluid/vacuum interface are

$$\begin{aligned} \Delta\left\langle -\left(p+\frac{\mathbf{B}\cdot\mathbf{B}}{8\pi}\right)\hat{\mathbf{n}} + \frac{\mathbf{B}}{4\pi}(\hat{\mathbf{n}}\cdot\mathbf{B})\right\rangle &= 0, && (2.59)\\ \Delta\left\langle \hat{\mathbf{n}}\cdot\mathbf{B}\right\rangle &= 0. && (2.60)\end{aligned}$$

Using (2.60) in (2.59) then gives

$$\Delta\left\langle p+\frac{B^2}{8\pi}\right\rangle = 0 \quad \text{and} \quad \Delta(\mathbf{n}\cdot\mathbf{B} < \mathbf{B} >) = 0 \tag{2.61}$$

on the surface. Noting that

$$\Delta p = -\gamma p\nabla\cdot\xi, \qquad \Delta\mathbf{B} = \delta\mathbf{B} + (\xi\cdot\nabla)\mathbf{B},$$

$$\text{and} \qquad \Delta\hat{\mathbf{n}} = \hat{\mathbf{n}}\times[\hat{\mathbf{n}}\times(\nabla\xi)\cdot\hat{\mathbf{n}}],$$

(Kovetz 1966) conditions (2.61) become

$$-\gamma p\nabla\cdot\xi + \frac{1}{4\pi}\mathbf{B}\cdot[\delta\mathbf{B} + (\xi\cdot\nabla)\mathbf{B}] = \frac{1}{4\pi}\mathbf{B}^{(V)}\cdot[\delta\mathbf{B}^{(V)} + (\xi\cdot\nabla)\mathbf{B}^{(V)}] \qquad \text{and}$$

$$(\mathbf{n}\cdot\mathbf{B})\Delta < \mathbf{B} >= (\mathbf{n}\cdot\mathbf{B})[\delta\mathbf{B}^{(V)} + (\xi\cdot\nabla)\mathbf{B}^{(V)} - \delta\mathbf{B} - (\xi\cdot\nabla)\mathbf{B}] = 0,$$

respectively. If the fields are assumed continuous across S then only the former condition need be considered. This accords with the comments of Goossens et al. (1976), who state that the introduction of an electromagnetic field does not change the number of conditions to be satisfied on S.

2.5 Global Stability Analysis: General Results

The results of this section are culled from a small number of seminal papers and texts, most of which employ the energy principle formalism. Excellent reviews of this technique may be found in Tassoul (1978) for non-magnetic fluids, and Bateman (1978) and Schmidt (1966) for MHD fluids.

2.5.1 Sufficient criteria for stability

Bernstein et al. (1958) derived necessary and sufficient conditions for the stability of an MHD fluid in static equilibrium using the energy principle. Frieman & Rotenberg (1960) (FR) extended the Bernstein et al. work to find sufficient criteria for stability in the case of *stationary* equilibria, i.e. those with fluid velocities and, in particular, rotation. Chandrasekhar (1964), Clement (1964), and Lynden-Bell & Ostriker (1967) applied these criteria to hydrodynamic fluid situations in astrophysics (i.e. stars and galaxies). Tayler (1973) examined the stability of non-rotating magnetized stars. All of these applications, however, are contained in the very general situation examined by Chanmugam (1979) (C79), who applied the FR results in the context of differentially rotating, magnetized stars. For this reason, I choose the latter study as a starting point.

An alternate derivation of the perturbation equations of §2.4.1 is the following. Beginning with the Euler equation (2.11), take the Lagrangian variation Δ of both sides, applying the definition (2.56). This gives

$$\rho\frac{D^2\xi}{Dt^2} = -\nabla\delta p + \frac{\delta\rho}{\rho}(\nabla p - \mathbf{J}\times\mathbf{B}) - \rho[\nabla\delta\Psi_{tot} + (\xi\cdot\nabla)r\Omega^2\hat{\mathbf{r}}] + \delta\mathbf{J}\times\mathbf{B} + \mathbf{J}\times\delta\mathbf{B}, \quad (2.62)$$

where $\Psi_{tot} \equiv \Psi_{int} + \Psi_{ext}$. Assuming a normal mode spectrum of the form $\xi(\mathbf{r},t) = \xi(\mathbf{r})e^{i\omega t}$, and substituting into (2.62), the latter becomes (FR; C79)

$$-\omega^2\rho\xi + 2i\omega\rho(\mathbf{u}\cdot\nabla)\xi - \mathbf{F}\{\xi\} = 0, \tag{2.63}$$

where
$$\mathbf{F}\{\xi\} = \nabla(\gamma p\nabla\cdot\xi + \xi\cdot\nabla p - \mathbf{B}\cdot\mathbf{Q}) + (\mathbf{B}\cdot\nabla)\mathbf{Q} + (\mathbf{Q}\cdot\nabla)\mathbf{B} + \nabla\cdot(\rho\xi)\nabla\Psi_{tot} + \nabla\cdot[\rho\xi(\mathbf{u}\cdot\nabla)\mathbf{u} - \rho\mathbf{u}(\mathbf{u}\cdot\nabla)\xi] \tag{2.64}$$

and $\mathbf{Q} \equiv \delta\mathbf{B} = \nabla\times(\xi\times\mathbf{B})$. The only difference between the equations of C79 and FR is the presence of the potential term in the former. Neither author examined the effect of self-gravity, so here $\delta\Psi_{int} = \delta\Psi_{tot} = 0$.[5] Equations (2.62) and (2.63) are "equations of motion" for the displacement ξ, where $\mathbf{F}(\xi)$ plays the role of the linearized "force density."

Multiplying equation (2.63) on the left by ξ^* and integrating over the entire volume τ (for now assumed arbitrary) gives

$$-\mathcal{A}\omega^2 + 2\mathcal{B}\omega + \mathcal{C} = 0, \tag{2.65}$$

where

$$\mathcal{A} \equiv \int \rho|\xi|^2 d\tau, \quad \mathcal{B} \equiv i\int \rho\xi^*(\mathbf{u}\cdot\nabla)\xi d\tau, \quad \text{and} \quad \mathcal{C} \equiv -\int \xi^*\cdot\mathbf{F}\{\xi\}d\tau$$

are real (FR). From equation (2.65) then,

$$\omega = [\mathcal{B} \pm (\mathcal{B}^2 + \mathcal{A}\mathcal{C})^{1/2}]/\mathcal{A}. \tag{2.66}$$

Since $\mathcal{A} > 0$, a sufficient criterion for stability (since ω must be real) is

$$\mathcal{C} > 0, \tag{2.67}$$

while a stronger sufficient condition is[6]

$$\mathcal{B}^2 + \mathcal{A}\mathcal{C} > 0. \tag{2.68}$$

---

[5] Moss & Tayler (1969) showed that the effect of $\delta\Psi_{int} \neq 0$ is *destabilizing*. This is not a concern if one simply wants to demonstrate instability, and not absolute stability.

[6] This condition is only sufficient *and* necessary if ξ are the exact eigenfunctions corresponding to ω (Lynden-Bell & Ostriker 1967). Since variational methods based on the energy principle often use (arbitrary) trial functions for ξ, (2.68) is only of practical utility as a sufficient condition.

In the specific case of an axisymmetric equilibrium with a purely azimuthal flow $\mathbf{u} = r\Omega(r)\hat{\phi} = \mathbf{\Omega} \times \mathbf{r}$, one can show that (C79; Kumar, Coleman & Kley 1994; Bernstein et al. 1958):

$$\begin{aligned}
\mathcal{B} &= \int [i\mathbf{\Omega}\cdot(\xi \times \xi^*) - m\Omega|\xi|^2)\rho d\tau, && (2.69)\\
\mathcal{C} &= f + 2[\delta\mathcal{E}^{(F)} + \delta\mathcal{E}^{(S)} + \delta\mathcal{E}^{(V)}] \\
&\qquad -m\int [m\Omega|\xi|^2 - 2i\mathbf{\Omega}\cdot(\xi \times \xi^*)]\Omega\rho d\tau, && (2.70)\\
f &\equiv \int \left[\Omega^2\left(\frac{\xi \cdot \nabla\rho}{\rho} + \nabla\cdot\xi\right) + \xi\cdot\nabla(\Omega^2)\right] r\rho\xi_r d\tau, && (2.71)\\
\delta\mathcal{E}^{(S)} &\equiv \frac{1}{2}\int (\xi\cdot\hat{\mathbf{n}})^2 \left\langle \nabla\left(p + \frac{|\mathbf{B}|^2}{8\pi}\right)\right\rangle \cdot d\mathbf{S}, && (2.72)\\
\delta\mathcal{E}^{(V)} &\equiv \int \frac{|\delta\mathbf{B}^{(V)}|^2}{8\pi} d\tau^{(V)}, && (2.73)
\end{aligned}$$

and

$$\delta\mathcal{E}^{(F)} \equiv \frac{1}{2}\int \left[\frac{|\mathbf{Q}|^2}{4\pi} - \frac{\mathbf{J}}{4\pi}\cdot(\mathbf{Q}\times\xi) + \gamma p(\nabla\cdot\xi)^2 + (\xi\cdot\nabla p)\nabla\cdot\xi + (\xi\cdot\nabla\Psi_{tot})\nabla\cdot(\rho\xi)\right] d\tau, \tag{2.74}$$

where the surface integral extends over the fluid-vacuum boundary. C79 ignored the latter two contributions, assuming a complete vacuum outside the star. This was an admissible assumption for his purpose, which was to derive sufficient conditions for axisymmetric ($m = 0$) stability in the presence of a purely azimuthal field, $\mathbf{B} = B_\phi(r)\hat{\phi}$, since the latter can in some sense be considered isolated from the region outside the star. For more general field configurations, however, the surface and vacuum contributions must be retained. $\delta\mathcal{W} \equiv \delta\mathcal{E}^{(F)} + \delta\mathcal{E}^{(S)} + \delta\mathcal{E}^{(V)}$ is the total change in potential energy due to the perturbations. In the absence of rotation, $\delta\mathcal{W} < 0$ is sufficient for instability. Determining the precise conditions under which inequalities (2.67) and (2.68) hold is extremely difficult for the general situation considered here. Several important results can be obtained in particular cases, however, and I presently consider these.

2.5.2 General axisymmetric results: hydrodynamics

When $m = \mathbf{B} = 0$, equations (2.65) - (2.71) remain unchanged, but $\delta\mathcal{E}^{(F)}$ simplifies tremendously and $\delta\mathcal{E}^{(S)}$ and $\delta\mathcal{E}^{(V)}$ vanish. It can be shown that substitution of $\delta\mathcal{E}^{(F)}$ into (2.68) gives the following conditions for stability (Tassoul 1978):

$$\begin{aligned} \frac{1}{r^3}(\hat{\mathbf{r}}\cdot\nabla\ell^2) - \frac{\mathbf{g}}{c_p}\cdot\nabla s &> 0, & (2.75) \\ (\nabla p \times \hat{\mathbf{r}})\cdot(\nabla\ell^2 \times \nabla s) &> 0, & (2.76) \end{aligned}$$

where $\mathbf{g} = \nabla p/\rho$ is the effective gravity. These are the Hoiland (1941) stability criteria, and are necessary and sufficient conditions for axisymmetric stability. In the absence of rotation, (2.75) and (2.76) reduce to

$$N^2 \equiv -\mathbf{g}\cdot\nabla s > 0, \qquad (2.77)$$

where N the Brunt-Väisälä frequency. Inequality (2.77) is the Schwarzschild (1906) criterion for convective stability. In the homentropic case, $\nabla s = 0$, the Hoiland criteria reduce to the Solberg (1936) criterion,

$$\kappa^2 \equiv \frac{(\ell^2)'}{r^3} > 0, \qquad (2.78)$$

where κ is the epicyclic frequency. The Solberg criterion generalizes to homentropic bodies the well-known Rayleigh (1916) criterion for an inviscid, incompressible fluid.

2.5.3 General axisymmetric results: MHD

Even a cursory inspection of the plasma physics, nuclear fusion, and geophysics literature shows that a large variety of instabilities are possible in MHD fluids. Many of these act in highly specialized situations which are of little interest in the present context; e.g. the *Kruskal-Schwarzschild (1954) instability* occurs when a plasma layer placed in a uniform gravitational field is supported by a horizontal vacuum magnetic field. Here I restrict consideration to the system whose stability is dictated by the equations of §2.5.1. Unless otherwise noted, all of the work in this section was carried out under the assumption that the magnetic field outside the fluid vanishes, and that surface currents are negligible; i.e. $\delta\mathcal{E}^{(S)} = \delta\mathcal{E}^{(V)} = 0$. Probable effects of ignoring these contributions will be discussed presently.

Papaloizou & Szuszkiewicz (1992) recently applied the sufficient criteria of §2.5.1 to an accretion disk with a purely vertical magnetic field, i.e. $\mathbf{B} = B_z\hat{\mathbf{z}}$.[7] Ignoring the surface

---

[7] Actually, these authors considered a *poloidal* magnetic field, i.e. $\mathbf{B} = B_r\hat{\mathbf{r}} + B_z\hat{\mathbf{z}}$, introducing a poloidal

and external vacuum terms, the authors showed that the sufficient condition for stability (2.67) becomes

$$r\hat{\mathbf{r}}\cdot\nabla\Omega^2-\frac{\mathbf{g}}{c_p}\cdot\nabla s+\zeta_0\frac{r^2B_z^2}{4\pi\rho}>0, \tag{2.79}$$

where ζ_0 is a positive constant geometrical factor, approximately equal to $r/(Hr_2^4)$ for a thin disk, H is a characteristic scale height at radius r, and r_2 is the outer radius of the disk.

Condition (2.79) contains two qualitatively new and important features when compared with the Hoiland criteria. First, *the gradient of the angular momentum is replaced by the gradient of the angular velocity.* Hence for homentropic configurations, an Ω which decreases outward is unstable, provided that B_z is small enough. This is the fundamental cause of the Velikhov-Chandrasekhar and Balbus-Hawley instabilities reviewed in the Introduction. Second, if the components of (2.79) are expanded in the flux coordinates used by Papaloizou & Szuszkiewicz, one can show that *if Schwarzschild's criterion is satisfied along every field line, then there always exists a value of B_z above which the system is stable.* This behavior has been confirmed in subsequent numerical analysis (Ch. 3). In the limit of vanishing B_z, (2.79) does *not* reduce to the Hoiland criterion (2.75); this curious consequence was already commented upon in the Introduction. The resulting criterion, however, can be shown to be both sufficient *and* necessary.

Stability criteria for purely toroidal magnetic field were derived by C79, again ignoring surface and vacuum terms. One of these sufficient criteria is (C79; Tayler 1973)

$$g_z\rho^{\bullet}-\frac{\rho^2g_z^2}{B_\phi^2/8\pi+\gamma p}>0, \tag{2.80}$$

which generalizes the Schwarzschild criterion to include the effect of B_ϕ and Ω (Ω is absent because rotation doesn't effect motion along z). Condition (2.80) implies that the toroidal field has a stabilizing effect on hydrostatic equilibrium in the z-direction. The other two sufficient criteria given by C79 are lengthy and are not reproduced here.

A final limit of interest in the axisymmetric case is that of a homogeneous ($\rho'=\rho^{\bullet}=0$) and incompressible ($\delta\rho=0$) fluid, in which $\gamma\to\infty$ but perturbations in pressure are still

---

potential and coordinates adapted to constant magnetic flux surfaces to "simplify" the analysis. As shown in §2.2, however, this configuration is inconsistent: a B_r component implies a nonzero B_ϕ.

allowed. Such a fluid is homentropic ($\nabla s = 0$). The only consistent, bounded equilibrium with a vanishing B_r in this case is an infinite cylinder (§2.2.2). Thus, all equilibrium quantities depend only on r, and one is free to Fourier decompose the perturbations in z according to $\delta X(r,z) = \delta X(r) \exp{(ik_z z)}$. In the context of Couette flow (i.e. rigid boundary conditions), Michael (1954) and Chandrasekhar (1961) derived necessary and sufficient criteria for the cases of purely toroidal and purely vertical fields, respectively. Kumar, Coleman & Kley (1994) extended this work to the case in which both radially-varying toroidal and axial fields were present. The sufficient criterion for stability is

$$\Omega_A^2 + r(\Omega^2)' - \left[\frac{2V_\phi^2}{r^2} + \frac{(V_\phi^2)'}{r}\right] > 0, \tag{2.81}$$

where $\Omega_A^2 \equiv k_z^2 V_z^2$, and where

$$V_z^2 \equiv \frac{B_z^2}{4\pi\rho}, \qquad V_\phi^2 \equiv \frac{B_\phi^2}{4\pi\rho} \tag{2.82}$$

are the vertical and azimuthal Alfvén speeds, respectively. Often one sees quoted the *mode-independent* version of this criterion, in which $k_z = 0$, signifying that this is in fact the most unstable wavenumber (Ch. 3). Using the incompressible version of the equation of motion (2.62), Kumar et al. were able to place the following upper bound on the growth rate of an unstable mode:

$$|\omega_I| < (4\Omega^2 + \kappa_m^2 - \kappa^2 - \Omega_A^2)^{1/2}_{max}, \tag{2.83}$$

where $\kappa_m^2 \equiv 2V_\phi[2V_\phi/r + r(V_\phi/r)']/r$ is a "toroidal angular frequency," and where the subscript on the RHS indicates the maximum value of the enclosed quantity over the flow.

The replacement of the rigid boundary condition with the free boundary condition is necessary for most astrophysical applications. It can be shown that the conclusions of Chandrasekhar (1961) carry through with little change. In particular, ω^2 is real and condition (2.81) still holds. A similar result to (2.83) can be derived from Chandrasekhar's equations and their free-boundary counterparts, namely

$$|\omega_I| < \Omega_A \left(\frac{4\Omega^2}{\kappa^2} - 1\right)^{1/2}_{max}. \tag{2.84}$$

In the Keplerian case, e.g., $\kappa^2 = \Omega^2$ and the $B_\phi = 0$ upper bound according to (2.84) is $|\omega_I| < \sqrt{3}\Omega_A$. However, this is less restrictive than the mode-independent upper bound given by (2.83), i.e. $|\omega_I| < \sqrt{3}\Omega_{\max} = \sqrt{3}\Omega(r_1)$, where the latter relation holds for all of the angular velocity profiles I consider (i.e. I do not treat the case of a boundary layer).

2.5.4 General nonaxisymmetric results: hydrodynamics

As pointed out by PP (1984), there exists no general sufficient criterion for hydrodynamic stability to nonaxisymmetric modes. The Solberg and Rayleigh criteria are necessary, but not sufficient, for stability. Thus it is more fitting to review here (and in the MHD companion section that follows) some results pertaining to particular instabilities that occur in the flow described above. For this reason, I confine attention here to non-self-gravitating, hydrodynamic tori. In that case, equations (2.49) - (2.51) can be written (PP 1984, 1985):

$$\mathcal{D}\delta u_r = i\sigma\left[\left(\frac{\delta p}{\rho}\right)' + \frac{2m\Omega}{\sigma r}\frac{\delta p}{\rho}\right], \tag{2.85}$$

$$\mathcal{D}\delta u_\phi = -\frac{1}{r}\left[\ell'\left(\frac{\delta p}{\rho}\right)' + m\sigma\frac{\delta p}{\rho}\right], \tag{2.86}$$

$$i\sigma\delta u_z = -\left(\frac{\delta p}{\rho}\right)^\bullet, \tag{2.87}$$

where $\mathcal{D} \equiv \sigma^2 - \kappa^2$ and $\kappa^2 = 2\Omega\ell'/r$ is the epicyclic frequency.

By introducing the variable

$$W \equiv \frac{\delta p}{\rho\sigma} \tag{2.88}$$

(whose significance will become clear presently), substituting the components of $\delta\mathbf{u}$ into the continuity equation (2.47), and using equations (2.52) and (2.88) to eliminate $\delta\rho$ in favour of W, PP were able to reduce the entire system to the following perturbation equation for W:

$$\frac{1}{r}\left(\frac{\rho r\sigma^2 W'}{\mathcal{D}}\right)' + (\rho W^\bullet)^\bullet + \left[\frac{\sigma m}{r}\left(\frac{\rho\ell'}{r\mathcal{D}}\right)' - \frac{\rho m^2\sigma^2}{r^2\mathcal{D}} + \frac{\sigma^2\rho^2}{\gamma p}\right]W = 0. \tag{2.89}$$

On the boundary, the density is expected to vanish. Thus equation (2.89) is automatically satisfied on the boundary, provided that W and its derivatives are regular there.

Consider now the case of constant angular momentum, $\ell' = \kappa = 0$. Then the above simplifies to

$$\nabla\cdot(\rho\nabla W) + \frac{\sigma^2\rho^2}{\gamma p}W = 0. \tag{2.90}$$

Multiplying through this equation by W^* (where an asterisk denotes the complex conjugate), integrating over the torus cross-section applying the above boundary condition, and taking the imaginary part of the resulting expression, one finds

$$\omega_I \int \frac{|W|^2 \rho^2 \sigma_R}{\gamma p} r dr dz = 0, \tag{2.91}$$

where $\sigma_R = \omega_R + m\Omega$ and $\sigma_I = \omega_I$ are the real and imaginary parts of σ, respectively. This equation shows that if $\omega_I \neq 0$, $\sigma_R = 0 \Rightarrow \omega_R = -m\Omega$ somewhere interior to the torus. Defining the "pattern speed" by $\Omega_p \equiv -\omega_R/m$, this condition becomes $\Omega_p = \Omega$; i.e. *unstable modes must corotate with the equilibrium flow at some point.* The derivation given here is due to Blaes (1985), but a more general proof for non-constant, power-law angular momentum flows was given by PP (1985). The corotation theorem also holds for incompressible fluids.[8]

The constant angular momentum flow has the property that its vorticity, $\nabla \times \mathbf{u}$, vanishes. By Kelvin's circulation theorem, this property is likely to carry over to the perturbed flow (Moncrief 1980). Thus, in the ℓ = constant case, one expects $\nabla \times \delta\mathbf{u} = 0$. This implies that a perturbed velocity *potential*, W, exists such that

$$\delta\mathbf{u} = \nabla W. \tag{2.92}$$

Hence the flow is termed a potential flow. Using equations (2.85) - (2.87), it is easy to show that the function W chosen by PP indeed satisfies equation (2.92) (modulo constant factors). Its choice therefore has an underlying physical basis that utilizes the special properties of constant ℓ flows. In the incompressible, constant ℓ case, equation (2.90) becomes simply Laplace's equation, $\nabla^2 W = 0$. Then analytic solutions exist for W and all other perturbed quantities. The eigenvalue spectrum for this case (which corresponds to an infinite cylinder) was first calculated by Blaes & Glatzel (1986), and later extended to $\ell \neq$ constant by Goldreich, Goodman & Narayan (1986) (GGN), Jaroszyński (1988), and Sekiya & Miyama (1988). Due to the near-independence of the PP instability on vertical structure (Ch. 1), the essentially two-dimensional analysis of constant ℓ, incompressible

---

[8] Since ρ disappears from equation (2.89) in the incompressible case, one must retain surface terms in the integration and utilize the "true" boundary condition, $\sigma^2 W + g_{eff} W' = 0$, to establish the theorem.

cylinders compares quite well with full three-dimensional numerical calculations (Hawley 1987, 1991).[9]

2.5.5 General nonaxisymmetric results: incompressible MHD cylinders

In §2.4.1, I noted the increased complexity of the MHD perturbation equations due to additional couplings from z derivatives in the induction equation. To cast the problem in a form more suitable to further analytic work, I now make the additional assumption that all equilibrium quantities are independent of z. This is a serious restriction in that it precludes a proper treatment of the vertical boundaries of the disk. Nevertheless, it allows us to Fourier transform all perturbed quantities in z, thereby alleviating the above-mentioned difficulties in obtaining a single perturbation equation. Replacing $\partial/\partial z$ with ik_z in equations (2.47) - (2.55) gives

$$i\sigma\delta\rho + \frac{1}{r}(r\rho\delta u_r)' + \frac{im\rho}{r}\delta u_\phi + ik_z\rho\delta u_z = 0, \tag{2.93}$$

$$\frac{1}{r}(r\delta\Psi'_{int})' - \left(\frac{m^2}{r^2} + k_z^2\right)\delta\Psi_{int} = 4\pi G\delta\rho, \tag{2.94}$$

$$\begin{aligned} i\sigma\delta u_r - 2\Omega\delta u_\phi + \frac{(\delta p_T)'}{\rho} + (\delta\Psi_{int})' - \frac{\delta\rho}{\rho^2}\left(p'_T + \frac{B_\phi^2}{4\pi r}\right) & \\ -\frac{1}{4\pi\rho}\left[i\Gamma\delta B_r - \frac{2B_\phi\delta B_\phi}{r}\right] &= 0, \end{aligned} \tag{2.95}$$

$$\begin{aligned} i\sigma\delta u_\phi + \frac{\ell'}{r}\delta u_r + \frac{im}{r}\left(\frac{\delta p_T}{\rho} + \delta\Psi_{int}\right) - \frac{1}{4\pi\rho}\left[\frac{(rB_\phi)'}{r}\delta B_r + i\Gamma\delta B_\phi\right] &= 0, & (2.96)\\ i\sigma\delta u_z + ik_z\left(\frac{\delta p_T}{\rho} + \delta\Psi_{int}\right) - \frac{1}{4\pi\rho}\left[B'_z\delta B_r + i\Gamma\delta B_z\right] &= 0, & (2.97)\\ \delta p_T = \frac{\gamma p}{\rho}\delta\rho + \frac{1}{4\pi}(B_\phi\delta B_\phi + B_z\delta B_z), & & (2.98)\\ i\sigma\delta B_r - i\Gamma\delta u_r &= 0, & (2.99)\\ i\sigma\delta B_\phi - ik_zB_z\delta u_\phi + (B_\phi\delta u_r)' + ik_zB_\phi\delta u_z - r\Omega'\delta B_r &= 0, & (2.100)\\ i\sigma\delta B_z + B'_z\delta u_r + \frac{B_z}{r}[(r\delta u_r)' + im\delta u_\phi] - \frac{im}{r}B_\phi\delta u_z &= 0, & (2.101) \end{aligned}$$

---

[9] GGN showed that the height-integrated surface density has an effective polytropic index $N = n+1/2$, so that a three-dimensionally incompressible torus ($n = 0$) behaves as a *compressible* fluid in two dimensions.

where $\Gamma \equiv mB_\phi/r + k_z B_z$. This is the set of equations on which I base all further analysis.

To proceed further, note that the second-order equation (2.94) forces the choice of $\delta\Psi_{int}$ as the final variable en route to a single perturbation equation. However, as the global effects of self-gravity will be ignored in the remainder of this thesis, I drop equation (2.94) from the above system and set $\delta\Psi_{int} = 0$ (this does *not* mean that $\delta\rho = 0$). The choice of the final variable is now quite open. The magnetic field perturbations can be entirely eliminated via equations (2.99) - (2.101).

To draw an analogy with the results of the previous section, it would be useful to know whether a potential function still exists in the MHD case. However, the MHD equivalents of equations (2.85) - (2.87) are still quite complicated, due mainly to the coupling between the magnetic field and compressible modes. To address this issue, I examine the simplest possible extension of §2.5.4; the case of a homogeneous and incompressible fluid with $B_z =$ constant.

In this case, $\rho' = \rho^\bullet = \delta\rho = 0$ and equations (2.85) - (2.87) are unchanged. Their MHD equivalents are

$$\mathcal{G}\delta u_r = i\sigma\left[\left(\frac{\delta p_T}{\rho}\right)' + \frac{2m\sigma\Omega}{r\tilde{\sigma}^2}\frac{\delta p_T}{\rho}\right], \tag{2.102}$$

$$\mathcal{G}\delta u_\phi = \frac{\mathcal{G} - \tilde{\sigma}^2}{2\Omega}\left(\frac{\delta p_T}{\rho}\right)' - \frac{m\sigma}{r}\frac{\delta p_T}{\rho}, \tag{2.103}$$

$$i\frac{\tilde{\sigma}^2}{\sigma}\delta u_z = -ik_z\frac{\delta p_T}{\rho}, \tag{2.104}$$

where $\tilde{\sigma}^2 \equiv \sigma^2 - k_z^2 B_z^2/4\pi\rho$ and

$$\mathcal{G} \equiv \tilde{\sigma}^2 - \kappa^2 - \frac{4\Omega^2\Omega_A^2}{\tilde{\sigma}^2}.$$

Despite certain formal similarities between equations (2.85) - (2.87) and (2.102) - (2.104), it is now shown that there can exist no perturbed velocity potential in the magnetic case. Proceeding by contradiction, let such a potential be defined by $\delta\mathbf{u} = \nabla\mathcal{W}$. Then equation (2.104) dictates the choice

$$\mathcal{W} = \frac{i\sigma}{\tilde{\sigma}^2}\frac{\delta p_T}{\rho}.$$

This implies

$$\delta u_\phi = \frac{1}{r}\frac{\partial\mathcal{W}}{\partial\phi} = -\frac{m\sigma}{r\tilde{\sigma}^2}\frac{\delta p_T}{\rho},$$

which contradicts equation (2.103) unless

$$\kappa^2 + \frac{4\Omega^2\Omega_A^2}{\bar{\sigma}^2} = 0. \tag{2.105}$$

One fully expects $\kappa^2 = 0$ in order for $\mathcal{W}$ to exist, but there is no reason for the second LHS term in equation (2.105) to vanish. If one supposes that such a potential exists even for $\kappa^2 \neq 0$, equation (2.105) puts an a priori restriction on σ, which is equally unreasonable. Thus it has been proved that *a perturbed velocity potential cannot exist in a homogeneous, incompressible, B_z = constant fluid.*

There is good reason to believe, from a physical standpoint, that this result holds for *any* differentially rotating configuration with vertical field, even compressible and inhomogeneous. This is because vorticity need not be conserved in a magnetized fluid. On the contrary, the displacement of fluid elements in the ideal MHD fluid occurs at *constant angular velocity*, due to Ferraro's theorem, and therefore at nonzero vorticity. Thus, just as when viscosity is introduced into the fluid equations, Kelvin's circulation theorem no longer holds (Tassoul 1978).[10] The existence of W is still useful in the MHD problem, however, since one method of solution is to consider the magnetic field as a small perturbation on the hydrodynamic flow. In the incompressible case, one is then perturbing about an *exact* solution of the fluid equations.

The incompressible versions of the perturbation equations (2.93) - (2.101), possess certain notable symmetries. One can show, e.g., given the solution

$$(\omega, m, k_z, \delta p, \delta u_r, \delta u_\phi, \delta u_z, \delta B_r, \delta B_\phi, \delta B_z, \xi_r, \xi_\phi, \xi_z),$$

that

$$(-\omega, -m, -k_z, \delta p, -\delta u_r, \delta u_\phi, \delta u_z, -\delta B_r, \delta B_\phi, \delta B_z, \xi_r, -\xi_\phi, -\xi_z),$$

$$(\omega^*, m, k_z, \delta p^*, -\delta u_r^*, \delta u_\phi^*, \delta u_z^*, -\delta B_r^*, \delta B_\phi^*, \delta B_z^*, \xi_r^*, -\xi_\phi^*, -\xi_z^*),$$

and

$$(-\omega^*, -m, -k_z, \delta p^*, \delta u_r^*, \delta u_\phi^*, \delta u_z^*, \delta B_r^*, \delta B_\phi^*, \delta B_z^*, \xi_r^*, \xi_\phi^*, \xi_z^*)$$

are also solutions. Hence, to every growing ($\omega_I < 0$) solution with given wavenumbers (m, k_z) there exists a damped ($\omega_I > 0$) solution with the same (m, k_z). Also, to every

---

[10] The analog of Kelvin's theorem in MHD is simply the flux-freezing condition (Alfvén's theorem), which implies that the topological structure of **B**, expressed by the *magnetic helicity*, $I_m = \int_{V_m} \mathbf{A} \cdot \mathbf{B} dV$ is constant in time (Moffatt 1978). Here **A** is the magnetic vector potential and V_m is any volume within the fluid on whose surface $\mathbf{n} \cdot \mathbf{B} = 0$. This suggests a choice of W somehow involving the helicity, but this has not been pursued further.

growing (damped) solution with given (m, k_z), there exists another solution for $(-m, -k_z)$ with exactly the same growth (damping) rate. Note that all four of the above solutions have the same pattern speed $\Omega_p = -\omega_R/m$. There should be no loss of generality then, in considering modes with positive (m, k_z) only.[11].

I now return to the system of equations (2.93) - (2.101). Acheson (1973) has examined these equations in the Boussinesq approximation, wherein the gradient of the equilibrium density is supposed so weak that it may be treated as a constant everywhere save in the buoyancy term of the Euler equation (cf. Chandrasekhar 1961). Eliminating all variables in favour of the radial Lagrangian displacement $\xi_r = \delta u_r / i\sigma$, Acheson derived the single equation

$$\tilde{\sigma}^2 \xi_r'' + \left[(\tilde{\sigma}^2)' + \frac{\tilde{\sigma}^2}{r} \frac{3m^2 + r^2k_z^2}{m^2 + r^2k_z^2} \right] \xi_r' + k_z^2 \mathcal{H}(r) \xi_r = 0, \tag{2.106}$$

where

$$\begin{aligned} \mathcal{H}(r) &\equiv r \left[(\Omega^2)' - \left(\frac{V_\phi^2}{r^2} \right)' \right] + \frac{N^2}{r^2k_z^2}(m^2 + r^2k_z^2) - \frac{(V_z^2)'}{r} - \frac{2m\mathcal{Q}}{m^2 + r^2k_z^2} \\ &\quad + \frac{\mathcal{Q}^2}{\tilde{\sigma}^2} - \frac{\tilde{\sigma}^2}{m^2 + r^2k_z^2} \left[r^2k_z^2 + 1 + 2m^2 + \frac{m^2}{r^2k_z^2}(m^2 - 1) \right], & (2.107) \\ \mathcal{Q}(r) &\equiv 2 \left[\frac{V_\phi}{r} \left(\frac{mV_\phi}{r} + k_z V_z \right) - \sigma\Omega \right], & (2.108) \\ \tilde{\sigma}^2 &\equiv \sigma^2 - \left(\frac{mV_\phi}{r} + k_z V_z \right)^2. \quad \text{and} \quad N(r) = \left[\frac{\rho'}{\rho} \left(g_r + r\Omega^2 \right) \right]^{1/2} \end{aligned}$$

is the Brunt-Väisälä frequency (§2.5.2).

Equation (2.106) can be rewritten as

$$\left(\frac{r^3 \tilde{\sigma}^2 \xi_r'}{\zeta^2} \right)' + \frac{r^3 k_z^2 \mathcal{H} \xi_r}{\zeta^2} = 0, \tag{2.109}$$

where

$$\zeta^2 \equiv r^2k_z^2 + m^2. \tag{2.110}$$

Multiplying through (2.109) by ξ_r^* and applying rigid boundary conditions, i.e. $\xi_r(r_1) =$

---

[11] When a singularity occurs in the perturbation equations, such as the corotation singularity in the hydrodynamical problem, unstable and damped modes no longer occur in complex conjugate pairs. To calculate the damping rate requires a special treatment (Drury 1985; GGN 1986; Glatzel 1987a); fortunately, the growing mode is unaffected and the (m, k_z) to $(-m, -k_z)$ correspondence remains valid (Blaes 1986).

$\xi_r(r_2) = 0$, one finds

$$\int_{r_1}^{r_2} \frac{r^3}{\zeta^2}(k_z^2\mathcal{H}|\xi_r|^2 - \bar{\sigma}^2|\xi_r'|^2)dr = 0,$$

the imaginary part of which is

$$\sigma_I \int_{r_1}^{r_2} \frac{r^3}{\zeta^2}\left\{-\sigma_R|\xi_r'|^2 + \left[\frac{2m\Omega}{\zeta^2} + \frac{4k_z^2 S_2(r)}{|\bar{\sigma}^2|^2} - S_1(r)\right] k_z^2|\xi_r|^2\right\} dr = 0, \tag{2.111}$$

where

$$S_1(r) \equiv \frac{\sigma_R}{\zeta^2}\left[\zeta^2 + m^2 + 1 + \frac{m^2}{r^2k_z^2}(m^2-1)\right], \tag{2.112}$$

$$S_2(r) \equiv -\sigma_R\overline{\Gamma}^2\left(\Omega^2 + \frac{V_\phi^2}{r^2}\right) + \frac{\Omega V_\phi}{r}\overline{\Gamma}(\overline{\Gamma}^2 + \sigma_R^2 + \sigma_I^2), \tag{2.113}$$

and $\overline{\Gamma} \equiv \Gamma/\sqrt{4\pi\rho}$.

Unstable modes ($\sigma_I = \omega_I < 0$) can exist only if the integrand in equation (2.111) changes sign somewhere in (r_1, r_2). Assuming Ω to be a positive-definite and monotonic function of r, several conclusions may be drawn from this relation:

(a) If $V_z = 0$ (purely azimuthal field) or $V_\phi = 0$ (purely vertical field), then an examination of the signs of the terms in equations (2.111) - (2.113) shows that all growing disturbances must have $\sigma_R/m > 0$ somewhere in the fluid, from which it follows that

$$\omega_R > -m\Omega, \tag{2.114}$$

or $\Omega_p < \Omega_{max} = \Omega(r_1)$. The above constitutes an "almost corotation theorem": *unstable disturbances must propagate* against *the direction of rotation somewhere within the cylinder.*

(b) Even if neither field vanishes, the above conclusion still holds if $|k_zV_z| < |mV_\phi/r|$.

(c) In the case of a purely vertical field ($V_\phi = 0$), no purely exponentially-growing instability is possible. That is, ω_R *must* be nonzero.

(d) If the magnetic fields are weak, i.e. $V_z, V_\phi \ll r\Omega$, then (c) still holds.

Conclusions (a) and (b) are due to Acheson (1973), while (c) and (d) are apparently new. All of these results hold for nonaxisymmetric perturbations. When $m = 0$, one can note further that:

(e) Purely exponentially-growing instabilities can exist only if $V_\phi V_z$ changes sign somewhere in (r_1, r_2). This generalizes the result of Knobloch (1992), who proved the same for $V_z =$ constant.

By way of justification, some brief comments on the restriction to incompressible flows may be in order. Generally speaking, compressible flows offer more routes to instability than incompressible ones. This can be seen formally by a look back at the energy integrals of §2.5.1. Since γ appears only in a positive-definite term in the energy integral $\delta\mathcal{E}^{(F)}$, it follows that the larger γ is, the more stable the system (Schmidt 1966). In other words, an incompressible fluid ($\gamma \rightarrow \infty$) is at least as stable as a compressible one of the same configuration. In astrophysical contexts then, one can be quite confident that having demonstrated the existence of an incompressible instability a compressible counterpart will also exist, possibly complemented by other instabilities of an intrinsically compressible nature (e.g. Rayleigh-Taylor instability). A similar "comparison theorem" holds in the fluid exterior. If one replaces the exterior vacuum field with a complete vacuum, the latter system is at least as stable as the former (Schmidt 1966).

2.6 Local Stability Analysis

To study certain physical phenomena of interest in accretion disks, it is not necessary to solve for the global modes. Rather, one can ask whether a *localized* parcel of gas at (r_0, ϕ_0, z_0), immersed in the fluid and subject to differential rotation, magnetic fields, gravity, etc. is stable with respect to infinitesimal disturbances. Mathematically, this is achieved by assuming that the wavelength of the perturbations is much less than any radial or vertical scale height, which allows Fourier transforms in the spatial variables; i.e. $\partial/\partial r \rightarrow ik_r$ and $\partial/\partial z \rightarrow ik_z$, k_r, k_z large.[12] This reduces the coupled, partial differential system (2.47) - (2.55) to an *algebraic* system, solvable for the frequency ω.

A very general approach to the determination of local, axisymmetric stability in thick, hydrodynamic accretion disks was initiated by Abramowicz et al. (1984b). Under the above assumptions, these authors derived a fifth-order dispersion relation in the frequency ω. All terms were retained in the original equations and the authors conceived a clever prescription for discerning the magnitude of each term relative to the others. Only then were

---

[12] Note that while formally this would force one to neglect derivative terms in the equilibrium quantities, these can be retained provided that one follows the prescription $k_r r \gg \partial X/\partial r$, and similarly for k_z, for keeping dominant terms.

subdominant terms ignored, so that the resulting simplification allowed stability criteria to be derived. Abramowicz et al. were able to recover the well-known Hoiland, Schwarzschild, and Rayleigh criteria by this method. In the light of recent debate regarding how a local stability analysis "should" be done (Knobloch 1992; Hawley & Balbus 1992; Gammie & Balbus 1994), this careful paper should act as a model for all such future calculations.

The local method has a distinct advantage in that its comparative mathematical simplicity allows one to include more physics. A case in point is the study of Fricke (1969), who considered the effect of B_ϕ and $\mathbf{B_p} = B_r\hat{\mathbf{r}} + B_z\hat{\mathbf{z}}$ separately on $m = 0$ perturbations of a differentially rotating, radiating, compressible star. Self-gravity was not included, and the Boussinesq approximation was used in the poloidal field case (having been found valid only near the rotation axis in the toroidal field case). Fricke's conclusions on purely toroidal fields have important consequences for stars; he found, e.g., that in the absence of rotation a star with such a field cannot be stable. Conversely, in the absence of any magnetic field it was already known that for stars in radiative equilibrium, a stationary state of rotation of the form $\Omega = \Omega(r)$ is not possible (von Zeipel's paradox; cf. Tassoul 1972). Fricke then discussed whether the simultaneous presence of both B_ϕ and $\Omega(r)$ could be stabilizing. As the issue remains unresolved today, I refer the reader to Tassoul (1972) for further details.

Fricke's important result in the purely poloidal field case was the following necessary condition for stability:

$$r\frac{k_z^2}{k^2}\left(\frac{k_r}{k_z}\frac{\partial\Omega^2}{\partial z} - \frac{\partial\Omega^2}{\partial r}\right) < \frac{(\mathbf{k}\cdot\mathbf{B})^2}{4\pi\rho}, \tag{2.115}$$

where $k^2 \equiv k_r^2 + k_z^2$. Fricke rederived this result heuristically, clearly showing the competition of magnetic restoring and centrifugal forces. Equation (2.115) reduces to that of Balbus & Hawley (1991) when $k_r = \partial\Omega/\partial z = 0$. The effect of the $\partial\Omega/\partial z$ term has so far been ignored in the magnetized accretion disk context (see Kumar & Coleman (1993) for an application to nonmagnetized disks). Evidently, an $\Omega(r, z)$ which decreases with z (which seems most reasonable) has a stabilizing effect on the BH instability.

The role of self-gravity was not investigated by Fricke; yet, it is not significantly more difficult to handle within the local approximation. I outline here the first steps in such an analysis, treating the axisymmetric case only. The latter restriction is made not for simplicity but out of prudence, heeding the cautionary note of Knobloch (1992) that local analysis can give specious results in certain $m \neq 0$ stability problems.

Replacing the r and z derivatives in equations (2.47) - (2.55) with ik_r and ik_z, and writing the resulting system in matrix form, one has

$$\begin{pmatrix} i\omega\rho & A & 0 & B & C & 0 & D & E & \rho D \\ F & i\omega\rho & 0 & G & B & 0 & 0 & 0 & 0 \\ 0 & 0 & i\omega\rho & H & 0 & B & J & K & \rho J \\ 0 & 0 & 0 & 0 & L & M & 1 & N & 0 \\ -i\Gamma & 0 & 0 & i\omega & 0 & 0 & 0 & 0 & 0 \\ P & Q & R & S & i\omega & 0 & 0 & 0 & 0 \\ T & 0 & 0 & 0 & 0 & i\omega & 0 & 0 & 0 \\ U & 0 & V & 0 & 0 & 0 & 0 & i\omega & 0 \\ 0 & 0 & 0 & 0 & 0 & 0 & 0 & -4\pi G & W \end{pmatrix} \begin{pmatrix} \delta u_r \\ \delta u_\phi \\ \delta u_z \\ \delta B_r \\ \delta B_\phi \\ \delta B_z \\ \delta p_T \\ \delta\rho \\ \delta\Psi_{int} \end{pmatrix} = 0,$$

where A, B, $\ldots W$ are $r-$ and $z-$ dependent coefficients containing equilibrium quantities only. Setting the determinant of the matrix equal to zero for a nontrivial solution, one obtains a dispersion relation of the form

$$ia_6\omega^6 + a_4\omega^4 - ia_3\omega^3 + a_2\omega^2 + a_1\omega + a_0 = 0, \tag{2.116}$$

where a_0, a_1, $\ldots a_6$ are functions of $A - W$ and a neutral mode has been factored out (i.e. $\omega = 0$). By way of comparison, the axisymmetric, hydrodynamic dispersion relation of Abramowicz et al. (1984b) is of fifth order in ω, while the MHD relations of Fricke (1969) are of fifth and seventh order for purely toroidal and purely poloidal magnetic fields, respectively.

Equation (2.6) has not been analyzed further, but it is likely that in the absence of self-gravity, $\delta\Psi_{int} = 0$, many of the results of §2.5.2 and §2.5.3 could be rederived. For $\delta\Psi_{int} \neq 0$, entirely new physical effects may be present (cf. Matsumoto, Nakamura, & Hanawa 1994).

2.7 A Note on Methods of Stability Analysis

The recent history of the instabilities discussed in this thesis would not be complete without some mention of what one might call the "methods controversy." Stability analysis is a topic of such importance to physics that numerous techniques have been devised to facilitate it. That two or more of these methods might lead to identical results for a given physical system is generally acknowledged, and is indeed heartening. However, what seems to be often overlooked is that different techniques applied to what is ostensibly the same system can have such varied *mathematical* assumptions that they end up probing vastly different *physical* regimes.

A case in point concerns the argument of Knobloch (1992) against the relevance of the BH instability for accretion disks. The principal issue was BH's claim that a nonzero B_ϕ had no effect on their conclusions, provided that it was subthermal in strength. This assumption allowed BH to ignore terms $O(1/r)$ in comparison with those $O(k_r)$ in the perturbation equations (2.47) - (2.55). Applying a global stability analysis with rigid boundary conditions, Knobloch showed that without any prior restriction on B_ϕ, the purely exponential instability of BH could not occur. Rather, unstable modes in the presence of B_ϕ possess a real part, i.e. are overstable.

The apparent controversy, which is not merely semantical, rests upon a loose physical application of these mathematical results. Although both parties claim to be investigating the stability of accretion disks, BH can only comment upon local properties by virtue of their analysis. Their results apply to any locally shearing, magnetized medium, which would certainly include the interior of an accretion disk (questions of ionization fraction aside; §1.5.2), but do not depend on any "disklike" geometry whatsoever. Knobloch, on the other hand, examined an entirely different problem: how unstable *global* modes (which he showed exist) are affected by the presence of radial boundaries. This model is marginally more realistic, as it crudely describes a disk in the radial dimension, but it is as equally crude as BH's equilibrium in the z-direction.

As will become clear in the next chapter, both unstable global modes and local instabilities (not properly termed "modes") are present in magnetized accretion disks. The two methods of stability analysis apply to the same system on widely different spatial scales, and thus examine different physics. The stability results of Knobloch, whose model we have attempted to improve upon in this thesis, can be expected to apply to issues of global disk physics and perhaps the very viability of disks as equilibrium structures. Conversely, the approach of BH can only be expected to have relevance to local properties of fluid motions; e.g. to calculate the Shakura-Sunyaev α, a locally defined quantity (§1.2). On the other hand, the nonlinear evolution of an instability can be followed quite effectively in a local approximation, which has made it the method of choice for such calculations (Hawley & Balbus 1992; Goodman & Xu 1994; Hawley et al. 1995).

Finally, it is important to mention one other model frequently used in stability analyses of disks, the shearing-sheet model of Goldreich & Lynden-Bell (1965), which falls in between the purely local and global techniques in terms of both its complexity and range of applicability. There are two principal simplifications of the full global equations used in this method. First, the model is local in the sense that it describes a region around some fiducial radius in the disk $r = r_0$ using Cartesian coordinates (x, y, z), and assumes a linear dependence of all x-dependent equilibrium quantities about $x_0 \leftrightarrow r_0$. This has the obvious disadvantage that it eliminates the possibility of applying boundary conditions at finite (cylindrical) radius. However, boundary properties can sometimes be *imposed* by considering the asymptotic form of solutions at spatial infinity (cf. Goldreich & Narayan 1985). The existence of intrinsically global modes which would be missed in a local analysis can therefore be established by this technique, but their detailed spatial structure cannot.

The second simplification in the shearing-sheet analysis is the introduction of a change of coordinates which essentially trades the linear x-dependence for an explicit time-dependence of the perturbations (i.e. "shearing coordinates"). This allows one to study perturbations whose growth is not exponential, e.g. spiral waves, and which display transient growth but cannot be termed global modes. The growth is transient because the radial wavenumber in the comoving frame of the fluid is time-dependent. The end product of such a calculation is usually the amplification factor of an infinitesimal disturbance over a finite time interval (cf. Tagger et al. 1992).

In lieu of imposing a spectrum of global normal modes, the examination of stability via the evolution of an initial value problem has been carried out by Coleman, Kley, & Kumar (1995) for certain special cases of the situations examined in detail in this thesis, and was shown to be largely equivalent to the normal mode analysis.

The technique of global analysis is used in this study for several reasons. First, the few (mainly geometrical) approximations it utilizes have consequences that are easily discerned later; e.g., one's conclusions need not be limited to a particular region of wavenumber space. Second, although it often misses transient phenomena by virtue of the imposition of normal modes (§2.4.1), the global analysis *includes* local phenomena as limiting cases of high spatial wavenumber. Finally, while local and transient instabilities indicate potential processes of interest in accretion disks, globally unstable modes, should they exist, often have much wider-ranging consequences for disk evolution.

THE ASTROPHYSICAL JOURNAL, 434:206–220, 1994 October 10

Chapter 3

ON THE GLOBAL STABILITY OF MAGNETIZED ACCRETION DISKS.

I. AXISYMMETRIC MODES

CHARLES CURRY, RALPH E. PUDRITZ, and PETER G. SUTHERLAND
Department of Physics and Astronomy
McMaster University, Hamilton, Ontario L8S 4M1, Canada

Email:curry@jabba.physics.mcmaster.ca,pudritz@.physun.physics.mcmaster.ca,pgs@physun.physics.mcmaster.ca

ABSTRACT

We investigate the global stability of a differentially rotating fluid shell threaded by a constant vertical magnetic field to linear, axisymmetric perturbations. Such a system is known to be unstable due to the interaction between the magnetic field and fluid shear, and should mimic the behavior of an accretion disk far from its vertical boundaries. The magnetic field *exterior* to the fluid has an effect on the radial boundary motion, and we derive the appropriate boundary conditions. The growth rates of the instability, associated radial eigenfunctions, and critical field strengths for stability are presented for a wide variety of radii, rotation profiles, and magnetic field strengths. The growth rates of unstable global modes are always less than, but comparable to, the corresponding local growth rates. For near-critical field strengths, non-rigid boundary conditions lead to much higher growth rates than do (physically unrealistic) rigid boundary conditions. Also, we find that the critical Alfvén speed for stability is large (of order the sound speed) for realistic disk sizes, thus implying that the instability is always present. Finally, the connection between the global and local characters of the instability is elucidated.

Subject headings: accretion, accretion disks - instabilities - magnetohydrodynamics - ISM: magnetic fields

3.1 Introduction

The formation, stability, and evolution of gaseous accretion disks are issues of central importance in star formation and high-energy astrophysics. There are indications, both from theory and observation, that magnetic fields may have significant dynamical effects in the disk environment. Several current models of bipolar outflows in young stellar objects, for instance, involve magnetized disks which can serve to drive or collimate winds, removing angular momentum from the disk and protostar (see Blandford 1989 for a review). Regardless of whether a wind is present, an important theoretical problem is the radial transport of angular momentum, molecular viscosity alone being insufficient for this task (Pringle 1981). In this connection, the promise of magnetic fields was recognized early on (for references, see Tout and Pringle 1992), but most of the candidate mechanisms depended on a pre-existing disordered magnetic field, always of unknown origin.

Fresh incentive was provided by Balbus & Hawley (1991), who recognized the astrophysical importance of an earlier fluid mechanics result of Velikhov (1959) and Chandrasekhar (1960, 1961). The latter authors examined the stability of a magnetized incompressible fluid, placed between two rigid rotating cylinders. Whereas in the unmagnetized fluid a necessary and sufficient condition for stability is the Rayleigh criterion, $d(r^2\Omega)^2/dr > 0$, in the event that the fluid is threaded by a vertical magnetic field B the corresponding condition is $d\Omega^2/dr > 0$; a condition which would be violated in accretion disks.[1] If the lack of correspondence between the two criteria seems puzzling, we need only return to the approximation in which the latter is derived, that of ideal magnetohydrodynamics (MHD). In this, the field lines have a permanent attachment to the fluid, regardless of the strength of the field. The primary effect of this attachment is to enforce isorotation of the fluid, i.e. $\mathbf{B} \cdot \nabla\Omega = 0$ (Ferraro 1937). Infinitesimal, axisymmetric perturbations to this equilibrium (we denote these by a δ in front of the appropriate physical quantity) then have two distinct effects (Balbus & Hawley 1991; see also Shu 1992). Azimuthal stresses, $B\ \delta B_\phi/4\pi$, destabilize by spinning up (down) vertically adjacent fluid elements, causing them to move radially

---

[1] This includes Keplerian disks and also thick, pressure-supported disks, which are not so massive that self-gravity can affect their rotation profiles.

outward (inward) by conservation of angular momentum. Radial stresses, $B\ \delta B_r/4\pi$, attempt to compensate by exerting a restoring force opposite in direction to these radial displacements. Radial stresses "win" (i.e. stabilize) only if the equilibrium field is too strong, or if the vertical wavelength of the perturbation is sufficiently short. Either of these limits the magnitude of azimuthal field perturbations and their associated torques (Blaes & Balbus 1994). In the absence of a consensus, we will follow the convention of historical precedence for naming, and refer to the mechanism just described as the Velikhov-Chandrasekhar (VC) instability.

Any application of these results to real accretion disks is premature until a number of issues are resolved. Among these is the inadequacy of the linear stability analysis to determine the ultimate outcome of the initially quickly-growing instability. In particular, angular momentum transport arises from nonlinear terms in the perturbation equations. Several papers have addressed this aspect (Hawley & Balbus 1991, Hawley & Balbus 1992, Zhang, Diamond, & Vishniac 1994) while (of necessity) ignoring others.

Another major objective is to bring the original calculation into the realm of astrophysics. The role of compressibility, for instance, was examined by Hawley & Balbus (1991), who found it did not alter the qualitative nature of the VC instability. This is not surprising, since the instability proceeds via the propagation of torsional Alfvén waves (these create the azimuthal stresses referred to above), which are noncompressive. The self-gravity of the fluid has also been ignored, and is important for more massive disks. The state of ionization of the disk can have a large effect (Blaes & Balbus 1994); there are indications that the instability may be damped in protostellar disks, at least in regions of low ionization fraction (Dubrulle & Knobloch 1993, Stepinski, Reyes-Ruiz, & Vanhala 1993, Jin 1993). Radial, and especially azimuthal, equilibrium magnetic fields also alter the stability and evolution of disks, but early indications are that they are not damning to the basic VC mechanism, unless $B_\phi \gtrsim \sqrt{4\pi\rho}\, r\Omega$ (Hawley & Balbus 1992, Dubrulle & Knobloch 1993, Blaes & Balbus 1994).

In this paper, we focus on yet another obvious concern, that global, as well as local, instabilities may be present. For global modes the effect of boundary conditions is clearly important. We make a first attempt to examine this aspect of the problem, by considering the effect of radial boundaries on the linear development of global modes. Gammie and Balbus (1994) have recently similarly studied the role of *vertical* boundaries. We also point out that an understanding of the radial global mode structure is an essential element in the angular momentum transport issue.

The advantages of such an approach are the following. First, Balbus & Hawley (1991) showed that in the local limit, k (vertical wavenumber) $\rightarrow \infty, v_A$ (Alfvén speed) $\rightarrow 0$, and for a Keplerian disk, the growth rate $|\omega| \simeq 0.75\Omega$, implying that the instability was dynamically important. One can now ask whether a similar conclusion holds for all values of the model parameters $v_A, d\Omega/dr$, and r_2/r_1 (outer/inner radius), and for various boundary conditions. Dubrulle & Knobloch (1993) were able to find growth rates for a few specific values of these parameters, but did not determine the detailed dependence of $|\omega|$ on them. In addition, we consider non-Keplerian rotation laws, by which one can gauge the effects of the VC instability on thick, pressure-supported disks.

Second, although the local analysis shows that $v_{A,crit} = |k^{-1}\sqrt{rd\Omega^2/dr}|$, one cannot obtain from this a meaningful stabilizing value of the magnetic field, since k is (by assumption) arbitrarily large. Velikhov and Chandrasekhar carried out calculations to find $v_{A,crit}$ for certain global modes. Both obtained values which applied in the limit of very thin cylinders, and Velikhov also derived a result for high radial mode numbers. They recognized, however, that even these were lower bounds on the critical field for the fastest growing mode of a radially extended configuration. In this paper, we find an *upper bound* to this quantity and examine its dependence on the parameters of the problem.

Finally, given that the global and local stability criteria refer to the *same basic destabilizing mechanism*, it is of some value to explicitly demonstrate that a correspondence between global and local results holds in the appropriate limit. There has been some debate in the literature as to which formalism is more suitable to this and related problems (Knobloch 1992, Hawley & Balbus 1992, Gammie & Balbus 1994). We comment on this issue in light of our own results in the Discussion.

The format of the paper is as follows. The equilibrium state is described in Section 2, and the perturbations to this state in the following section. After developing an approximate solution of the problem in Section 4, we turn to numerical solutions in Section 5. The main body of the results is presented there. These are discussed and summarized in Section 6. Technical details of the calculations may be found in the two appendices.

3.2 The Equilibrium

We consider the following simplified model of an accretion disk in a state of pure rotation (Knobloch 1992, Dubrulle & Knobloch 1993). A cylindrical shell of homogeneous and incompressible fluid, of infinite extent in the z-direction, rotates about the z-axis (we adopt cylindrical polar coordinates (r, ϕ, z) throughout). A magnetic field $\mathbf{B}$ threads the fluid, which is assumed to be sufficiently ionized so that the equations of ideal MHD apply:

$$\begin{aligned} \rho\left[\frac{\partial \mathbf{u}}{\partial t} + (\mathbf{u}\cdot\nabla)\mathbf{u}\right] &= -\rho\nabla\Psi - \nabla\left(p + \frac{\mathbf{B}\cdot\mathbf{B}}{8\pi}\right) + \frac{1}{4\pi}(\mathbf{B}\cdot\nabla)\mathbf{B}, && (3.1) \\ \frac{\partial \mathbf{B}}{\partial t} &= \nabla\times(\mathbf{u}\times\mathbf{B}), && (3.2) \\ \nabla\cdot\mathbf{u} &= \nabla\cdot\mathbf{B} = 0. && (3.3) \end{aligned}$$

Here p is the gas pressure, ρ the constant density, $\mathbf{u}$ the fluid velocity, and Ψ the gravitational potential. Self-gravity is ignored, but a large mass M at $r = z = 0$ generates the potential

$$\Psi = -\frac{GM}{r}. \qquad (3.4)$$

The purely radial dependence of the potential is justified if, locally, the vertical scale height $H \ll r$, so that there is little variation of Ψ with z. In the absence of dissipative processes, equations (3.1) - (3.4) allow the following stationary solution, which depends only on the radial coordinate, r:

$$\mathbf{u} = [0, r\Omega(r), 0], \quad \mathbf{B} = [0, B_\phi(r), B_z(r)]. \qquad (3.5)$$

In particular, we shall consider a power-law distribution of angular velocity and a uniform axial magnetic field;

$$\Omega(r) = \Omega_0\left(\frac{r}{r_0}\right)^{-a}, \quad B_\phi(r) = 0, \quad B_z(r) = B, \qquad (3.6)$$

where Ω_0, a, B, and r_0 are constants. B is also supposed to permeate the regions both to the interior and exterior of the shell. Inserting equations (3.4) - (3.6) into (3.1), the radial component becomes

$$\frac{p'}{\rho} = r\Omega_0^2 \left(\frac{r}{r_0}\right)^{-2a} - \frac{GM}{r^2} \equiv g_{eff}, \tag{3.7}$$

where $' \equiv d/dr$ and g_{eff} is the effective gravity. A Keplerian disk ($a = 3/2$) has $g_{eff} = 0$ everywhere, so $\Omega_0^2 = GM/r_0^3$.

In a thick disk, the equilibrium is maintained by internal pressure gradients ($a \neq 3/2$), and $p' = 0$ only at the pressure maximum of the configuration (we ignore the possibility of "cusps" in the equipotential surfaces). Identifying r_0 with this maximum, we again find $GM = r_0^3\Omega_0^2$. Substituting the latter into equation (3.7) and integrating, one obtains the stationary pressure distribution;

$$\frac{p}{\rho} = (r_0\Omega_0)^2 \left[\frac{r_0}{r} - 1 + \frac{1-(r/r_0)^{-2(a-1)}}{2(a-1)} + \frac{\mu^2}{2}\right], \tag{3.8}$$

where μ^2 is a constant equal to the ratio of thermal to kinetic energy at r_0. The uniform field has no effect on the equilibrium, since the corresponding current, $\mathbf{J} = \nabla \times \mathbf{B} = 0$.

The inner and outer boundaries r_1 and r_2 of the fluid are determined by the zeros of equation (3.8), just as in the hydrodynamic case (see, e.g., Jaroszyński 1988). Setting $p(r_1)$ and $p(r_2)$ to zero in this equation, we obtain

$$\frac{r_0}{r_1} = \left\{\frac{1}{2(a-1)}\frac{r_2/r_1}{r_2/r_1 - 1}\left[1 - \left(\frac{r_2}{r_1}\right)^{-2(a-1)}\right]\right\}^{-\frac{1}{2a-3}} \equiv f, \tag{3.9}$$

and

$$\frac{\mu^2}{2} = 1 - f + \frac{f^{2(a-1)} - 1}{2(a-1)}.$$

Equation (3.9) gives the position of the pressure maximum relative to the inner radius. The constant μ is a direct measure of the thickness of the shell. At the pressure maximum, the pressure gradient vanishes as fluid elements rotate with the Keplerian angular velocity. Thin shells have both radii approaching r_0, so that according to equation (3.8), $\mu \to 0$ in this limit. For the thickest configurations, equation (3.8) with $p/\rho = 0$ and $r \to \infty$ gives

$$\mu = \mu_{max} \equiv \left(\frac{2a-3}{a-1}\right)^{\frac{1}{2}}. \tag{3.10}$$

We have assumed that $a \geq 1$, which is required if the pressure is to remain finite as $r_2 \to \infty$. For $r = r_0$ to be a pressure maximum, we must also check that $p'' < 0$ there. This restricts the allowed values of a to $a \geq 3/2$, the Keplerian limit. From above, a is bounded by $a \leq 2$, due to the Rayleigh criterion. Thus, the absolute maximum value of $\mu_{max} = 1$, which occurs for $a = 2$. It is customary and convenient to scale units of length and time with respect to the pressure maximum values r_0 and Ω_0^{-1}; thus in practice we will choose r_2/r_1, and find r_1/r_0 and r_2/r_0 from equation (3.9). In the Keplerian case, the latter becomes an indeterminate form; by taking the limit as $a \rightarrow 3/2$, one finds

$$\frac{r_1}{r_0} = \exp\left[\frac{\ln(r_2/r_1)}{r_2/r_1 - 1} - 1\right].$$

Of course, r_0 is no longer the pressure maximum here; it is simply an arbitrary point in the shell which happens to be approached by the pressure maxima for other values of a in a continuous manner (see Table 3.1). We will consider a variety of radial thickness ratios in our calculations.

Finally, note that in general a magnetized fluid is subject to the following boundary conditions (Tassoul 1978):

$$\left[-\left(p + \frac{\mathbf{B}\cdot\mathbf{B}}{8\pi}\right)\mathbf{n} + \frac{\mathbf{B}}{4\pi}(\mathbf{n}\cdot\mathbf{B})\right]_{1,2} = 0, \tag{3.11}$$

$$[\mathbf{n}\cdot\mathbf{B}]_{1,2} = 0, \tag{3.12}$$

where $\mathbf{n}$ is the normal directed outward from the fluid at a boundary surface and the square parentheses denote a jump in the enclosed quantity across the inner (1) and outer (2) surfaces, taken in the direction of $\mathbf{n}$. The first condition expresses the requirement that the normal component of the material and magnetic stresses be continuous across the surface, while the second expresses conservation of magnetic flux. One sees from equations (3.11) and (3.12) that the magnetic field outside the shell must be specified, and that, in particular, *the location of the boundaries depends not only on the magnetic field interior to the fluid, but also on that to its exterior.*

3.3 The Perturbations

3.3.1 The perturbation equation: interior

We now consider the response of the above equilibrium state to small, axisymmetric, Eulerian perturbations of the form

$$\delta X(r,z,t) = \delta X(r)e^{i(kz+\omega t)},$$

where X is any physical variable, and k and ω are the vertical wavenumber and frequency of the perturbation, respectively. Substituting the forms $X + \delta X$ along with equation (3.6) into equations (3.1) - (3.3), and only retaining terms of linear order in the perturbation quantities, we have

$$i\omega\delta\mathbf{u} + \nabla\delta h - \frac{ikB}{4\pi\rho}\delta\mathbf{B} - 2\Omega\delta u_\phi\hat{\mathbf{r}} + (2-a)\Omega\delta u_r\hat{\phi} = 0, \tag{3.13}$$

$$i\omega\delta\mathbf{B} - ikB\delta\mathbf{u} + a\Omega\delta B_r\hat{\phi} = 0, \tag{3.14}$$

$$\frac{1}{r}(r\delta u_r)' + ik\delta u_z = 0, \tag{3.15}$$

where

$$h \equiv \frac{p}{\rho} + \frac{B^2}{8\pi\rho}$$

is the specific enthalpy. Note that equations (3.14) and (3.15) imply $\nabla\cdot\delta\mathbf{B} = 0$.

Resolving equations (3.13) - (3.15) into components, and eliminating all variables in favour of the radial velocity perturbation, one obtains a second-order differential equation in δu_r:

$$(\delta u_r)'' + \frac{1}{r}(\delta u_r)' + \left[k^2(Er^{-2a} - 1) - \frac{1}{r^2}\right]\delta u_r = 0, \tag{3.16}$$

$$\begin{aligned} E &\equiv \frac{2}{\tilde{\omega}^4}[(2-a)\tilde{\omega}^2 + 2k^2v_A^2], \\ \tilde{\omega}^2 &\equiv \omega^2 - k^2v_A^2, \\ v_A &\equiv \frac{B}{\sqrt{4\pi\rho}}, \end{aligned} \tag{3.17}$$

where v_A is the Alfvén speed, and where we have scaled units of length and time to r_0 and Ω_0^{-1}, respectively.

3.3.2 The perturbation equation: exterior

The regions $r < r_1$ and $r > r_2$, while devoid of matter, are permeated by the uniform, axial magnetic field. The perturbations to this vacuum field are described by

$$\nabla \times \delta \mathbf{B}_{i,o} = 0, \quad \nabla \cdot \delta \mathbf{B}_{i,o} = 0, \tag{3.18}$$

where i and o refer to the regions $r < r_1$ and $r > r_2$, respectively. These imply

$$\delta \mathbf{B}_{i,o} = B \nabla \chi_{i,o}, \tag{3.19}$$

$$\nabla^2 \chi_{i,o} = 0, \tag{3.20}$$

where $\chi_{i,o} = \chi_{i,o}(r) e^{i(kz+\omega t)}$ are two scalar functions representing the perturbed field *potential* in the fluid-free regions (see, e.g., Simon 1958). Defining a new variable $\varpi = |k|r$, the solutions of (3.20) are given by

$$\chi_i(\varpi) = c_1 I_0(\varpi), \quad \chi_o(\varpi) = c_2 K_0(\varpi), \tag{3.21}$$

where I_0 and K_0 are modified Bessel functions of order zero, and we have imposed regularity conditions on the solutions at $r = 0$ and $r \to \infty$.

3.3.3 The boundary conditions

Previous analyses of this problem (Velikhov 1959, Chandrasekhar 1961, Knobloch 1992, Dubrulle & Knobloch 1993) assumed rigid cylindrical boundaries at r_1 and r_2, and thus avoided the problem of specifying the nature of the external field. However, unless one is willing to invent *ad hoc* values for the exterior fields on the boundaries, it is necessary to consider their behavior. Most importantly, the rigid boundary conditions are unsatisfactory from a physical point of view.[2] First, it is unlikely that the environment surrounding accretion disks is field-free. For example, the inner edge of a disk around a young stellar object is likely to be at the magnetopause radius in the star's magnetic field (Camenzind 1990, Königl 1991, Hartmann 1994). Second, accretion disks do not have rigid boundaries.

---

[2] Mathematically, these conditions are $\delta u_r(r_1) = \delta u_r(r_2) = 0$. Dubrulle and Knobloch also considered $\delta u_r'(r_1) = \delta u_r'(r_2) = 0$, but this is not really a "free" boundary condition, at least as far as the *Lagrangian* surface is concerned (see below).

When considering the response of the disk to small perturbations of equilibrium quantities, it is especially important to allow the boundaries the freedom to oscillate. One is reminded here of the marked effect of boundary conditions on the stability of thick hydrodynamic disks (see, e.g., Blaes & Glatzel 1986). Although in the axisymmetric case, the stability criterion is unlikely to be sensitive to the chosen boundary conditions, the growth rates may very well be.

At the fluid surfaces we will apply "free" boundary conditions; i.e., those which allow the boundaries to oscillate in response to the perturbation. Since the perturbations we consider are of small amplitude, it is sufficient to require the continuity of *Lagrangian* perturbations of the total normal stresses and magnetic flux across the boundaries (Tassoul 1978, Goossens, Smeyers, & Denis 1976). Denoting the Lagrangian perturbation operator by Δ, it follows from equations (3.11) and (3.12) that the appropriate conditions are

$$\Delta\left[-\left(p+\frac{\mathbf{B}\cdot\mathbf{B}}{8\pi}\right)\mathbf{n}+\frac{\mathbf{B}}{4\pi}(\mathbf{n}\cdot\mathbf{B})\right]_{1,2}=0, \tag{3.22}$$

$$\Delta[\mathbf{n}\cdot\mathbf{B}]_{1,2}=0. \tag{3.23}$$

Recall that the Lagrangian and Eulerian operators are related via $\Delta=\delta+\xi\cdot\nabla$, where

$$\xi=\frac{1}{i\omega}\delta\mathbf{u}+r\Omega'\delta u_r\hat{\phi}$$

is the Lagrangian displacement.

Noting that $\mathbf{B}\cdot\mathbf{n}=0$, and taking B to be continuous across the boundaries, the second condition becomes

$$[\delta B_r]_{1,2}=0. \tag{3.24}$$

By use of the induction equation (3.2) and equation (3.19), this may be written

$$\frac{k}{\omega}\delta u_r=\chi_i',\quad r=r_1, \tag{3.25}$$

$$\frac{k}{\omega}\delta u_r=\chi_o',\quad r=r_2. \tag{3.26}$$

Writing out the first condition (3.22) using (3.24), we find

$$\left\{[\delta h]_{1,2}+\frac{\delta u_r}{i\omega}[h]_{1,2}'\right\}\hat{\mathbf{r}}=0. \tag{3.27}$$

Since the perturbation equation (3.16) is in terms of δu_r, it is desirable to express δh in equation (3.27) in terms of δu_r, using equation (3.13). The boundary condition (3.27) then becomes

$$(\delta u_r)' + \left(\frac{1}{r} + \frac{k^2}{\bar{\omega}^2} g_{eff}\right) \delta u_r = -\frac{\omega k^3 v_A^2}{\bar{\omega}^2} \chi_i, \quad r = r_1, \tag{3.28}$$

$$(\delta u_r)' + \left(\frac{1}{r} + \frac{k^2}{\bar{\omega}^2} g_{eff}\right) \delta u_r = -\frac{\omega k^3 v_A^2}{\bar{\omega}^2} \chi_o, \quad r = r_2, \tag{3.29}$$

where

$$g_{eff} = r^{1-2a} - \frac{1}{r^2} \tag{3.30}$$

in our dimensionless units.

Dividing equation (3.28) by (3.25) and (3.29) by (3.26), one obtains two conditions which contain all the boundary information:

$$(\delta u_r)' + \left[\frac{1}{r} + \frac{k^2}{\bar{\omega}^2}\left(g_{eff} + k^2 v_A^2 \frac{\chi_i}{\chi_i'}\right)\right] \delta u_r = 0, \quad r = r_1, \tag{3.31}$$

$$(\delta u_r)' + \left[\frac{1}{r} + \frac{k^2}{\bar{\omega}^2}\left(g_{eff} + k^2 v_A^2 \frac{\chi_o}{\chi_o'}\right)\right] \delta u_r = 0, \quad r = r_2. \tag{3.32}$$

From equation (3.21) one finds

$$\left.\frac{\chi_i}{\chi_i'}\right|_{r=r_1} = \frac{1}{|k|}\frac{I_0(\varpi_1)}{I_1(\varpi_1)} \quad \text{and} \quad \left.\frac{\chi_o}{\chi_o'}\right|_{r=r_2} = -\frac{1}{|k|}\frac{K_0(\varpi_2)}{K_1(\varpi_2)}, \tag{3.33}$$

where $\varpi_{1,2} = |k| r_{1,2}$.

3.3.4 The eigenvalue problem

Equation (3.16) is of the standard Sturm-Liouville form. As such, the eigenvalues $E = E_0, E_1, E_2, \ldots E_n$, are infinite in number, and are all real and positive. Solving for ω^2 from Eq. (3.17), we find two solutions. One is always positive, corresponding to stable modes. The other can become negative, indicating instability; we then find

$$|\omega| = \left\{\left[\frac{(2-a)^2}{E^2} + \frac{4\Omega_A^2}{E}\right]^{\frac{1}{2}} - \Omega_A^2 - \frac{2-a}{E}\right\}^{\frac{1}{2}} \tag{3.34}$$

for the growth rate of the single unstable growing mode. Stability criteria have been known for some time, and are reviewed by Knobloch (1992) and Dubrulle & Knobloch (1993).

These were derived for rigid boundary conditions. It is not difficult to show that for the boundary conditions derived above, the stability criterion is still $d\Omega^2/dr > 0$ (see also Papaloizou & Szuszkiewicz 1992).

Via (3.34), the solution of equation (3.16), subject to the boundary conditions (3.31) and (3.32) constitutes a well-defined eigenvalue problem for the frequency ω. At present, exact analytic expressions for the eigenvalues do not exist. However, we show in the following section that equation (3.16) is ideally suited to an asymptotic treatment. This allows us to explore the important qualitative features of the problem, before embarking on a numerical solution in §5.

3.4 The WKB Approximation

Dubrulle & Knobloch (1993) noted that under the transformation $\psi \equiv \sqrt{r}\delta u_r$, the perturbation equation assumes the form

$$\epsilon^2\psi'' = Q(r)\psi, \tag{3.35}$$

where ϵ is a small parameter, which they take to be v_A. Equation (3.35) is a Schrödinger equation, singular as $\epsilon \to 0$. The WKB approximation is the asymptotic method of choice for such problems (Bender & Orszag 1978). To write down the leading-order WKB approximation to $\psi(r)$, we need only have knowledge of the zeros of $Q(r)$. In general, one sees that in regions where $Q < 0$, the solution of (3.35) is sinusoidal in character; where $Q > 0$, exponential. When $\epsilon = v_A$ and k is finite, $Q < 0$ and has no zeros for unstable modes ($\omega^2 < 0$), provided that $\Omega' < 0$. Thus Dubrulle & Knobloch found only sinusoidal solutions, leading to growth rates $|\omega| \sim kv_A$. It is known from the physics of the instability, however, that for either k or v_A large enough, the instability shuts off (this is both a local *and* a global result; see equation (2.17) of Velikhov (1959)). Thus it is apparent that taking $v_A \to 0$ misses some of the essential physics.

Under the same transformation, our equation (3.16) becomes

$$\psi'' + \left[k^2(Er^{-2a} - 1) - \frac{3}{4r^2}\right]\psi = 0. \tag{3.36}$$

Comparison with (3.35) suggests that we choose $\epsilon = 1/k$, making

$$Q(r) = 1 - Er^{-2a} + \frac{3\epsilon^2}{4r^2}. \tag{3.37}$$

The WKB limit is now $k \to \infty$. In order that E not vanish in this limit (see equation (3.17)), we will simultaneously require that v_A is small. Thus *the Alfvén frequency*, $\Omega_A \equiv kv_A$, *remains finite and nonzero in the WKB limit.* It is this feature that will allow us to examine the physics of both short and long wavelength perturbations.

The details of the WKB calculation may be found in Appendix A, where it is shown that the eigenvalue relations for rigid and free boundary conditions are

$$\cos\left[\frac{\mathcal{I}_2(r_1)}{\epsilon} + \frac{\pi}{4}\right] - 2\exp\left[\frac{2\mathcal{I}_1(r_2)}{\epsilon}\right]\sin\left[\frac{\mathcal{I}_2(r_1)}{\epsilon} + \frac{\pi}{4}\right] = 0, \tag{3.38}$$

and

$$\begin{aligned}\left\{\alpha - \frac{Q'(r_1)}{4Q(r_1)} + 2\gamma\frac{\sqrt{-Q(r_1)}}{\epsilon}\exp\left[\frac{2\mathcal{I}_1(r_2)}{\epsilon}\right]\right\}\cos\left[\frac{\mathcal{I}_2(r_1)}{\epsilon} + \frac{\pi}{4}\right] \\ + \left\{\frac{\sqrt{-Q(r_1)}}{\epsilon} - 2\gamma\left[\alpha - \frac{Q'(r_1)}{4Q(r_1)}\right]\exp\left[\frac{2\mathcal{I}_1(r_2)}{\epsilon}\right]\right\}\sin\left[\frac{\mathcal{I}_2(r_1)}{\epsilon} + \frac{\pi}{4}\right] &= 0,\end{aligned} \tag{3.39}$$

respectively, where

$$\begin{aligned}\mathcal{I}_1(r) &\equiv \int_{r_T}^{r}\sqrt{Q(t)}dt, \quad \mathcal{I}_2(r) \equiv \int_{r}^{r_T}\sqrt{-Q(t)}dt, \\ \alpha &\equiv \frac{1}{2r_1} + \frac{k^2}{\bar{\omega}^2}\left[g_{eff}(r_1) + \Omega_A^2\frac{\chi_i(r_1)}{\chi_i'(r_1)}\right], \\ \beta &\equiv \frac{1}{2r_2} + \frac{k^2}{\bar{\omega}^2}\left[g_{eff}(r_2) + \Omega_A^2\frac{\chi_o(r_2)}{\chi_o'(r_2)}\right], \\ \gamma &\equiv \frac{\beta - \frac{Q'(r_2)}{4Q(r_2)} + \frac{\sqrt{Q(r_2)}}{\epsilon}}{\beta - \frac{Q'(r_2)}{4Q(r_2)} - \frac{\sqrt{Q(r_2)}}{\epsilon}},\end{aligned} \tag{3.40}$$

and

$$r_T = E^{1/2a} - \frac{3}{8a}E^{-1/2a}\epsilon^2 \tag{3.41}$$

is the "turning point", i.e. the single positive real zero of $Q(r)$. At this radius, the character of solutions to equation (3.35) changes from sinusoidal to exponential, or vice-versa.

Physically speaking, waves travelling freely in the regions where $Q < 0$ begin to damp after passing through r_T.

These equations, despite their appearance, are much easier to solve than the full eigenvalue problem. In practice, one solves numerically for E (which is contained in Q), and then computes the growth rate $|\omega|$ from equation (3.34). Equations (3.38) and (3.39) each have an infinite number of solutions. We may characterize each of these by a mode number $n = 0, 1, 2, \ldots$, such that $E_0 < E_1 < E_2 < \ldots < E_{n-1} < E_n$. To draw an analogy with local analysis terminology, n is akin to the radial wavenumber, k_r, of a given unstable mode.

3.4.1 The local limit

Further WKB analysis, specifically in the limits k large, E finite and E large, k finite, leads to the conclusion that for both sets of boundary conditions,

$$E = \frac{E^{(0)}(a)}{k^2} + \ldots + E_{min}(a), \tag{3.42}$$

where $E_{min}(a) \equiv r_1^{2a}$ and $E^{(0)}(a)$ are constants for a given a (see Appendix A for details). The (unknown) intermediate terms must behave as constant$/k^{\alpha}$, $0 < \alpha < 2$. Consequently, an absolute upper limit on $|\omega|$ is, taking the $k \to \infty$ limit,

$$|\omega| \leq |\omega^{(\ell)}| \equiv \left\{ \left[\frac{(2-a)^2}{r_1^{4a}} + \frac{4\Omega_A^2}{r_1^{2a}} \right]^{\frac{1}{2}} - \Omega_A^2 - \frac{2-a}{r_1^{2a}} \right\}^{\frac{1}{2}}. \tag{3.43}$$

This result reproduces the *local* dispersion relation of Balbus & Hawley (1991) (hereafter BH), neglecting buoyancy forces and taking a more general power-law rotation curve. This is indeed expected, since the local analysis assumes $k_r(r_2 - r_1) \gg 1$ and consequently is not affected by whatever boundary conditions are imposed. Note that the growth rate is solely a function of the Alfvén frequency; this is peculiar to the local limit, and is not the case generally. Figure 3.1 is a plot of equation (3.43) for various values of a allowed by our equilibrium. The $a = 1.5$ curve corresponds to that of BH's Figure 1c, except scaled in units of the angular frequency at the pressure maximum (their results are implicitly scaled in units of r_1 and $\Omega^{-1}(r_1)$; see below). The maxima of these curves occur at

$$\Omega_A = \Omega_{A,max}^{(\ell)} \equiv \frac{1}{r_1^a}[1 - (2-a)^2/4]^{1/2}, \tag{3.44}$$

giving an absolute upper bound to the growth rate of

$$|\omega| \leq |\omega_{max}^{(\ell)}| \equiv \frac{a}{2r_1^a}. \qquad (3.45)$$

A few representative values may be found in Table 3.1. Note that for an inner radius scaling ($r_1 = 1$) and $a = 3/2$, equation (3.45) gives $\omega_{max}^{(\ell)} = 0.75$, the value obtained by BH.

Another quantity of interest is the critical wavenumber above which perturbations are stable. Marginal stability occurs at $\omega^2 = 0$. From equation (3.34) one then finds

$$\Omega_{A,crit} = \sqrt{2a/E} \qquad (3.46)$$

in general, and

$$\Omega_{A,crit}^{(\ell)} = \sqrt{2a/E_{min}} = \sqrt{2a}/r_1^a$$

in the local limit. Thus $k_{crit} = \sqrt{2a/(v_A^2 E)}$ diverges in the local limit, and so is not a meaningful quantity (it is for *finite* v_A, however). Values of $\Omega_{A,crit}^{(\ell)}$ for various a may be found in Table 3.1.

3.4.2 Eigenfunctions δu_r

We now point out some important qualitative features of the solutions of equation (3.36), which may be found in Appendix A. As $Q(r)$ has but a single turning point, r_T, the eigenfunctions are exponentially decreasing in the region $r_T < r < r_2$ (hereafter region I), Airy function-like for $r \approx r_T$ (region II), and sinusoidal for $r_1 < r < r_T$ (region III). In the short-wavelength, $\epsilon \rightarrow 0$ limit considered above, the turning point approaches the inner radius: $r_T \rightarrow E^{1/2a} \rightarrow r_1$ (Appendix A). Consequently, region III shrinks to zero size, and region I constitutes almost the entire shell (excepting the region $\epsilon^2 \ll r - r_T \ll \epsilon^{2/3}$, which is Airy-like). This corresponds to the $k_r = 0$ case considered by BH; the eigenfunctions are essentially flat over all of the shell. In the long-wavelength limit, $k \rightarrow 0$, E may become large enough that $r_T > r_2$; i.e. the turning point lies *outside* the shell. Then the perturbations are sinusoidal everywhere within the fluid. This is the situation examined by Dubrulle & Knobloch (1993), who considered the equivalent limit (in the sense that the δu_r have the same sinusoidal character) $v_A \rightarrow 0, k$ finite.

Before exhibiting the full range of WKB results, it is desirable to check their accuracy. This is done via comparison with a direct numerical integration which we develop in the next section.

3.5 Numerical Solution and Results

We have carried out the solution of equation (3.16) by a standard shooting method as adapted for eigenvalue problems (Press et al. 1992). The eigenvalue (E in the rigid case, $\tilde{\omega}^2$ in the free case) is treated as an independent variable, with governing equation dE/dr or $d\tilde{\omega}^2/dr = 0$. Initial values at the left-hand boundary are required for E and $\delta u_r'$ in the rigid case, and $\tilde{\omega}^2$ and δu_r in the free case. We chose the arbitrary but graphically convenient normalizations $\delta u_r'(r_1) = 25$ in the rigid case and $\delta u_r(r_1) = 1$ in the free case. The WKB eigenvalues were used as starting values for E and $\tilde{\omega}^2$.

The behavior of the WKB eigenfunction in region I is a combination of growing and decaying exponentials (Appendix A). When k becomes large (ϵ small), such a solution becomes very difficult to follow numerically (Acton 1970). This practical upper limit on k translates into a lower limit on v_A, since the fastest growing modes are characterized by $\Omega_{A,max} = k_{max}v_A = O(1)$ (Figure 3.1). We were therefore only able to obtain reliable numerical results for $v_A \gtrsim 0.3$. Fortunately, the WKB approximation is able to cover smaller values of v_A, with an acceptable level of error, for almost all of the parameter space.

3.5.1 Mode structure

Taking $v_A = 0.3$ and $r_2/r_1 = 100$ as fiducial values, we have used both WKB and numerical methods to obtain dispersion curves, i.e. $|\omega|$ vs. kv_A, for the principal ($n = 0$) mode. In addition, we have numerically solved for the next two fastest growing modes, $n = 1$ and $n = 2$, and also for the $n = 0, 1$, and 2 eigenfunctions. These are the only unstable modes for this value of v_A. The results are shown in Figure 3.2 for three different values of a, and for rigid boundary conditions. Results in the free boundary case are shown in Figure 3.3.

Let us first examine the accuracy of the WKB approximation of §3.4 For both rigid and free boundary conditions, the approximate and exact curves are in agreement to an accuracy of better than 4 % at the peak $|\omega|$, for all values of a. As a consequence, we can be quite confident in using the WKB method for values of $v_A \lesssim 0.3$, since the agreement can only get better for larger k. Note that our approximations always *overestimate* the growth rate.

A decided advantage of the global solution method is that the radial eigenfunctions are now available (Figures 3.2 & 3.3). Aside from the inner boundary constraint, the rigid and free boundary eigenfunctions show few differences. The general behavior is as predicted in §3.4.2; sinusoidal in the inner regions, exponentially decaying for larger r. The most striking feature is how strongly peaked δu_r is near the inner radius. All three modes, in fact, reach their maximum amplitudes between r_1 and the pressure maximum r_0 (equal to 1 in our units). The principal mode, $n = 0$, has its turning point, r_T, between these two radii. For smaller v_A, and therefore larger k at peak growth rate, r_T approaches r_1, so δu_r is even more localized near the inner radius. In fact, the eigenfunction is so strongly peaked for $v_A \lesssim 0.3$ that our numerical routine breaks down.

For smaller fields, the eigenvalue spectrum shows an interesting evolution toward the limiting curves of Figure 3.1. This is shown in Figure 3.4, a plot of growth rate vs. Alfvén frequency for the same three modes, but for $v_A = 0.05$. WKB curves have been plotted for both sets of boundary conditions. Two points are immediately evident: (i) the differences between the principal and higher-order modes are lessening, and (ii) the effect is the same regardless of the boundary conditions. We have verified that the curves become even closer for smaller field values. Moreover, the number of unstable modes increases as v_A decreases; e.g., there are more than twenty for $v_A = 0.01$. One is thereby led to the conclusion that *in the local (i.e. $k \to \infty, v_A \to 0$) limit, the higher-order modes merge with the principal mode, until they eventually become indistinguishable from it.* As mentioned in §3.4.2, the corresponding eigenfunctions are constant (in fact, zero, due to the boundary conditions) over most of the shell, so that for *all finite n*, the mode structure is identical to that of the $k_r = 0$ local analysis. In addition, *differences between free and rigid boundaries vanish in the local limit.* That this should be the case was already argued by previous authors.

3.5.2 Effect of boundary conditions

Comparison of Figures 3.2 and 3.3 shows that the growth rates are systematically larger for free over rigid boundaries. This is most evident in the Keplerian case, where the peak $|\omega|$ is $\sim 50\%$ higher for free boundaries. The difference becomes even more marked as the field strength is increased. This is demonstrated in the dispersion curves of Figure 3.5a, which are numerical solutions for $v_A = 0.7$ and $n = 0$. At their respective peaks, the free boundary growth rate more than doubles that of the rigid. For boundaries which are closer together, this disparity becomes more pronounced (see §3.5.4). In Figure 3.5b, we plot the corresponding eigenfunctions at maximum growth rate. Note that the peaks have shifted closer to the pressure maximum for the higher field value.

As explained in §1, the VC instability will not grow if the equilibrium field strength is too large. This is due to the enforced rigidity of the fluid by the magnetic field. It may therefore seem strange that free boundaries allow faster growing modes than do rigid ones in the presence of barely sub-critical v_A. We postpone an explanation of this behavior until §3.5.5, where related results are presented.

3.5.3 Effect of magnetic field strength

The results of the previous sections point to different responses of the system to linear perturbations, depending on the magnitude of v_A. To summarize these effects, we plot in Figure 3.6 the peak growth rate of the VC instability as a function of the Alfvén speed, using the WKB and numerical methods in the appropriate regimes. Each of the curves corresponds to a different shear, the constant angular momentum case ($a = 2$) giving the largest peak $|\omega|$ for nearly all v_A. The only departure from this behavior occurs at larger field strengths ($v_A \gtrsim 0.2$) where, especially in the free boundary case, the $a = 1.5$ and $a = 1.7$ growth rates can exceed those of $a = 2$. Note that the critical field for stability, given by $|\omega|_{max} = 0$, is larger for free boundary conditions than for rigid. This is not surprising, in light of the results of the previous section. We will discuss $v_{A,crit}$ further in §3.5.5

3.5.4 Effect of radial thickness

Thus far, we have only considered models of considerable radial extent, $r_2/r_1 = 100$. The fact that the growth rates of Figure 3.6 approach their limiting values at small v_A (Figure 3.1) tells us that even more extended models offer no surprises. More slender shells, however, should begin to display boundary effects, even for smaller fields. The growth rate as a function of shell radial thickness is plotted in Figure 3.7. Although the growth rates for free boundaries generally exceed those for rigid, the differences do indeed become larger for more slender configurations ($r_2/r_1 \lesssim 3$) (although differences due to shear become less evident). At $r_2/r_1 \simeq 1.5-2$, rigidly bounded models stabilize, while freely bounded models remain unstable down to $r_2/r_1 \simeq 1.05$. The free boundary growth rates are less sensitive to different rotation laws, but show two interesting crossovers. The $a = 1.5$ growth rate exceeds that of $a = 1.7$ for $r_2/r_1 \gtrsim 6$, and that of both $a = 1.7$ and $a = 2$ for $r_2/r_1 \gtrsim 30$. These crossovers occur *only* for free boundaries, and agree with Figure 3.6b for $v_A = 0.3$.

3.5.5 Critical field strength for stability

In §3.4.1 we derived the critical Alfvén frequency for stability, equation (3.46). The critical Alfvén speed is therefore

$$v_{A,crit} = \sqrt{\frac{2a}{k^2E}}. \tag{3.47}$$

We are interested in an upper bound on $v_{A,crit}$ or, equivalently, a lower bound on k^2E.[3] Since E is bounded from below by $E_{min} = r_1^{2a}$, a lower bound must be given by $\lim_{k\to 0} k^2E$. As E is necessarily large in this limit (equation (3.42)), we can evaluate k^2E in a different WKB regime (Appendix B). By the results of §3.5.4, one expects that the absolute maximum value of $v_{A,crit}$ is achieved as $r_2/r_1 \to \infty$. The values of k^2E and $v_{A,crit}$ in this limit may be found in Table 3.1. The values of $v_{A,crit}$ for free boundaries are in fact extreme upper limits, and appear to be $\sim 30\%$ too high (see below and Appendix B).

The larger value of $v_{A,crit}$ for free versus rigid boundaries is no doubt related to the growth rate discrepancy found in §3.5.2 To explain this behavior, we reexamine the free

---

[3] Chandrasekhar (1961), in considering the case of r_2/r_1 small, isolated the quantity $a^2\lambda$, which is equivalent to our k^2E. He noticed that this quantity achieves its maximum value as $a \to 0$ (in his notation).

boundary conditions themselves. As r_2 is removed to infinity in the Table 3.1 results, the differences cannot be due to any property of the outer boundary; thus, it is sufficient to consider equation (3.31) alone. Write this equation as $\delta u_r/(\delta u_r)' = 1/g(k)$, where all quantities are to be evaluated at r_1. Then, taking $k \to \infty$, one immediately sees that the rigid boundary condition, $\delta u_r(r_1) = 0$, is recovered, as would be expected in the local (small field) limit. For higher field values, k is reduced, since one always has $kv_A = O(1)$ for unstable modes. For example, k decreases by a factor ~ 4 at peak growth between Figures 3.3e and 3.5a. Thus $\delta u_r/(\delta u_r)'$ *increases* for decreasing k, and we can imagine that the resulting boundary motion enhances the growth of the mode. Of course, this cannot continue indefinitely; eventually v_A becomes so large that the restoring force of the field prevents a large centrifugal excess *anywhere* in the fluid, and the system is stabilized. The resulting value of $v_{A,crit}$ is larger for free boundaries than for rigid ones, since the boundary motion ensures nonzero oscillation amplitudes even for relatively large v_A.

Returning now to the calculation of the critical field, the behavior of $v_{A,crit}$ for finite values of r_2/r_1 is shown in Figure 3.8. Note that $v_{A,crit} \to 0$ as $r_2/r_1 \to 1$. This is expected, since in this limit the shell disappears, leaving a uniform vacuum magnetic field, which is of course stable. The region above the curves in the $(v_{A,crit}, r_2/r_1)$ plane is stable; below, unstable. In addition, fields in excess of $v_A/(r_0\Omega_0) \sim 1$ are almost certain to be unstable to magnetic bouyancy in a vertically stratified disk. But note that this value of $v_A/(r_0\Omega_0)$ corresponds to $r_2/r_1 \sim 2-3$ in Figure 3.8b; thus, these results would seem to imply that *most disks with realistic field strengths lie in the unstable region.*

Although these curves represent exact solutions of the original VC problem (and the free boundary version), they are admittedly somewhat unastrophysical. A real disk, with finite vertical scale height, H, can never allow $k = 0$ perturbations. A more interesting number is the critical field for the longest vertical wavelength that can fit inside the disk: $\lambda_{crit} = 2\pi/k_{crit} = 2H$. We have tabulated $v_{A,crit}$ for several values of λ_{crit} in Table 3.2. The above conclusions continue to hold down to a (simulated) scale height of $H/r_1 \approx 5$, after which $v_{A,crit}$ begins to drop below unity. At $\lambda_{crit}/r_1 = 0.1$, a reasonable value for a thin Keplerian disk, we find $v_{A,crit}/(r_0\Omega_0) \approx 0.04$. From the (non-self-gravitating) thin disk equation, $H = c_s\sqrt{2}/\Omega$, where c_s is the sound speed in the gas, along with the *local* Keplerian critical field estimate $v_{A,crit}/c_s = \sqrt{6}/\pi$ (BH), we obtain $v_{A,crit}/(r_0\Omega_0) = \sqrt{3}H(r_1/r_0)/(\pi r_1) \approx 0.07$. This gives us some confidence in extending our results to the thin disk regime. It is interesting that $v_{A,crit} \sim c_s$; this may be the strongest possible field which can be contained in certain equilibrium disk models (Stella & Rosner 1984). A more detailed examination of this issue is beyond the scope of this paper, however.

3.6 Discussion and Summary

Let us now examine how the results of the previous section enhance our basic understanding of the VC instability, as outlined in §1.

First there is the property, observed in the eigenfunctions δu_r, that the largest amplitudes always occur in the inner regions. In fact, the eigenfunctions of the fastest-growing modes appear always to achieve their maxima between the pressure maximum and the inner boundary. To understand this, recall from §1 that instability occurs when the azimuthal component of magnetic stress, $B\ \delta B_\phi/4\pi$, dominates the radial component, $B\ \delta B_r/4\pi$. The ϕ component of equation (3.14) relates the two perturbations as follows:

$$\delta B_r = \frac{i}{a\Omega}(kB\delta u_\phi - \omega\delta B_\phi),$$

where δu_ϕ is the azimuthal velocity perturbation. For *fixed* ω, k, and B then,

$$|\delta B_r| \lesssim \left|\frac{\omega}{a}\frac{\delta B_\phi}{\Omega}\right|.$$

Restoring stresses are less effective in the inner regions (Ω large) than in the outer regions, thus leading to a larger centrifugal excess, and a larger amplitude in the radial velocity perturbation, for smaller r.

It is interesting that the instability growth rates are relatively insensitive to the rotation profile, even in a global calculation such as we have presented. In general, the results indicate that the growth rate is larger for larger shear. This is entirely as we would have expected from our basic physical understanding of the instability. Hence it appears that the VC instability is no more (or less) important for thick, pressure-supported disks than for thin Keplerian ones.

Papaloizou & Szuszkiewicz (1992) derived global stability criteria for a thin MHD disk with constant vertical field, using an effective variational principle. Although growth rates were not obtained, they were able to estimate $v_{A,crit}$, finding (in proper units)

$$v_{A,crit} \sim r_2^2[H(r)/r]^{1/2} \left(\frac{1}{r}\left|\frac{d\Omega^2}{dr}\right|\right)^{1/2}. \tag{3.48}$$

As this is in fact a *local* criterion in r, it is difficult to compare directly with our results. We can, however, compare the dependence on scale height. Imagine two disks with identical radial, but different vertical structure. At some point $r = r_X$ in the two disks, the corresponding scale heights are $H_1(r_X)$ and $H_2(r_X)$. The ratio of the critical Alfvén speeds according to equation (3.48) should then be $\sim \sqrt{H_1/H_2}$. Consulting Table 3.2, we see that there is approximate agreement with this estimate for Keplerian disks with rigid boundaries and the smallest few values of H. Exact agreement would not be expected, since Papaloizou & Szuszkiewicz considered different geometry and boundary conditions (see also Gammie & Balbus (1994)). As we consider this a fairly tenuous connection between the two models, we do not comment upon it further.

A recent paper by Kumar, Coleman, and Kley (1994) bears on our work in the following way. They recovered the BH results analytically in a slender Keplerian annulus approximation, with $k \gg 1$. We have shown that only $k \gg 1$ is necessary. In the same approximation, with $k \sim 1$, Kumar et al. then used a numerical method to find a similar mode structure to our Figure 3.2 (they employed rigid boundary conditions only), but with much smaller field strengths and growth rates, due to their slender approximation. Finally, they claim that $|\omega/\Omega_0|_{max}$ increases with k, and then, for very large k, begins to *decrease*. We find no evidence for this behavior, and indeed it would seem to be at odds with the very notion that $|\omega/\Omega_0|_{max}$ achieves its maximum in the local ($k \rightarrow \infty$) limit.

Although we cannot claim to have treated the vertical structure in an at all consistent manner, our calculations of $v_{A,crit}$ given in Table 3.2 allow us to make some comment upon the need (or lack thereof) for global analysis in this and related problems. In particular, there has been some dispute regarding the role of azimuthal magnetic field. Hawley & Balbus (1992) and Gammie and Balbus (1994) have claimed that the global effects of such a field (which appear to be stabilizing; see Knobloch 1992, Blaes & Balbus 1994) are unimportant in a thin disk, since the terms containing these effects are of order $v_A/(r_0\Omega_0)$. The results of §5 and Table 3.2, which show that this quantity must indeed be quite small for the instability to operate in thin disks, support this view. However, if the azimuthal field is strong (i.e. thermal), or if field gradients (azimuthal or vertical) exist, it is likely that a global analysis will be necessary.

While in the protostellar context the VC instability has been suggested as a possible mechanism of angular momentum transport, in the black hole/AGN accretion disk context, it may have quite a different role. A generic feature of general relativistic gravitational fields is the existence of a cusp near the inner radius through which accretion occurs, even in the absence of viscosity. The fact that the most unstable mode of the VC instability is extremely localized near the inner radius may have an interesting consequence. Some of the angular momentum (possibly) advected outwards via the instability will instead be redirected *inwards* onto the central object. One is reminded here of the fate of nonaxisymmetric instabilities in accreting tori; they are stabilized for very modest accretion rates (Blaes 1987). This issue is seemingly a very difficult one to resolve, given the three-dimensional nature of the instability and the presence of magnetic field.

On the issue of boundary conditions, we feel that the Lagrangian free-boundary approach used here is the most physically sensible one, and may in fact be essential in order to arrive at the correct stability properties in the case of nonaxisymmetric modes. Two further improvements that could be made to our model are: (i) a realistic density structure, especially at the boundaries, and (ii) a richer field structure (say, force-free) in the vacuum regions. Also, although some work has been done on the effect of azimuthal magnetic field, we feel that its role in a global model such as we have formulated is not well understood. We will consider these issues in future work.

Our finding that global modes grow at comparable rates to local ones suggests that accretion disks have interestingly complex magnetic field structures. In addition to the small scale, strong magnetic fluctuations analyzed by BH, global or mean magnetic field components will also be present. Thus one may not need to rely upon a dynamo mechanism to amplify BH "turbulence" into large-scale fields as suggested by Tout & Pringle (1992). A deeper understanding of accretion disk magnetic fields awaits nonlinear analysis for both global and local instabilities.

In summary, we have calculated, by both analytical and numerical techniques, the radial axisymmetric global modes of an idealized accretion disk, threaded by a constant vertical magnetic field. Boundary conditions are derived which account for the interaction between the radial boundaries and the external magnetic field, and we find that non-rigid boundaries allow faster-growing modes to occur for all but the weakest fields. In all cases, the limiting global growth rate is the corresponding *local* one, and we have explicitly shown how the local limit is obtained in the global picture. The critical field strengths for stability found in this analysis are near equipartition values, suggesting that a very broad class of disks is susceptible to the VC instability.

It is a pleasure to thank Omer Blaes for encouragement and critical comments on the manuscript, Fred Kus for advice on numerical methods, and Jim Stone for informing us of the work of Gammie and Balbus. The comments of the referee, Prof. Frank Shu, improved the clarity of the presentation.

C. C. acknowledges the financial support of McMaster University and an Ontario Graduate Scholarship. The research of R. E. P. and P. G. S. is supported by grants from the Natural Sciences and Engineering Research Council of Canada.

Appendix A: WKB Approximations

Large k

The character of solutions to equation (3.35) depends on the function $Q(r)$, given by equation (3.37); in particular, on the number and multiplicity of its zeros ("turning points"). On the interval $[r_1, r_2]$, Q possesses but a single turning point, at

$$r_T = E^{1/2a} - \frac{3}{8a}E^{-1/2a}\epsilon^2 + O(E^{-3/2a}, \epsilon^4). \qquad \text{(A.1)}$$

Since Q contains a term $O(\epsilon^2)$, we will ignore terms of higher order in (A.1).

The boundary conditions are:

$$\psi(r_1) = \psi(r_2) \quad = \quad 0, \quad \text{(RIGID)} \tag{A.2}$$

and

$$\begin{aligned} \psi'(r_1) + \alpha\psi(r_1) &= 0, \\ \psi'(r_2) + \beta\psi(r_2) &= 0, \quad \text{(FREE)} \end{aligned} \tag{A.3}$$

where α and β are defined in the text. Following Bender & Orszag (1978), we introduce $x \equiv r - r_T$, so that the space is naturally divided into three regions: $x > 0$ (region I), $x < 0$ (region III), and $|x| \ll 1$ (region II). The leading-order, $\epsilon \to 0$, WKB solution takes on a distinct form in each region; we find:

$$\psi_I(x) = C[\overline{Q}(x)]^{-1/4} \left\{ \exp\left[\frac{\overline{\mathcal{I}}_1(x)}{\epsilon}\right] - \exp\left[\frac{2\gamma\overline{\mathcal{I}}_1(x_2) - \overline{\mathcal{I}}_1(x)}{\epsilon}\right] \right\}, \tag{A.4}$$

$$x > 0, x \gg \epsilon^{2/3};$$

$$\psi_{II}(x) = C\sqrt{\pi}(\eta\epsilon)^{-1/6} \left\{ \mathrm{Bi}(\epsilon^{-2/3}\eta^{1/3}x) - 2\exp\left[\frac{2\gamma\overline{\mathcal{I}}_1(x_2)}{\epsilon}\right] \mathrm{Ai}(\epsilon^{-2/3}\eta^{1/3}x) \right\}, \tag{A.5}$$

$$|x| \ll 1;$$

$$\psi_{III}(x) = C[-\overline{Q}(x)]^{-1/4} \left\{ \cos\left[\frac{\overline{\mathcal{I}}_2(x)}{\epsilon} + \frac{\pi}{4}\right] - 2\exp\left[\frac{2\gamma\overline{\mathcal{I}}_1(x_2)}{\epsilon}\right] \sin\left[\frac{\overline{\mathcal{I}}_2(x)}{\epsilon} + \frac{\pi}{4}\right] \right\}, \tag{A.6}$$

$$x < 0, (-x) \gg \epsilon^{2/3};$$

where

$$\overline{\mathcal{I}}_1(x) \equiv \int_0^x \sqrt{\overline{Q}(t)}dt, \quad \overline{\mathcal{I}}_2(x) \equiv \int_x^0 \sqrt{-\overline{Q}(t)}dt,$$
$$\overline{Q}(x) = 1 - E(x + r_T)^{-2a} + \frac{3\epsilon^2}{4(x + r_T)^2},$$

C is an arbitrary constant, $x_{1,2} \equiv r_{1,2} - r_T$, and $\eta \equiv \overline{Q}'(x = 0) = 2aEr_T^{-2a-1} - 3\epsilon^2/(2r_T^3)$. For rigid boundaries, γ should be set equal to unity, while for free boundaries it is given by equation (3.40). Note that although there are both growing and decaying exponential contributions in equation (A.4), the overall behavior is guaranteed to be decaying (due to the difference of the two terms) as one approaches x_2.

In deriving these approximations to the eigenfunctions, we have applied the boundary conditions at x_2 only, and matched the solutions in the overlap regions. Applying the boundary condition at x_1 to equation (A.6) leads to the eigenvalue conditions (3.38) and (3.39). In the extremely small ϵ limit, both (3.38) and (3.39) reduce to $\sin[\mathcal{I}_2(r_1)/\epsilon+\pi/4]=0$ which, in order to be satisfied for all finite n, necessarily requires

$$\int_{r_1}^{r_T} \sqrt{Et^{-2a}-1}\,dt \to 0,$$
$$\Rightarrow r_T \to r_1, \quad \text{or} \quad E \to r_1^{2a} \equiv E_{min},$$

where we have used equation (A.1). That is, for *all* modes in this limit, the turning point approaches the inner radius. This is an important and useful lower bound on E.

Large E

Choosing $\epsilon = 1/\sqrt{E}$, equation (3.36) takes the form (3.35), with

$$Q(r) = \epsilon^2\left(k^2+\frac{3}{4r^2}\right) - k^2 r^{-2a}. \tag{A.7}$$

If we ignore the term $O(\epsilon^2)$, then Q has no turning points and the leading-order WKB solution is

$$\begin{aligned} \psi(r) &= c_1(-Q)^{-1/4}\sin\left[\frac{1}{\epsilon}\int_{r_1}^{r}\sqrt{-Q(t)}dt\right] + c_2(-Q)^{-1/4}\cos\left[\frac{1}{\epsilon}\int_{r_1}^{r}\sqrt{-Q(t)}dt\right] \\ &= \frac{r^{a/2}}{\sqrt{k}}\left\{c_1\sin\left[\frac{k\sqrt{E}}{a-1}(r_1^{1-a}-r^{1-a})\right] + c_2\cos\left[\frac{k\sqrt{E}}{a-1}(r_1^{1-a}-r^{1-a})\right]\right\}. \end{aligned} \tag{A.8}$$

Note that the solution is sinusoidal everywhere, since there is no turning point. For rigid boundary conditions, we have $\psi(r_1) = \psi(r_2) = 0$. The former implies $c_2 = 0$; the latter then gives

$$E = \left[\frac{n\pi(a-1)}{k(r_2^{1-a}-r_1^{1-a})}\right]^2, \quad n \to \infty. \tag{A.9}$$

The requirement $n \to \infty$ must be made for consistency of our approximation. Thus $E \sim k^{-2}$ for E large. One can proceed to derive the eigenvalue condition for free boundaries from equations (A.3), but it is sufficient for our purposes to note that the resulting expression reduces to (A.9) when E is sufficiently large.

Appendix B:
Critical Field Strengths for Stability

Equation (A.9) implies that $k^2E \sim$ constant for E large. To find the critical field strength for stability, it is essential to know $\lim_{k\to 0} k^2E$ for any given a (§3.5.5). Equation (A.9), however, gives an incorrect value for this quantity, because the assumptions leading to (A.8) no longer hold.

We need to return to equation (A.7), with the assumption now that $k \sim \epsilon$. With an error $O(\epsilon^4)$ then,

$$Q(r) = \frac{3\epsilon^2}{4r^2} - k^2r^{-2a}. \tag{B.1}$$

Q has a turning point at

$$r_T = \left(\frac{4k^2}{3\epsilon^2}\right)^{\frac{1}{2(a-1)}} = \left(\frac{4}{3}k^2E\right)^{\frac{1}{2(a-1)}}. \tag{B.2}$$

The eigenfunctions in this case look identical to equations (A.4) - (A.6), except that here $\epsilon = 1/\sqrt{E}$ and Q and r_T are as above. Also, $\eta = 2ak^2r_T^{-2a-1} - 3\epsilon^2/(2r_T^3)$. Since r_T approaches a constant in this asymptotic limit, the region of sinusoidal behavior is always of finite size, in contrast to the situation of Appendix A, where it vanishes as $\epsilon \to 0$. Applying the boundary conditions to equation (A.6) again yields equations (3.38) and (3.39), with the above-noted changes in certain variables. Observe that

$$\frac{\mathcal{I}_1(r)}{\epsilon} = \int_{r_T}^{r} \sqrt{Q(t)/\epsilon^2}\, dt = \int_{r_T}^{r} \sqrt{\frac{3}{4t^2} - k^2Et^{-2a}}\, dt = \int_{r_T}^{r} \sqrt{\frac{3}{4t^2} - \frac{2at^{-2a}}{v_A^2}}\, dt,$$

where we have used equation (3.47), and let $v_A = v_{A,crit}$ for simplicity. With a similar result for $\mathcal{I}_2/\epsilon$, one sees that direct numerical solution of (3.38) for v_A is possible. The same is true in the free boundary case. To see this, set $\omega^2 = 0$, whence α and β become

$$\alpha = \frac{1}{2r_1} - \frac{g_{eff}(r_1)}{v_A^2}, \quad k \to 0$$

and

$$\beta = \frac{1}{2r_2} - \frac{g_{eff}(r_2)}{v_A^2}, \quad k \to 0,$$

so that Eq. (3.39) is a function of v_A.

Taking $r_2 \to \infty$, Eqs. (3.38) and (3.39) become (to leading order in ϵ):

$$\sin\left[\frac{\mathcal{I}_2(r_1)}{\epsilon} + \frac{\pi}{4}\right] = 0 \quad \text{and} \quad \cos\left[\frac{\mathcal{I}_2(r_1)}{\epsilon} + \frac{\pi}{4}\right] = 0,$$

respectively, whence one obtains

$$\begin{aligned} \int_{r_1}^{r_T} \sqrt{\frac{2at^{-2a}}{v_A^2} - \frac{3}{4t^2}}\, dt &= \left(n - \frac{1}{4}\right)\pi \qquad \text{(RIGID)} \\ &= \frac{2n-1}{4}\pi, \qquad \text{(FREE)} \end{aligned}$$

with $n \to \infty$. The integral can be evaluated numerically, yielding the critical Alfvén speeds for different a. These are shown for the lowest-order modes ($n = 1$) in Table 3.1. The free boundary results are in fact extreme upper limits; they are typically ~ 30% larger than those found numerically (see Figure 3.8b). This is likely due to the fact that, compared to equation (3.38), more terms are neglected in equation (3.39) en route to the leading order approximation.

a	r_1/r_0 $(r_2 \to \infty)$	E_{min}	$\Omega^{(\ell)}_{A,crit}$	$\lvert\omega^{(\ell)}_{max}\rvert$	k^2E $(k \to 0)$	$v_{A,crit}$	
						Rigid	Free
1.5	0.3679	0.04979	7.76	3.36	2.082	1.20	1.91
1.6	0.4019	0.05409	7.69	3.44	2.317	1.18	1.95
1.7	0.4312	0.05727	7.71	3.55	2.552	1.15	1.98
1.8	0.4569	0.05961	7.77	3.69	2.788	1.14	2.00
1.9	0.4796	0.06130	7.87	3.84	3.025	1.12	2.03
2.0	0.5000	0.06250	8.00	4.00	3.263	1.11	2.05

Table 3.1: Model characteristics in two limiting cases: $k \to \infty$ (columns 3, 4, and 5), and $k \to 0$ (columns 6, 7, and 8). All frequencies (velocities) are in units of Ω_0 $(r_0\Omega_0)$. See text for details.

λ_{crit} (units of r_1)	a		
	1.5	1.7	2.0
100	1.433	1.436	1.446
	1.056	1.043	1.022
50	1.394	1.402	1.418
	1.014	1.013	1.001
20	1.270	1.284	1.312
	0.903	0.922	0.933
10	1.088	1.105	1.142
	0.769	0.803	0.832
5	0.833	0.847	0.889
	0.605	0.647	0.689
1	0.287	0.303	0.339
	0.250	0.280	0.317
0.5	0.165	0.178	0.205
	0.151	0.172	0.199
0.1	0.040	0.045	0.054
	0.039	0.045	0.053

Table 3.2: Critical Alfvén speeds, $v_{A,crit}/(r_0\Omega_0)$, for selected perturbation wavelengths λ_{crit} and shear parameters a. The top line for each λ_{crit} is for free boundaries; bottom for rigid. We have taken $r_2/r_1 = 100$. See text for details.

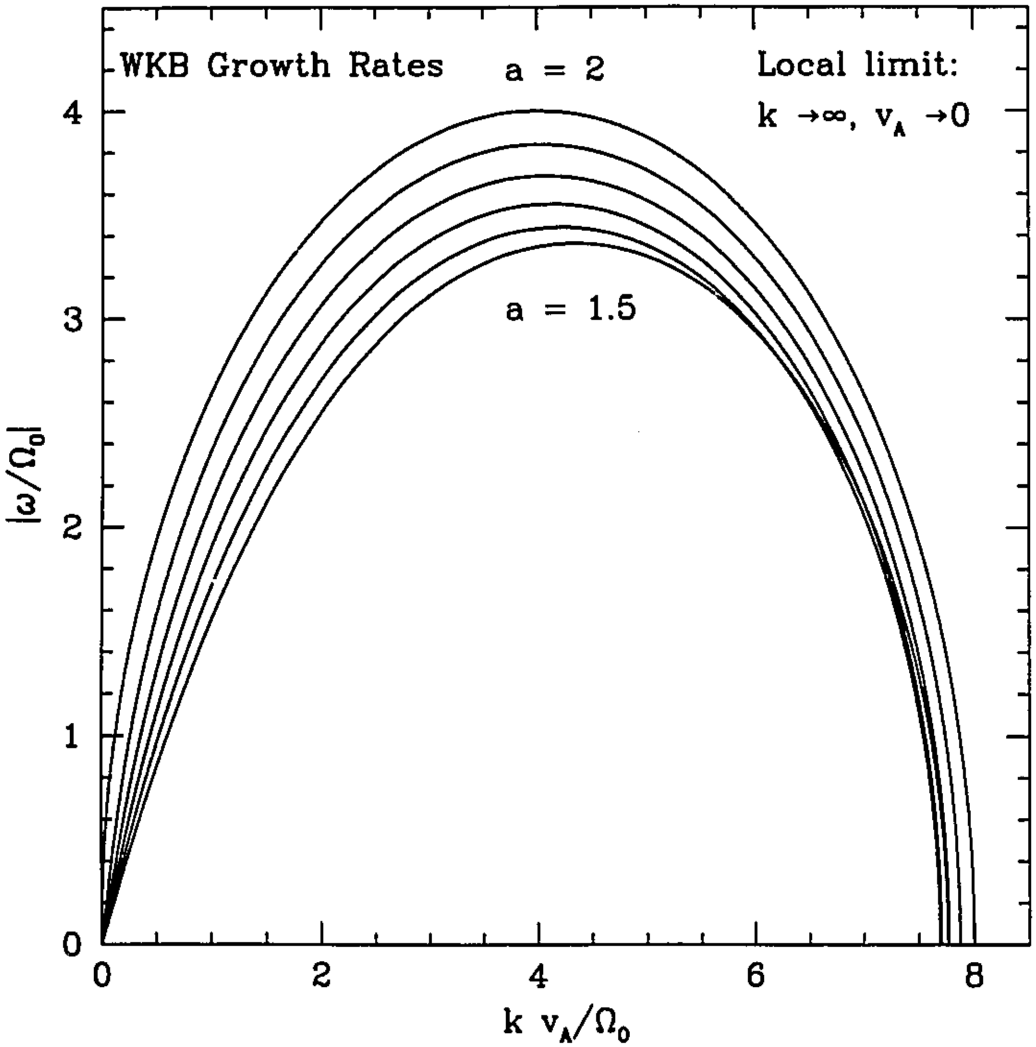

Figure 3.1: Limiting growth rates ($k \to \infty, v_A \to 0$) as a function of Alfvén frequency for rotation law indices (from top to bottom) a = 2, 1.9, 1.8, 1.7, 1.6, and 1.5. Note that $\Omega_{A,crit}(a = 1.5) > \Omega_{A,crit}(a = 1.7) > \Omega_{A,crit}(a = 1.6)$; this ordering is due to the changing location of the pressure maximum with respect to a (see Table 3.1 and text for details).

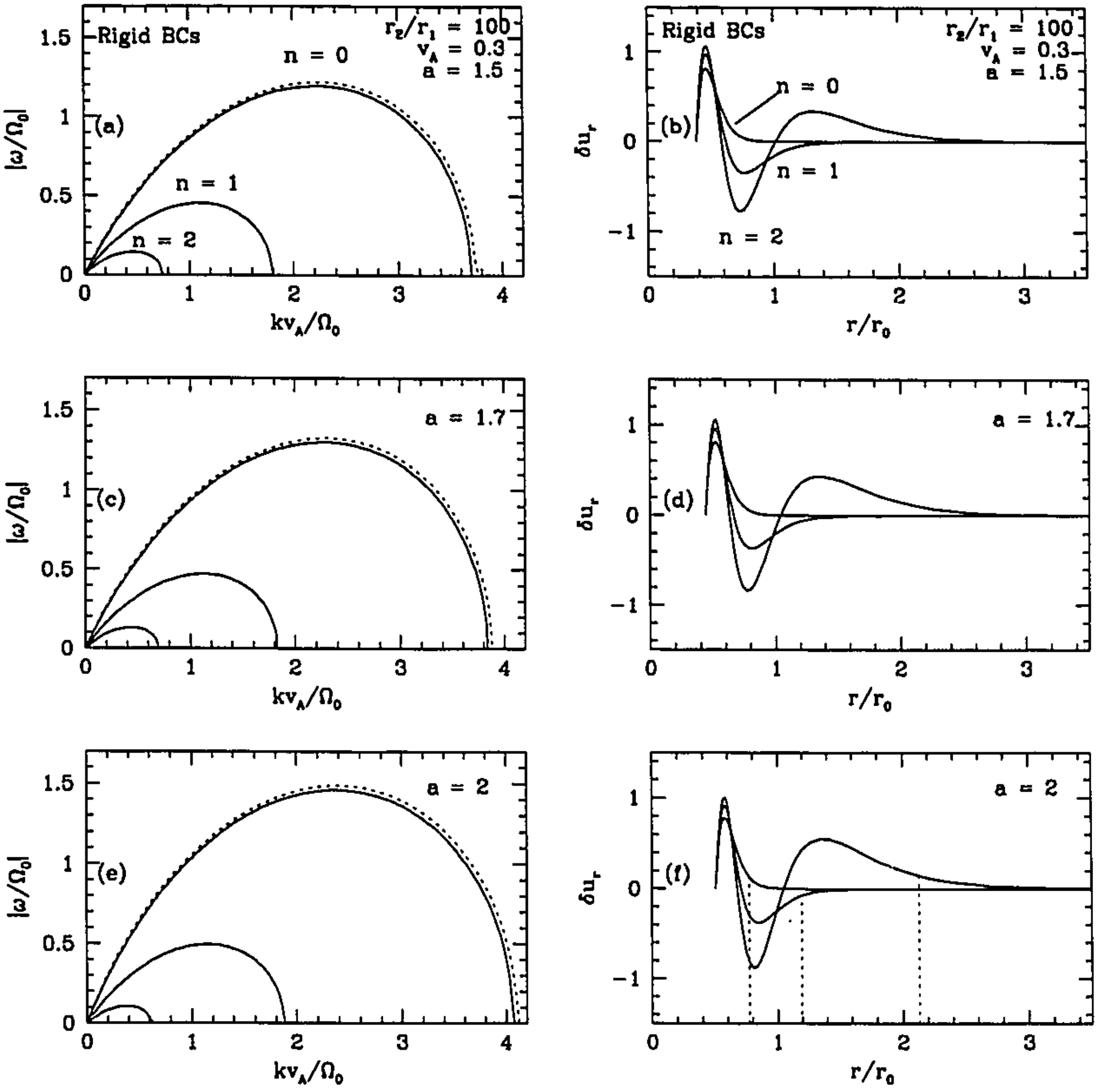

Figure 3.2: For rigid boundary conditions, (a) growth rates and (b) eigenfunctions at maximum growth rate for the three unstable modes at $v_A/(r_0\Omega_0) = 0.3$, with $r_2/r_1 = 100$ and $a = 1.5$. The dotted curve is the WKB approximation for the $n = 0$ mode. Panels (c), (d) are for $a = 1.7$; (e), (f) for $a = 2$. In (f), the dotted lines show the location of the turning points, r_T, for each of the modes.

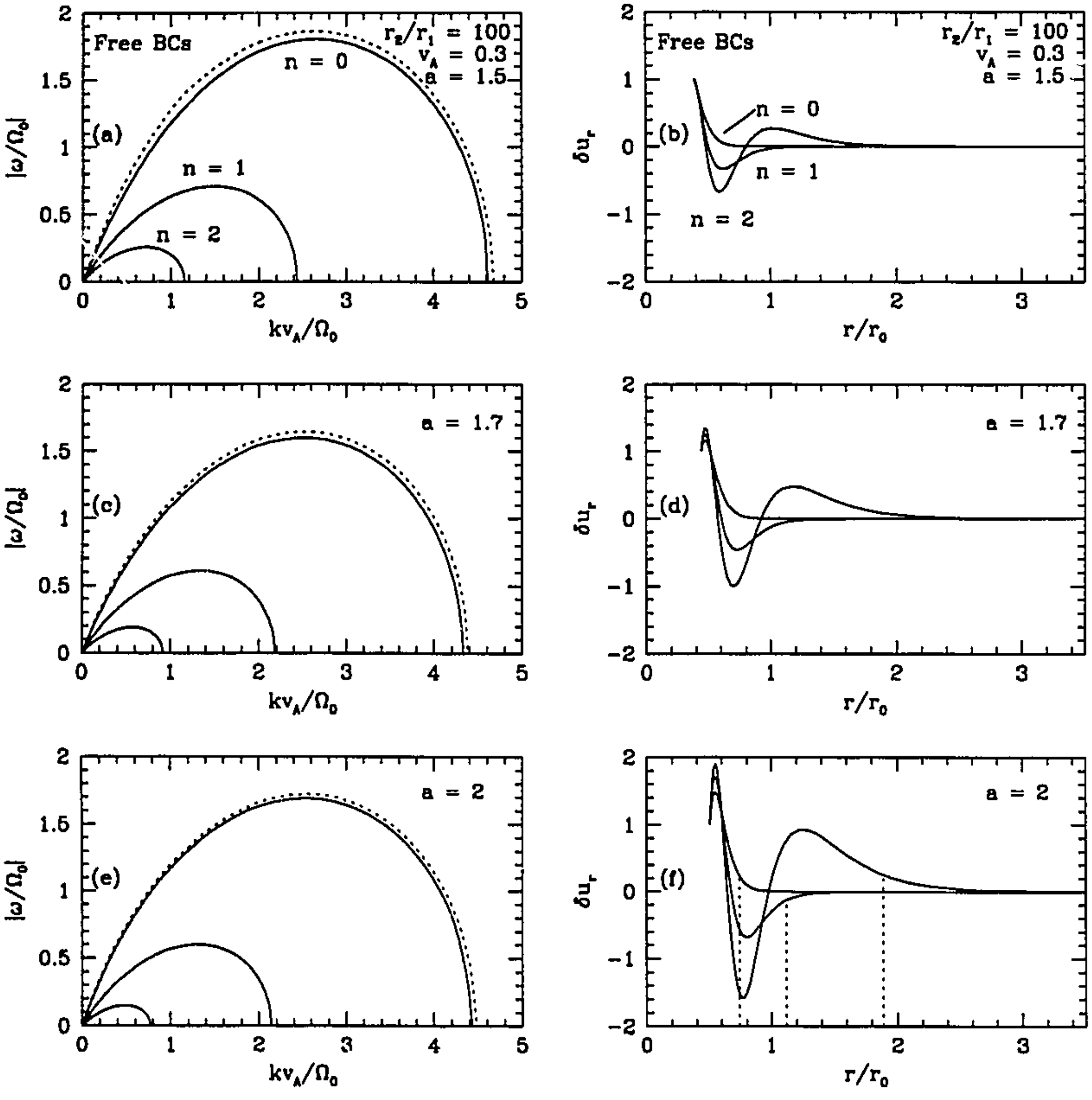

Figure 3.3: Same as Figure 3.2, but for free boundary conditions.

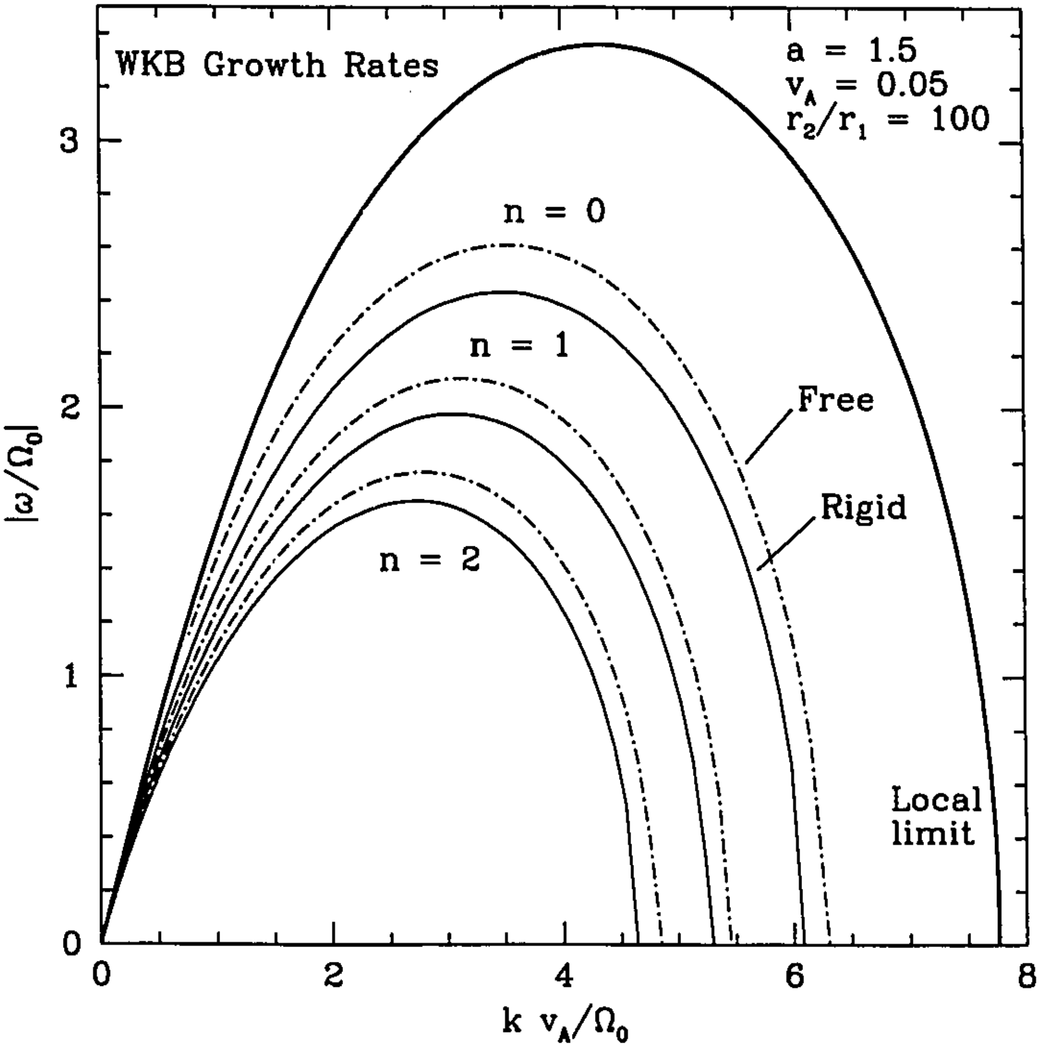

Figure 3.4: WKB growth rates, for both rigid and free boundaries, Keplerian rotation, and $v_A/(r_0\Omega_0) = 0.05$. Only the three fastest growing modes are shown. The heavy line is the limiting growth rate curve for $a = 1.5$ from Figure 3.1.

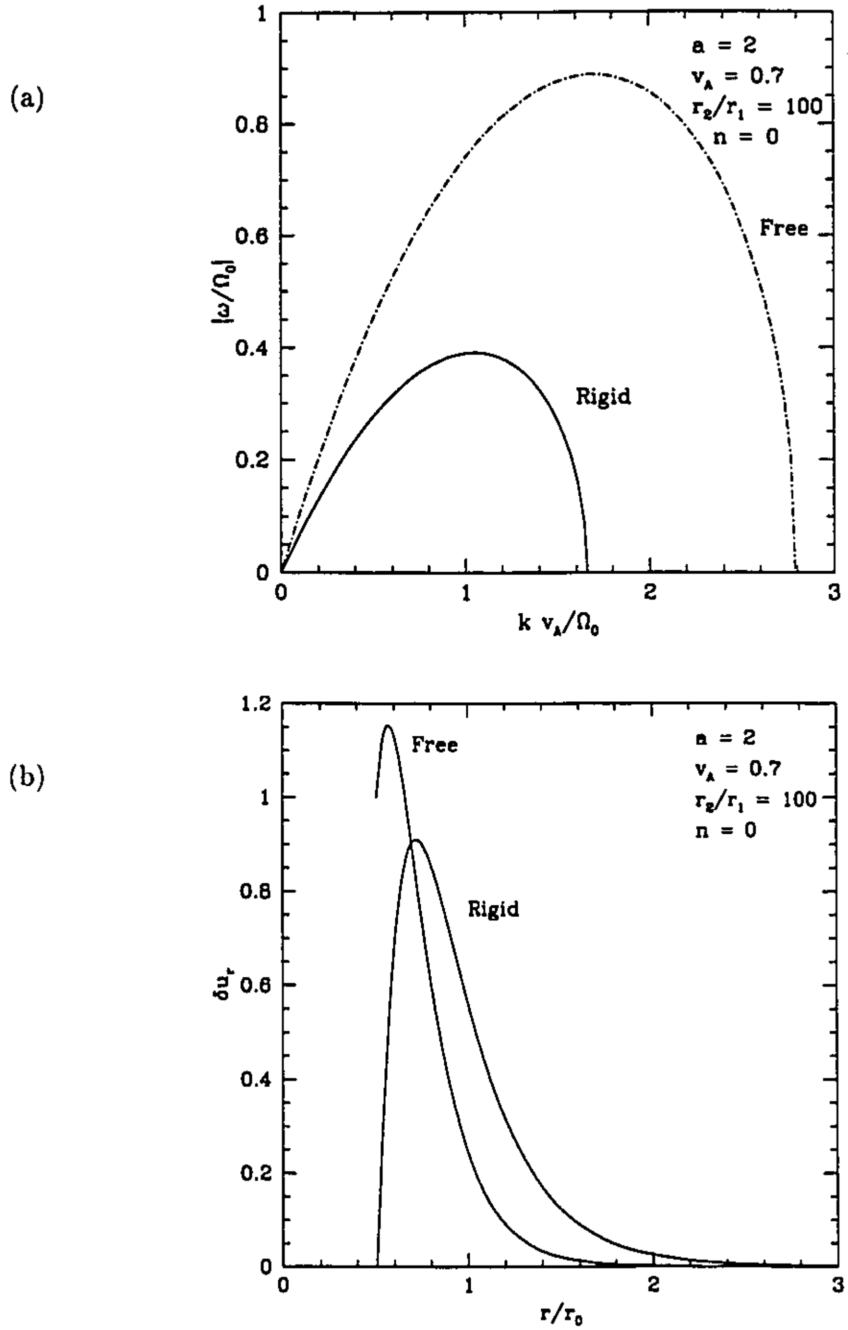

Figure 3.5: Comparison of numerical (a) growth rates and (b) eigenfunctions at maximum growth rate of the $n = 0$ mode of instability for rigid vs. free boundary conditions. The rotation law is that of constant angular momentum ($a = 2$), and $v_A/(r_0\Omega_0) = 0.7$.

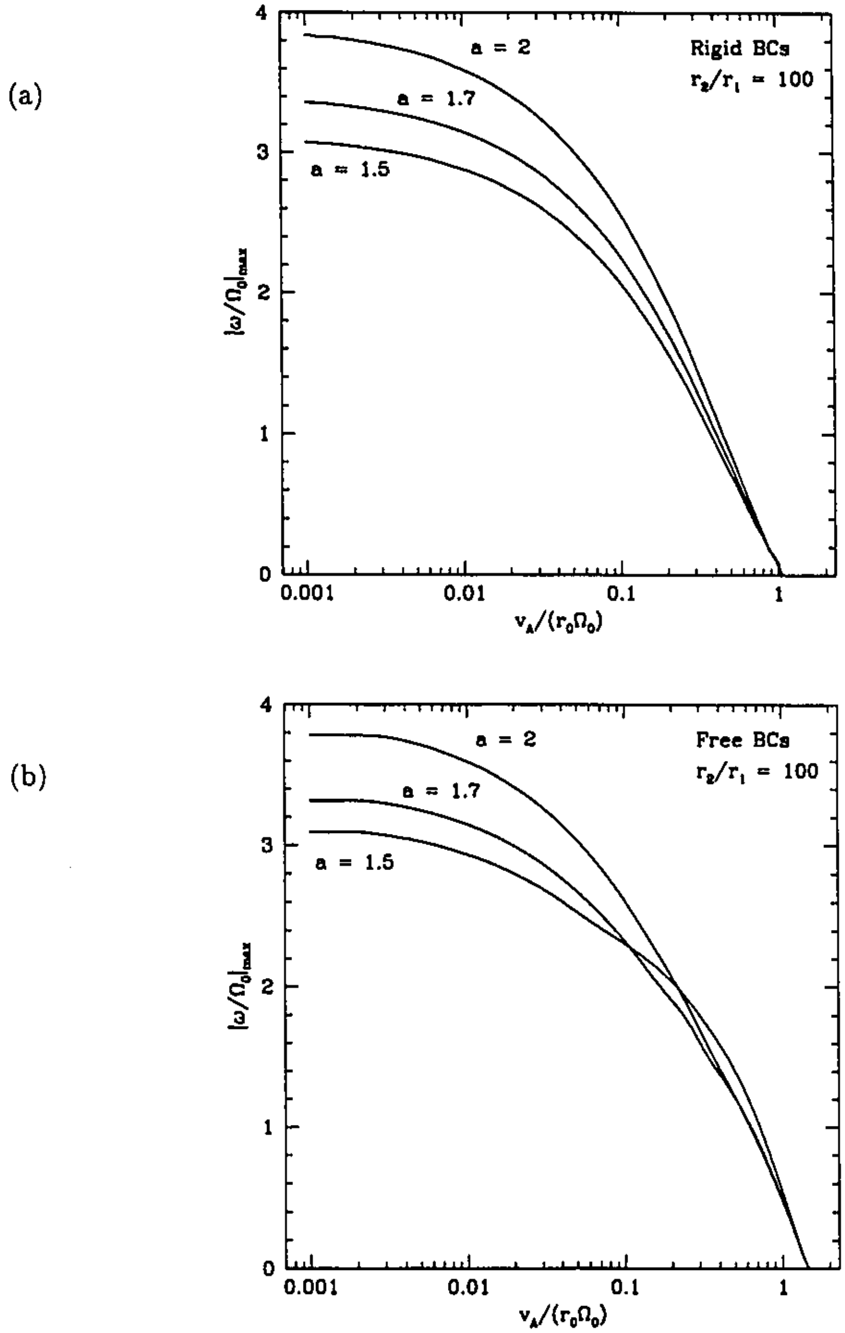

Figure 3.6: Maximum growth rates as a function of Alfvén speed for different a and (a) rigid boundaries; (b) free boundaries.

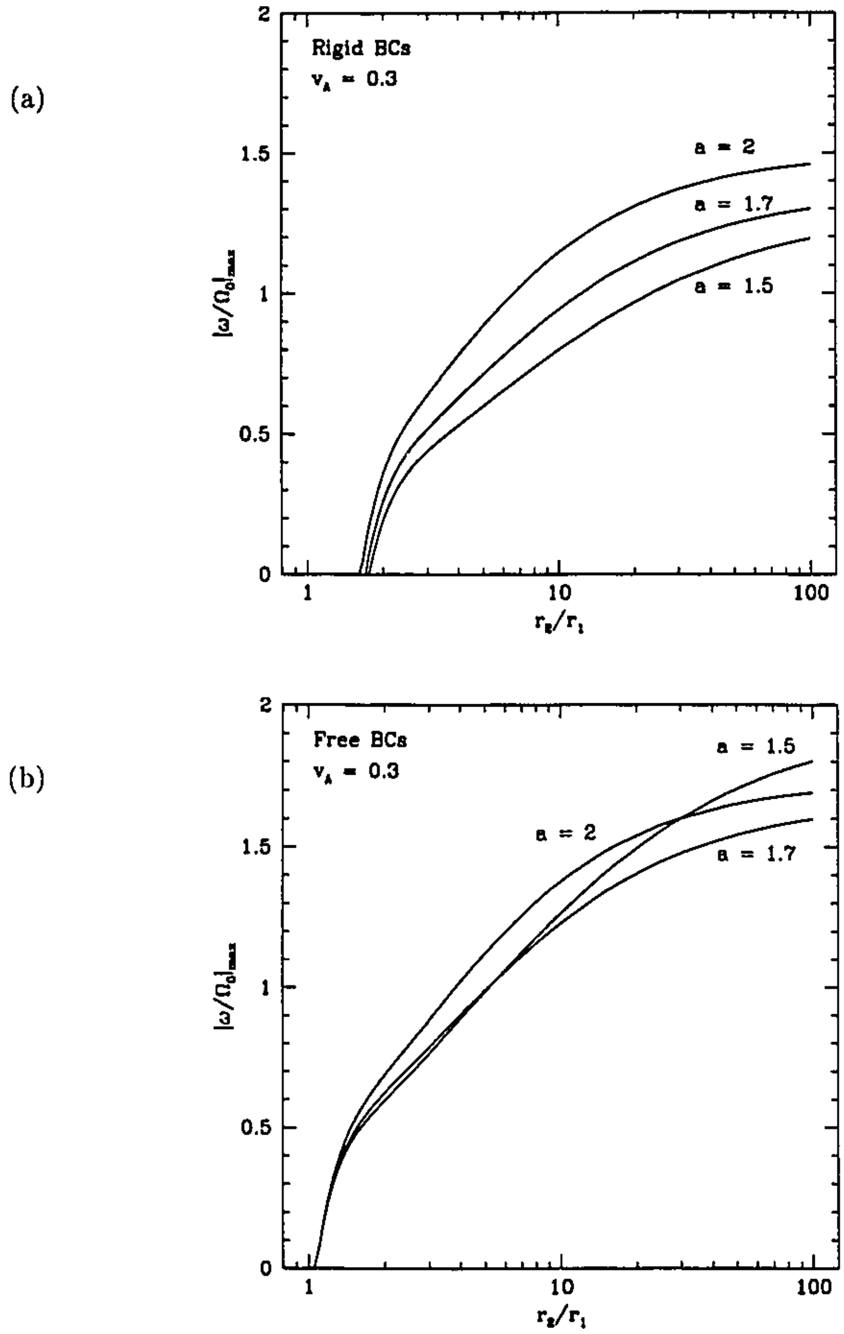

Figure 3.7: Maximum growth rates as a function of r_2/r_1 for $v_A/(r_0\Omega_0) = 0.3$, different a and (a) rigid boundaries; (b) free boundaries.

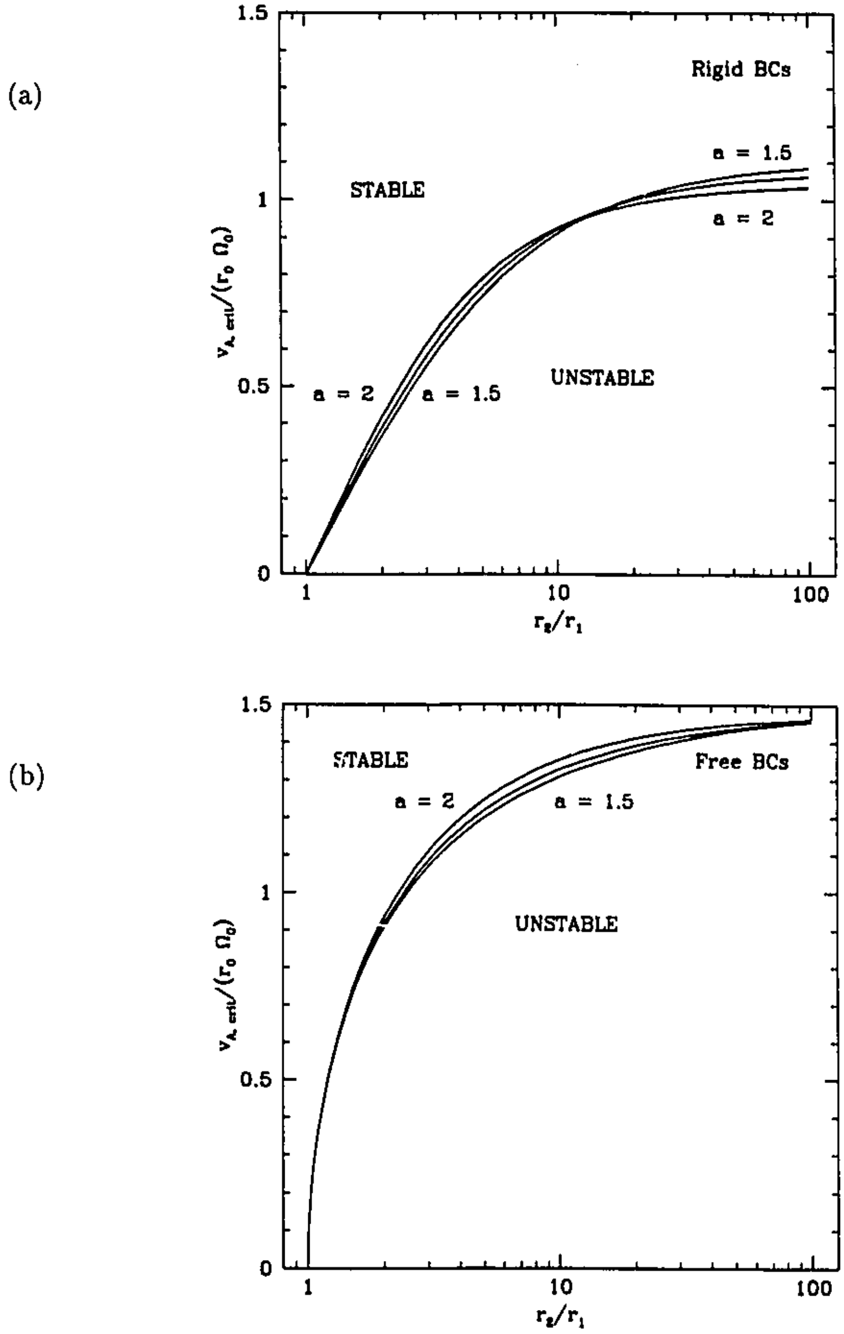

Figure 3.8: Critical Alfvén speed $v_{A,crit}/(r_0\Omega_0)$ as a function of r_2/r_1 for different a (middle curve is for $a = 1.7$) and (a) rigid boundaries; (b) free boundaries. Models which lie above the curves are stable; below, unstable.

Chapter 4

ON THE GLOBAL STABILITY OF MAGNETIZED ACCRETION DISKS.

II. VERTICAL AND AZIMUTHAL MAGNETIC FIELDS

CHARLES CURRY and RALPH E. PUDRITZ
Department of Physics and Astronomy
McMaster University, Hamilton, Ontario L8S 4M1, Canada

Email:curry@jabba.physics.mcmaster.ca,pudritz@physics.mcmaster.ca

ABSTRACT

We investigate the global stability of a differentially rotating fluid shell threaded by vertical and azimuthal magnetic fields to linear, axisymmetric perturbations. This system, which models a thick accretion disk in the vicinity of its midplane, is susceptible to the Velikhov-Chandrasekhar (VC) instability in the absence of the azimuthal field. In most cases, the azimuthal field tends to stabilize the VC instability, although strong fields (Alfvén speed of order the characteristic rotational speed in our incompressible model) are required for complete stabilization. Stability diagrams are constructed, indicating critical values of the two fields for instability. We find an additional strong field instability that arises when the azimuthal Alfvén speed exceeds the characteristic rotational speed. This instability, in the case of a freely bounded configuration, has certain similarities to the sausage instability for interpenetrating fields in plasma physics, and may be important for very massive disks or filamentary molecular clouds. An application to the L1641 region in Orion A is briefly discussed. Finally, we find that the effect of a radially varying vertical field (without an azimuthal field) is mainly stabilizing.

Subject headings: accretion, accretion disks - instabilities - ISM: magnetic fields - MHD

4.1 Introduction

One of the more interesting recent developments in the theory of accretion disks was the discovery of virulent instabilities that develop only in the presence of magnetic fields. Balbus & Hawley (1991) (hereafter BH) showed that a Keplerian disk in a state of pure rotation threaded by a weak axial field was subject to a local instability whose growth rate was on the order of the local rate of rotation. In a previous paper, we examined the global counterpart of this instability, the Velikhov-Chandrasekhar (VC) instability, showing that growth persisted at comparable rates (Curry, Pudritz, & Sutherland 1994, hereafter CPS). There remain serious questions, however, concerning how the instability is affected as models are augmented by additional physics. In particular, the influence of the more complicated magnetic field structures expected to exist in protostellar, CV, and AGN disks has yet to be carefully addressed. In this paper, we extend the model of CPS to include disks with radially varying vertical (B_z) and azimuthal (B_ϕ) fields.

There are many reasons to expect an azimuthal field to be an important, sometimes dominant, magnetic field component in accretion disks. Strong differential rotation can generate B_ϕ from a radial field component B_r, which can itself be created either by dynamo processes or accretion. The BH instability has been shown to generate strong B_r and B_ϕ from an initially weak B_z (Hawley, Gammie, & Balbus 1995). If B_z is inherited from the central object or the interstellar medium, disk torques can convert it directly to B_ϕ. Thus it is most likely that all three components of **B** are dynamically important for most types of disks. Of course, as has been made clear by all work following BH, one needs very little initial B_z in order for that component to be "dynamically important."

The observational evidence for B_ϕ in protostellar disks is at the present time quite sparse, mainly due to uncertainties about the nature of the detected disks themselves. Recent mid-infrared spectropolarimetry of high-mass star-forming regions by Aitken et al. (1993) revealed a high correlation between objects with elongated molecular disk-like structures (numbering 10 in their sample) and magnetic fields oriented along the long axis of the disk (7 of these 10). The authors claim this as evidence for a predominantly azimuthal field structure in these regions. One should note, however, that the objects in question are 10^3

to 10^4 AU in extent, with masses $\sim 10^3 M_\odot$, and so are not likely to represent Keplerian accretion disks. As evidence for large-scale rotation is lacking, they may in fact be self-gravitating toroids or "pseudodisks," supported to some extent by the field itself (Galli & Shu 1993).

Keplerian disks with magnetic field components in both the azimuthal and vertical directions have been actively studied as possible sources of centrifugally driven winds and outflows (e.g. Blandford & Payne 1982, Uchida & Shibata 1985, Pelletier & Pudritz 1992). This suggests an additional motivation for the present study: to determine whether the various equilibria assumed in models of magnetically driven outflows are stable. A first step in this direction was taken recently by Lubow, Papaloizou & Pringle (1994).

In a different context, Galactic center molecular disk observations (Genzel 1989, Hilderbrand et al. 1990) indicate that $B_r \sim B_\phi \sim 1$ mG, with a somewhat weaker B_z. This is in contrast to the larger-scale field structure (i.e. the inner 70 pc of the Galaxy), which is almost purely vertical, i.e. perpendicular to the Galactic plane. Wardle & Königl (1990) have modeled this region using a self-similar magnetized disk model, under the assumption that the inner field structure results from advection of the large-scale field by inflowing matter, with differential rotation subsequently leading to a strong azimuthal component. As observations of other galactic nuclei and AGN are still not able to resolve the inner disks, much less any associated magnetic field structure, it would be unwise to speculate further along these lines. However, since the inner regions of AGN are expected to possess "thick" rather than thin Keplerian disks, we use the same equilibrium sequence as introduced in CPS; namely, one in which radial pressure gradients oppose the central gravity for non-Keplerian rotation laws. The situation examined in the present paper is even more interesting, however, since radial *magnetic* gradients are also present.

As a final possible application of the work presented here, we cite evidence that elongated filaments of gas in molecular clouds are associated with helical velocity and magnetic fields (Bally 1989). The latter are indicative of the simultaneous presence of B_ϕ and B_z. The model employed in this paper, although formulated primarily for accretion disks, yields interesting results in the parameter range expected to hold in such regions. In particular, we find a new instability which sets in when the azimuthal Alfvén speed is greater than the rotational speed.

We defer to a later section a detailed description of previous work on the effect of B_ϕ on the VC and BH instabilities, but it is of use to review here what is known generally about the stability of rotating configurations with azimuthal field. Since we do not attempt to account for the vertical structure of the disk in this study, the following discussion is restricted to purely radial distributions of angular velocity and magnetic field. The central question is this: given a rotation profile $\Omega(r)$ and field distribution $B_\phi(r)$, $B_z(r)$, can one predict, even locally, whether a configuration is stable to infinitesimal perturbations in the fluid quantities ? What is needed is a necessary *and* sufficient criterion for stability, such as exists for purely vertical and purely azimuthal fields. These are, respectively;

$$\frac{d\Omega^2}{dr} \geq 0$$

and

$$\frac{1}{r^2}\frac{d}{dr}(r^2\Omega)^2 - \frac{r^2}{4\pi\rho}\frac{d}{dr}\left(\frac{B_\phi}{r}\right)^2 \geq 0. \tag{4.1}$$

The first criterion is due to Chandrasekhar (1960), and the second to Michael (1954). For the combined fields, no similar criteria are known. *Sufficient* criteria are available, however; these are (Chandrasekhar 1961; Howard & Gupta 1962; Dubrulle & Knobloch 1993; Kumar, Coleman, & Kley 1994):

$$\begin{aligned} \frac{d}{dr}(rB_\phi)^2 &\leq 0 \qquad (\Omega = 0), \\ \text{and} \qquad r\frac{d\Omega^2}{dr} - \frac{2B_\phi}{4\pi\rho r^2}\frac{d}{dr}(rB_\phi) &\geq 0 \qquad (\Omega \neq 0). \end{aligned} \tag{4.2}$$

Sufficient criteria can only be regarded as incomplete guides to the global stability of systems; the inherent limitations of criterion (4.2) will be made manifest later on in the paper.

As to the actual distribution of B_ϕ and B_z across the disk, there seem to be very few restrictions at this time[1]. By considering power-law distributions in these two field components, we hope to cover a range of plausibility.

It is important to emphasize that the goal of this series of papers is not to replace the many local analyses that exist in the literature. Rather, a model such as we utilize below,

---

[1] Because an equilibrium B_r immediately implies a time-dependent, growing B_ϕ (BH) which destroys the time-invariance of the resulting equations, we ignore this field component in the present work.

while idealized and unrealistic in many respects, highlights intrinsically global behavior which will not be discovered in any local analysis. Examples of this found in the present work and in CPS are effects which involve coherent motions over large portions of the disk, and phenomena modified or even enhanced by the presence of a disk boundary, imperfectly modelled though it may be. Thus the present work complements, not replaces, existing local analyses.

The format of the paper is as follows. The equilibrium state is described in §2, and the perturbations to this state in the following section. Quantitative results for the combined effect of azimuthal and constant vertical fields are presented in §4, and those for a radially varying vertical field in §5. In the final section, our results are compared with those of other investigators, and we make some additional comments on a new instability found in §4, before giving a final summary. Technical details of the calculations may be found in the four appendices.

4.2 The Equilibrium

4.2.1 Basic equations

The equilibrium was described in detail in CPS, and has also been employed in stability analyses of thick, pressure-supported disks; see, e.g., Blaes & Glatzel (1986), Sekiya & Miyama (1988), and Jaroszyński (1988). The model is a simplified form of the "thick torus" model for AGN (see, e.g., Paczyńsky & Wiita 1980), supplemented by gradients of magnetic field pressure, but lacking vertical structure. It should therefore adequately describe a small region straddling the midplane of a real disk, *with radial gas and magnetic pressure support taken fully into account.* Thus the equilibrium is *not* that of a Keplerian disk, although this case is naturally included in the equilibrium sequence (CPS).

Consider a cylindrical shell of homogeneous, incompressible, ideal MHD fluid, of infinite extent in the z-direction, rotating about the z-axis in the Newtonian point-mass potential $\Psi = -GM/r$. The purely radial dependence of the potential is justified if, at every radius r, the vertical scale height of the "disk" $H \ll r$, so that there is little variation of Ψ with z. The stationary solution of the MHD equations depends only on the radial coordinate,

r. To calculate explicit quantities of interest, we take the following power-law dependences for the angular velocity, azimuthal, and vertical magnetic fields, respectively:

$$\Omega(r) = \Omega_0 \left(\frac{r}{r_0}\right)^{-a}, \quad B_\phi(r) = B_{\phi 0} \left(\frac{r}{r_0}\right)^{-b+1}, \quad B_z(r) = B_{z0} \left(\frac{r}{r_0}\right)^{-c+1}, \tag{4.3}$$

where $\Omega_0, B_{\phi 0}, B_{z0}, a, b, c$, and r_0 are constants. As in CPS, we consider the effect of both rigid and free boundaries. In the latter case, $\mathbf{B}$ is supposed to permeate the regions both to the interior and exterior of the shell, as well as within the fluid. Using equations (4.3), the radial component of the equation of motion becomes (Appendix A)

$$\frac{p'}{\rho} = r_0 \Omega_0^2 \left(\frac{r}{r_0}\right)^{1-2a} - \frac{GM}{r^2} - \frac{1}{r_0}\left[(2-b)V_{\phi 0}^2 \left(\frac{r}{r_0}\right)^{1-2b} + (1-c)V_{z0}^2 \left(\frac{r}{r_0}\right)^{1-2c}\right], \tag{4.4}$$

where the prime symbol $\equiv d/dr$, $V_{\phi 0, z0}^2 \equiv B_{\phi 0, z0}^2/4\pi\rho$ are the azimuthal (ϕ) and vertical (z) Alfvèn speeds at r_0, and M is the mass of the central object (self-gravity is ignored).

Inspection of equation (4.4) shows that the magnetic terms aid rotation and oppose the central gravity if $b > 2$ and/or $c > 1$, and vice-versa if $b < 2$ and/or $c < 1$. As in CPS, we consider configurations in which the gas pressure vanishes at the boundaries, and identify r_0 with the gas pressure maximum, where $p' = 0$. Equation (4.4) then gives

$$\frac{GM}{r_0^2} = r_0 \Omega_0^2 - [(2-b)V_{\phi 0}^2 + (1-c)V_{z0}^2]/r_0. \tag{4.5}$$

This is merely a statement of radial magnetostatic equilibrium at the pressure maximum. In order for r_0 to be a maximum, we must have $p''(r_0) < 0$. From equation (4.4), this requires

$$(2b-3)(b-2)\overline{V}_{\phi 0}^2 + (2c-3)(c-1)\overline{V}_{z0}^2 + 2a - 3 > 0, \tag{4.6}$$

where an overline indicates that the Alfvén speeds are now scaled with respect to $r_0\Omega_0$, the circular speed at r_0. Note that the above gives $a > 3/2$ when $V_{\phi 0} = 0$ and $c = 1$, as expected. Condition (4.6) should be satisfied for each equilibrium we examine.

Integrating equation (4.4) and eliminating GM via equation (4.5), one obtains the stationary pressure distribution

$$\begin{aligned}\frac{p}{\rho} = \frac{\mu^2}{2} + \frac{1}{r} - 1 + \frac{1 - r^{-2(a-1)}}{2(a-1)} - (2-b)\overline{V}_{\phi 0}^2 \left[\frac{1}{r} - 1 + \frac{1 - r^{-2(b-1)}}{2(b-1)}\right] \\ -(1-c)\overline{V}_{z0}^2 \left[\frac{1}{r} - 1 + \frac{1 - r^{-2(c-1)}}{2(c-1)}\right],\end{aligned} \tag{4.7}$$

where we have chosen our units such that $r_0 = \Omega_0 = 1$, and where μ^2 is a constant equal to the ratio of thermal to kinetic energy at r_0. We assume, as in CPS, that the gas and magnetic pressures remain finite as $r_2 \to \infty$; this implies that $a, b, c \geq 1$.

4.2.2 Special cases

(i) $B_z =$ *constant*

Much of this paper is based on the particular case of a constant vertical field; i.e. $c = 1$. Then equation (4.5) and inequality (4.6) lead to the inequalities (in dimensionless units)

$$1 - (2-b)V_{\phi 0}^2 > 0,$$
$$(2b-3)(b-2)V_{\phi 0}^2 + 2a - 3 > 0,$$

where we have dropped the overlines on the Alfvén speeds for convenience. Considering all possible values of a and b leads to the conclusion that only certain values of $V_{\phi 0}$ are permitted for a given (a, b).

In the case of rigid boundaries, the inner and outer boundaries of the fluid are determined by the zeros of equation (4.7). For free boundaries, this is still true provided that **B** is continuous across the boundaries, and we shall assume that this is the case. Thus a given model is fixed by choosing r_2/r_1, a, b, and $V_{\phi 0}$. CPS found a monotonic increasing dependence of the VC instability growth rate on r_2/r_1, with a maximum at $r_2/r_1 \gtrsim 100$; thus, we choose $r_2/r_1 = 100$ as a fiducial value for all calculations in this paper. The zeros of equation (4.7) can be positive, negative, or complex. The latter two (unacceptable) possibilities can occur even for $(a, b, V_{\phi 0})$ obeying the above inequalities. We therefore conducted a three-parameter search for acceptable equilibria; the results are summarized in Figures 4.1a and b.

In Fig. 4.1a, various critical values of the azimuthal Alfvén speed are denoted by V_1, V_2, V_3, ...; each is a function of a and b. Although we calculated equilibria for all a, b in the range $1 \leq (a, b) \leq 3$, Fig. 4.1b shows only $3/2 \leq (a, b) \leq 2$. We will restrict consideration for most of the paper to this range, since it reduces exactly to the equilibrium of CPS when $B_\phi = 0$. The upper surface in Fig. 4.1b represents $V_5(a > b)$ and $V_6(a < b)$.

Note that for a given a, $3/2 < a < 2$, $V_5 > V_6$.

There is another interesting property of the equilibrium relation (4.7): when $b = 2$ and $c = 1$, we get the equilibrium of CPS. It may be checked that, for the power law fields we assume, this is the unique solution for which the current density, $\mathbf{J} = \nabla \times \mathbf{B}/\mu_0$, vanishes. Hence, the value of a is restricted to $3/2 \leq a \leq 2$, just as in that study, and the location of the inner radius given by equation (3.9) of CPS. Since this special case allows us to examine the effect of the azimuthal field without the added complication of a current, we will assume $b = 2,\ c = 1$ (corresponding to $B_\phi \sim r^{-1}$, $B_z =$ constant) when considering free boundaries in the sections to follow.

(ii) $B_z = B_z(r),\ B_\phi = 0$

In this case equations (4.5) and (4.6) give

$$1 - (1-c)V_{z0}^2 > 0,$$

$$(2c-3)(c-1)V_{z0}^2 + 2a - 3 > 0.$$

As above, these inequalities and equation (4.7) impose restrictions on allowed equilibria; these are summarized in Figs. 4.2a and b. We now examine perturbations to the above-described equilibria.

4.3 The Perturbations

4.3.1 The perturbation equations

We now consider the response of the above equilibrium state to small, axisymmetric, Eulerian perturbations of the form

$$\delta X(r,z,t) = \delta X(r)e^{i(kz+\omega t)}, \tag{4.8}$$

where X is any physical variable, and k and ω are the vertical wavenumber and frequency of the perturbation, respectively. Substituting the forms $X + \delta X$ along with equation (4.3) into the ideal MHD equations, linearizing, and eliminating all variables in favor of the radial velocity perturbation (see Appendix A for details), one obtains a second-order differential equation in δu_r:

$$\frac{1}{r}[r\tilde{\omega}^2(\delta u_r)']' + q(r)\delta u_r = 0, \tag{4.9}$$

where

$$\begin{aligned} q(r) \equiv k^2 r\left[\left(\Omega^2 - \frac{V_\phi^2}{r^2}\right)' - \frac{(V_z^2)'}{r^2}\right] &+ \frac{4k^2}{\tilde{\omega}^2}\left(\frac{kV_\phi V_z}{r} - \omega\Omega\right)^2 \\ &- \tilde{\omega}^2\left(k^2 + \frac{1}{r^2}\right), \end{aligned}$$

$$\tilde{\omega}^2 \equiv \omega^2 - k^2 V_z^2(r),$$

and $V_{\phi,z}(r) = B_{\phi,z}(r)/\sqrt{4\pi\rho}$ are the azimuthal and vertical Alfvén speeds. The power-law form of the above (in dimensionless units) is

$$\begin{aligned} q(r) &= 2k^2\left[bV_{\phi 0}^2 r^{-2b} - ar^{-2a} + (c-1)V_{z0}^2 r^{-2c}\right] \\ &+ \frac{4k^2}{\tilde{\omega}^2}(kV_{\phi 0}V_{z0}r^{1-b-c} - \omega r^{-a})^2 - \tilde{\omega}^2\left(k^2 + \frac{1}{r^2}\right). \end{aligned} \tag{4.10}$$

An alternative form of the perturbation equation useful for analytic purposes is obtained via the transformation

$$\psi \equiv (r\tilde{\omega}^2)^{1/2}\delta u_r,$$

whence equation (4.9) becomes

$$\psi'' = k^2 Q(r)\psi, \tag{4.11}$$

with

$$\begin{aligned} Q(r) &= \frac{2}{\tilde{\omega}^2}\left\{ar^{-2a} - bV_{\phi 0}^2 r^{-2b} - (c-1)V_{z0}^2 r^{-2c} - \frac{2}{\tilde{\omega}^2}(kV_{\phi 0}V_{z0}r^{1-b-c} - \omega r^{-a})^2\right\} \\ &+ \left(1 + \frac{1}{k^2 r^2}\right) - \frac{1}{2k^2}\left[\frac{1}{2}\frac{(r\tilde{\omega}^2)'^2}{(r\tilde{\omega}^2)^2} - \frac{(r\tilde{\omega}^2)''}{r\tilde{\omega}^2}\right]. \end{aligned} \tag{4.12}$$

When discussing free-boundary configurations, one must consider the form of the vacuum field perturbations in addition to those within the fluid. We will restrict ourselves to the *current-free* case, i.e. $b = 2, c = 1$, since then the perturbed magnetic field in the interior ($r < r_1$, denoted by subscript i) and exterior ($r > r_2$, subscript o) regions is completely specified by a scalar potential χ, such that

$$\delta\mathbf{B}_{i,o} = B_z\nabla\chi_{i,o},$$

$$\chi_i(\varpi) = c_1 I_0(\varpi), \quad \chi_o(\varpi) = c_2 K_0(\varpi), \tag{4.13}$$

where $\chi_{i,o} = \chi_{i,o}(r)e^{i(kz+\omega t)}$, $\varpi \equiv |k|r$, and I_0 and K_0 are modified Bessel functions of order zero.

4.3.2 The boundary conditions

We solve equation (4.9) subject to both rigid and free boundary conditions (BCs). The former are

$$\delta u_r(r_1) = \delta u_r(r_2) = 0.$$

Free BCs require the continuity of Lagrangian perturbations of the total normal stresses and magnetic flux across the boundaries. In the cylindrical geometry we are considering, both B_ϕ and B_z are everywhere perpendicular to the surface normal $\mathbf{n}$; thus $\mathbf{B} \cdot \mathbf{n} = 0$, and provided that both fields are continuous across the boundaries, the appropriate BC is unchanged from the constant B_z case; that is (CPS),

$$(\delta u_r)' + \left[\frac{1}{r} + \frac{k^2}{\tilde{\omega}^2}\left(g_{eff} + k^2 V_{z0}^2 \frac{\chi_{i,o}}{\chi'_{i,o}}\right)\right] \delta u_r = 0.$$

The subscript i applies at r_1, subscript o at r_2.

For general power laws in $B_\phi(r), B_z(r)$, and in dimensionless units, the effective gravity is given by

$$g_{eff} = r^{1-2a} - \frac{1}{r^2} - (2-b)V_{\phi 0}^2 r^{1-2b} - (1-c)V_{z0}^2 r^{1-2c}.$$

For vanishing current, this becomes identical to the g_{eff} of CPS; i.e. $g_{eff} = r^{1-2a} - 1/r^2$.

From equation (4.13) one finds

$$\left.\frac{\chi_i}{\chi'_i}\right|_{r=r_1} = \frac{1}{|k|}\frac{I_0(\varpi_1)}{I_1(\varpi_1)} \quad \text{and} \quad \left.\frac{\chi_o}{\chi'_o}\right|_{r=r_2} = -\frac{1}{|k|}\frac{K_0(\varpi_2)}{K_1(\varpi_2)},$$

where $\varpi_{1,2} = |k|r_{1,2}$.

4.4 Results: Constant Vertical Field

The majority of our results have been obtained for the special case V_z = constant.

4.4.1 The case of $a = b$

When $a = b$, the rotation frequency Ω and its magnetic analog, V_ϕ/r, have an identical scaling with radius. Equation (4.9) with (4.10) becomes

$$\frac{1}{r}[r(\delta u_r)']' + Q(r)\delta u_r = 0, \tag{4.14}$$

where

$$\begin{aligned} Q(r) &= k^2(Er^{-2a} - 1) - \frac{1}{r^2}, && (4.15)\\ E &\equiv \frac{2}{\tilde{\omega}^4}\left[a\tilde{\omega}^2(V_\phi^2 - 1) + 2(\Omega_A V_\phi - \omega)^2\right], && (4.16)\end{aligned}$$

$\Omega_A \equiv kV_z$ is the Alfvén frequency, and where we have dropped the zero subscripts on V_ϕ and V_z for convenience. The reader should note that these are *constants* throughout this section.

Equation (4.14) with equation (4.15) is identical in form to the perturbation equation examined in CPS; for rigid BCs, the two problems are formally identical. The eigenvalue E is a known function of a and k (see CPS and ff. equation (4.21)), but here its definition in terms of ω differs. The latter are solutions of the quartic polynomial obtained from equation (4.16):

$$E\omega^4 - 2[E\Omega_A^2 + a(V_\phi^2 - 1) + 2]\omega^2 + 8\Omega_A V_\phi\omega + \Omega_A^2[E\Omega_A^2 + 2a(V_\phi^2 - 1) - 4V_\phi^2] = 0. \tag{4.17}$$

The eigenvalue spectrum for E is infinite and every member is real and positive. For free BCs, the situation is complicated by the fact that ω appears in the BC itself. The problem is then no longer a standard Sturm-Liouville one and the introduction of E is not a particularly useful calculational device. In fact, when $V_\phi \neq 0$, the resulting E is always *complex*. This leads to some interesting consequences which will be discussed presently.[2] For both sets of BCs, the resulting ω occur in complex conjugate pairs (Frieman & Rotenberg 1960).

For simplicity, we begin by considering rigid BCs only. There are two special cases in which the roots of equation (4.17) have simple analytic forms. One is when $V_\phi = 1$, which

---

[2] When $V_\phi = 0$ and for free BCs, as in CPS, it can be shown that the problem is still of Sturm-Liouville type, since ω^2 is real and certain required conditions on the BC coefficients are satisfied; cf., Birkhoff & Rota (1989).

will be examined in the next section. The other is when $a = 2$. In that case, two of the roots are always stable, and the other two are

$$\omega = \frac{V_\phi \pm (V_\phi^2 + E\Omega_A^2 - 2E^{1/2}\Omega_A)^{1/2}}{E^{1/2}}. \qquad (4.18)$$

The critical Alfvén frequency for stability, where the imaginary part of equation (4.18) vanishes, is then

$$\Omega_{A,crit} = \frac{1 \pm (1 - V_\phi^2)^{1/2}}{E^{1/2}}. \qquad (4.19)$$

Two points are worth noting. First, V_ϕ has a *stabilizing* influence here. This could not be predicted from the sufficient criterion (4.2) given in the introduction, since $b = 2 \Rightarrow (rB_\phi)' = 0$. Second, $\Omega_{A,crit}$ is an explicit function of V_ϕ, and has *two* distinct non-zero solutions. That is, *the stability criterion is altered in the presence of an azimuthal field,* contrary to the claims of some recent investigators (see ff. §6.1). In the local limit, i.e. $k \to \infty$, $V_z \to 0$, we have $E \to r_1^{2a} = r_1^4$ (CPS); then equation (4.18) gives

$$\omega = \frac{1}{r_1^2}[V_\phi - (V_\phi^2 - 2\Omega_A r_1^2 + \Omega_A^2 r_1^4)^{1/2}]$$

for the growing unstable mode.

We solved equation (4.14) numerically, subject to both rigid and free boundary conditions, for a variety of (a, b, V_ϕ) allowed by the equilibrium. As in CPS, we use the WKB approximation when $V_z \lesssim 0.3$, since then the eigenfunctions δu_r are so sharply peaked that numerical solutions are difficult to obtain.

The principal results are as follows:

(i) The VC instability persists for all $V_\phi < 1$, $3/2 \leq a \leq 2$, but with reduced growth rate. This conflicts with the naive prediction based on the sufficient criterion (4.2), since here $(rB_\phi)' \geq 0$. The growth rate approaches zero as $V_\phi \to 1$.

(ii) The presence of the azimuthal field also changes the stability criterion itself. Growth is damped at both short and long wavelengths.

(iii) When $V_\phi > 1, a \neq 2$, a new instability sets in, increasing in growth rate as V_ϕ. This large-field instability can be stabilized if V_z is made sufficiently large.

(iv) All of the unstable modes propagate; i.e. the real part of ω is $\omega_R \sim kV_\phi V_z$.

(v) The mode structure is unchanged from CPS; i.e. there exists a finite, ordered spectrum of unstable modes, whose growth rates are inversely proportional to a positive power of E. For the remainder of this paper, we will restrict consideration to the fastest-growing, or $n = 0$, mode.

In Figures 4.3a and b, we plot the dimensionless growth rate as a function of the Alfvén frequency $\Omega_A = kV_z$. These curves show directly the effect of azimuthal field on the VC instability. We have chosen $a = b = 2$, but the curves are similar for other $a = b$. To display the effect for both strong and weak axial fields, Fig. 4.3a has $V_z = 0.3$ and Fig. 4.3b, $V_z = 0.05$. Feature (i) is apparent in both figures; growth is clearly halted as $V_\phi \rightarrow 1$. In the presence of B_ϕ, growth rates are reduced due to vertical motions induced by magnetic pressure gradients (Blaes & Balbus 1994) (in the absence of B_ϕ, $\delta u_z \sim \delta p$; compare equation (3.13) of CPS and equation (A.4), Appendix A). The instability couples to (stable) inertial modes, reducing its efficacy. The additional stabilization provided by V_ϕ at shorter wavelengths (large Ω_A) is also apparent in both figures. The physical explanation for this is the same as in CPS; namely, that the restoring stress on a fluid element is more effective for distortions of larger curvature, i.e. at short wavelengths (also, see below).

A new effect, the long-wavelength stabilization, is much more prominent in the weak axial field case (Fig. 4.3b). Even at $V_\phi \approx 0.7$, one sees stabilization at long wavelengths (small Ω_A) for $V_z = 0.05$. This behavior is entirely due to the presence of toroidal field lines, which provide an additional return force on a fluid element at long wavelengths. This can be seen by an explicit calculation of the perturbed magnetic tension, i.e.

$$\frac{\delta(\mathbf{B}\cdot\nabla)\mathbf{B}}{4\pi} = \frac{1}{4\pi}\left(ikB_z\delta\mathbf{B} - \frac{2B_\phi\delta B_\phi}{r}\hat{\mathbf{r}}\right), \tag{4.20}$$

where we have assumed without loss of generality that $B_\phi \sim 1/r$. As $k \rightarrow 0$ in the $B_\phi = 0$ case, the tension vanishes, indicating that instability persists up to the longest wavelengths. However, the second RHS term is independent of k, so that for nonzero B_ϕ there exists an additional radial tension, which is always stabilizing. In addition, the effect is enhanced at small B_z. It is this behavior that we observe at small Ω_A in Fig. 4.3.

The real parts of all four roots for ω are shown in Figures 4.4a and b, for the same two values of V_z and $V_\phi = 0.9$. The corresponding imaginary parts are shown as dotted lines. The unstable modes (one growing, one damping) are created out of two real modes which merge for intermediate values of Ω_A.

Increasing V_ϕ to values in excess of 1 with $a = b = 2$ leads to no further instability. However, a new instability *does* occur for other values of a. The Keplerian case, for example, is shown in Figure 4.5. Each curve is labeled by its corresponding field values V_ϕ, V_z. As V_z is held fixed at 0.3 and V_ϕ increased, the peak growth rate increases (solid curves). Were it not for the equilibrium constraint $V_\phi \lesssim 1.42$ (see Fig. 4.1a), this growth would continue without bound as V_ϕ is increased. Now keeping V_ϕ fixed and increasing V_z from 0.3 (dashed curves) leads to stabilization, until complete stability is achieved at $V_z \simeq 0.81$, implying $(V_z/V_\phi)_{crit} \simeq 0.57$. We consider this large-field instability further in §4.4.3

4.4.2 Critical stability curves

In CPS, it was shown that E behaves as

$$E = \frac{E_2(a)}{k^2} + \ldots + E_0(a), \tag{4.21}$$

where $E_0(a) \equiv r_1^{2a}$ and $E_2(a) \equiv \lim_{k \to 0} k^2 E$. Since the longest wavelength perturbations are always unstable in that case, one could then calculate the critical field strength for stability, $V_{z,crit}$, by taking the limit of the dispersion relation as $\omega \to 0$, $k \to 0$. When $V_\phi \neq 0$, the values of (V_ϕ, V_z) for which marginal stability holds constitute *curves* in the (V_ϕ, V_z) plane. This section will be concerned with the construction of such curves.

When $V_\phi \neq 0$, there is an added complication. Fig. 4.3 shows that the most persistent unstable mode is not always that with $k \to 0$. Rather, the last unstable mode which persists as $V_\phi \to 1$ has intermediate k; the precise value is a function of V_z. We note here that in the local limit, $k \to \infty$, $V_z \to 0$, the growth rate curves are perfectly symmetrical about $\Omega_A = 4$, which is the value for peak growth when $a = 2$ and $V_\phi = 0$.

When $V_\phi = 1$, equation (4.17) has the four roots

$$\Omega_A \text{ (twice)}, \quad \pm 2E^{-1/2} - \Omega_A, \tag{4.22}$$

all of which are real, provided that E is real. This result is independent of both V_z and k. Thus the line $V_\phi = 1$ must lie in an absolutely stable region in the (V_ϕ, V_z) plane. Further, taking $V_\phi = 1 \pm \epsilon$ with ϵ small and positive, and expanding ω in orders of ϵ, one finds from the first-order correction that as long as $a < 2$, instability occurs. Thus *the line* $V_\phi = 1$ *constitutes an absolutely stable region in the* (V_ϕ, V_z) *plane.* We need not take any special care when considering $V_z \to 0$.

For larger values of V_z, say $V_z \gtrsim 0.3$, the limit $k \to 0$ *does* give a reliable estimate of the critical curve (Fig. 4.3a). Now taking

$$\omega = k\omega_1 + k^2\omega_2 + k^3\omega_3 + \dots$$

along with equation (4.21), equation (4.17) becomes, to first order,

$$E_2\omega_1^4 - 2[E_2V_z^2 + a(V_\phi^2 - 1) + 2]\omega_1^2 + 8V_zV_\phi\omega_1 + V_z^2[EV_z^2 + 2a(V_\phi^2 - 1) - 4V_\phi^2] = 0. \quad (4.23)$$

Solving equation (4.23) for the loci of $\omega_1 = 0$ in the (V_ϕ, V_z) plane gives the critical stability curves we seek. These have been plotted in Figure 4.6. The $V_\phi = 0$ results, which were derived in CPS, are obtained where curves intersect the V_z axis. One sees that as V_ϕ is increased from zero, smaller values of V_z are needed for stabilization, until at $V_\phi = 1$ complete stabilization occurs for all a. For $a = 2$, all $V_\phi \geq 1$ are completely stable; this is represented by the heavy line along the $a = 2$ curve and continuing along the V_ϕ axis from $V_\phi = 1$ to infinity. For $a < 2$, the plane above $V_\phi = 1$ is divided into an unstable part (adjoining the V_ϕ axis) and a stable part (to the right of a given critical curve). The unstable region at $V_\phi > 1$ extends to infinity and shrinks to zero size as $a \to 2$. Actually, the size of the unstable region for $a \neq 2$ depends on the particular value of a (and when $a \neq b$, on b as well). This is due to the equilibrium constraints placed on V_ϕ by Fig. 4.2b. The largest allowed V_ϕ for each a has been indicated in Fig. 4.6 by a large dot on the appropriate critical curve. We extend the curves to higher values of V_ϕ merely to display their asymptotic behavior (see below); such large field values will not be attainable in reality.

4.4.3 The large-field instability

The almost linear behavior of the curves in Fig. 4.6 at large V_ϕ, V_z is intriguing. In this limit, and again taking $k \to 0$, equation (4.17) gives

$$\omega_1^2 = \frac{\Omega_A^2[E_2\Omega_A^2 + 2(a-2)\Omega_\phi^2]}{2k^2(E_2\Omega_A^2 + a\Omega_\phi^2)},$$

where $\Omega_\phi \equiv kV_\phi$. This implies

$$V_z/V_\phi > (V_z/V_\phi)_{crit} \equiv \sqrt{2(2-a)/E_2} \tag{4.24}$$

for stability. Values of E_2 and $(V_z/V_\phi)_{crit}$ for $3/2 \leq a \leq 2$ may be found in Table 1. The equality in (4.24) gives the asymptotic (i.e. large V_ϕ, V_z) behavior of the critical stability curves, as shown by the dotted lines in Fig. 4.6.

The nature of this large-field instability (LFI) is easily understood upon comparison with the equivalent nonrotating system. The equilibrium pressure distributions are compared in Appendix B, where it is shown that *when* $V_\phi \gg r_0\Omega_0$, *the system reduces to its nonrotating equivalent.* For the latter, Chandrasekhar (1961) derived the necessary and sufficient stability criterion

$$I_1 B_z^2 > \int_{r_1}^{r_2} \frac{\xi_r^2}{r^2}\frac{d}{dr}(rB_\phi)^2 dr, \tag{4.25}$$

where I_1 is a positive-definite integral function of r.[3] Differentiating both sides of this inequality, and assuming that $k \gg \partial/\partial r$ (this is equivalent to considering the longest-wavelength radial perturbations, which should be the most unstable), we obtain its local version;

$$k^2 B_z^2 > \frac{1}{r^3}\frac{d}{dr}(rB_\phi)^2 = \frac{2B_\phi}{r}J_z, \tag{4.26}$$

where J_z is the axial current. The LHS of (4.26) represents the restoring force exerted on a radially displaced fluid element by the perturbed vertical field, while the RHS is the excess Lorentz force on that element due to perturbations of B_ϕ. *The latter is the exact analogue of the destabilizing centrifugal force in the BH instability.* Since $J_z = (2-b)B_\phi/r$, configurations with $V_\phi \gg r_0\Omega_0$ and $b \geq 2$ are stable to the LFI. In essence, the LFI is the result of an imbalance between radial gravity and a radially stratified, buoyant magnetic field (see also Appendix B).

---

[3] Compare criterion (4.25) with that for the VC instability; i.e.

$$I_1 V_z^2 > -\int_{r_1}^{r_2} (r\xi_r)^2 \frac{d\Omega^2}{dr} dr.$$

4.4.4 Free boundaries

The only case to be considered here is $a = b = 2$, since we restrict consideration to the current-free situation. The critical stability curve is shown in Figure 4.7. The most significant difference is *the disappearance of the absolutely stable line at* $V_\phi = 1$. A glance back at the roots (4.22) of the polynomial (4.17) shows how this happens. When $V_\phi \neq 0$, E is no longer real, and one of these roots becomes growing unstable. The actual behavior is as follows. Consider a line of constant V_z, such that $0 < V_z < 1$. The peak growth rate for a given V_ϕ decreases from a maximum at $V_\phi = 0$, to some minimum in the vicinity of $V_\phi \approx 1$, and then increases again without bound as V_ϕ is made larger. Note also how much more extended is the unstable region in the free case versus the rigid one.

Global effects must clearly be at work here, since $V_\phi > 1$ is unstable only in the free-boundary case. As rotation is not likely to be important in this region, it is instructive to consider the equivalent nonrotating problem. A situation similar, although not identical, to the latter is that of the plasma "pinch" (e.g., Chandrasekhar 1961, Ch. XII, §115). This consists of a filled cylindrical column of plasma, threaded by a uniform B_z, and surrounded by a vacuum region containing the same B_z together with an azimuthal field $B_\phi \propto r^{-1}$. The entire arrangement is usually encircled by a concentric conducting wall, but we are free to place this at infinity and so ignore it for our present purpose. For the extended configurations we consider ($r_2/r_1 = 100$), the (nonrotating) situation is nearly identical except for the fact that in our problem B_z and B_ϕ interpenetrate *everywhere*, not just in the vacuum region. However, such interpenetrating fields have been considered by Tayler (1957), with the finding that such arrangements are more unstable.

When all fields are continuous across the plasma/vacuum boundary, the fluid is susceptible to the well-known ($m = 0$) sausage instability, which can be stabilized if and only if $V_z^2 > V_\phi^2/2 \Rightarrow (V_z/V_\phi)_{crit} \gtrsim 0.707$. It is of interest to compare this figure with the inverse of the slope of the critical curve for $a = b = 2$ in Fig. 4.7, which is $(V_z/V_\phi)_{crit} \approx 1.5$. The latter situation is more unstable, we posit, due to the interpenetration of B_ϕ and B_z in the fluid region. Since the exterior B_ϕ is the cause of the sausage instability in the first place, it is not hard to imagine that its presence *inside* the fluid will inhibit the stabilizing effect of B_z.

4.4.5 The general case: $a \neq b$

Rigid Boundaries

When $a \neq b$, the reduction of the full eigenvalue problem, equations (4.9) and (4.10), to a single characteristic polynomial is no longer possible. Before proceeding to a numerical solution, however, it is of use to present such analytic formulae as are available. There are two approaches which have had some success in this regard, and which lead to identical results. One is the local analysis of Dubrulle & Knobloch (1993), which ignores radial variations in equilibrium quantities compared with those of perturbed ones (i.e. $r(\delta X)'/\delta X \gg 1$). The other is the slender annulus approximation adopted by Kumar, Coleman, & Kley (1994) which we follow here to preserve the global character of the analysis (Appendix C).[4] In the limit $V_z \to 0$, both give the following condition for stability,

$$[2 - a - (2 - b)V_\phi^2](a - bV_\phi^2) < 0. \tag{4.27}$$

For example, if $0 < b < 2$ and $b < a$, stability holds if

$$\frac{2-a}{2-b} < V_\phi^2 < \frac{a}{b}, \tag{4.28}$$

whereas for b in the same range and $a < b$, stability holds if

$$\frac{a}{b} < V_\phi^2 < \frac{2-a}{2-b}. \tag{4.29}$$

It is easy to see that both of these inequalities bracket $V_\phi = 1$.

As regards the (V_ϕ, V_z) critical stability plane, equations (4.28) and (4.29) imply the existence of a stable region along the V_ϕ axis bracketing $V_\phi = 1$. How this limiting behavior is related to the critical curves for general V_ϕ, V_z, and r_2/r_1 will now be investigated.

For configurations with rigid boundaries, all (a, b, V_ϕ) consistent with Fig. 4.1b may be considered. Qualitatively, there are some significant differences from the $a = b$ case. These

---

[4] This approach is actually superficially global, in that although radial BCs are applied, the authors assume that the boundary separation is proportional to $\sqrt{k}$, $k \gg 1$.

differences may be classified according as $a > b$ or $a < b$. Several representative critical stability curves are shown in Figure 4.8. Beginning at the far right-hand side of the diagram, we have a stable region at large V_z. When $a > b$, the curves achieve a minimum value of V_z for some $V_\phi \gtrsim 1$, and then display the linear asymptotic behavior found in the previous section. *For $a > b$, there exists no stable region (not even $V_\phi = 1$) at small V_z.* This result contradicts the local prediction (4.28) of a stable region as $V_z \rightarrow 0$. As a is reduced to values nearer to b, e.g. $a = 1.7$, $b = 1.6$, the "knee" of the curve bends inward to smaller values of V_z; it is easy to imagine what happens in the limit as $a \rightarrow b$ from above; the knee of the $a > b$ curve deforms into the *line* $V_\phi = 1$, which extends all the way to $V_z = 0$ as in Fig. 4.6.

If a is decreased further such that $a < b$, the situation is less clear. We have been able to confirm numerically the persistence of two distinct unstable regions, one at $V_\phi \gtrsim 1$ (LF unstable) and one at $V_\phi \lesssim 1$ (VC unstable), down to values of $V_z \simeq 0.2$. *Between the two stability curves lies an absolutely stable region*, bracketing $V_\phi = 1$. At smaller V_z, mode crossing becomes a significant hindrance to the numerical algorithm, and precise determination of the critical curves is difficult. For $a = 1.7$, $b = 1.75$, we were able to follow the $n = 0$ mode down to $V_z \simeq 0.2$ (solid curves in Fig. 4.8); beyond this, we join the numerical curves onto the values given by the local relation (4.29) at $V_z = 0$ (dashed curves).

It should be mentioned that this region of parameter space, i.e.,

$$V_z \rightarrow 0,\ V_\phi \approx 1,\ a < b,$$

is highly restricted by the equilibrium constraints. A glance at Fig. 4.1a reveals that we must have $a \geq 3/2$. Since the LFI requires $b < 2$, we therefore have $3/2 < a < 2$, $a < b$ as our region of interest. Widely separated values of a and b in this range have limiting Alfvén speeds well below unity; e.g. when $a = 1.55$, $b = 1.95$, $V_6 = 0.46$. Hence, the LFI is not a concern. Less separated values of the two parameters allow larger equilibrium fields; e.g., $a = 1.85$, $b = 1.95 \Rightarrow V_6 = 2.93$. But it is likely that for such a, b the critical stability curves are qualitatively similar to the $a = 1.7$, $b = 1.75$ case shown in Fig. 4.8. To confirm this, we developed an approximation whose validity depends on the smallness of the parameter

a/b, but imposes no restrictions whatsoever on the global geometry.[5] The critical stability curves found by this method *always contain a stable region bracketing* $V_\phi = 1$.

To explain the existence of a stable region at small V_z, it is instructive to look at the dependence of the perturbations on a and b. The VC instability arises from an imbalance of the destabilizing stress $B_z\delta B_\phi/4\pi$ and the stabilizing stress $B_z\delta B_r/4\pi$. When an azimuthal field is present, the ratio of these as found from equations (A.7) and (A.8) is

$$\frac{\delta B_\phi}{\delta B_r} = \frac{i\omega}{kB_z\tilde{\omega}^2}\left[2kB_z\Omega - \frac{B_\phi}{r\omega}(b\tilde{\omega}^2 + 2\Omega_A^2)\right]. \tag{4.30}$$

The first term in the square brackets behaves as r^{-a}, the second term as r^{-b}. Consider unstable modes only, so that $\omega \sim \Omega_A$ (this is still true when $V_\phi \lesssim 1$). The relative magnitude of the two terms then depends on: (a) the relative magnitude of a and b, (b) the relative magnitude of Ω and B_ϕ/r, and (c) whether $r < 1$ or $r > 1$ (i.e. inside or outside the pressure maximum, respectively). Assume that $\Omega \gtrsim B_\phi/r$; i.e. that we are in the VC regime. Recall from CPS how strongly peaked were the radial eigenfunctions of the unstable modes interior to the pressure maximum; this suggests that the region $r < 1$ is far more important than $r > 1$ for the linear stage of instability. We therefore restrict consideration to that region. Now, when $a > b$, the first term in the above dominates the second, and $\delta B_\phi/\delta B_r$ retains the *same* sign as it had in the absence of B_ϕ, where its effects were always destabilizing. Thus while one would expect a reduction in the growth rate near $V_\phi \simeq 1$, it should not completely vanish.

On the other hand, when $a < b$, the second term in equation (4.30) can be comparable to the first even when $B_\phi/r \lesssim \Omega$, and so a change of sign in $\delta B_\phi/\delta B_r$ occurs at some $V_\phi \lesssim 1$, signifying stabilization. Such stabilization cannot be maintained at higher values of V_ϕ, however, once the LFI begins to set in. This gives the upper boundary of the stable region. Physically, B_ϕ overwhelms Ω in the inner disk when $b > a$, leading to momentary stabilization until the field becomes so strong that rotation is no longer a viable means of support. At this point, the LFI takes over. Because the local analysis gives no information about the radial dependence of the eigenfunctions, Dubrulle & Knobloch were not able to

---

[5] Specifically, we define a new variable, $x \equiv 1 - r^{a/b-1}$, $a < b$, and expand the perturbation equation (4.11) in powers of x. Finding a series solution and subjecting it to rigid BCs, one obtains a fourth-order dispersion relation similar to equation (4.23), which can be solved numerically for ω.

detect this interesting dependence of the stability properties on the relative magnitudes of a and b.

Inapplicability of the Local Approximation

There are two particular cases in which the local criterion predicts qualitatively different behavior than that examined above. When either $a = 2$ or $b = 2$, criterion (4.27) yields the following results:

(i) $a = 2,\ b > 2;\ V_\phi > \sqrt{2/b}$,
(ii) $a = 2,\ b < 2;\ V_\phi < \sqrt{2/b}$,
(iii) $b = 2,\ a < 2;\ V_\phi > \sqrt{a/2}$,
(iv) $b = 2,\ a > 2;\ V_\phi < \sqrt{a/2}$.

In all these cases, there exists only a single critical curve. Since (ii) and (iv) have $a > b$, we expect the local prediction to be unreliable by extension of the results of the previous section; thus we do not expect a critical stability curve to extend all the way to $V_z = 0$. In cases (i) and (iii), however, there is no a priori reason to doubt the local results.

As test cases, consider the physically interesting power law indices

(i) $a = 2,\ b = 3; \Rightarrow V_\phi > 0.82$,
(iii) $b = 2,\ a = 1.5; \Rightarrow V_\phi > 0.87$.

The first case is that of constant angular momentum, with a rapidly decreasing azimuthal field. The second is a zero-current, Keplerian configuration. By the results of §4.4.3, both systems should be stable to the LFI. In addition, both the Michael (equation (4.1)) and the Howard & Gupta (equation (4.2)) criteria are satisfied. The equilibrium constraints place no restrictions on the value of V_ϕ for these (a, b). The critical stability curves, calculated numerically, are shown in Figure 4.9. Again, it is difficult to extend the curves much past $V_z \lesssim 0.2$, but in case (i) we have been able (quite remarkably) to follow the curve down to $V_z = 0.05$. As in the rest of the paper, the results are for $n = 0$, which we have always found to be the fastest growing radial mode.

The results are surprising in that they bear no resemblance to the local predictions (the dashed and dotted lines in Fig. 4.9) as $V_z \rightarrow 0$. The $a = 2$, $b = 3$ curve, e.g., shows that the VC unstable region is five times as large at $V_z = 0.1$ than the local prediction, and the curve even appears to be diverging as $V_z \rightarrow 0$, instead of approaching a constant value. One reason why the local approximation fails here can be found via inspection of the relevant eigenfunctions, a few of which are plotted in Figure 4.10. When $V_\phi \neq 0$, δu_r has both real (solid line) and complex (dashed line) components. As V_ϕ is increased from zero, one sees a gradual spreading of the eigenfunction from the inside regions outward. In the region near the critical curves as $V_z \rightarrow 0$, δu_r is *much* more extended than in any other case examined thus far. The peak of the eigenfunction at maximum growth is no longer confined to the small region between r_1 and r_0; e.g. when $V_z = 0.3$, $V_\phi = 1.5$ (Fig. 4.10d), it lies at $r/r_0 \approx 3$, and δu_r has a nonnegligible amplitude over the entire shell. This feature alone is enough to show that the local and thin shell analyses are inadequate to capture the true behavior of the system in this parameter regime. It also confirms one of the main findings of CPS; namely, that the local and 'critical' limits are antipodal: the latter can only be reached via a global analysis.

Free Boundaries

For $b = 2$, we plot a variety of a values in Fig. 4.7. Again, in contrast to the rigid BC case, *there exists no stable region around* $V_\phi = 1$; this is easily understood in light of the discussion given in §4.4.4 The unstable regions are larger for $a \neq 2$ than for $a = 2$; this is due to the fact that *two* instabilities, the current-driven LFI, and the sausage instability, act simultaneously. The asymptotic critical values for these curves range from $(V_z/V_\phi)_{crit} = 1.5$ for $a = 2$ to $(V_z/V_\phi)_{crit} = 2.3$ for $a = 1.5$. The V_z-axis intercepts of the curves match the values found in CPS.

4.4.6 The effect of simulated vertical boundaries

In CPS, we calculated the critical V_z for several *fixed*, nonzero values of k, corresponding to vertical wavelengths, λ_{crit}, between 100 and 0.1 in units of the inner radius r_1. The intent was to gauge the probable effect of vertical disk boundaries on $V_{z,crit}$, under the hypothesis that the longest unstable wavelength could not exceed the disk thickness. The interesting result was that for $\lambda_{crit} = 0.1$, a reasonable value for a thin Keplerian disk, $V_{z,crit} \simeq 0.04 \approx V_{z,K}$, where $V_{z,K} \equiv \sqrt{6}\, c_s/\pi$ is the local Keplerian critical field estimate (BH). Thus, the super-rotational Alfvén speed required for stability in the infinite incompressible cylindrical shell model translates to a *super-thermal* V_z in a thin, isothermal disk.

In the presence of an azimuthal field, we have found that for small V_z, values of $V_\phi \sim r_0\Omega_0$ are required for critical stability. This therefore begs the same question as asked in CPS: does the same result hold for thin disks, or does critical stability again require $V_\phi \sim c_s$?

Following the same calculational procedure as in CPS, we calculated critical stability curves for $a = b = 2$, rigid boundaries, and a range of λ_{crit} (Figure 4.11). Mode confusion prevents us from going to $\lambda_{crit} < 0.2$, but the trend is clear. The curves do not all approach $V_\phi = 1$ as $V_z \to 0$, since they are for *fixed* k; the small Ω_A stabilization discussed in §4.4.1 takes over when V_z becomes small. This can be seen explicitly by deriving the following "local" critical stability relation. In the local limit, $E \to r_1^4$, so $E^{1/2} \approx (0.5)^2 = 0.25$ for $a = 2$, and equation (4.19) gives (in proper units)

$$k_{crit} = \frac{2\pi}{\lambda_{crit}} = \frac{4\Omega_0}{V_z}\left\{1 \pm \left[1 - \left(\frac{V_\phi}{r_0\Omega_0}\right)^2\right]^{1/2}\right\}.$$

Assuming the azimuthal field is subthermal so that it does not significantly alter the overall structure of the disk, the critical stability requirement $\lambda_{crit} \approx 2H = 2\sqrt{2}c_s/\Omega(r_1)$ then yields

$$\left(\frac{V_\phi}{r_0\Omega_0}\right)^2 \approx 1 - \frac{\pi^2}{2}\left(\frac{V_z}{c_s} - \frac{\sqrt{2}}{\pi}\right)^2 = 1 - \left(\frac{V_z}{r_0\Omega_0}\frac{2\pi\, r_1}{\lambda_{crit}} - 1\right)^2. \tag{4.31}$$

For $\lambda_{crit} = 0.1\ r_1$, equation (4.31) gives the long-dashed curve shown in Figure 4.11. Although equation (4.31) concurs with the sequence of curves shown and highlights their key qualitative features, it cannot be rigorously correct for two reasons: first, one cannot actually have a "thin" disk with $a = 2$; and second, the derivation is inconsistent for $V_\phi/r_0\Omega_0 \sim 1 \gg V_\phi/c_s$.

Regardless of the applicability of equation (4.31), the numerical curves in Figure 4.11 unambiguously show that although $V_{z,crit}$ decreases with decreasing λ_{crit} (or decreasing scale height H), *the same is not true of* $V_{\phi,crit}$. Even in the thin disk limit, one still requires $V_{\phi,crit} \sim r_0\Omega_0$ for complete stabilization; i.e. for all wavelengths and at any V_z. This result can be understood by recalling the physical cause of the LFI: it can *only* occur when rotation is relatively unimportant in comparison with the azimuthal field, a requirement that does not change when the effective scale height is reduced.

In a real, compressible, vertically stratified accretion disk, Parker (vertical magnetic buoyancy) instability is known to act when $V_\phi \gtrsim c_s \ll r_0\Omega_0$. Thus, the above result could have at least two important consequences for such a disk. First, it argues persuasively against the possibility of the LFI ever occurring, since for $V_\phi \gtrsim c_s$, Parker instability would already have caused a rearrangement of the magnetic equilibrium. Second, and more importantly, the above result suggests that *the VC instability is unlikely to be stabilized by an azimuthal field of* any *power-law index or strength* $V_\phi \lesssim c_s$. We will discuss other possible environments for the LFI in §6.2.

4.5 Nonconstant Vertical Field

Should an accretion disk be threaded by a vertical magnetic field, the latter is more likely to vary with radius than be uniform. Although we do not explicitly model the accretion flow in this study, its overall effect is to drag field lines radially inward (by flux-freezing), leading to a higher B_z flux in the inner regions. In this section we consider the effect of a radially varying vertical magnetic field on the VC instability, and neglect the azimuthal field. Although for completeness it would be desirable to consider the most general situation of nonconstant vertical *and* azimuthal fields, we defer that to a future work. An additional complication arises in that case, since resonances can occur where the real part of $\omega^2 - k^2V_z^2(r) = 0$. This is not a concern for the unstable modes considered in this section, since they always have $\omega^2 < 0$; a proof of this is given in Appendix D. We consider only rigid BCs, since the zero-current restriction on our freely-bounded equilibria requires $c = 1$.

Even with the restriction to rigid BCs and the knowledge that ω^2 is real, analytic progress is difficult, since the r-dependence of $\tilde{\omega}^2$ means that the perturbation equation (4.9) is not of standard Sturm-Lioville type. Regrettably, the global WKB approach used in CPS does not give satisfactory results in this case, for the following reason. Choosing $1/k$ as a small parameter, the last RHS term of equation (4.12) cannot be neglected, due to the presence of ω-dependent terms. However, use of the thin shell approximation of Appendix C gives the result

$$\begin{aligned}\omega^2 &= \frac{\Omega_{A0}^2[2(k^2+c)+\eta/2]+2(2-a)k^2}{2(k^2+3/4)} \\ &\pm \{\Omega_{A0}^4[k^2(\eta+1)+\eta(\eta/4+2c-3/4)+3(1-2c)+4c^2] \\ &+ 2k^2\Omega_{A0}^2[8k^2+3a+(2-a)(4c+\eta)]+4k^4(2-a)^2\}^{1/2}/2(k^2+3/4),\end{aligned}$$

where $\eta \equiv 3-8c+4c^2$ and $\Omega_{A0} = kV_z(r_0)$. This solution can be regarded as quantitatively valid only in a small neighbourhood of the pressure maximum. However, it exhibits roughly the same qualitative behavior as the exact numerical solutions discussed below. In addition, taking $k \gg 1$ leads to the local dispersion relation of CPS and BH.

Exact numerical growth rates as a function of Ω_{A0} for various values of $c > 1$ and the fiducial values $a = 2$, $V_{z0} = 0.3$, $r_2/r_1 = 100$ are plotted in Figure 4.12. The different curves are labelled by their corresponding c values. *For $c > 1$, the growth rate is always reduced from its constant V_z value.* The critical Alfvén frequency for stability, $\Omega_{A0,crit}$, decreases with increasing c, until at some critical value, $c \approx 2.5-3$, it begins to increase again. The peak growth rate, however, continues to decrease. We have difficulty finding $|\omega|$ for $c \gtrsim 3.5$ and large Ω_{A0}, possibly due to the simultaneous presence of several unstable modes with the same growth rate.

The particular laws $c = 9/4$ and $c = 5/2$ correspond to the flux distributions for two popular centrifugally-driven wind models; Blandford & Payne (1982) and Pelletier & Pudritz (1992), respectively. As far as the *stability* of these distributions is concerned, there is no great distinction between either; both are VC unstable. One should note, however, that both models require $B_\phi \neq 0$; in the former $B_\phi \sim B_z$, while in the latter, $B_\phi \sim r^{-1}$. Thus while the results of the present paper suggest that $V_\phi \lesssim r_0\Omega_0$ will further stabilize, a calculation explicitly incorporating B_ϕ is still necessary.

The run of peak growth rate with c is shown in Figure 4.13, for $V_z = 0.3$, $r_2/r_1 = 100$, and different values of a. The $a = 1.5$ curve is incomplete because $1 < c < 3/2$ is forbidden by the equilibrium (Fig. 4.2b). The large dot on the vertical axis shows the constant V_z value (see Fig. 4.7a of CPS).

The physical reason for the stabilization observed here is the same as for an azimuthal field in the presence of a constant V_z, except that now the additional vertical motions are induced by the gradient of the vertical field (see equation (A.4)). As for the effect on the stability criterion, we advance the following argument. In the inner region of the disk, $V_z(r < r_0) > V_z(r_0)$. Thus, the *local* instability at $r < r_0$ will be attenuated compared to the constant $V_z = V_z(r_0)$ situation. By the same argument, the local growth rate should be enhanced outside the pressure maximum. However, the unstable eigenmodes are strongly peaked inside $r = r_0$, when $c \approx 1$; this region is more important for the action of the VC instability. Thus for $c \gtrsim 1$, the attenuation effect dominates, and the critical wavenumber for stability, $k_{crit} = \Omega_{A0,crit}/V_{z0}$, is reduced from its value in CPS. For c significantly greater than 1, an interesting phenomenon occurs (Figure 4.14). The peak of the eigenfunction δu_r gradually moves from inside the pressure maximum (for $c \approx 1$) to $r/r_0 \approx 1$ (for $c = 7/2$), and presumably beyond for more extreme field gradients. Thus it is likely that for larger c, the above argument no longer holds. That is, the enhancement effect of the VC instability at $r > r_0$ *does* contribute, leading to a reversal in the trend of $\Omega_{A0,crit}$.

We have searched for other unstable modes, e.g. at $V_z \gg 1$, with no success. Interchange modes, which might be expected to act at large field strengths, do not occur here because we consider only axisymmetric perturbations (see, e.g., Kaisig, Tajima, & Lovelace 1992, Lubow & Spruit 1995).

4.6 Discussion

4.6.1 Comparison with previous results

Here we compare our results for the effect of the azimuthal field on the VC instability with those of four recent papers, finding some significant discrepancies.

Dubrulle & Knobloch (1993) (DK), via a WKB method, found that the imaginary part of the eigenfrequency, $\omega_I \sim \Omega_A/(1+\text{const.}\times V_\phi^2)$ in the limit $V_z \to 0$. The same result holds for both rigid and "free" BCs, $\delta u_r'(r_1) = \delta u_r'(r_2) = 0$ (these conditions differ from ours in the respect that the configuration is bounded by a *complete* vacuum; i.e. one devoid of external fields.) Thus it would appear that one needs an infinite V_ϕ to stabilize the system. Our results are clearly at odds with DK in this respect. Although the finite-sized stable region found by DK was also found here, we have shown that such a region exists *only* in the presence of rigid boundaries, and then only for $a < b$.

Kumar, Coleman, & Kley (1994) (KCK) concluded, on the basis of the sufficient stability criterion (4.2), that "toroidal fields only destabilize the flow". As regards the VC instability, we have found that the opposite is in fact the case, at least when we consider the "principal range" $3/2 \le a \le 2$, $b \ge 1$. It is only in the large-field ($V_\phi \gtrsim r_0\Omega_0$) regime that B_ϕ destabilizes. Had the authors continued their thin-shell calculation to $\mathrm{O}(V_\phi^2)$, they would have discovered that the correction to ω at peak growth is

$$\omega_{2,max} = \frac{i}{2}(b - a^2/2 + a^3/8),$$

which is always damping provided that $3/2 \le a \le 2$ and $b \ge 1$.

As regards the enhancement of the instability for free boundaries, we note that the global energy change due to the perturbations, $\delta\mathcal{E}$, consists of three different contributions, in general. The first is the energy change in the fluid *interior*, derived by KCK as

$$\delta\mathcal{E}_F = \pi\int\left(\frac{|\delta\mathbf{B}|^2}{4\pi} - \mathbf{J}\cdot\delta\mathbf{B}\times\xi^* + 2\rho r\Omega\Omega'|\xi_r|^2\right) r\,dr, \tag{4.32}$$

where $\xi = \delta\mathbf{u}/i\omega + r\Omega'\delta u_r\hat{\phi}$ is the Lagrangian displacement vector. The second contribution is due to perturbations of the external vacuum field,

$$\delta\mathcal{E}_V = \frac{1}{4}\int_{vacuum}|\delta\mathbf{B}|^2 r\,dr, \tag{4.33}$$

while the third is a surface contribution, $\delta\mathcal{E}_S$, which vanishes unless the equilibrium has surface currents (cf., Schmidt 1966). We avoid the latter here, and so the effect of free boundaries is given entirely by the integral (4.33), which is always positive. This led KCK to conclude that "stability criteria are not affected" by the BCs. However, one should be careful upon drawing such a conclusion from *sufficient*, but not *necessary*, criteria. In fact, as noted by Bateman (1978), there are numerous instances when free boundary instabilities grow faster than fixed boundary ones, even though $\delta\mathcal{E}_V > 0$. The reason for this is simply that by allowing $\xi \neq 0$ at the edge of the fluid, free-boundary instabilities can make more effective use of the *internal* fluid potential energy, represented by the first two terms on the RHS of equation (4.32). We found ample evidence of such behavior in the preceding sections, and in CPS.

Blaes & Balbus (1994) (BB) considered two-fluid models of ions and neutrals coupled by collisions, ionization, and recombinations. Their analysis is local, but includes an equilibrium azimuthal field. They found that B_ϕ can alter the stability criterion only in the limit of ionization equilibrium (as opposed to ion conservation), and can in fact produce total stabilization for $B_\phi \gtrsim 10B_z$ if the ion-neutral collision frequency is below a certain threshold. In all other cases, B_ϕ can cause a small reduction in growth rate, but does not affect the stability criterion (i.e. the critical Alfvén frequency for stability is unchanged from the $B_\phi = 0$ case)[6]. They take $c_s = 10V_z$, so that the critical V_ϕ for stability is $V_\phi \sim c_s$. This differs from our result, $V_{\phi,crit} \sim r_0\Omega_0$, since BB's compressible model is sensitive to the coupling between magnetosonic and rotation-modified Alfvén modes, which is stabilizing. BB's model does not include vertical gravity, however, so buoyancy instabilities which would be expected to become important near $V_\phi \sim c_s$ were not detected.

Gammie & Balbus (1994) (GB) considered an accretion disk model which was local in the radial coordinate, but global in z; i.e. they solved for the vertical eigenmodes. One should be cautious in comparing our results directly to theirs, but their vertical node number n should compare roughly with our k, and their radial wavenumber k with our radial node number n. The near-coincidence of notation here is unfortunate; let us unambiguously re-label these parameters as n_z, k_z, k_r, and n_r, respectively. For a Keplerian disk, they plotted curves of constant growth rate in the (V_ϕ, V_z) plane for $k_r = 0$ and $n_z = 1$ (their Fig. 2), finding that stabilization is achieved for $V_z \simeq 1.5$ irrespective of V_ϕ; this value agrees

---

[6] A point of formalism is worth stressing here. The finding that B_ϕ does not affect the stability criterion, regardless of its strength, is not surprising in a purely local model such as that of BB. This is because terms behaving as B_ϕ/r, which are crucial in the global model, are ignored in local calculations. The disappearance of B_ϕ from the stability criterion in the latter case can be seen immediately from equations (4.20) and (4.30).

quite well with the free-boundary results of CPS (we found $V_{z,crit} \simeq 1.43$ for $a = 1.5$). Their BCs are similar to ours in the sense that far from the disk, the field lines move about freely, exerting no stress on the disk.

On the other hand, although GB find that the growth rate decreases for increasing V_ϕ (they consider values up to $V_\phi/c_s = 5$), it apparently never vanishes, nor does V_ϕ affect the stability criterion. The discrepancy between these results and those of the present paper could be telling us something about the relative importance of vertical motions (which they treat in detail, and we do not) and radial ones (vice-versa). To date, nonlinear calculations of the BH instability have indicated that inward and outward radial motions at different z (the so-called "channel solutions") are the immediate outcome of the linear stage of the instability. It may be that the unstable modes are more sensitive to variations in radial structure than in vertical. GB's local approximation in r could therefore have missed the most important effect associated with strong B_ϕ; namely, the prevention of the channel solution from ever forming.

Due to the apparent similarity between GB's Fig. 2 and our Fig. 4.6, one might be tempted to make a direct comparison between the two. We caution the reader against it, for the following reason. The results in the former figure are for the longest vertical wavelength ($n_z = 1$ or $k_z = 0$) mode only. For this mode, the $V_z \rightarrow 0$ limit is automatically stable, since $\omega_I \sim \Omega_A \rightarrow 0$. By contrast, our critical stability curves are *mode-independent*; i.e. they reflect the requirements for stability to perturbations of *arbitrary* k. This explains the rather puzzling feature of GB's Fig. 2 in the $V_\phi \rightarrow 0$ limit, namely, that the absolute maximum growth rate is attained not at $V_z = 0$ as in CPS, but at $V_z \simeq 0.85$. As an example, consider the $a = b = 2$ case, whose growth rate is given by the imaginary part of equation (4.18). In the $k \rightarrow 0$ limit, $E \rightarrow E_2(2)/k^2$, giving

$$\omega_I = -k(V_\phi^2 + E_2 V_z^2 - 2E_2^{1/2} V_z)^{1/2}/E_2.$$

Considered as a function of V_z, the maximum of ω_I occurs at $V_z = 0.52$, independent of V_ϕ. The point this argument overlooks is that as V_z becomes small, k necessarily becomes large for the most unstable mode; e.g., when $V_z = 0.05$ and $V_\phi \gtrsim 0.7$, there are *no unstable modes* whatsoever at $k = 0$ (Fig. 4.3b). GB's Fig. 4 in fact shows that $n_z = 1$ is *not* the fastest growing mode for nonzero V_ϕ. One should therefore not treat GB's Fig. 2 as our Fig. 4.6; i.e. as a critical stability diagram.

Finally, we note that in the context of uniformly rotating magnetic stars, which are expected to have distributions of B_ϕ *increasing* with radius, Pitts & Taylor (1985) identified an instability having the same characteristics as the LFI (i.e. stability was ensured for low m (azimuthal wavenumber) modes provided that $r_0\Omega_0 \gtrsim V_{\phi 0}$), but did not obtain detailed growth rates or critical stability curves.

4.6.2 The large-field instability: possible environments

The results of §4.4.6 suggest that the LFI is not likely to be a threat in standard thin accretion disks. In some environments, however, the characteristic value for the LFI, $V_\phi/r_0\Omega_0 \gtrsim 1$, might in fact be achieved. Recent observations of flattened structures in massive star-forming regions (e.g., Aitken et al. 1993) suggest that such 'pseudo-discs' are very massive ($\sim 10^3 M_\odot$) and also that the dominant magnetic field component is toroidal. Such massive objects are likely to be self-gravitating and sub-Keplerian, so that rotation may not be as important a mechanism of support as in thin disks. It remains to be seen how the LFI is affected by self-gravity.

On larger scales, roughly 50 % of giant molecular clouds and somewhat fewer individual dark clouds and cores (Goldsmith & Arquilla 1985) possess measured velocity gradients which have been interpreted as being due, at least in part, to large-scale rotation (Blitz 1993). As the magnetic fields in such objects are substantial (magnetic energy ~ gravitational energy ~ kinetic (nonthermal) energy; cf., Myers & Goodman 1988), the condition $V_\phi/r_0\Omega_0 \gtrsim 1$ is likely to be satisfied in at least some regions. Of course, the effects of compressibility and self-gravity are also likely to be important, so a new model is needed.

A concrete example displaying appropriate conditions for the LFI may already exist. The L1641 region of Orion A consists of several low-density filaments, whose major axes run in a roughly north-south direction. In addition to a north-south velocity gradient which extends across all of Orion A (~ 8 km s^{-1}), L1641 also contains an east-west gradient, ~ 2 km s^{-1}, indicating that the overall velocity field of Orion A is *helical* in nature (Bally 1989).

Further, the surrounding magnetic field displays the same symmetry (Heiles 1987). It is well-known that such a helical field is characteristic of superposed vertical and azimuthal fields. While figures for L1641 alone are hard to come by, the average east-west gradient in the Orion A cloud as a whole (40 pc × 2 pc) has been estimated at 0.135 km s^{-1} pc^{-1} (Kutner et al. 1977, Genzel & Stutzki 1989). If this is entirely due to rotation of a cylindrical region $\simeq$ 20 pc in radius, then a crude estimate of the rotation velocity gives $V_c \simeq 2.7$ km s^{-1}. Comparing this with $V_A \simeq 1.8$ km s^{-1}, the density-averaged Alfvén speed for the region (Heiles et al. 1993), one obtains $V_A/V_c \simeq 0.67$. Given the likelihood that $V_A \approx V_\phi$ (due to the predominantly toroidal appearance of the field), and that V_c is probably an overestimate, one sees that values of $V_\phi/(r_0\Omega_0) \gtrsim 1$ should not be out of reach in this environment, and perhaps several others.

4.6.3 Summary

In this paper we have examined a variety of magnetic field distributions and orientations, with the principal intent of gauging their effect on the VC instability of magnetized accretion disks. The main results are: (1) An azimuthal field, varying as some inverse power of radius, has a stabilizing effect on the VC instability if its characteristic Alfvén speed, $V_{\phi0}$, is less than the characteristic rotational speed, $r_0\Omega_0$. (2) If $V_{\phi0} \gtrsim r_0\Omega_0$, the system is susceptible to the LFI, whose peak growth rate increases with $V_{\phi0}$. This instability is more likely to affect thick, massive disks and molecular clouds than thin accretion disks. (3) Our calculations for finite vertical wavenumbers suggest that complete stabilization of thin disks by an equilibrium B_ϕ is unlikely, since the required field ($V_\phi \sim r_0\Omega_0 \gg c_s$) is prone to Parker instability. (4) In contrast to CPS, taking free boundaries into account gives qualitatively different behavior. In particular, whereas absolute stability can be achieved for certain rigidly-bounded configurations, none of the freely-bounded equilibria we examined are similarly stable. (5) In the absence of an equilibrium azimuthal field, a configuration with a radially-varying vertical field has a smaller peak growth rate than in the constant field case. However, the most unstable wavenumber for fields which decrease extraordinarily quickly with radius may be unaffected or even increased.

The advantages of adopting a global analysis to address questions of stability in the presence of strong magnetic fields are even more apparent in the present work than in CPS. In particular, our results show that differentially rotating gaseous bodies threaded by strong azimuthal, but weak vertical fields should be highly unstable for certain specific rotational and azimuthal field profiles (§4.4.5), a result not definitively shown by any local or thin shell analysis. It is hoped that future work will focus on these particular profiles, in order to more fully examine the consequences of the ensuing instabilities.

We thank Peter Sutherland for reading an earlier version of the manuscript and Omer Blaes for several useful discussions. C.C. is grateful to McMaster University for financial support, while the research of R.E.P. is supported by the Natural Sciences and Engineering Research Council of Canada.

Appendix A:
The Perturbation Equations

We begin with the equations of ideal MHD in cylindrical polar coordinates (r, ϕ, z):

$$\begin{aligned} \rho\left[\frac{\partial \mathbf{u}}{\partial t} + (\mathbf{u}\cdot\nabla)\mathbf{u}\right] &= -\rho\nabla\Psi - \nabla\left(p + \frac{\mathbf{B}\cdot\mathbf{B}}{8\pi}\right) + \frac{1}{4\pi}(\mathbf{B}\cdot\nabla)\mathbf{B}, && \text{(A.1)} \\ \frac{\partial \mathbf{B}}{\partial t} &= \nabla\times(\mathbf{u}\times\mathbf{B}), && \text{(A.2)} \\ \nabla\cdot\mathbf{u} &= \nabla\cdot\mathbf{B} = 0. && \text{(A.3)} \end{aligned}$$

Here p is the gas pressure, ρ the constant density, $\mathbf{u}$ the fluid velocity, and $\Psi = -GM/r$ the gravitational potential. Substituting perturbations of the form (4.8) into these equations and only retaining terms of linear order in perturbed quantities, we obtain

$$\begin{aligned} i\omega\delta\mathbf{u} + \nabla\delta h - \frac{ikB_z}{4\pi\rho}\delta\mathbf{B} + 2\left(\frac{B_\phi}{4\pi\rho r}\delta B_\phi - \Omega\delta u_\phi\right)\hat{\mathbf{r}} & \\ +2\left(\frac{\overline{\mathcal{B}}}{4\pi\rho}\delta B_r - \mathcal{B}\delta u_r\right)\hat{\phi} - \frac{B_z'}{4\pi\rho}\delta B_r\hat{\mathbf{z}} = 0, & \qquad \text{(A.4)} \end{aligned}$$

$$i\omega\delta\mathbf{B} - ikB_z\delta\mathbf{u} + 2(\mathcal{A}\delta B_r - \overline{\mathcal{A}}\delta u_r)\hat{\phi} + B_z'\delta u_r\hat{\mathbf{z}} = 0, \qquad \text{(A.5)}$$

$$\frac{1}{r}(r\delta u_r)' + ik\delta u_z = 0, \qquad \text{(A.6)}$$

where $h = p/\rho + B^2/(8\pi\rho)$ is the specific enthalpy, $\mathcal{A} = -r\Omega'/2$, $\mathcal{B} = -[(r\Omega)' + \Omega]/2]$ are the usual Oort shear parameters, and $\overline{\mathcal{A}} \equiv -r(B_\phi/r)'/2$, $\overline{\mathcal{B}} \equiv -(B'_\phi + B_\phi/r)/2$ are their magnetic counterparts. For future reference, we note that with the power-law forms (4.3), the first two of these equations become

$$\begin{aligned} i\omega\delta\mathbf{u} + \nabla\delta h - \frac{ikB_z}{4\pi\rho}\delta\mathbf{B} + 2\left(\frac{B_\phi}{4\pi\rho r}\delta B_\phi - \Omega\delta u_\phi\right)\hat{\mathbf{r}} \\ + \left[(2-a)\Omega\delta u_r - \frac{(2-b)B_\phi}{4\pi\rho r}\delta B_r\right]\hat{\phi} - \frac{(1-c)B_z}{4\pi\rho r}\delta B_r\hat{\mathbf{z}} = 0, \end{aligned} \tag{A.7}$$

$$i\omega\delta\mathbf{B} - ikB_z\delta\mathbf{u} + \left(a\Omega\delta B_r - \frac{bB_\phi}{r}\delta u_r\right)\hat{\phi} + (1-c)\frac{B_z}{r}\delta u_r\hat{\mathbf{z}} = 0. \tag{A.8}$$

Note that equations (A.5) and (A.6) imply $\nabla \cdot \delta\mathbf{B} = 0$. Resolving equations (A.7) and (A.8) into components, and using equation (A.6), one can eliminate all variables except δu_r, leading to the perturbation equation (4.9).

Appendix B:
Rotating vs. Nonrotating Equilibria

The stationary pressure distribution in the nonrotating case can be found from equation (4.4) with $\Omega_0 = 0$. When V_z = constant, the pressure maximum relation is simply

$$\frac{GM}{r_0} = (b-2)V_{\phi 0}^2. \tag{B.1}$$

Note that this requires $b > 2$ for a sensible equilibrium. Using this to eliminate GM in equation (4.4) and integrating gives

$$\left.\frac{p}{\rho}\right|_{\Omega=0} = \frac{p_0}{\rho} + V_{\phi 0}^2(b-2)\left[\frac{r_0}{r} - 1 + \frac{1-(r/r_0)^{-2(b-1)}}{2(b-1)}\right]. \tag{B.2}$$

For a constant vertical field, equation (4.7) reads (in proper units)

$$\begin{aligned} \frac{p}{\rho} &= \frac{p_0}{\rho} + (r_0\Omega_0)^2 \times \\ &\left\{\frac{r_0}{r} - 1 + \frac{1-(r/r_0)^{-2(a-1)}}{2(a-1)} - (2-b)\frac{V_{\phi 0}^2}{r_0^2\Omega_0^2}\left[\frac{r_0}{r} - 1 + \frac{1-(r/r_0)^{-2(b-1)}}{2(b-1)}\right]\right\}. \end{aligned}$$

When $b = a$, this becomes

$$\frac{p}{\rho} = \frac{p_0}{\rho} + [(r_0\Omega_0)^2 - (2-b)V_{\phi 0}^2]\left[\frac{r_0}{r} - 1 + \frac{1-(r/r_0)^{-2(b-1)}}{2(b-1)}\right]$$

$$= \frac{p_0}{\rho} + V_{\phi 0}^2 (b_{eff} - 2) \left[\frac{r_0}{r} - 1 + \frac{1 - (r/r_0)^{-2(b-1)}}{2(b-1)} \right], \tag{B.3}$$

where

$$b_{eff} \equiv \left(\frac{r_0 \Omega_0}{V_{\phi 0}} \right)^2 + b.$$

Clearly, equation (B.3) is identical to equation (B.2), but for the replacement of b by b_{eff}. The two equations become identical in the limit $V_{\phi 0} \gg r_0 \Omega_0$, which is precisely the regime of the LFI found in this paper. In fact, as soon as $V_{\phi 0} \gtrsim r_0 \Omega_0$, one would expect that the rotating system should start to display much of the qualitative behavior of its nonrotating counterpart, since then the contribution of the magnetic terms to the pressure is of the same sign in equations (B.2) and (B.3) for $b \gtrsim 1$. Finally, one might be tempted to blame the LFI for $b < 2$ entirely on the violated equilibrium condition (B.1). However, this condition applies only when $V_{\phi 0} \gg r_0 \Omega_0$. As an example, take $b = 1.7$. Then Fig. 4.1b shows that all equilibria with $0 \le V_\phi \le 1.83$ are allowed.

Appendix C:
Thin-Shell Approximation

Following Kumar, Coleman, & Kley (1994), we adopt a thin shell approximation, in which the radial dependence of equilibrium quantities is ignored to first order, but their derivatives are not. The perturbation equation (4.14) then becomes

$$\frac{d^2\psi}{d\zeta^2} + Q_0 \psi = 0, \tag{C.1}$$

where

$$Q_0 = \frac{2k^2 V_\phi^2}{\tilde{\omega}^4}(b\tilde{\omega}^2 - 2\Omega_A^2) + \frac{2k^2}{\tilde{\omega}^4}(2\omega^2 - a\tilde{\omega}^2) - \frac{8k^2 \omega \Omega_A V_\phi}{\tilde{\omega}^4} - (k^2 + 3/4), \tag{C.2}$$

$\psi \equiv \sqrt{r}\delta u_r$, and $\zeta \equiv r - 1$. Since Q_0 is a constant, the solution of equation (C.1) is $\psi = c_1$ sin $\sqrt{Q_0}\ \zeta + c_2$ cos $\sqrt{Q_0}\ \zeta$; applying the rigid BCs then gives $Q_0 = (n\pi/s)^2$, where s is the shell half-thickness and n the radial mode number. Assuming $ks \gg n$, equation (C.2) yields the following characteristic polynomial:

$$\omega^4 + [2(a - 2 - bV_\phi^2) - 2\Omega_A^2]\omega^2 + 8\Omega_A V_\phi \omega + \Omega_A^2[\Omega_A^2 + 2(b-2)V_\phi^2 - 2a] = 0, \tag{C.3}$$

where the reader is reminded that all equilibrium quantities are to be evaluated at $r = r_0 = 1$.

The roots of equation (C.3), although calculable analytically, are algebraically complicated and do not give much physical insight. Kumar et al. (1994) adopted a procedure equivalent to expanding ω in powers of V_ϕ, taking the latter as a small quantity. As our object is to obtain the critical stability curves, it is more useful for our needs to place no restriction on V_ϕ; rather, we take Ω_A as a small parameter. Expanding ω as

$$\omega = \omega_0 + \Omega_A\omega_1 + \Omega_A^2\omega_2 + \cdots,$$

substituting into equation (C.3), and solving the resulting equation in orders of Ω_A, we find there are two branches of the dispersion relation. One gives all real contributions to ω; the other has $\omega_0^2 = 0$ and

$$\omega_1^2 = \frac{-2V_\phi \pm [b(b-2)V_\phi^4 + 2(a+b-ab)V_\phi^2 - a(2-a)]^{1/2}}{a - 2 - bV_\phi^2}. \tag{C.4}$$

Positivity of the square-root argument leads to the stability criterion (4.27).

Appendix D:
Proof That ω^2 Is Real When $B_z = B_z(r)$ and $B_\phi = 0$

The perturbation equation in this case is [equation (4.9)]:

$$\frac{1}{r}[r\tilde{\omega}^2(\delta u_r)']' + \left\{k^2 r\left[(\Omega^2)' - \frac{(V_z^2)'}{r}\right] + \frac{4k^2\omega^2\Omega^2}{\tilde{\omega}^2} - \tilde{\omega}^2\left(k^2 + \frac{1}{r^2}\right)\right\}\delta u_r = 0.$$

Multiplying through by $r\delta u_r^*$ (an asterisk denotes the complex conjugate) and integrating, one finds

$$\int_{r_1}^{r_2}\left\{k^2 r\left[(\Omega^2)' - \frac{(V_z^2)'}{r}\right] + \frac{4k^2\omega^2\Omega^2}{\tilde{\omega}^2} - \tilde{\omega}^2\left(k^2 + \frac{1}{r^2}\right)\right\} r|\delta u_r|^2 dr + I = 0, \tag{D.1}$$

where

$$I \equiv \int_{r_1}^{r_2} \delta u_r^*[r\tilde{\omega}^2(\delta u_r)']'dr = r\tilde{\omega}^2(\delta u_r)'\delta u_r^*\Big|_{r_1}^{r_2} - \int_{r_1}^{r_2} r\tilde{\omega}^2|(\delta u_r)'|^2 dr. \tag{D.2}$$

The latter result is obtained via integration by parts.

We consider rigid BCs only, since we restrict consideration to B_z = constant in the free boundary case to avoid currents (§4.2.2). Applying $\delta u_r(r_1) = \delta u_r(r_2) = 0$ to equation (D.2), the first RHS term vanishes. Substituting the result back into equation (D.1) and taking the imaginary part of the entire expression gives

$$(\omega^2)_I \int_{r_1}^{r_2} \left\{ |(\delta u_r)'|^2 + \left[\frac{4k^4}{|\tilde{\omega}^2|^2} V_z^2 \Omega^2 + k^2 + \frac{1}{r^2} \right] |\delta u_r|^2 \right\} r dr = 0,$$

where a subscript I indicates the imaginary part. The integrand is positive definite for all r, showing that $(\omega^2)_I = 0$.

a	$E_2(a)$	$(V_z/V_\phi)_{crit}$
1.5	2.55	0.63
1.6	2.78	0.54
1.7	3.01	0.45
1.8	3.26	0.35
1.9	3.50	0.24
2.0	3.75	0.

Table 4.1: Ratio of critical Alfvén speeds, $(V_z/V_\phi)_{crit}$, as a function of shear parameter a for the LFI. See text for the definition of $E_2(a)$.

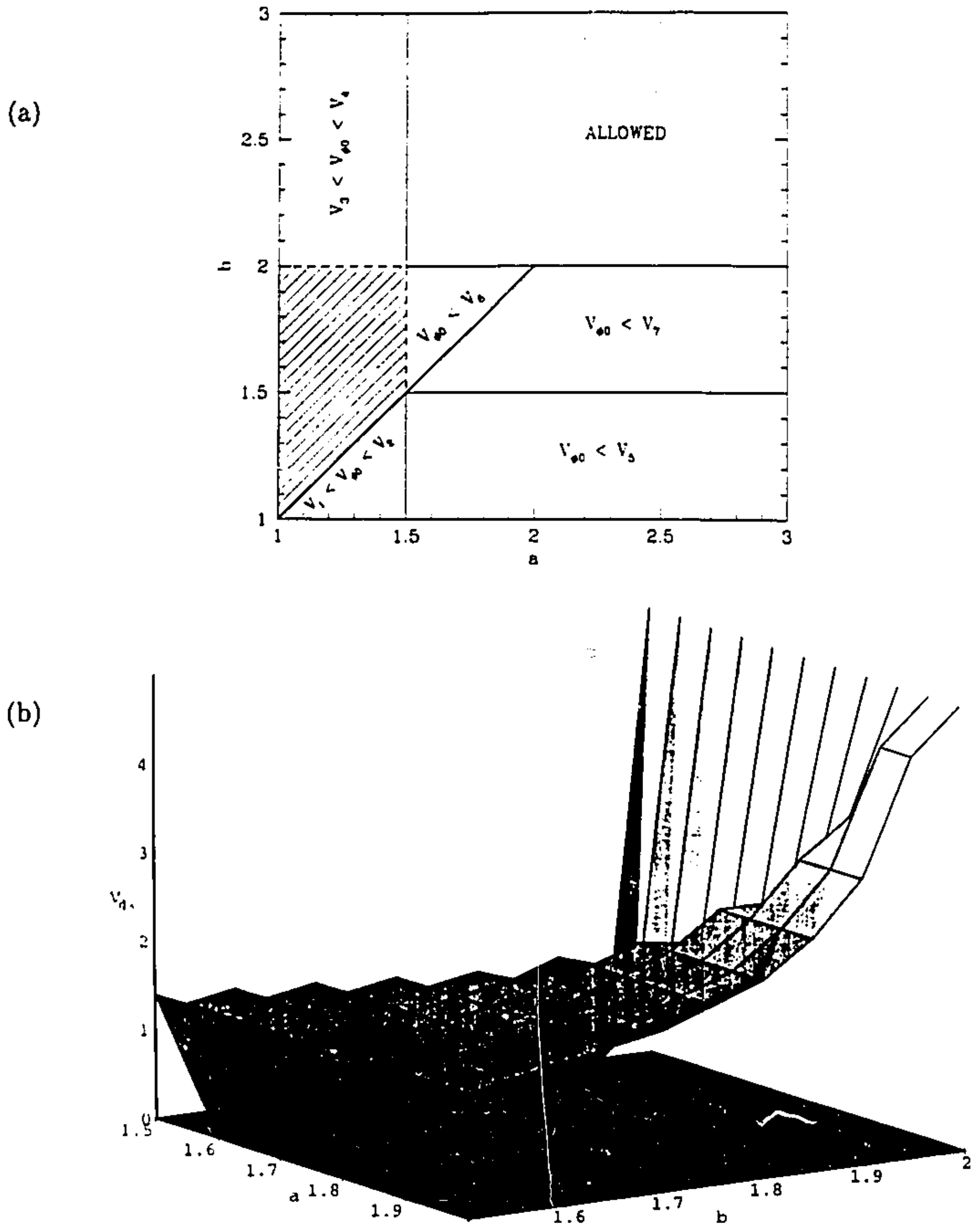

Figure 4.1: (a) Allowed regions and limiting azimuthal Alfvén speeds in the (a, b) plane, obtained from solution of the equilibrium equation (4.7) where $p = 0$, with $r_2/r_1 = 100$. Equilibria for values of a and b lying in the shaded region and along dashed lines are not allowed for any $V_{\phi 0}$. (b) 3D plot of allowed equilibria. Only the range $3/2 \leq (a,\ b) \leq 2$ is shown. Permissible $V_{\phi 0}$ for a given a, b lie between the upper and lower surfaces. The upper surface represents $V_5(a > b)$ and $V_6(a < b)$.

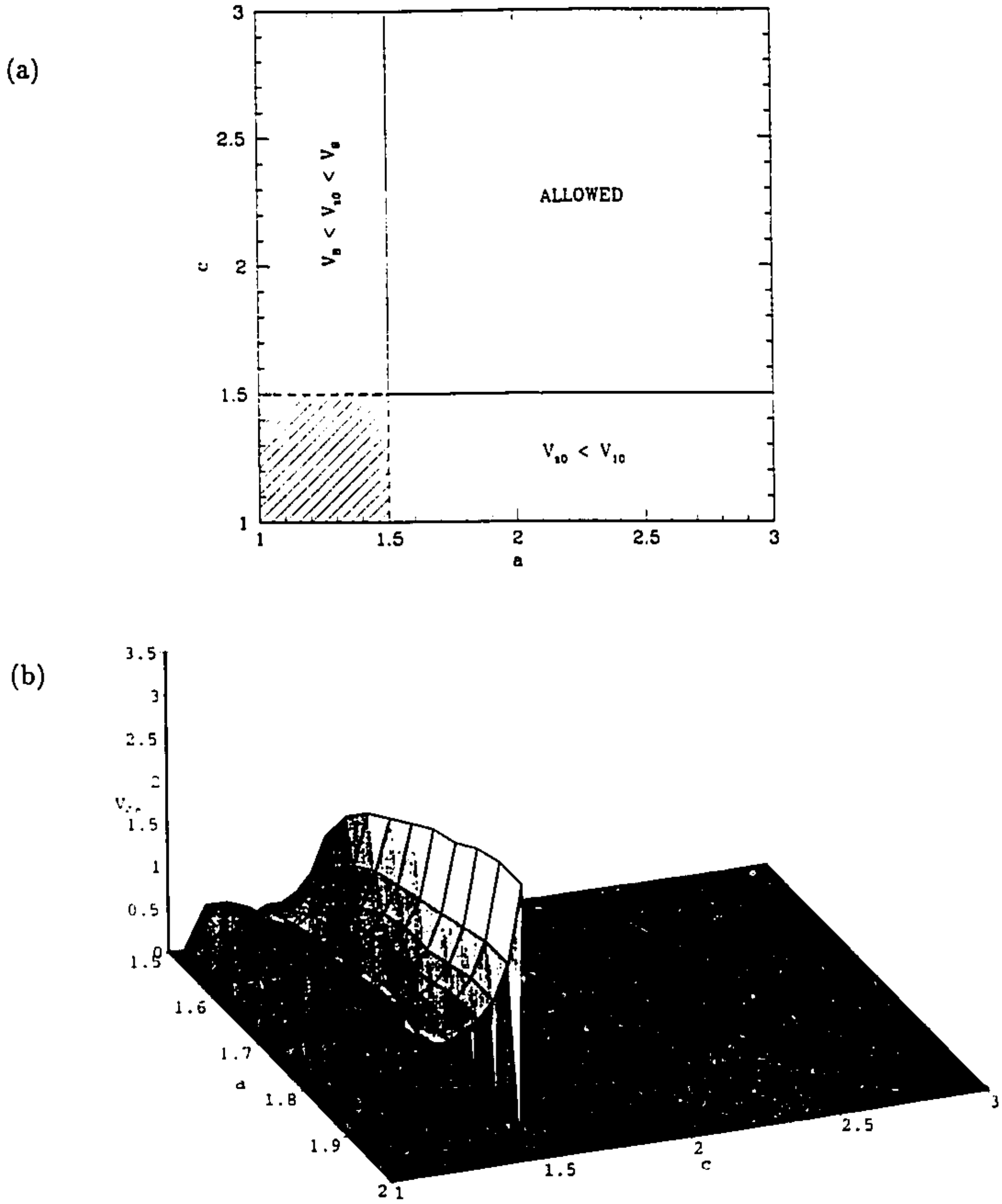

Figure 4.2: (a) Allowed regions and limiting vertical Alfvén speeds in the (a, c) plane. (b) 3D plot of allowed equilibria. For the range of a shown, restrictions on V_{z0} apply only for $1 \leq c \leq 3/2$. The upper surface represents V_{10}. See text and Fig. 4.1 caption for details.

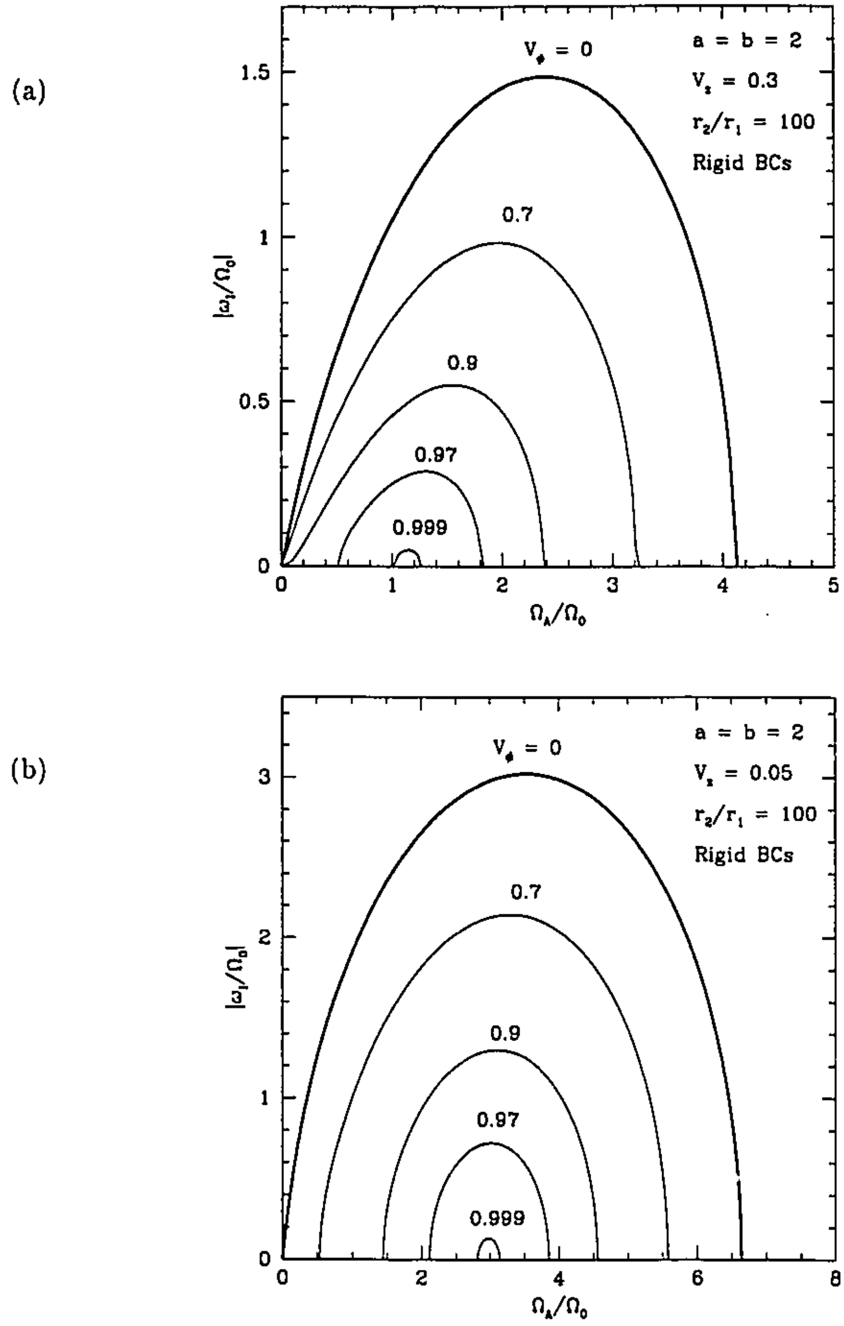

Figure 4.3: WKB growth rates as a function of Alfvén frequency $\Omega_A = kV_z$ for the fastest-growing ($n = 0$) mode, a range of V_ϕ, and two different vertical field values: (a) $V_z = 0.3$; (b) $V_z = 0.05$. Other model parameters are shown at upper right.

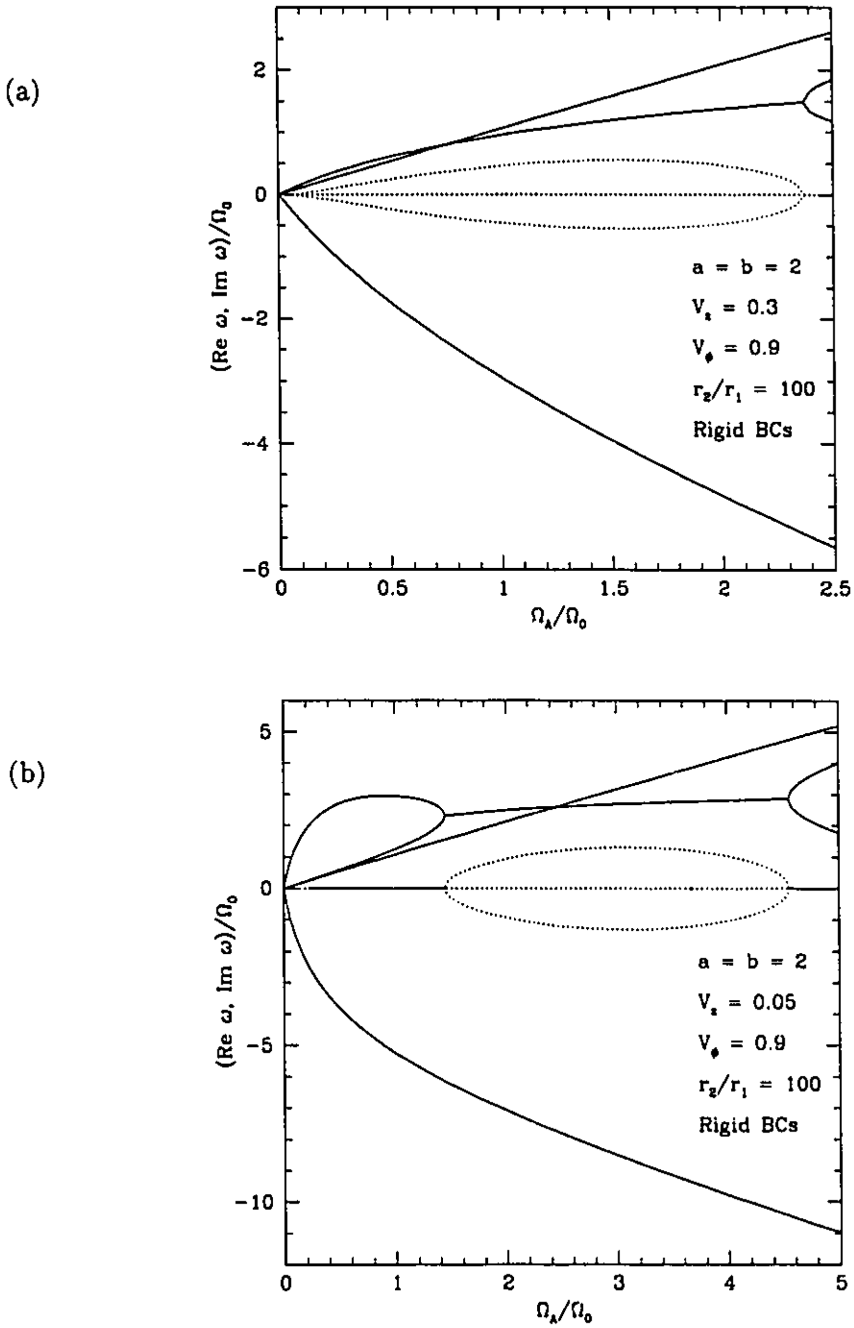

Figure 4.4: Real (solid lines) and imaginary (dotted) parts of the eigenfrequency ω as a function of Alfvén frequency for $V_\phi = 0.9$ and (a) $V_z = 0.3$; (b) $V_z = 0.05$. Other parameters are the same as in Fig. 4.3.

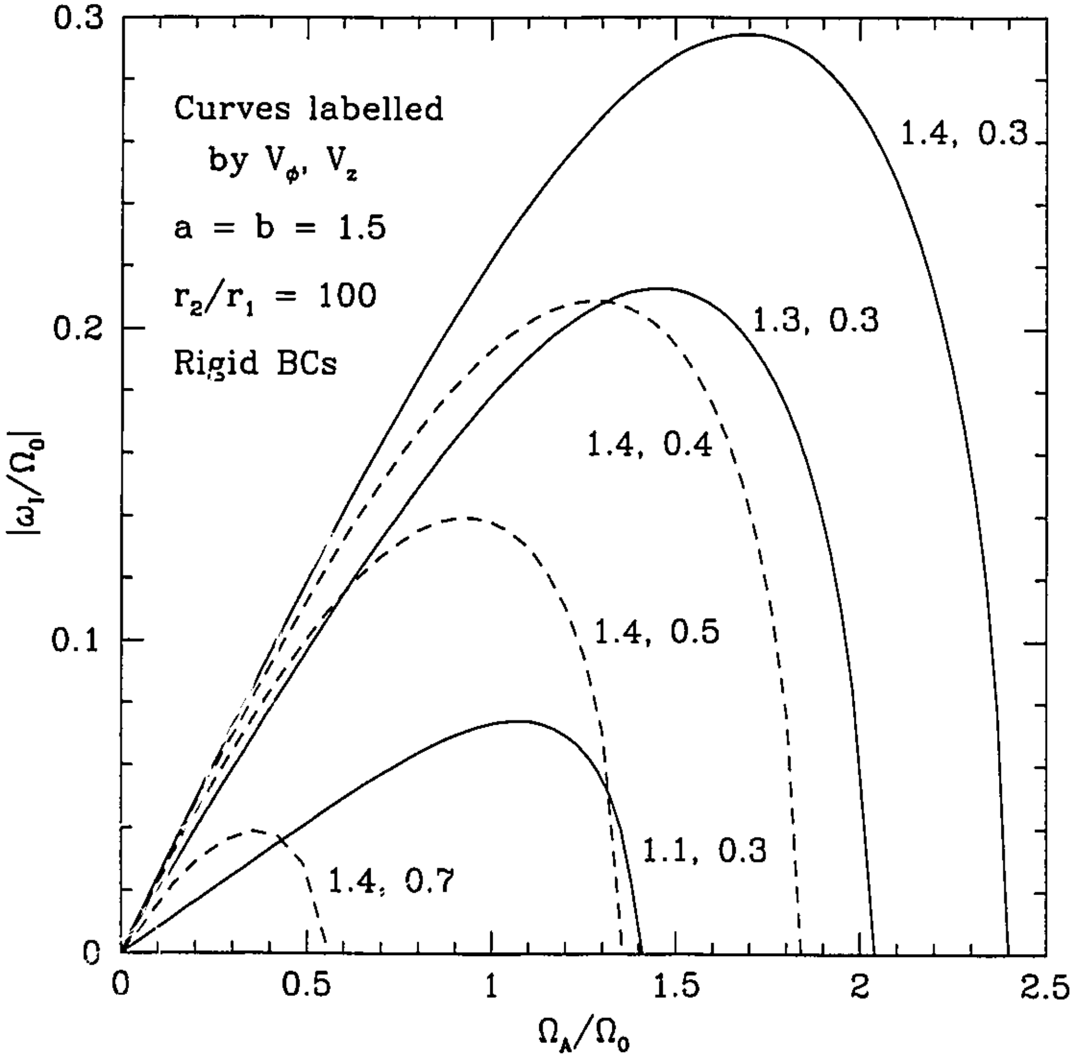

Figure 4.5: Growth rates of the large-field instability as a function of Alfvén frequency for Keplerian rotation and rigid BCs. Each curve is labelled by its corresponding V_ϕ, V_z. Solid curves have $V_z = 0.3$, while dashed curves have $V_\phi = 1.4$. The chosen Alfvén speeds are consistent with the equilibrium constraint $V_\phi \leq 1.42$.

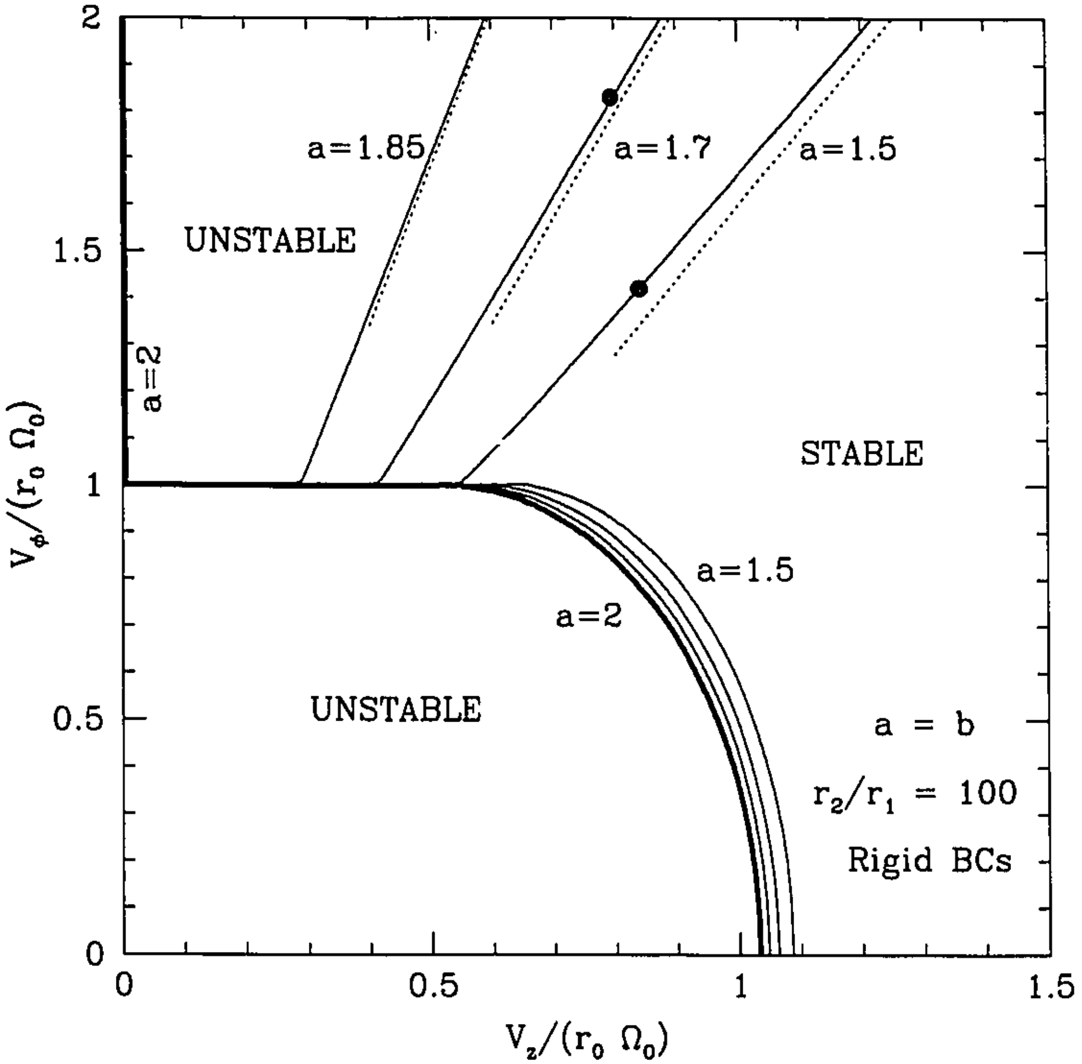

Figure 4.6 Critical stability curves, Im $\omega = 0$, in the (V_ϕ, V_z) plane for rigid BCs and (from right to left) $a = b = 1.5$, 1.7, 1.85, and 2. Growth rates increase from zero on both sides of each critical curve. The region at lower left is VC unstable for all a; the similar region at top left is large-field unstable for all a except $a = 2$. The dotted lines are the slopes of the LFI found analytically from equation (4.24). The large dots indicate upper limits on V_ϕ from equilibrium constraints; the curves are continued to larger V_ϕ for purposes of illustration. See text for details.

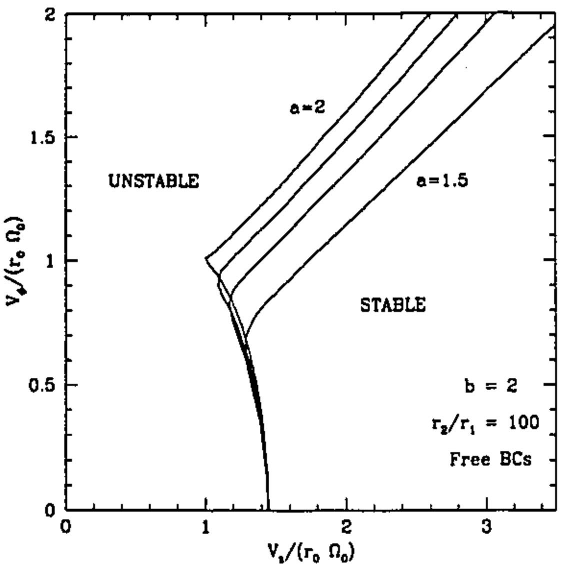

Figure 4.7: Same as Fig. 4.6, but for free BCs. From lower right to top left, curves are for $a = 1.5$, 1.7, 1.85, and 2. The region to the left of each curve is unstable; that to the right, stable.

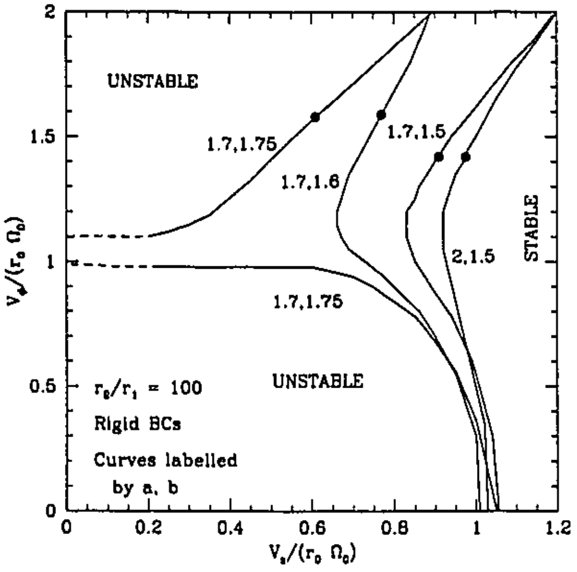

Figure 4.8: Same as Fig. 4.6, but for $a \neq b$. Each curve is labelled by its corresponding a, b. For $a > b$, unstable regions lie to the left of each curve, stable regions to the right. For each $a < b$, there are two branches of the critical stability curve. One, at $V_\phi < 1$, bounds the VC unstable region from above; the other, at $V_\phi > 1$, bounds the large-field unstable region from below. The large dots indicate upper limits on V_ϕ from equilibrium constraints. See text for details.

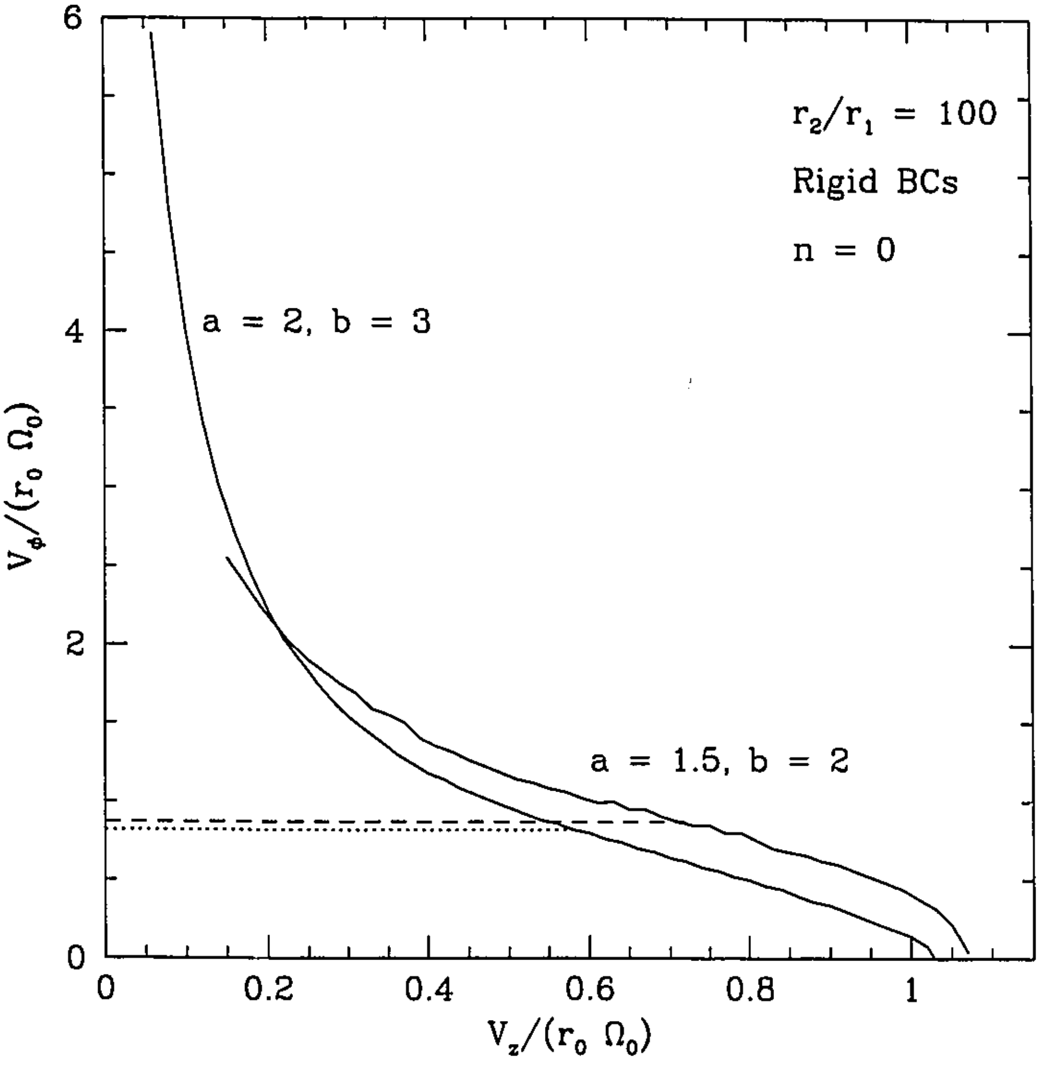

Figure 4.9: Critical stability curves for two special cases examined in §4.4.5 The dashed and dotted lines indicate the local predictions; they intersect the V_ϕ axis at $V_\phi = 0.87$ and $V_\phi = 0.82$, respectively.

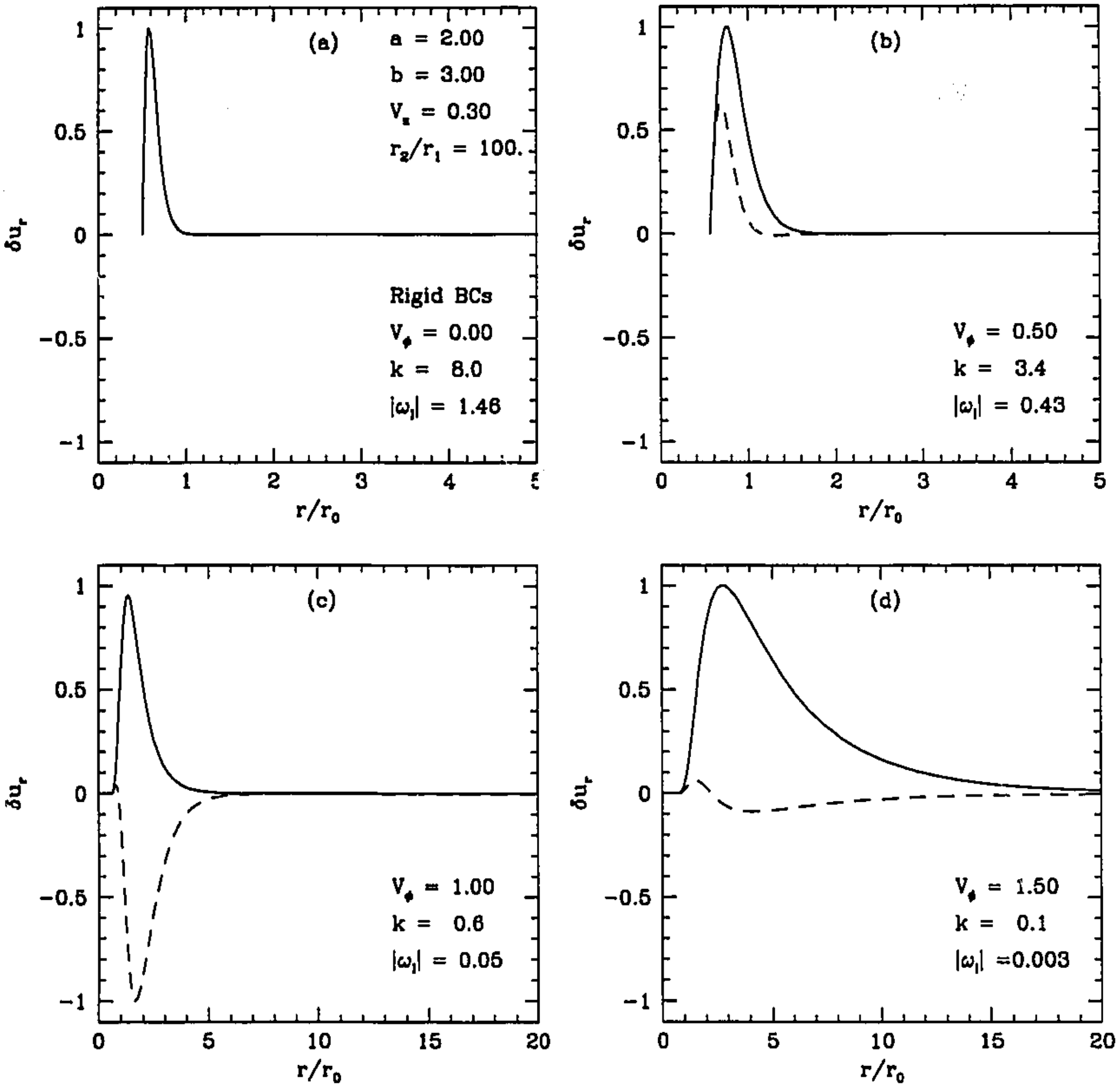

Figure 4.10: Selected eigenfunctions at peak growth for $a = 2$, $b = 3$, and increasing V_ϕ from top left to lower right. The solid line indicates the real part of δu_r; the dashed line, the imaginary part. Each eigenfunction is normalized to its peak value.

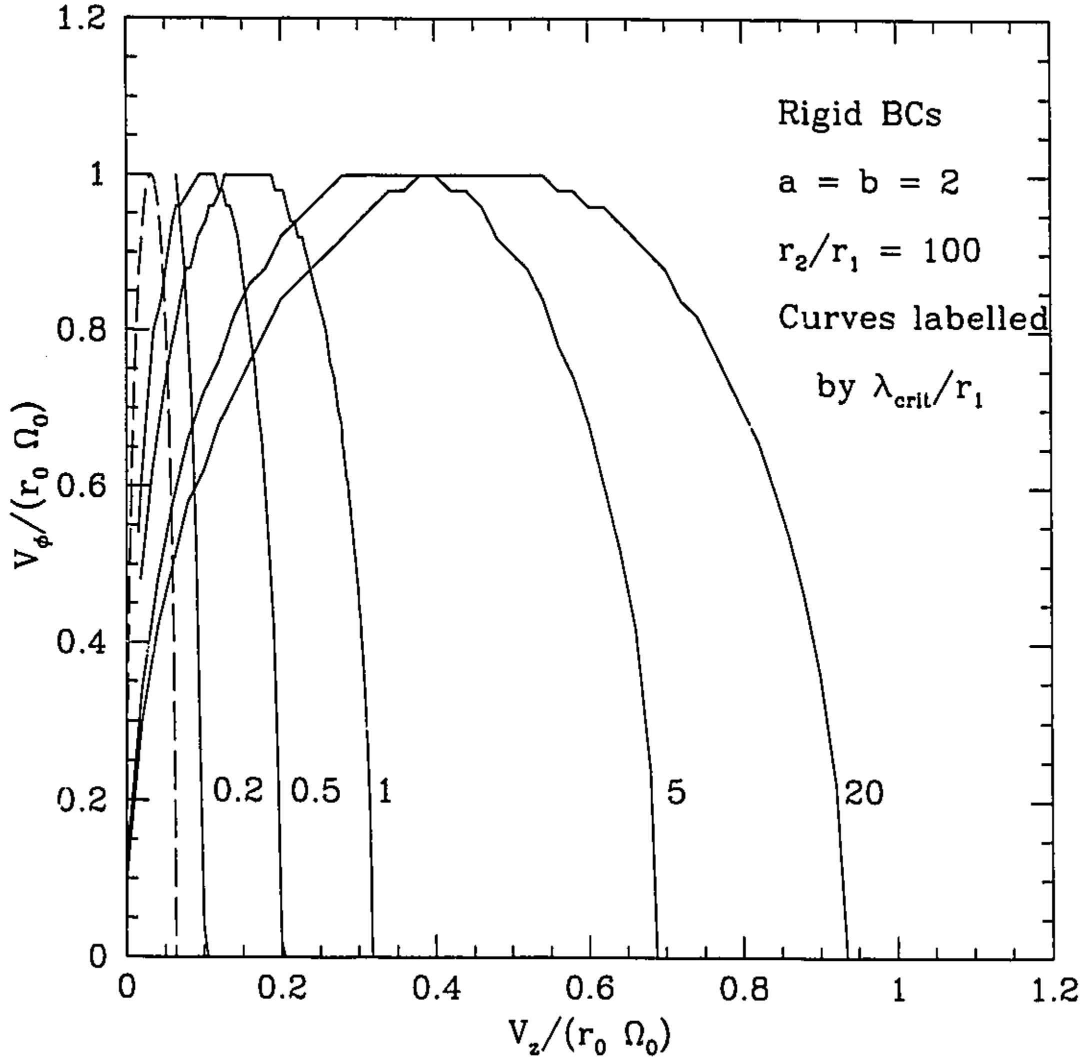

Figure 4.11: Critical stability curves for selected perturbation wavelengths λ_{crit}, for $a = b = 2$ and rigid BCs. The long-dashed curve is the "local" critical curve given by equation (4.31) with $\lambda_{crit} = 0.1\ r_1$.

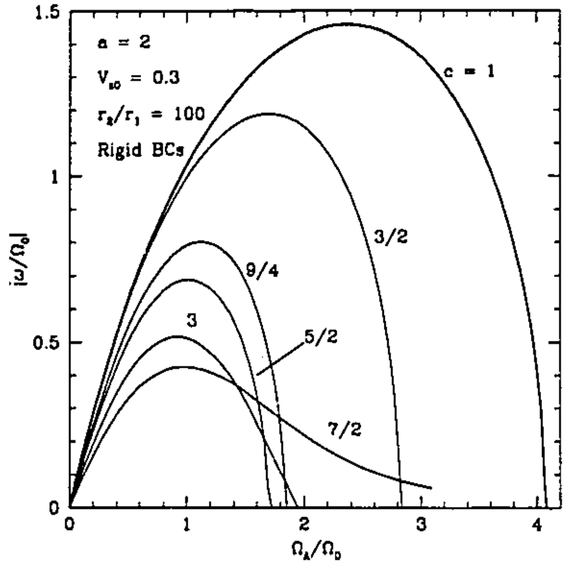

Figure 4.12: Numerical growth rates as a function of Alfvén frequency for $V_\phi = 0$ and $V_z = V_{z0} r^{1-c}$($n = 0$ mode). Curves are labelled by their corresponding c values. Other model parameters are shown at upper left.

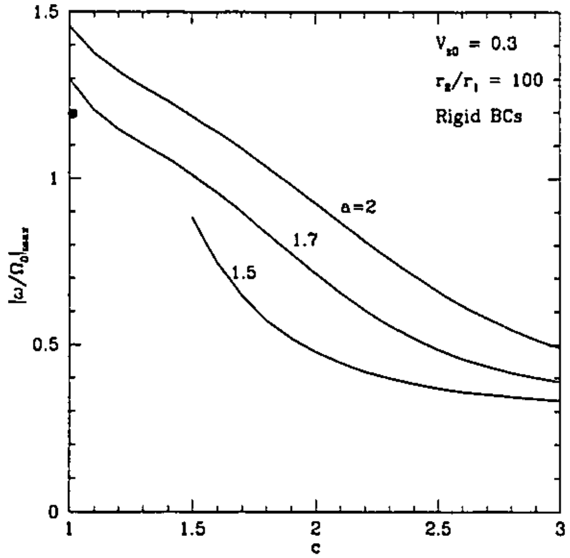

Figure 4.13: Maximum growth rates as a function of vertical field index c for different rotation indices a. The lower curve is incomplete since equilibria with $a = 1.5$ and $1 < c < 1.5$ are not allowed (Fig. 4.2a). The maximum growth rate at $c = 1$, found in CPS, is shown as a large dot slightly offset (for clarity) from the vertical axis.

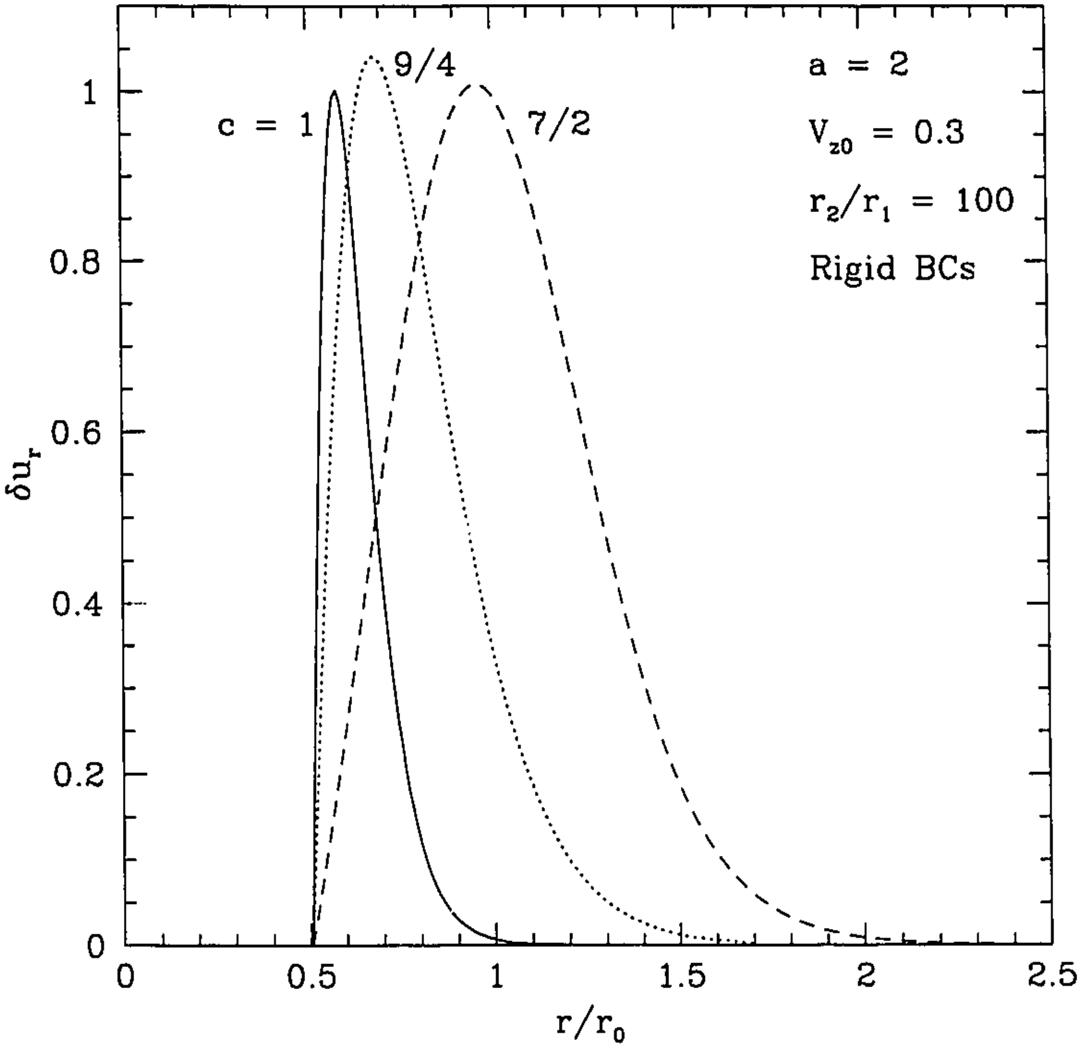

Figure 4.14: Radial eigenfunctions ($n = 0$ mode) at peak growth rate for various c. The overall normalizations have been adjusted to unity for purposes of comparison.

Chapter 5

ON THE GLOBAL STABILITY OF MAGNETIZED ACCRETION DISKS. III. NONAXISYMMETRIC MODES

5.1 Introduction

In the two preceeding chapters, we examined the global stability of a differentially rotating fluid shell threaded by vertical and azimuthal fields to linear, axisymmetric perturbations (Curry, Pudritz, & Sutherland 1994; Curry and Pudritz 1995). The growth rates of the instability found there (the Velikhov-Chandrasekhar, hereafter VC, instability) were on the order of the rotation period of the shell, as evaluated at its pressure maximum. Here we extend that work to nonaxisymmetric perturbations.

Papaloizou & Pringle (1984) (hereafter PP) showed that non-self-gravitating hydrodynamic disks are susceptible to global, nonaxisymmetric instabilities with significant linear growth occurring over a few rotation times. Several important properties of the PP instability, notably the basic physical mechanism, were elucidated and clarified by subsequent investigators (see Narayan & Goodman 1989, hereafter NG, for the most complete review to that time and references to other work). Although the instability is expected to occur in Keplerian disks, it is probably more important in thick pressure-supported "tori," which have a nonzero component of surface gravity at their inner edge. *Radiation* pressure-supported tori are still touted as the central engines of AGN, mainly due to their ability to drive energetic jets by an extremely efficient radiation mechanism (Ch. 1). However, this mechanism may not be able to account for the superluminal motions commonly observed in the jets (Sikora & Wilson 1981). Hydromagnetic models in which the jet consists of gas flung centrifugally outward from a magnetized Keplerian disk are somewhat more successful in this respect (Blandford & Payne 1982; Camenzind 1990).

The underluminous nuclear regions of extended radio galaxies (which nevertheless possess highly energetic jets) have prompted a third model: the ion torus (Rees et al. 1982). In this picture the disk is geometrically thick, but optically thin. The support is provided by a hot gas of ions that are poorly coupled to the electrons, and which radiate primarily by nonthermal processes. Most importantly for our present purpose, the ion torus is expected to be strongly magnetized and because it is thick, may be susceptible to the same instabilities as radiation tori.

The likely presence of magnetic fields in the ion torus immediately begs the question of whether such a configuration is dynamically stable. Indeed, the global dynamical stability of magnetized tori has been recognized as an important problem (cf. Goldreich, Goodman, & Narayan 1986; Blandford 1990), but has not yet been investigated. With the recent renewed interest in magnetic processes spurred by the Balbus-Hawley (1991) instability, it seems only natural to consider whether a global, nonaxisymmetric counterpart exists in tori. Indeed, as Hawley (1991) has commented, "The final word on the viability of thick disks may very well rest with this magnetic instability." Interestingly, our results indicate that thick *and* thin disks are equally susceptible to the magnetic version of the PP instability, so applications need not be limited to the AGN context. *Any* disk which has significant pressure support and a magnetic field (Ch. 1) should be susceptible to the instabilities found in this chapter.

Even in the MHD fluid approximation, the stability of magnetized tori is a difficult problem. There are several good reasons for this, which were outlined in Ch. 2. These complications motivate the adoption of a much simpler equilibrium model for the stability analysis, the incompressible MHD cylinder. Its hydrodynamic counterpart has been used successfully to understand the basic physics of the PP instability, which we review in §5.2. A linear stability analysis of this configuration is set up in §5.3. The main body of results were obtained numerically and are presented in §5.4, 5.5 and 5.6. In §5.4 three distinct instabilities are identified, and their behavior classified in §5.5 on the basis of three different types of wave propagation. The sensitivity of the modes to various system parameters is examined in §5.6, as are the implications of the instability for the dimensions of stable disks. Section 5.7 draws attention to hydrodynamic work which might be useful for further progress, and sums up. The appendix contains some analytic results of interest.

5.2 The Incompressible Hydrodynamic Cylinder

Before examining the stability of the incompressible MHD cylinder, we will benefit from a brief summary of the key results pertaining to its hydrodynamic cousin. We concern ourselves here with the principal branch of the PP instability only, since these modes have the highest growth rates in the linear regime: $\simeq 1/3$ of the rotation frequency Ω at the pressure maximum. Instability occurs via the resonant coupling of shear-modified surface waves propagating along the fluid surfaces, which interfere constructively if the boundaries are sufficiently close together (Blaes & Glatzel 1986, hereafter BG; Blaes 1986; Goldreich, Goodman, & Narayan 1986, hereafter GGN). Fluid motions induced by the principal branch instability were shown to be nearly independent of height (z) (Ch. 1; Blaes 1986; GGN); this accounts for the success of the cylindrical approximation in predicting the growth rates and other important features of the PP instability.

Despite early indications that only the steepest angular velocity gradients were unstable, i.e. $\Omega \sim r^{-a}$, $\sqrt{3} \leq a \leq 2$ (Glatzel 1987a; Zurek & Benz 1986), subsequent work showed that in fact this was only true to first order in the shell thickness; thicker shells with angular velocities approaching Keplerian ($a = 3/2$) are still unstable, albeit with a greatly reduced growth rate (Sekiya & Miyama 1988; Jaroszyński 1988). Such configurations were also shown to be more susceptible to intrinsically compressible (i.e. acoustic wave) instabilities, causing vertical fluid motions and necessitating a fully 3D treatment (Glatzel 1987a). In the incompressible case, the mode structure is particularly simple: to each integral azimuthal wavenumber m, there corresponds a single unstable mode on the principal branch (Blaes 1986; Glatzel 1987a).

The effect of *imposed* vertical perturbations on the principal mode instability was examined in an important and largely neglected paper by Jaroszyński (1988). He showed that vertical Fourier perturbations of wavenumber $k_z \gtrsim m/r_0$ (where r_0 is the central pressure maximum) lead to *complete stabilization* of the principal branch instability in the incompressible cylinder. Presumably, the introduction of vertical motions breaks the resonant coupling of the azimuthally-propagating surface modes. Since an understanding of this coupling is important for many of the results to follow, and since the physics of the $k_z \neq 0$ situation has not been discussed elsewhere, it is worth going into in some detail.

In an incompressible cylinder, the PP instability results from the merger of two surface gravity waves that are isolated at large thicknesses μ. This is shown in Figure 5.1, a plot of the real (dots) and imaginary (solid lines) parts of ω (perturbations evolve as $e^{i\omega t}$) as a function of shell thickness (μ) for the case of a constant angular momentum distribution, $\Omega \sim r^{-2}$. As discussed by BG and GGN, at large μ there exist four neutrally stable modes. Two of these propagate on the inner surface ($r = r_1$), with approximate frequencies (see Appendix)

$$\omega_1 = -m\Omega_1 \pm \left[\frac{mg_1}{r_1} + k_z g_1 \frac{K_{m-1}(\varpi_1)}{K_m(\varpi_1)}\right]^{1/2}, \tag{5.1}$$

and two on the outer surface ($r = r_2$), with frequencies

$$\omega_2 = -m\Omega_2 \pm \left[-\frac{mg_2}{r_2} - k_z g_2 \frac{I_{m+1}(\varpi_2)}{I_m(\varpi_2)}\right]^{1/2}, \tag{5.2}$$

where $g_{1,2}$ is the effective gravity on the inner/outer surface, $\varpi_{1,2} \equiv k_z r_{1,2}$, and I_m and K_m are modified Bessel functions of order m. It is convenient to label the inner "upstream" mode (given by the + sign in equation (5.1)) by P_1^-, the inner "downstream" mode by P_1^+, and similarly for the outer modes (P_2^- and P_2^+). We follow Christodoulou & Narayan (1992) in using the notation 'P' to denote the PP mode; in the current context, it further refers to the principal PP mode.[1] As seen in Fig. 5.1, equations (5.1) and (5.2), shown by the

---

[1] To make a connection to the nomenclature of stellar oscillation theory, one might also note that the P

dotted lines, are good approximations to the exact P modes at large thickness (Appendix).

Due to differential rotation, the four modes at large μ have rather different frequencies. However, as the shell is narrowed, the rotational contributions to equations (5.1) and (5.2) become more similar, and the faster outer mode (P_2^+) catches up to the slower inner mode (P_1^-), merging with it at $\mu \simeq 0.6$. In the $k_z = 0$ case, the surface gravity waves always propagate in the same plane as the shear; one can think of these waves as effectively "tapping the shear energy." When $k_z \neq 0$ and $m = 0$, one has pure surface gravity waves in the z-direction ($\omega_R \sim \sqrt{k_z g_{1,2}}$; Drazin & Reid 1981). These waves do not achieve a resonant condition for any μ, and are hence stable. In the general case, $m \neq 0$, $k_z \neq 0$, however, the resultant wave is helical, with components both parallel and perpendicular to the shear. If the perpendicular component dominates (and this happens for all r if $k_z \gtrsim m/r_1$) resonance cannot occur, and there is no growth. As r_0 is usually only a factor two or so greater than r_1, this explains Jaroszyński's result.

In attempting to predict the stability of the MHD cylinder to the same perturbations, it is important to realize that in the presence of a purely vertical magnetic field, perturbed fluid motions are affected by the field *only* for $k_z \neq 0$. That is, setting $k_z = 0$ in the perturbation equation given below reduces the problem to the hydrodynamic one. Thus we are faced with a most difficult prediction, since magnetic effects can only become important in the regime where the fastest-growing hydrodynamic instability begins to wane.

As a final comment, note that the regime where $k_z \gg m/r_0$ is not of primary interest in this chapter, since it corresponds to localized perturbations whose wavelengths are much smaller than any equilibrium sizescale. Balbus & Hawley (1992) explored this limit in their study of $m \neq 0$ perturbations in a shearing sheet (Goldreich & Lynden-Bell 1965). In the shearing sheet model, however, the radial wavenumber k_x is time-dependent, and so the solutions do not represent global eigenmodes (§2.7; Matsumoto & Tajima 1995). Thus, Balbus & Hawley's finding that the growth rates of the $m \neq 0$ instability are an order of magnitude below the $m = 0$ instability has little bearing on the issue of global mode growth.

---

mode is more similar physically to the stellar p-mode than to the f- or g-modes (Cox 1980).

5.3 The Incompressible MHD Cylinder

The equilibrium is identical to that of Ch. 3: a cylindrical shell of homogeneous, incompressible, ideal MHD fluid, of infinite extent in the z-direction, rotates about the z-axis in the Newtonian point-mass potential $\Psi = -GM/r$. The unperturbed magnetic field is purely vertical and uniform ($\mathbf{B} = B_z\hat{\mathbf{z}}$), and the rotation frequency is taken to be a power law in r: $\Omega \sim r^{-a}$. As in Ch. 3 and 4, we consider the effect of both rigid and free boundaries. While both boundary conditions yield qualitatively similar behavior in the axisymmetric case, the difference is crucial to the physics of nonaxisymmetric perturbations. Indeed, this is expected since the principal mode instability of PP does not occur in rigidly-bounded configurations. In the free case, B_z is supposed to permeate the regions both to the interior and exterior of the shell, as well as within the fluid. Equations giving the exact location of the inner and outer boundaries r_1 and r_2 may be found in Ch. 3. As usual, we rescale units of length and time such that $r_0 = \Omega_0 = 1$.

5.3.1 The perturbation equations

The equations governing the motion of the perturbed fluid are given by (2.93) - (2.101) with $\delta\rho = \delta\psi_{int} = 0$. We derived a single perturbation equation for the radial Lagrangian displacement in §2.5.5; it reads

$$\xi_r'' + \left[\frac{(\tilde{\sigma}^2)'}{\tilde{\sigma}^2} + \frac{1}{r}\frac{3m^2 + r^2k_z^2}{\zeta^2}\right]\xi_r' + \frac{k_z^2}{\tilde{\sigma}^2}\mathcal{H}\xi_r = 0. \tag{5.3}$$

For our present purpose, $\mathcal{H}$ has a simpler form than that given in equation (2.107), namely

$$\mathcal{H} = 2\Omega^2 s + \frac{4m\sigma\Omega}{\zeta^2} - \frac{\tilde{\sigma}^2}{\zeta^2}\left[\zeta^2 + m^2 + 1 + \frac{m^2}{r^2k_z^2}(m^2 - 1)\right], \tag{5.4}$$

where $\tilde{\sigma}^2 \equiv \sigma^2 - \Omega_A^2$, $\sigma \equiv \omega + m\Omega(r)$, $\zeta^2 \equiv m^2 + r^2k_z^2$, and $s \equiv 2\sigma^2/\tilde{\sigma}^2 - a$. We ignore the effect of radial density gradients, azimuthal fields, and vertical field gradients.

Note that equation (5.3) is singular at $\tilde{\sigma}^2 = 0$, corresponding to

$$\omega_R = -m\Omega \pm \Omega_A, \quad \omega_I = 0. \tag{5.5}$$

A similar singularity exists in the hydrodynamic case, the *corotation singularity* at $\omega_R = -m\Omega$, $\omega_I = 0$. However, while a corresponding corotation theorem ensures that for an unstable mode $\omega_R = -m\Omega$ is actually attained within the fluid, no similarly strong requirement rules the MHD case. The only known result in this respect is the "almost" corotation theorem, $\omega_R > -m\Omega$ within the fluid (for instability), which is known to hold for rigidly-bounded configurations (§2.5.5). In other contexts, the mathematical singularities at $\tilde{\sigma}^2 = 0$ have been termed "shear Alfvén singularities" (Ross, Chen, & Mahajan 1982; Matsumoto & Tajima 1995). By analogy with the role of the corotation singularity in hydrodynamic flow, a shear Alfvén singularity may be expected to possess resonant properties as regards the propagation and amplification of internal waves. Radially propagating waves should alter their properties near the characteristic radii given by equation (5.5); i.e.

$$r_{A,1} \equiv \left(-\frac{\omega_R - \Omega_A}{m}\right)^{-1/a} \quad \text{and} \quad r_{A,2} \equiv \left(-\frac{\omega_R + \Omega_A}{m}\right)^{-1/a}. \tag{5.6}$$

The corresponding corotation radius is given by

$$r_{CR} \equiv (-\omega_R/m)^{-1/a}. \tag{5.7}$$

Note that $r_{A,1}$ and $r_{A,2}$ are only singularities of equation (5.3) when $\omega_I = 0$ (the same holds for r_{CR} in the corresponding hydrodynamic equation). Due to its more physically descriptive quality, we shall use the term "Alfvén resonance" rather than "shear Alfvén singularity" in this chapter.

In the absence of **B**, wave motion in a homogeneous and incompressible fluid can be supported only on the boundaries; any instabilities present must therefore be due to surface wave interactions. In the corresponding magnetic configuration, however, torsional Alfvén waves can propagate.[2] Indeed, should there exist waves of the form (5.5), which we term "Alfvén-modified corotation waves," they can propagate anywhere within the fluid. These issues will be discussed in greater detail in §5.5.

---

[2] Compressional Alfvén waves and Alfvén *surface* waves are also possible in a compressible medium (Cross 1988), but will not occur in the present context.

5.3.2 Exterior perturbations and boundary conditions

As in Ch. 3, the perturbed magnetic field in the interior ($r < r_1$, denoted by subscript i) and exterior ($r > r_2$, subscript o) regions is assumed to be current-free, whence

$$\delta \mathbf{B}_{i,o} = B_z \nabla \chi_{i,o}, \tag{5.8}$$

$$\chi_i(\varpi) = c_1 I_0(\varpi), \quad \chi_o(\varpi) = c_2 K_0(\varpi). \tag{5.9}$$

Following the procedure of Ch. 3 leads to the free boundary condition

$$\xi_r' + \left[1 - \frac{2\sigma m\Omega}{\tilde{\sigma}^2} + \frac{\zeta^2}{r\tilde{\sigma}^2}\left(g_{eff} + \Omega_A^2 \frac{\chi_{i,o}}{\chi_{i,o}'}\right)\right]\frac{\xi_r}{r} = 0. \tag{5.10}$$

5.4 The MHD instability: general characteristics

We solved equation (5.3) subject to the free boundary condition (5.10) using a standard shooting method as adapted for eigenvalue problems (Press et al. 1992). In contrast to the hydrodynamic problem, a constant angular momentum profile ($a = 2$) does not lead to significant simplification of the perturbation equations (for reasons outlined in §2.5.5). Nevertheless, we choose this value of a for ready comparison with the literature on the PP instability. We also take $m = 1$ and $k_z = 1.5$ as fiducial values, to isolate the effect of magnetic field strength. Recall that the latter value of k_z is roughly that at which the PP instability is suppressed (§5.2). Other values of these parameters are explored in subsequent sections.

The effect of a constant vertical magnetic field on the principal branch of the PP instability is shown in Figure 5.2, a plot of the growth rate, $-\omega_I$, as a function of the thickness parameter, μ. The hydrodynamical growth rate curve is shown by a dotted line, and is reduced by over 50 % from its peak $k_z = 0$ value (BG). The MHD growth rates are shown by solid lines, and clearly exceed the hydrodynamic growth rates in nearly all cases. For this value of k_z, peak growth occurs near $V_z = 0.35$ (see inset), for shells of thickness $\mu \simeq 0.21 \Rightarrow r_2/r_1 = (1 + \mu)/(1 - \mu) \simeq 1.53$. Some general features should be noted from these curves:

(a) The magnetic field stabilizes for thicknesses $\mu < \mu_{min}$, where μ_{min} increases with V_z.

(b) For intermediate-strength fields ($0.15 \lesssim V_z \lesssim 0.7$) even the most extended shells are unstable, in contrast to the hydrodynamic case.

(c) Each configuration of specified μ possesses a critical field strength $V_{z,crit}$ above which it is stable. $V_{z,crit} \simeq 1.4$ for the parameters shown in Fig. 5.2.

Qualitative differences in the curves of Fig. 5.2 suggest the consideration of three separate regimes in field strength: (i) weak ($V_z < 0.15$), (ii) moderate ($0.15 \lesssim V_z < 0.7$), and (iii) strong ($V_z \gtrsim 0.7$). We examine each of these in turn.

(i) The weak field regime

The real part of the eigenfrequency ω_R for $V_z = 0.1$ is shown in Figure 5.3a. The main difference from Fig. 5.1 is the existence of two entirely new neutrally stable modes at large μ. We label these by $\mathcal{A}^+$ and $\mathcal{A}^-$, since they are certainly magnetic ("Alfvénic") in origin. One indication of this is that the frequency of $\mathcal{A}^-$ approaches $-\Omega_A$ as $\mu \rightarrow 1$. The merger of $\mathcal{A}^+$ and $\mathcal{A}^-$ (at $\mu \simeq 0.1$) leads to a weak instability ($\omega_{I,max} \approx 0.05$), not shown in Fig. 5.2. As $\mu \rightarrow 0$, this unstable mode splits once again into two neutrally stable modes, with frequencies

$$\omega_R = -m\Omega_0 \pm \Omega_A \tag{5.11}$$

at $\mu = 0$. These are the Alfvén-modified corotation waves (hereafter AMCWs) discussed in §5.3.1 and are the analog of the single corotating mode found in the zero-thickness hydrodynamic cylinder (Blaes 1986). In this limit one also identifies the MHD counterparts of the P_1^+ and P_2^- neutral modes, which now occur at much larger frequencies. The latter modes have nothing to do with any of the instabilities found here, and therefore will not be shown in subsequent graphs.

As well as the purely Alfvénic wave branch, there also exists an analog of the unstable surface wave branch discussed in §5.2. However, the frequencies of the isolated surface waves at large μ are no longer described, even approximately, by equations (5.1) and (5.2). Due to the presence of field lines on the boundaries, there is no doubt a new contribution due to the Alfvén frequency Ω_A. For this reason, we denote the large μ neutral modes by $\mathcal{P}_1^-$ and $\mathcal{P}_2^+$. The merger of these waves (denoted by $\mathcal{P}$) at $\mu \simeq 0.63$ corresponds exactly to the large μ cutoff of the curve shown in Fig. 5.2. As $\mu \to 0$, this unstable branch splits into two neutral modes, which attain the same frequencies as the $\mathcal{A}$ branch waves (equation (5.11)) at $\mu = 0$.

In addition to the two instabilities already discussed, both of which grow fastest at low μ, there exists in the weak-field case a *third* instability, seen in Fig. 5.3a beginning at $\mu \simeq 0.4$ and persisting as $\mu \to 1$. We have not been able to attribute this instability to the merger of two neutrally stable waves. The only hint to its origin is what appears as a slight mutual "attraction" of the $\mathcal{A}^-$ and $\mathcal{P}$ modes near $\mu = 0.4$. At larger fields this is more pronounced (see (ii) below), and has the appearance of an "avoided crossing" (Craik 1985; Aizenman, Smeyers, & Weigert 1977). The instability in question is still much more slowly growing ($-\omega_{I,max} \simeq 0.06$) than that of the $\mathcal{P}$ branch. To distinguish this mode from the other two, we label it the $\mathcal{R}$ mode.

(ii) The moderate field regime

Here we consider Alfvén velocities in the range $0.15 \lesssim V_z < 0.7$. As can be seen in Fig. 5.2, these configurations are distinguished by the persistence of instability to large ($\mu \simeq 0.95$) shell thicknesses. Unfortunately, our mode-finding code is not sufficiently refined to find all of the neutral modes, but we will glean what we can from the somewhat incomplete picture given in Fig. 5.3b, which gives ω_R for $V_z = 0.3$.[3] Once again, a weakly unstable mode in addition to that shown in Fig. 5.2 exists at low μ, but we fail to detect the third unstable mode mentioned above. Clearly, the mode structure at large μ is quite different from the hydrodynamic and weak field cases. The $\mathcal{A}$ and $\mathcal{P}$ modes have exchanged their relative locations in frequency space; i.e. $\mathcal{A}^-$ now lies *below* $\mathcal{P}$ at large μ (compare Fig. 5.3a). The two modes draw close together near $\mu = 0.4$, eventually merging at $\mu \simeq 0.9$. The frequency of the merged modes approaches $-\Omega_A = 0.45$ as $\mu \to 1$. In the weak field case examined above, this merger did not occur. Rather, the two modes simply crossed at $\mu \simeq 0.1$ (Fig.

---

[3] The structure of the neutral mode branches often goes a long way toward explaining the physical mechanisms behind instability; cf. Glatzel (1987a, b) and Christodoulou (1993).

5.3a). We have confirmed that the unstable tail of the $V_z = 0.3$ growth rate curve is in fact identifiable with the $\mathcal{R}$ mode of the $V_z = 0.1$ case. Thus it appears that the $\mathcal{P}$ and $\mathcal{R}$ modes have merged, producing growth over the entire shell. We denote this merger by $\mathcal{P}/\mathcal{R}$.

(iii) The strong field regime

It is clear from Fig. 5.2 that the instability curves change their qualitative character once again between $V_z = 0.5$ and 0.7, whence they become nearly symmetric and have both a lower *and* an upper stability threshold in μ (except for the $V_z = 1.3$ curve). As a representative example of the strong field regime we take $V_z = 0.7$, and its mode structure is shown in Fig. 5.3c. It is apparent from this figure that a simple crossing occurs between the $\mathcal{P}$ and $\mathcal{A}$ modes, and that the former once again splits into two stable modes at $\mu \simeq 0.62$. As in the weak-field regime, the $\mathcal{A}$ and $\mathcal{R}$ modes appear distinct from the $\mathcal{P}$ mode. As the field strength is increased, there are hints of more complicated mode structure at large μ and high frequency (Figs. 5.3b & c). Some of these branches are as yet unidentified.

We restrict our attention in the remainder of this chapter to the moderate field regime, represented by $V_z = 0.3$. Before investigating the detailed dependence of the $\mathcal{P}$, $\mathcal{A}$, and $\mathcal{R}$ instabilities on the system parameters, we provide in the following section a simple means of classification based on the propagation properties of the waves.

5.5 Unstable Wave Properties

5.5.1 Destabilization of thin shells

First, consider the merger of the AMCWs that causes both the $\mathcal{P}$ and $\mathcal{A}$ instabilities at small μ. In the zero-thickness limit, $\mathcal{A}^+$ and $\mathcal{A}^-$ have very different frequencies and propagate in opposite senses with respect to a corotating observer at $\Omega = \Omega_0$. Since Ω_A is fixed in each of Figs. 5.3a, b, and c, changes in the frequencies of $\mathcal{A}^+$ and $\mathcal{A}^-$ as μ is increased from zero are entirely due to the variation in Ω over the shell. The condition for a merger is $\omega(\mathcal{A}^+) = \omega(\mathcal{A}^-)$; the smallest μ at which this can be achieved is given by

$$-m\Omega_1 + \Omega_A = -m\Omega_2 - \Omega_A,$$

which in the case $a = 2$ leads to the result

$$\mu = \mu_c \equiv \frac{\Omega_A}{2m}. \tag{5.12}$$

For example, $\mu_c = 0.075$, 0.225, and 0.525 for the parameters of Figs. 5.3a, b, and c, respectively. These values correspond quite closely with the locations of the $\mathcal{A}^+$ and $\mathcal{A}^-$ mergers at small μ. It may not be a coincidence that μ_c also seems to fall near the maximum of the $\mathcal{P}$ mode instability. The lower μ value corresponding to the merger of AMCWs into the $\mathcal{P}$ mode instability can probably be calculated only by considering both the Alfvénic *and* characteristic surface gravity frequencies (§5.2).

5.5.2 Characteristic radii

To elucidate the role of the Alfvén resonances given by equations (5.6), various radii of interest have been plotted in Figure 5.4a, along with the real and imaginary parts of $-\omega$. While r_{CR} lies within the shell at all μ for an unstable mode, the same is not true of $r_{A,1}$ and $r_{A,2}$. In fact, $r_{A,2}$ always lies *outside* r_2 for the parameters shown. $r_{A,1}$, on the other hand, starts out in the vacuum interior ($r < r_1$) for thin shells, but then moves inside the fluid at $\mu \simeq 0.2 \Rightarrow r_2/r_1 = 1.5$. This is, perhaps not coincidentally, very near the location of the maximum growth rate $-\omega_I$ and the merger point of the $\mathcal{A}^+$ and $\mathcal{A}^-$ modes ($\mu_c = 0.225$). Note that r_{CR} lies between $r_{A,1}$ and the outer boundary r_2.

As will become clear in subsequent sections, all of the $m \neq 0$ unstable modes of the incompressible MHD cylinder can be classified on the basis of diagrams similar to Fig. 5.4a. These diagrams generally fall into three types, of which Fig. 5.4a is one variety (Type 1). Note that the $\mathcal{R}$ mode instability is always of this type. Type 2 is shown in Fig. 5.4b for the model parameters shown at upper left, and is distinguished by the fact that the outer Alfvén radius $r_{A,2}$ passes inside the shell at some μ. The inner Alfvén radius lies outside the shell at small μ and then passes inside at $\mu \simeq 0.53$, staying inside thereafter. $r_{A,1}$ remains very close to r_1 for all μ. Note that r_{CR} lies inside the shell between the two Alfvén radii. Many of the same features are found in Fig. 5.4c, which shows the $\mathcal{A}$ mode in the Keplerian case, with one crucial difference: $r_{A,1}$ *always lies just to the (vacuum) interior of* r_1. This is Type 3. Note that the $\mathcal{A}$ mode is always of Type 2 or 3. It is the difference between these two types that suggests a mechanism for maintaining unstable growth at large μ.

Resonances as wave amplifiers

Before discussing the particular mechanism believed to be at work here, it is useful to make a connection once again with hydrodynamic theory. *Over-reflection* of internal waves is a process known to lead to instability in shearing, hydrodynamic disks. The basic physical mechanism is shown schematically in Figure 5.5 and works as follows (see Mark 1976; Cairns 1979; Drury 1985; Goldreich & Narayan 1985; and NG for further details and embellishments). A wave incident on a resonance from the inner disk ($r < r_0$) will produce a reflected and (by the usual wave-tunneling process) a transmitted wave. Both the incident and reflected waves have negative action (e.g. energy or angular momentum) relative to the equilibrium flow because their pattern speeds Ω_p are lower. Conversely, the transmitted wave has positive action. Due to the conservation of action, the reflected waves must have more negative action than the incident waves and must therefore be amplified. The inner edge of the disk, acting as a reflector, provides a feedback mechanism to generate more incident waves. A reflecting outer boundary produces a similar result, while two reflecting boundaries can cause correlated growth on both sides of corotation if a certain phase condition is satisfied (Narayan, Goldreich, & Goodman 1987). To act as a reflector (of sound waves in this case), the density at the edge of the disk must cut off on a scale shorter than the radial wavelength of the mode. This is easy to satisfy in our case, since the density is a step function at the fluid surfaces.

Alfvén resonances as wave attenuators

In the MHD system considered here, r_{CR} loses its significance as a wave amplifier since it is no longer a singularity of the perturbation equations. It still serves as a point of reference for defining positive and negative wave action, however. It is well known that interactions between waves of positive and negative action can lead to instability (Cairns 1979; Craik 1985; Glatzel 1987b). Indeed, the mergers of the AMCWs which produce both the unstable $\mathcal{P}$ and $\mathcal{A}$ modes appear to be of this type. Yet in the absence of the corotation resonance, the system lacks an efficient wave amplifier.

Figure 5.6, from Matsumoto & Tajima (1995) (hereafter MT), shows the effect of the Alfvén resonances when both lie within the flow. Waves are amplified within the resonant cavity created by $r_{A,1}$ and $r_{A,2}$, but are strongly damped outside this region. This is similar to the Type 2 situation described above, after $r_{A,1}$ has passed inside the shell (i.e. at large μ). Although it appears that virulent local instabilities (such as those found by MT) can be generated in this manner, globally unstable modes will not develop since neither of the boundaries are involved. This is in agreement with the observed dimunition of the Type 2 growth rate at large μ (Fig. 5.4b).

Alfvén resonances as wave amplifiers

When only one Alfvén resonance lies inside the shell, as in Types 1 and 3 and Type 2 for $\mu < 0.53$, over-reflection occurs between the resonance and one of the boundaries. Which boundary depends on the location of r_{CR}. *Wave amplification can only take place between an Alfvén resonance and a boundary if r_{CR} lies in between.* Presumably, this is required because mergers between waves of opposite sign in the action cause the instability (Cairns 1979). In the Type 1 instability, wave amplification occurs between $r_{A,1}$ and r_2 (with r_{CR} in between) until at large μ the divergence of these two radii becomes so rapid that standing waves can no longer be maintained. The opposite situation occurs in Type 3. Here $r_{A,2}$ lies inside the shell and approaches r_1 asymptotically as $\mu \to 1$. This scenario is ideal for sustained growth since $r_{A,1}$ lies *inside* r_1 (i.e. in the vacuum interior) at all μ and therefore cannot act to radially confine the waves (MT). The Type 3 behavior corresponds closely to a known property of the hydrodynamic system, namely, that the growth rate is higher the closer corotation is to the inner boundary (Glatzel 1987b).

5.5.3 Eigenfunctions

To test these ideas, we examined the degree of localization of the various modes exhibited in Fig. 5.4 by looking at their radial eigenfunctions. An example of extreme localization can be seen in Figure 5.7, which shows the eigenfunctions for the $a = 1.6$ $\mathcal{A}$ mode of Fig.

5.4b. Plotted are the real and imaginary parts of the radial velocity perturbation δu_r (but denoted simply by δu), and the total (gas + magnetic) pressure δh over the entire shell thickness. The filled and open arrowheads at the top and bottom of the figure indicate the location of the inner and outer Alfvén radii, respectively, and the crosses mark the position of the corotation radius. The magnitudes of the eigenfunctions have been normalized to unity. The eigenfunctions become even more localized at larger μ, and the resulting radial confinement of the mode leads to a vanishing growth rate as $\mu \rightarrow 1$ (MT).

The eigenfunctions for the Keplerian case of Fig. 5.4c are essentially identical to those of Fig. 5.7 due to the close proximity of $r_{A,1}$ and r_1. Thus we do not display them here. However, we shall find examples in later sections that adequately support the above scenario for sustained growth.

For thin configurations and a weak field, the $\mathcal{P}$ mode is primarily a surface mode. To see this, the eigenfunctions corresponding to the hydrodynamic case and the MHD case of Fig. 5.4a are plotted in Figures 5.8a and b for a thin shell, $\mu = 0.1$. Although δu_R is nearly flat over the entire shell, the other perturbations show definite enhancements at the boundaries and little interior structure. Fig. 5.8a agrees in character with Fig. 5(i) of Glatzel (1987a), who considered a compressible fluid. Another argument for its surface nature is the fact that it the $\mathcal{P}$ mode does not exist in configurations with rigid boundaries (see ff. §5.6.4). Finally, Alfvén resonances are not a consideration, since both $r_{A,1}$ and $r_{A,2}$ lie outside the shell for the adopted parameters in Fig. 5.8b.

It is interesting to observe how the eigenfunctions change with increasing shell thickness. Figures 5.8c and d are equivalent to Fig. 5.8b, except for $\mu = 0.4$ and 0.8, respectively. Note that $r_{A,1}$ has entered the shell at these higher μ values. In Fig. 5.8c, the eigenfunctions are generally more oscillatory than in Fig. 5.8b, revealing the influence of internal Alfvén waves on the fluid motions. The local extrema near $r_{A,1}$ hint that the $\mathcal{R}$ mode is feeling the influence of a resonance. This conjecture is supported by Fig. 5.8d, which shows a drastic change in the eigenfunctions as they pass through $r = r_{A,1}$.

5.6 Further Results

In this section we round out the above physical discussion by examining the behavior of the instabilities for a wide range of system parameters. We begin by gauging the effect of the rotation law.

5.6.1 Nonconstant angular momentum

Here we explore the effect of nonconstant angular momentum distributions ($a \neq 2$) on the $\mathcal{P}$, $\mathcal{R}$, and $\mathcal{A}$ instabilities. In the hydrodynamic $k_z = 0$ case, the peak growth rate decreases steadily from $-\omega_{I,max} \simeq 0.26$ at $a = 2$ to zero at $a = 1.5$ (Jaroszyński 1988). In the presence of vertical perturbations, the rate of decrease is more rapid, with $-\omega_{I,max} \lesssim 0.02$ by $a = 1.85$. At the same time, the PP instability for $a \neq 2$ has a nonzero growth rate for shells of *arbitrary* thickness μ, i.e. even for $\mu \to 1$.

Choosing $V_z = 0.3$, we have plotted in Figure 5.9a the merged $\mathcal{P}$ and $\mathcal{R}$ mode growth rates for a range of a between 1.5 and 2. Although there is a slight decrease in the peak growth rate (which always occurs near $\mu = 0.2$), and a slight increase in $-\omega_I$ at large μ as a is decreased, the behavior for $a < 2$ does not appear significantly different than for $a = 2$. As one approaches the Keplerian case, however, a sharp cusp develops in the growth rate curve at a thickness of $\mu \simeq 0.24$, where the growth rate momentarily reverses its decreasing trend. We interpret this feature as further evidence of a merger between the pure surface $\mathcal{P}$ mode and the higher-μ $\mathcal{R}$ mode, shown separately in Fig. 5.3a. We draw particular attention to the Keplerian curve, *since the corresponding growth rate in the hydrodynamic case is entirely negligible* (Jaroszyński 1988).

In contrast to the $\mathcal{P}/\mathcal{R}$ mode, the $\mathcal{A}$ mode growth rates are quite sensitive to the shear (Fig. 5.9b). The peak growth rate *increases* with decreasing a, and there are two particular values of a worth noting. The first is $a \simeq 1.6$, less than which the growth rate at $\mu \gtrsim 0.2$ exceeds that of the $\mathcal{P}/\mathcal{R}$ mode. The second is $a = a_c \approx 1.53985$, less than which $-\omega_I$ is nonzero even as $\mu \to 1$. This is an important result, as it shows that *Keplerian and near-Keplerian disks display a dynamically significant instability, independent of their radial extent.* The peculiar behavior of the $a < a_c$ cases turns out to be more a result of the particular k_z chosen here, than of the rotation law. This will become clear in §5.6.3.

While we have displayed the $\mathcal{P}/\mathcal{R}$ and $\mathcal{A}$ curves separately here for clarity, the situation is actually more complicated for $a < a_c$ (as already evinced by Fig. 5.4c). For these a, a further interaction occurs between all three modes, whereby the $\mathcal{A}$ and $\mathcal{P}$ modes merge, leaving the decoupled $\mathcal{R}$ mode alone at lower growth rate. This is shown in Figure 5.10, in which the merged $\mathcal{A}$ and $\mathcal{P}$ modes have almost identical real parts at $\mu \simeq 0.24$. This makes the argument for a mode exchange even more plausible, as does the fact that we find no modes other than those shown. Note that it is now the $\mathcal{R}$ mode that approaches $-\Omega_A$ as $\mu \to 1$. Recall that the $\mathcal{P}/\mathcal{A}$ mode was our prototype 3 in §5.5.2 (Fig. 5.4c). For completeness, we also display the Keplerian counterparts to the Fig. 2 growth rate curves in Figure 5.11. The critical Alfvén velocity for stability, $V_{z,crit} \simeq 1.2$ in this case.

5.6.2 Higher m modes

To examine the behavior of the unstable $\mathcal{P}/\mathcal{R}$ mode for higher azimuthal wavenumbers, the $m = 2$ equivalents of the Fig. 5.2 and Fig. 5.11 curves are plotted in Figure 5.12. For both $a = 2$ and $a = 1.5$, the instability is virtually suppressed for $V_z \gtrsim 1$, while in the former case the growth rate barely exceeds that of the hydrodynamic instability, even at its peak value ($\simeq 0.27$ for $V_z \simeq 0.1$).

The growth rates at higher m are shown in Figure 5.13 for $a = 2$, $a = 1.5$, $k_z = 1.5$ and $V_z = 0.3$. In the $a = 2$ case, it is seen that higher-m modes are stable for all but a small range of slender shells ($0.057 \lesssim \mu \lesssim 0.34$ for $m = 2$). The Keplerian shell is slightly more unstable (out to $\mu \simeq 0.8$ for $2 \leq m \leq 5$), but the growth rate dies off more quickly with increasing m than in the $a = 2$ case. Note also that the cusp in the curve disappears at the larger m values.

These results agree qualitatively with Fig. 5.13c, which shows the corresponding hydrodynamic behavior (see also Jaroszyński 1988). In the latter case, stabilization at larger μ occurs because the penetration depth for surface gravity waves decreases with increasing m. Thus the inner and outer modes become independent for high m (Blaes 1986). In the MHD case the same phenomenon occurs, but note that the critical μ for merger of $\mathcal{P}_1^-$ and

$\mathcal{P}_2^+$ is virtually *independent* of m. Another important qualitative difference is the fact that here *the fastest-growing mode is always* $m = 1$, whereas in the $a = 2$ hydrodynamic case maximum growth is found in the limit $m \rightarrow \infty$ (BG).

5.6.3 The effect of k_z and the high-k_z limit

Choosing $m = 1$ and $V_z = 0.3$ as fiducial values in this section, we now explore the effect of varying k_z on the unstable modes. Figure 5.14 shows the growth rate as a function of thickness for $0 \leq k_z \leq 14$, $a = 2$ (a) and $a = 1.5$ (b). Comparison of these curves with Fig. 5.2 indicates that the effect of increasing k_z is similar to that of increasing V_z, in that μ_{min} is a monotonically increasing function of both. However, with regard to the peak growth rate, the effect of large k_z is clearly very different. A qualitative change occurs between $k_z = 3$ and 5 in the $a = 2$ case, and $k_z = 1$ and 1.5 in the $a = 1.5$ case: the growth rate no longer vanishes at $\mu = 1$ for k_z values in excess of these. In fact, $-\omega_I$ appears to increase without bound as k_z is increased. At the same time, *only the most extended (large μ) configurations are unstable at large k_z.*

Fig. 5.14b shows that the anomalously large growth found in Fig. 5.4 for $a = 1.5$ may be regarded as a consequence of the value of k_z we chose (i.e. $k_z = 1.5$). In fact, *all* vertical wavenumbers of this magnitude and larger display growth out to $\mu = 1$. While Fig. 5.9b *appears* to indicate a critical value of a at which the large μ growth rate changes character, *it is really the fact that there exists a critical value of k_z for each value of a that causes the qualitative change in $-\omega_I$.* We have confirmed this by increasing k_z for each $a \neq 2$ shown in Fig. 5.9b, until a change in the inflection of the growth rate curve was observed. This critical k_z value increases with increasing a, but not drastically. By $k_z = 3$, all curves with $a \leq 1.85$ have the character of the $k_z \geq 1.5$ curves in Fig. 5.14b. *It is also at this critical k_z that the $\mathcal{R}$ and $\mathcal{A}$ modes exchange roles: the $\mathcal{R}$ and $\mathcal{P}$ modes decouple, while the $\mathcal{P}$ and $\mathcal{A}$ modes merge* (§5.6.1). The constant angular momentum case seems to be the only exception to this rule; as k_z is increased, the $a = 2$ $\mathcal{A}$ mode in Fig. 5.9b increases its growth rate, but never exceeds that of the $\mathcal{P}/\mathcal{R}$ mode, and never changes inflection.

The characteristic radii and eigenfunctions for a typical large k_z case are shown in Figure

15a and b.[4] The $a = 2$, $k_z = 5$ case is a good example of the enhanced growth which can result from a Type 3 interaction. The characteristic radii in Fig. 5.15a clearly identify it as Type 3, while Fig. 5.15b shows the behavior of the eigenfunctions. As expected, these are highly concentrated near r_1 and damped between $r_{A,2}$ and r_2. It is also important to note that significant growth occurs near μ_{min}, where neither $r_{A,1}$ nor $r_{A,2}$ lies within the shell. This indicates either that surface modes are still active for thinner shells, or that unstable coupling of pure Alfvén waves is occurring, or both. As μ_{min} increases (i.e. at larger k_z), the latter seems more likely.

Overall, the large k_z behavior is not unlike what happens in the $m = 0$ case (Ch. 3). There, the largest growth rates are found in the limit $k_z \to \infty$, $V_z \to 0$. However, the steady increase of μ_{min} with k_z was not found in the axisymmetric case, and is due to the consequent increase in Ω_A (§5.5.1, equation (5.12)).

In the limit $k_z r \gg m$, $m = O(1)$, the perturbation equation (5.3) simplifies considerably. Introducing the new dependent variable $\psi \equiv (r\tilde{\sigma}^2)^{1/2}\xi_r$ and noting that $k_z r \gg \omega/\Omega$ (the latter is $O(1)$; see Fig. 5.14), equation (5.3) becomes simply

$$\psi'' + k_z^2\left(2s\frac{\Omega^2}{\tilde{\sigma}^2} - 1\right)\psi = 0. \tag{5.13}$$

This is similar to the $m = 0$ perturbation equation [equation (3.36)], and can be solved by an identical WKB prescription. We have not done so but point out that, as some of the same numerical difficulties occur here as in the $m = 0$ problem (e.g. the extreme localization of eigenfunctions), a further examination of equation (5.13) would help clarify the large k_z behavior of the $m \neq 0$ instabilities.

Recall that the principal action of a nonzero k_z in the $V_z = 0$ problem is to stabilize those perturbations of the P mode having $k_z \gtrsim m/r_0$. In light of the above results, one might then ask: what is the critical value of V_z such that this behavior ceases, and allows such rapid growth at large k_z? We have examined this issue only for $a = 2$, finding that the critical value lies somewhere between $V_z = 0.02$ and 0.03. Thus, even very weak fields can reverse the stabilizing trend of k_z. One might imagine that the effect of a finite but small

---

[4] We take "large k_z" to mean values such that large growth occurs as $\mu \to 1$, and such that the eigenfunctions are highly localized. The present example clearly shows that k_z need not be very large to achieve both of these goals.

V_z on the hydrodynamic fluid is to create a field line tension that prohibits z-dependent motions induced by nonzero k_z. This behavior is not surprising in light of the fact that the VC instability is most powerful in the weak-field limit (Ch. 3).

Finally, we performed calculations in which *both* m and k_z are large, finding that although μ_{min} can be decreased, the growth rates are also substantially reduced. Hence, this extremely localized mode is probably of little interest.

5.6.4 Rigidly-bounded configurations

As a final check of the results and their interpretation, we have attempted to find unstable modes for rigid boundary conditions. We failed to find the $\mathcal{P}$ mode for any range of parameters examined in the previous sections. This makes sense since it is primarily a surface mode. However, an instability with similar properties to the $\mathcal{R}$ mode was detected. In Figure 5.16a, b we plot the characteristic radii and eigenfunctions of this mode for $a = 2$, $k_z = 1.5$. Clearly, a rigid outer boundary is nearly as effective at reflecting internal waves as a step function in density (i.e. a free boundary). This is indeed expected from work on sonic instabilities in shear flows (Glatzel 1988). The $\mathcal{A}$ mode does not appear in the rigidly bounded case until rather large k_z ($\simeq 5$ for $a = 2$), where it is of Type 2 (i.e. damping at $\mu = 1$). One needs $k_z \gtrsim 7$ ($a = 2$) to obtain Type 3 growth, and this only occurs for $\mu \gtrsim 0.85$. Thus, it appears that the $m \neq 0$ unstable modes for rigid boundary conditions are much like their $m = 0$ counterparts, with considerably smaller growth rates. For example, $-\omega_I \simeq 0.38$ for $\mu = 0.96, a = 2$, and $k_z = 7$, versus $-\omega_I \simeq 1.62$ for the same parameters when $m = 0$.

5.6.5 Configurations with no external field

In some sense the opposite of the rigid boundary situation is one in which the external field is removed (i.e. $\chi_i = \chi_o = 0$). Indeed, a recent paper by Coleman, Kley, and Kumar (1995) has assumed just such a boundary condition, namely, that the total pressure vanishes on the boundaries. The resulting configuration is somewhat worrysome, however, as it implies a nonzero surface current $\mathbf{J}_S$ on the boundaries; i.e.

$$\mathbf{J}_S = \frac{B_z}{4\pi}\hat{\phi}.$$

This represents a Lorentz force, $\mathbf{F}_S = \mathbf{J}_S \times \mathbf{B}$, in the $\hat{\mathbf{r}}$ direction. In the equilibrium, $\mathbf{F}_S$ can be balanced by the central gravity and/or pressure gradients, but in the perturbations it is an unbalanced force. This is a concern when performing stability analysis, since it presents an additional avenue for instability.

Numerical solutions for the case of vanishing external field are shown in Figure 5.17 for the Keplerian case with $m = 1$, $k_z = 1.5$, and a range of V_z. The most striking quality of this graph is the fact that for $V_z \leq 1.15$, the growth rate is *independent of* μ *as* $\mu \longrightarrow 0$. That is, the zero-thickness cylinder is highly unstable! We have found similar behavior in the axisymmetric case, with almost identical growth rates as $\mu \longrightarrow 0$. This is sensible, since the mechanism described above should be independent of the nature of the perturbation. In our view, the instability is unphysical and is entirely the result of an unrealistic boundary condition. It is interesting that the growth rate curves do approach zero at small μ when V_z exceeds 1.15; this is very near the critical V_z for stability indicated in Fig. 5.11, and in the axisymmetric case (Ch. 3).

5.6.6 Critical field strengths for stability

The results of §5.4 indicate the existence of a definite limit $\mu = \mu_{min}$ below which magnetized disks are stable to $m \neq 0$ perturbations. Here we investigate the dependence of this property on k_z, V_z, and a. The problem can be converted into a somewhat more familiar one by thinking of V_z *as a function of* μ_{min}. Then V_z represents the critical field above which a disk of radial scale μ_{min} is stable to $m \neq 0$ perturbations (§3.5.5).

Figure 5.18 shows the dependence of V_z on μ_{min} for four different k_z (0.5, 1.5, 5, and 13) and the extreme values $a = 1.5$ and $a = 2$. The critical Alfvén speed for stability can be read off the graph for a given thickness. Models lying above a given curve are stable to the $m = 1$ magnetic instability. Following §3.5.5, one may interpret the inverse of the wavenumber $\lambda = 2\pi/k_z$ as a critical wavelength above which unstable perturbations no longer fit inside a disk of scale height H $(= \lambda/2)$. The scale heights defined in this manner also appear on the graph.

Comparison with Fig. 3.8b (for $k_z \to 0$) and Table 3.2 shows that there is qualitative agreement between the $m = 1$ and $m = 0$ critical stability curves. However, disks large in both radial (large μ_{min}) and vertical (small k_z) dimension appear more unstable to $m \neq 0$ modes than to $m = 0$ ones. The higher m curves tend to have larger V_z for a given a, k_z, and μ_{min} and are therefore more unstable in this sense. However, as their growth rates are considerably smaller (Fig. 5.13), we do not trouble with them further.

5.7 Discussion and summary

In many respects, the additional freedom allowed the incompressible cylinder by the internal Alfvén modes makes it similar to the compressible, nonmagnetized cylinder. Glatzel (1987a) showed that the growth of the PP instability in the latter system is maintained out to $\mu \to 1$ by mergers of neutral sonic modes, beyond the range of μ where the P mode (due to surface gravity waves) is unstable (this behavior was found in the $a = 2$ case only). In both systems, resonant interactions between surface modes and internal modes can occur. Glatzel (1987b) examined the issue in some detail, and was able to attribute particular unstable bands to these wave-wave interactions.

In the case of only two waves attaining resonance, linear theory can be used to predict instability on the basis of energy considerations alone. Applying well-known results of plasma physics, Cairns (1979) showed that a class of fluid instabilities (among them Kelvin-Helmholtz instability) are produced by the coalescence of positive and negative energy modes.[5] Modes of the same sign in energy produce an avoided crossing in frequency space, while independent modes (such as P_1^- and P_2^+ in the decoupled hydrodynamic case; Appendix) merely cross [see Fig. 3 of Cairns (1979)]. Applying these arguments, Glatzel (1987b) was able to define a canonical energy for the waves and show that the relative signs of the P_1^- and P_2^+ modes concur with this description. Unfortunately, this approach requires an analytic expression for the dispersion relation of the waves, which has not yet

---

[5] A wave has negative energy if the total energy of the system is lowered in the process of exciting the wave.

	Type 1	*Type 2*	*Type 3*
$\mathcal{P}^a$	No	No	No
$\mathcal{A}$	No	Yes; k_z small	Yes; k_z large
$\mathcal{R}$	Yes	No	No

[a] The $\mathcal{P}$ mode is a surface mode that does not depend on the location, nor indeed the existence, of Alfvén resonances.

Table 5.1: Classification scheme for the $m \neq 0$ unstable modes.

been obtained in the MHD problem. In addition, the results of §5.6.1 are suggestive of mode interactions between *more than two waves at one time*, e.g. the exchange that occurs between the $\mathcal{P}/\mathcal{R}$ and $\mathcal{P}/\mathcal{A}$ modes at larger values of k_z. Nevertheless, we feel that this is an approach worth pursuing, especially as it may yield physical insight not obtainable from the numerical solutions alone.

In closing, we have demonstrated the existence of globally unstable, nonaxisymmetric modes in incompressible MHD cylinders and, by extension, in astrophysical disks. There are three classes of unstable modes and three basic mechanisms for instability, which are summarized in Table 5.1. For radially extended configurations, the largest growth rates are obtained in the $k_z r_0 \gg m$ limit, as claimed by Balbus & Hawley (1992) and as found for the VC instability (Ch. 3). In more slender systems, however, the surface wave PP instability can maintain growth at considerably larger growth rates than for $m = 0$. This is even true in the Keplerian case, which is *stable* to the purely hydrodynamic PP mode.

In the context of the simple model adopted here, our results show that the PP instability is certainly *not* stabilized by a weak vertical magnetic field. Rather, the principal mode instability is enhanced, and entirely new modes of instability crop up. Stronger fields can stabilize disks of small radial and vertical extent, however, and this may be important in certain contexts such as protostellar or AGN disks with centrifugally-driven outflows (and the strong fields necessary to drive them). Since the instability acts for all allowable angular momentum distributions, both thick (i.e. radiation pressure supported and ion tori) and thin disks will be equally affected.

Appendix:
The Hydrodynamic Limit–Surface Gravity Waves

In order to describe the often complicated interactions between two or more neutral modes (cf. Craik 1985), a common technique is to examine the behavior of each mode in isolation, if possible. This has been successfully applied to the problem of nonradial stellar oscillations, e.g., by Aizenman, Smeyers, & Weigert (1977). One generally proceeds by omitting terms in the normal mode equations that correspond to particular physical effects associated with individual modes. BG and GGN achieved this in the simple problem considered in §5.2 by removing the inner boundary to $r = 0$ and the outer boundary to $r = \infty$ in turn, thereby decoupling the P_1 and P_2 modes.

Perturbations of the incompressible, constant angular momentum cylinder are governed by the equation (BG; Jaroszyński 1988)

$$W'' + \frac{W'}{r} - \left(\frac{m^2}{r^2} + k_z^2\right) W = 0, \tag{A.1}$$

where $W = \delta p/\rho\sigma$ is a perturbed velocity potential (§2.5.5). The general solution of equation (A.1) is

$$W(\varpi) = AI_m(\varpi) + BK_m(\varpi), \tag{A.2}$$

where $\varpi \equiv k_z r$ and A and B are constants of integration. The free boundary condition in this case is

$$\sigma^2 W + g_{eff} W' = 0 \quad \text{at} \;\; r = r_{1,2}. \tag{A.3}$$

Substituting (A.2) into (A.3) gives a 2×2 linear system whose vanishing determinant requires

$$\begin{aligned} &[\sigma_1^2 I_m(\varpi_1) + k_z g_1 \dot{I}_m(\varpi_1)][\sigma_2^2 K_m(\varpi_2) + k_z g_2 \dot{K}_m(\varpi_2)] \\ -&[\sigma_1^2 K_m(\varpi_1) + k_z g_1 \dot{K}_m(\varpi_1)][\sigma_2^2 I_m(\varpi_2) + k_z g_2 \dot{I}_m(\varpi_2)] \;\; = \;\; 0, \end{aligned} \tag{A.4}$$

where $\sigma_{1,2} \equiv \omega + m\Omega_{1,2} = \omega + mr_{1,2}^{-2}$, $g_{1,2} \equiv g_{eff}(r_{1,2})$, and an overdot denotes $d/d\varpi$.

Equation (A.4) is a 4th-order dispersion relation in the frequency ω. While an exact analytic solution can be derived, the roots are complicated and give little insight. Equation

(A.4) has been solved numerically by Jaroszyński (1988), and analytically by BG in the limits $k_z = 0$ and $m \rightarrow \infty$.

Following BG, an alternative approach is to consider simplified forms of the dispersion relation in the limits $r_1 \rightarrow 0$ and $r_2 \rightarrow \infty$. Taking the latter, e.g., implies $I_m \rightarrow \infty$ so we require $A = 0$ for a regular solution at infinity. Equations (A.2) and (A.3) then give

$$\sigma_1^2 K_m(\varpi_1) + k_z g_1 \dot{K}_m(\varpi_1) = 0,$$

which is easily solved for ω to yield

$$\omega_1 = -m\Omega_1 \pm \left[-k_z g_1 \frac{\dot{K}_m(\varpi_1)}{K_m(\varpi_1)}\right]^{1/2} .$$

Use of the identity $\dot{K}_m = -\frac{m}{\varpi} K_m - K_{m-1}$ then leads to equation (5.1). Taking $r_1 \rightarrow 0$ and r_2 finite, an identical procedure leads to equation (5.2). Equations (5.1) and (5.2) describe *stable* waves propagating along the inner and outer surfaces, respectively. They are a good approximation to the actual mode structure of two interacting surface modes except near a mode crossing (Fig. 5.1; Glatzel 1987b, 1988).

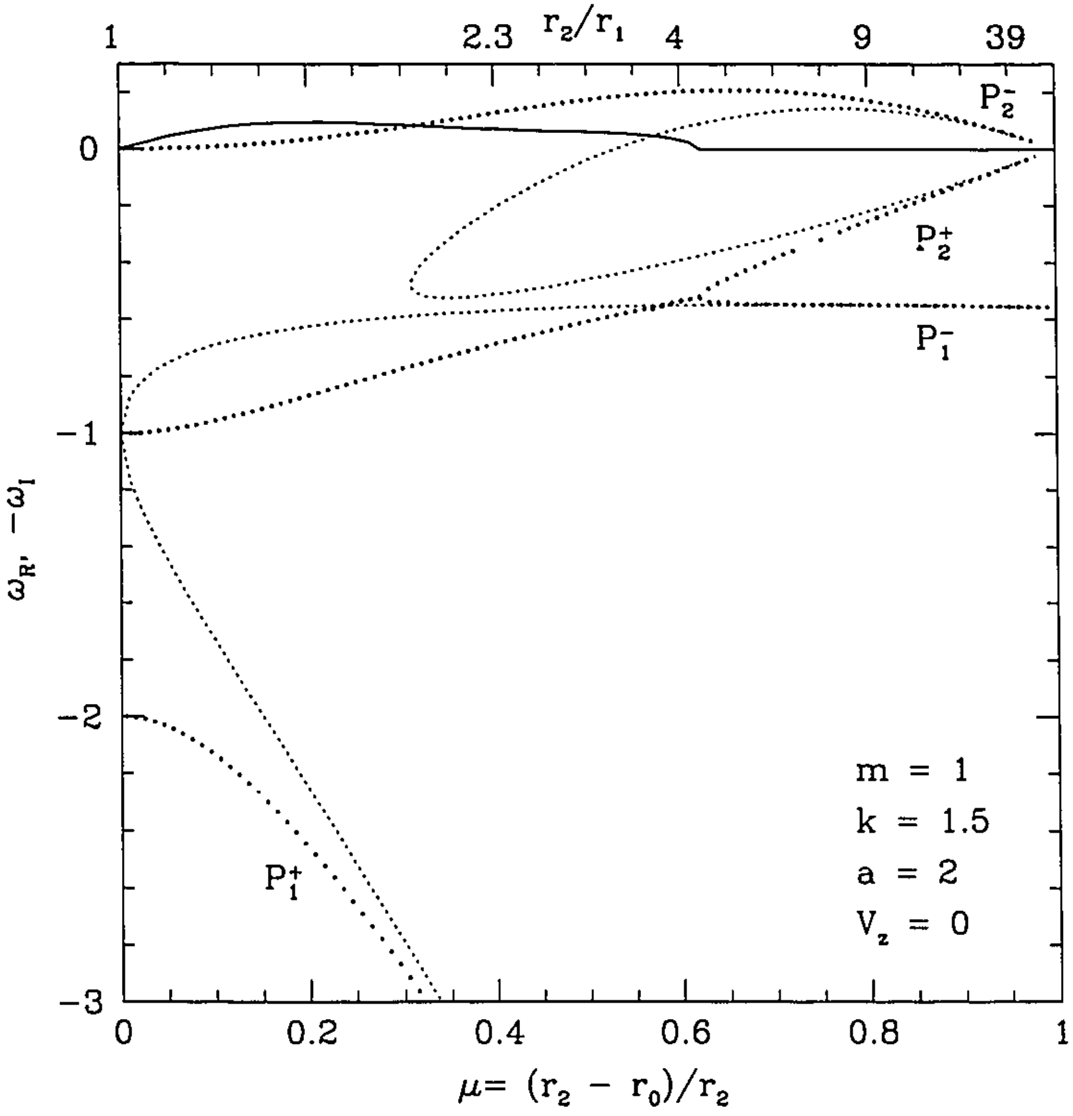

Figure 5.1: Hydrodynamic $m \neq 0$ mode structure. Each μ corresponds to a constant angular momentum shell of a given thickness. Solid line is the growth rate, $-\omega_I$, dots are ω_R, dotted line is ω as given by equations (5.1) and (5.2). Distinct modes are labelled according to text.

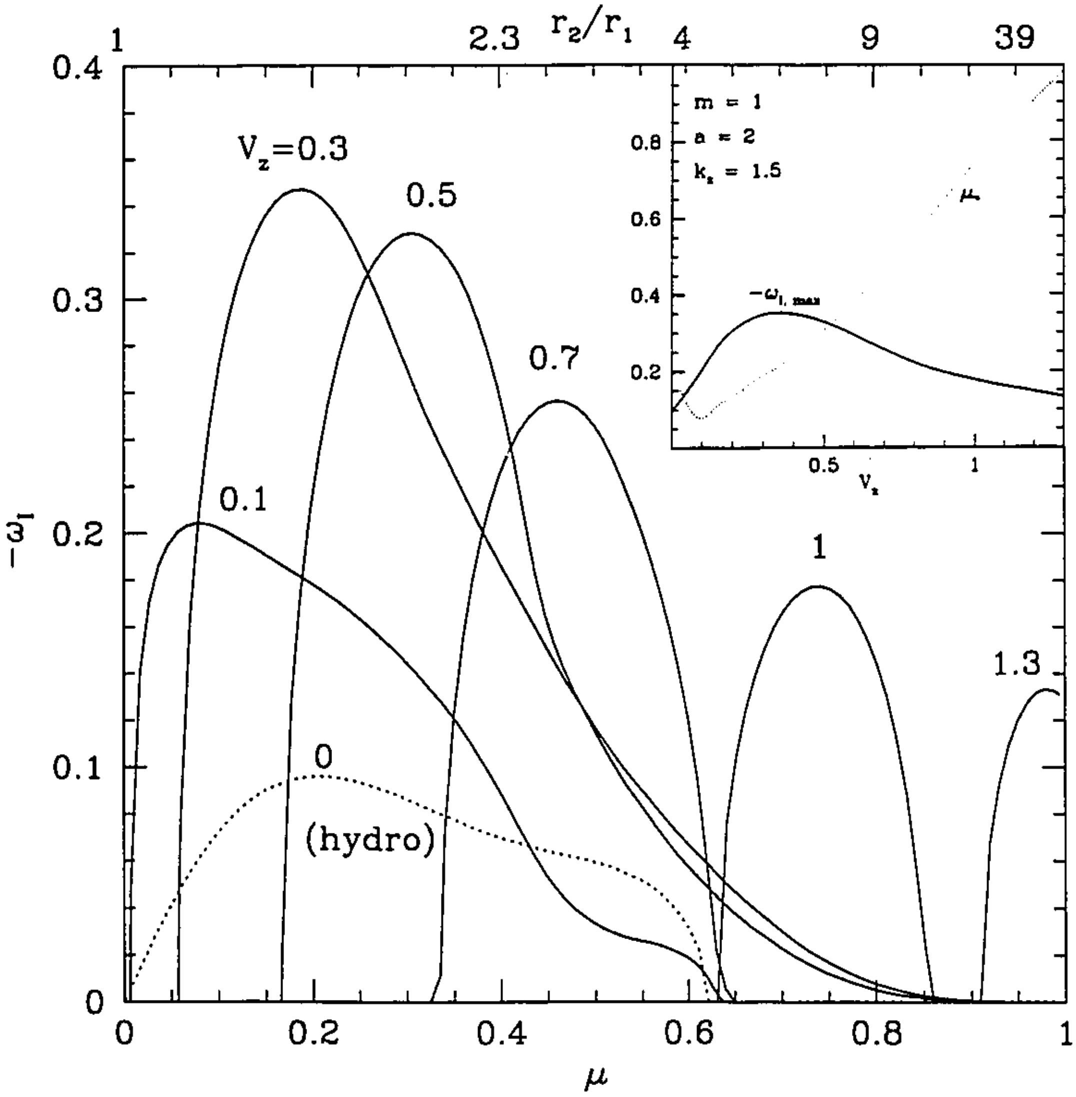

Figure 5.2: Growth rates of the $m \neq 0$ MHD instability as a function of μ for a range of V_z. Hydro case is shown by the dotted line. *Inset*: Solid curve is the peak growth rate, $-\omega_{max}$, as a function of V_z. Dotted curve is the thickness, $\mu = \mu_*$, at which $-\omega_{max}$ occurs.

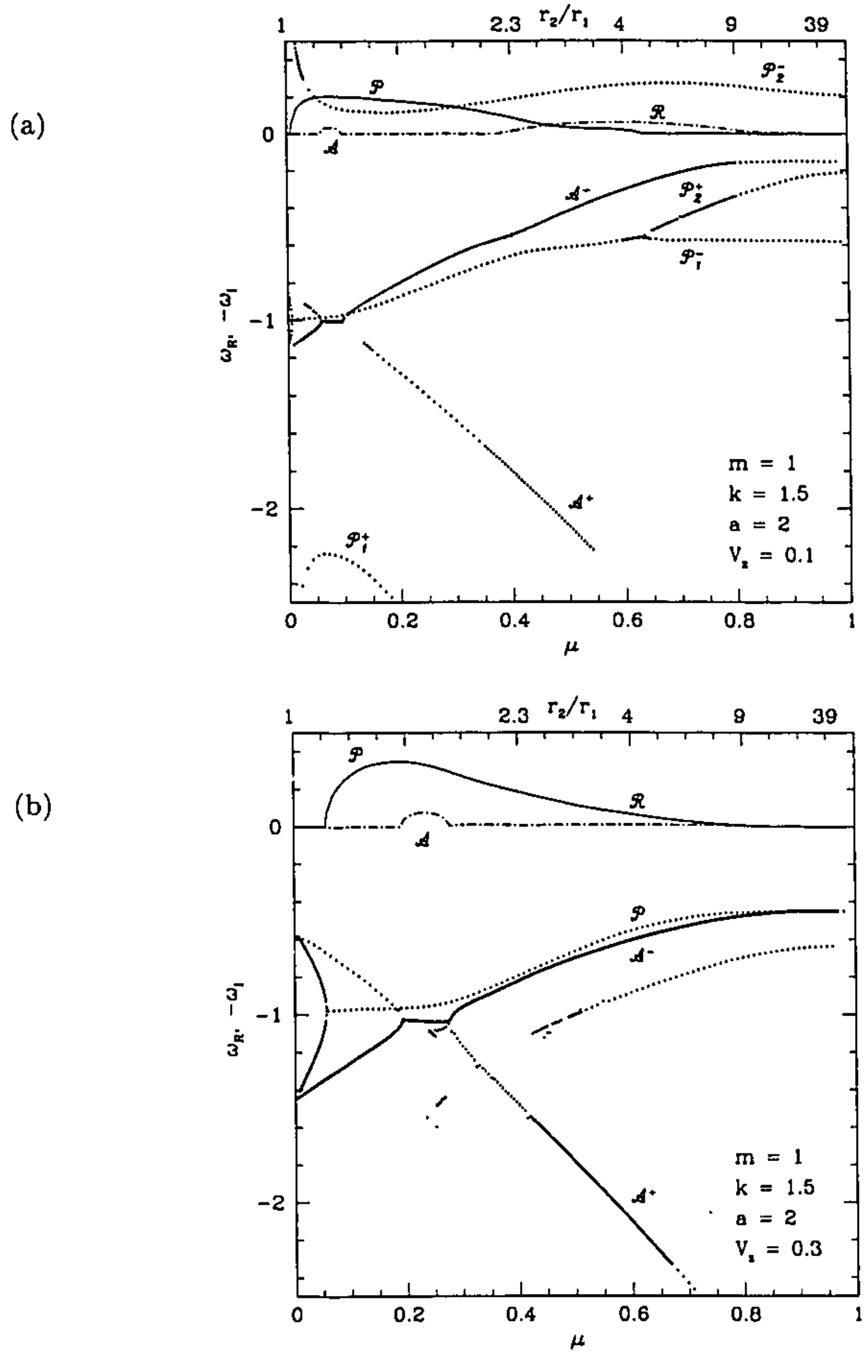

Figure 5.3: Mode structure in different field-strength regimes: (a) $V_z = 0.1$; (b) $V_z = 0.3$; (c) $V_z = 0.7$ (next page). Dots are eigenfrequencies, ω_R, of distinct modes as labelled in the text. Solid and dot-dashed lines are corresponding growth rates, $-\omega_I$, as labelled. + superscripts refer to downstream modes, − to upstream.

Fig. 3(c)

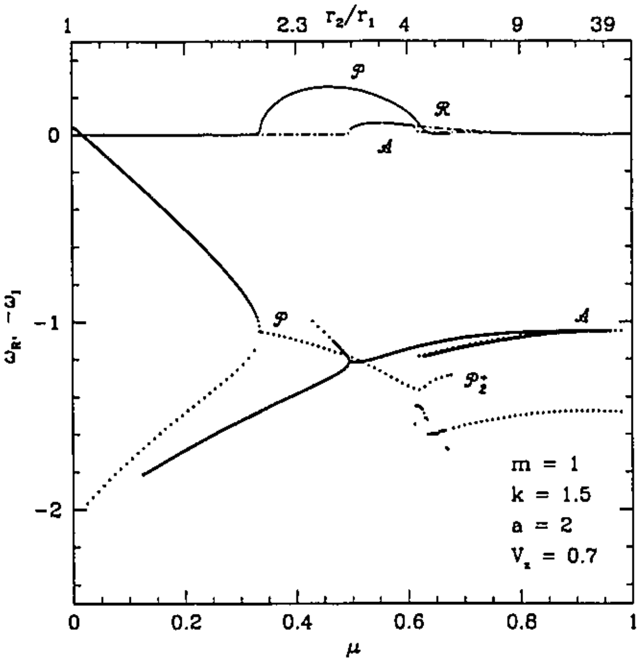
1
2.3
r_2/r_1
4
9
39
$\mathcal{P}$
$\mathcal{R}$
$\mathcal{A}$
0
-1
-2
$\omega_R, -\omega_I$
$\mathcal{P}$
$\mathcal{A}$
$\mathcal{P}_2^+$
m = 1
k = 1.5
a = 2
V_z = 0.7
0
0.2
0.4
0.6
0.8
1
μ

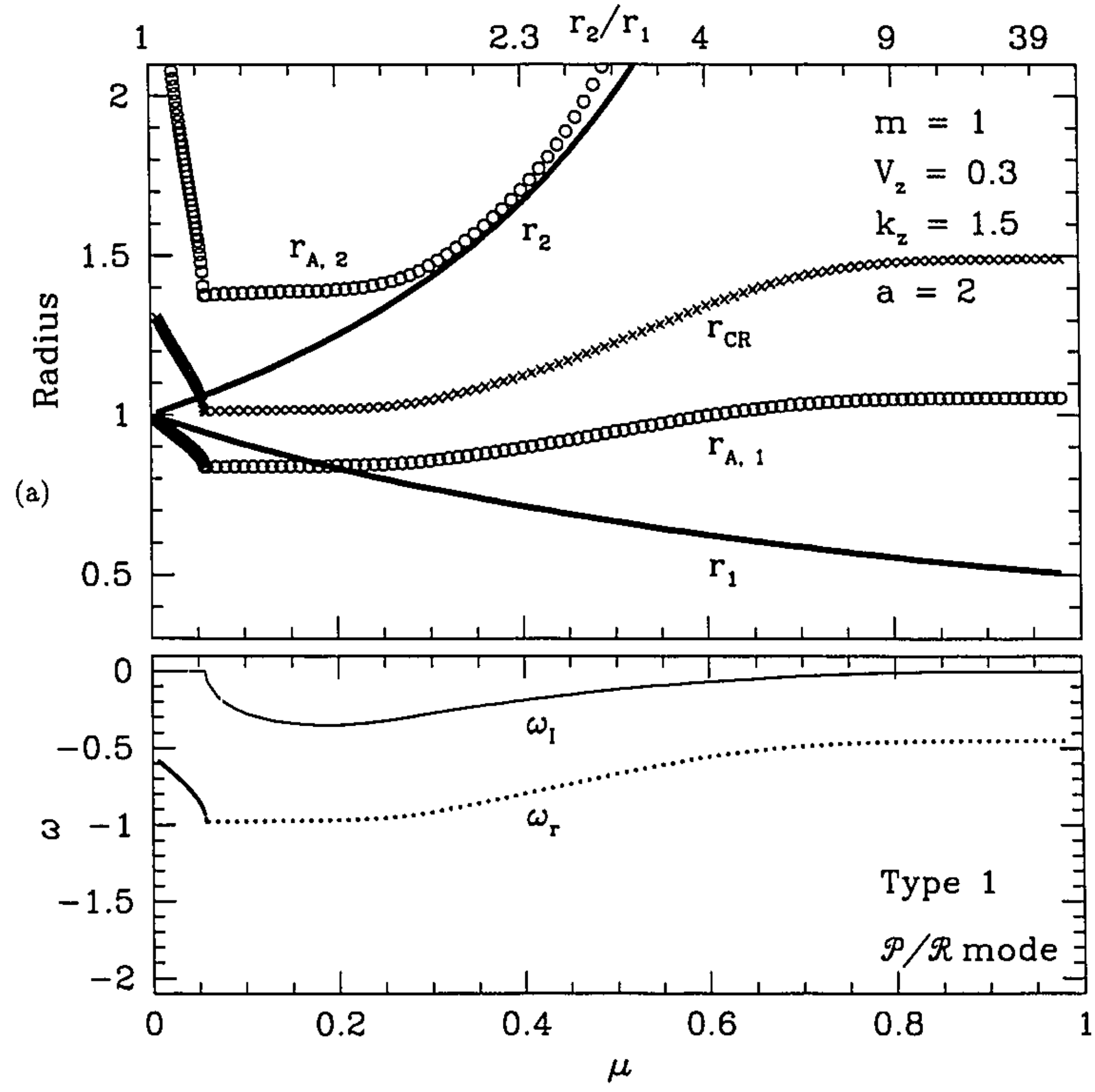

Figure 5.4: *Top panel:* Characteristic radii $r_{A,1}$ (inner Alfvén radius), $r_{A,2}$ (outer Alfvén radius), and r_{CR} (corotation radius) versus thickness, μ. The heavy lines are the inner (r_1) and outer (r_2) radii of the shell. *Lower panel:* Real and imaginary parts of the eigenfrequency as a function of μ for the same parameters as in top panel. (a) (this page) Type 1 behavior; (b) (next page) Type 2 behavior; (c) (following page) Type 3 behavior.

Fig. 4(b)

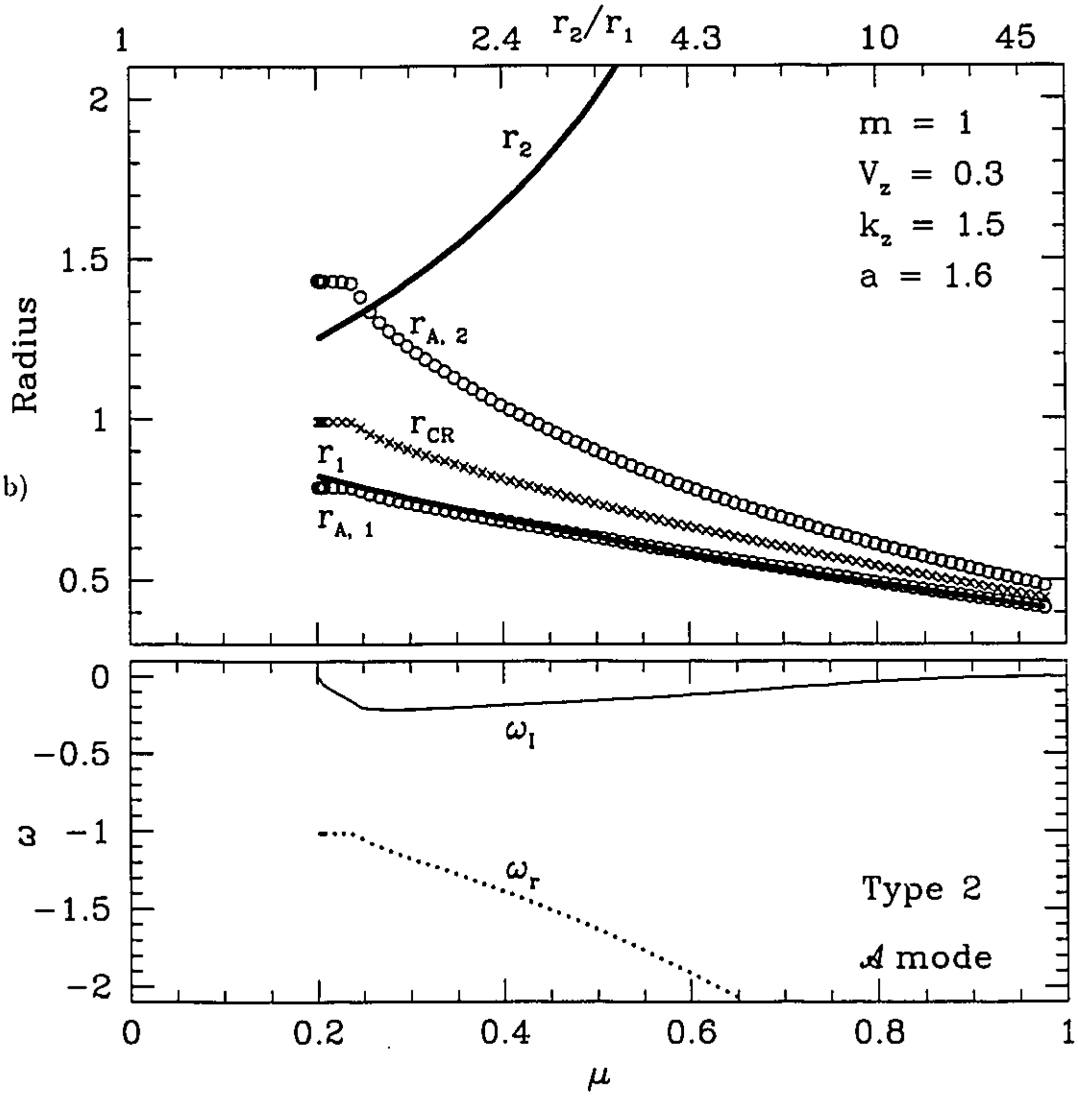
r₂/r₁
1
2.4
4.3
10
45
Radius
2
1.5
1
0.5
r₂
r_A, 2
r_CR
r₁
r_A, 1
m = 1
V_z = 0.3
k_z = 1.5
a = 1.6
ω
0
−0.5
−1
−1.5
−2
ω_I
ω_r
Type 2
𝒜 mode
0
0.2
0.4
0.6
0.8
1
μ

Fig. 4(c)

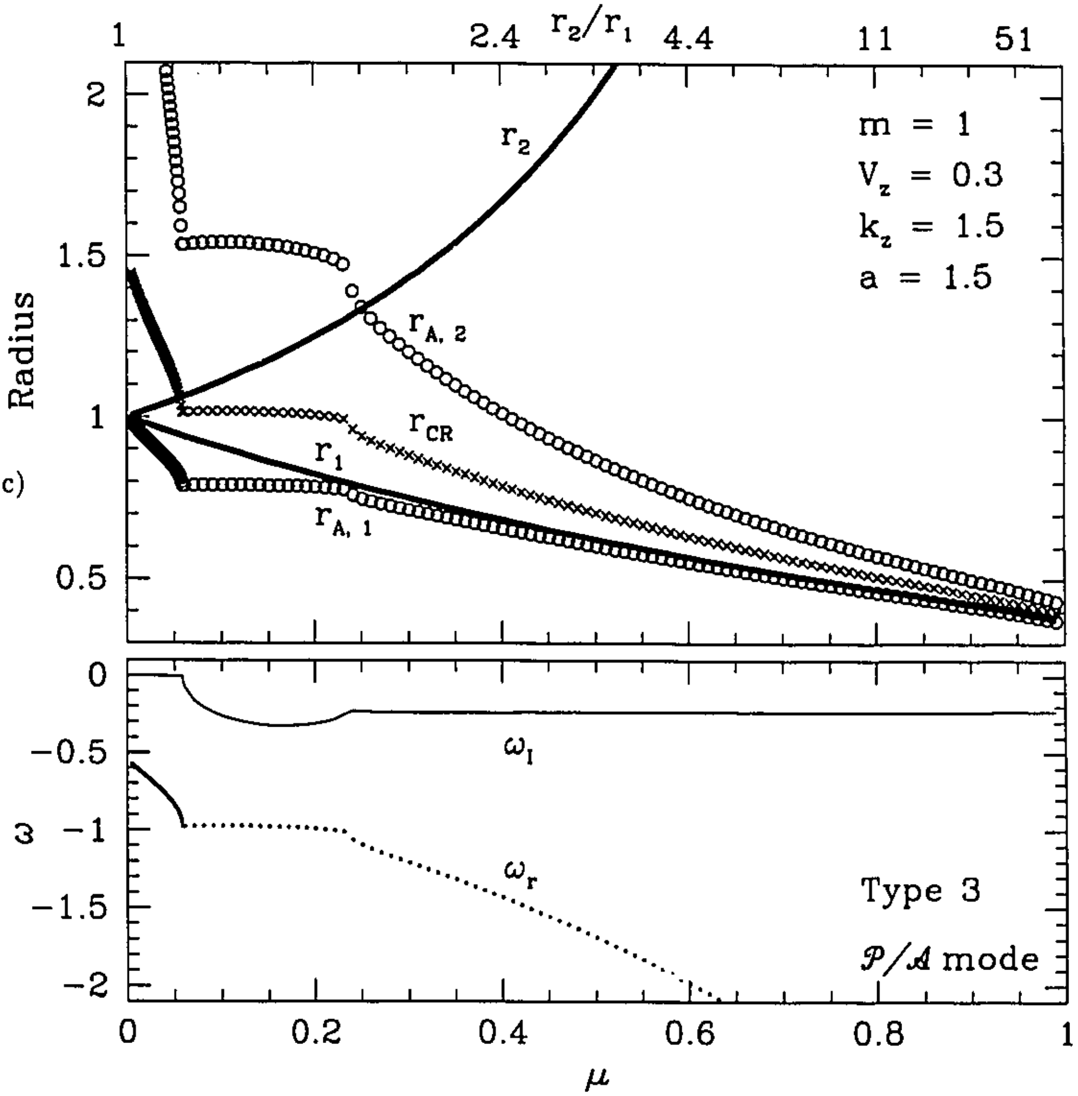
r_2/r_1
1
2.4
4.4
11
51
Radius
2
1.5
1
0.5
r_2
$r_{A,2}$
r_{CR}
r_1
$r_{A,1}$
m = 1
V_z = 0.3
k_z = 1.5
a = 1.5
ω
0
−0.5
−1
−1.5
−2
ω_I
ω_r
Type 3
𝒫/𝒜 mode
0
0.2
0.4
0.6
0.8
1
μ

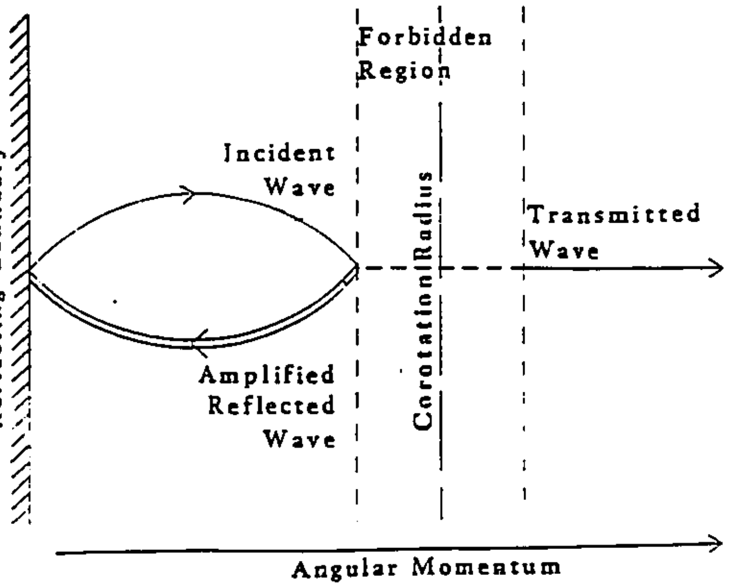

Figure 5.5: The phenomenon of over-reflection. Within the "forbidden region" the perturbations are evanescent, while outside this region they have a wave-like character. It is the interaction of these waves across the corotation radius that drives the instability (Blaes 1986).

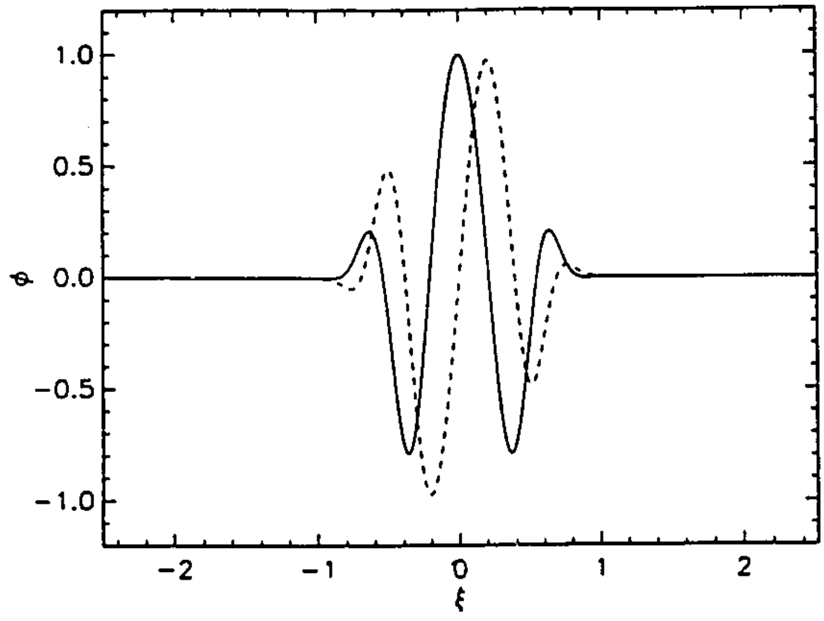

Figure 5.6: Localized eigenfunctions of the $m \neq 0$ mode, as found by Matsumoto & Tajima (1995). Their model parameters are: $a = 1.5$, $\Omega_A = k_z V_z = 0.1\Omega$, $k_y^2/k_z^2 = 0.01$ (k_y is the Cartesian version of m in their shearing-sheet model). The corresponding growth rate is $\omega = 0.0357\Omega i$; MT find $\omega_R = 0$ in this high k_z limit. The abscissa, $\xi = 2Ak_y x/\Omega_A$, where $A = 3\Omega/4$ is the local shear rate (Oort constant).

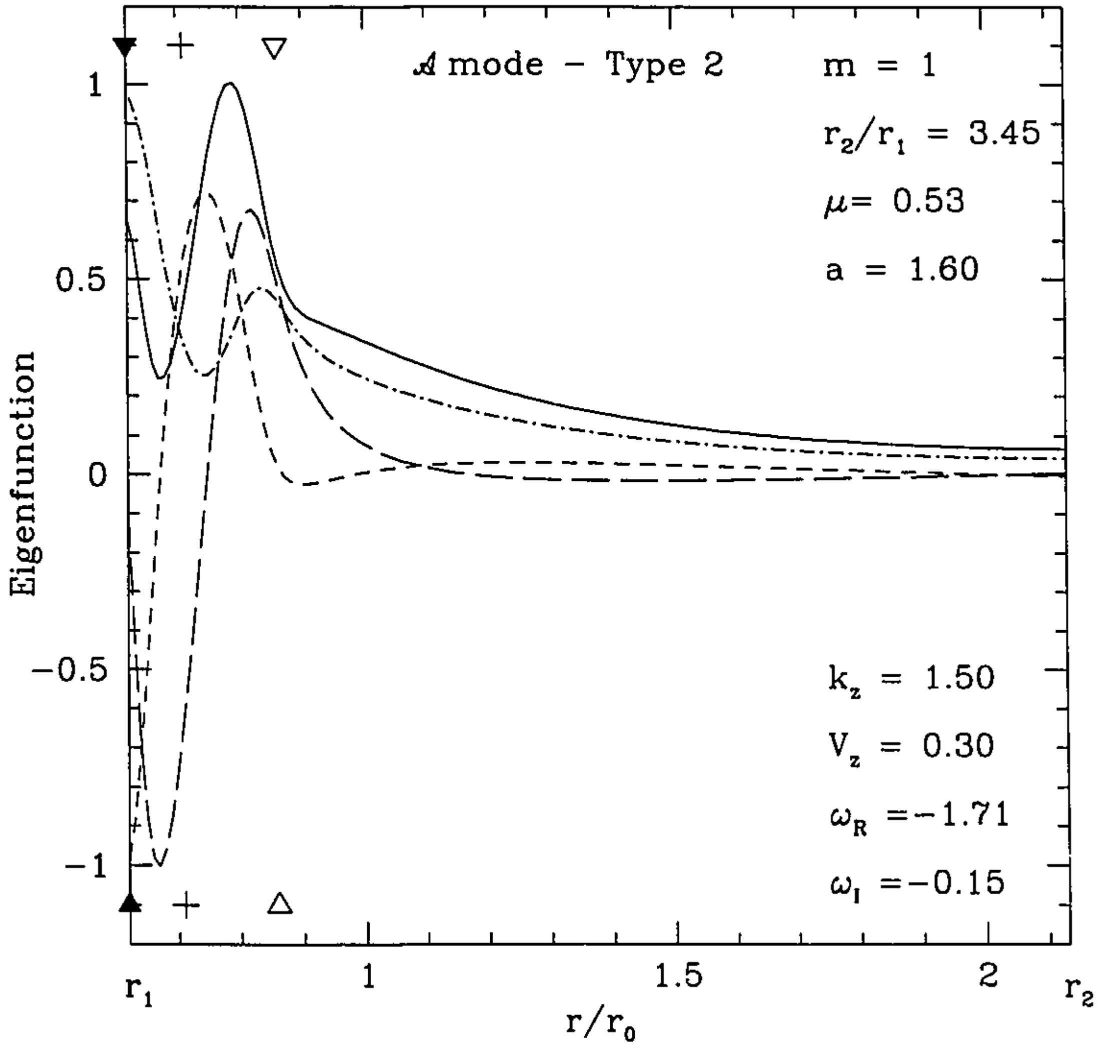

Figure 5.7: Eigenfunctions of a Type 2 mode. Plotted are the real (subscript R) and imaginary (subscript I) parts of the radial velocity (δu_R, solid; δu_I, dot-dashed) and total (gas + magnetic) enthalpy (δh_R, short dashed; δh_I, long dashed), normalized to unity. The symbols at top and bottom mark the characteristic radii: $r_{A,1}$ (solid arrowhead), r_{CR} (cross), and $r_{A,2}$ (open arrowhead).

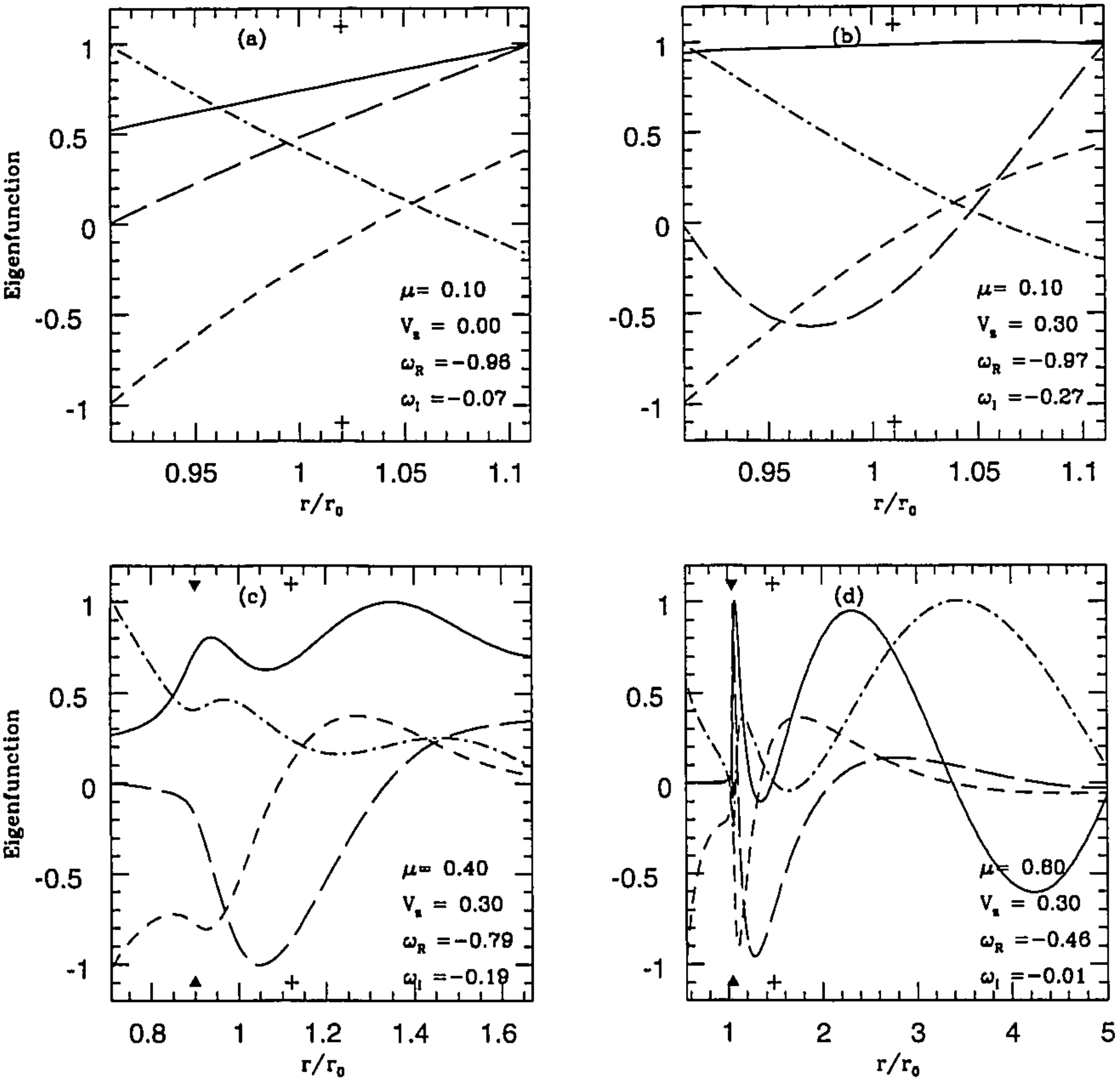

Figure 5.8: Eigenfunctions of the $\mathcal{P}/\mathcal{R}$ mode for the hydro case (a) and the magnetic case ($V_z = 0.3$) with three different μ: (b) $\mu = 0.1$; (c) $\mu = 0.4$; (d) $\mu = 0.8$. All plots are for $m = 1$, $a = 2$. Other conventions are the same as in Figure 5.7

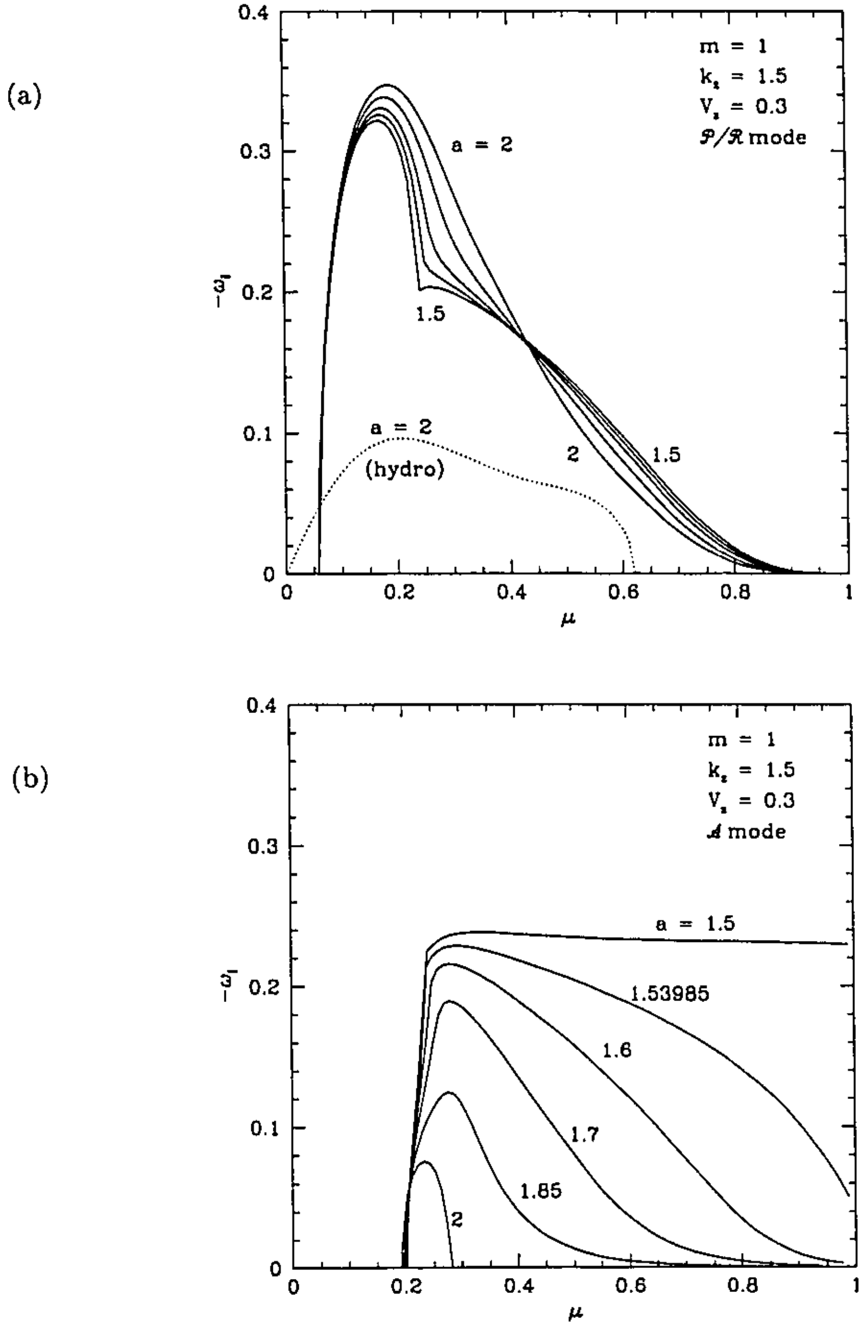

Figure 5.9: The effect of rotation law on growth rates of the (a) $\mathcal{P}/\mathcal{R}$ and (b) $\mathcal{A}$ modes.

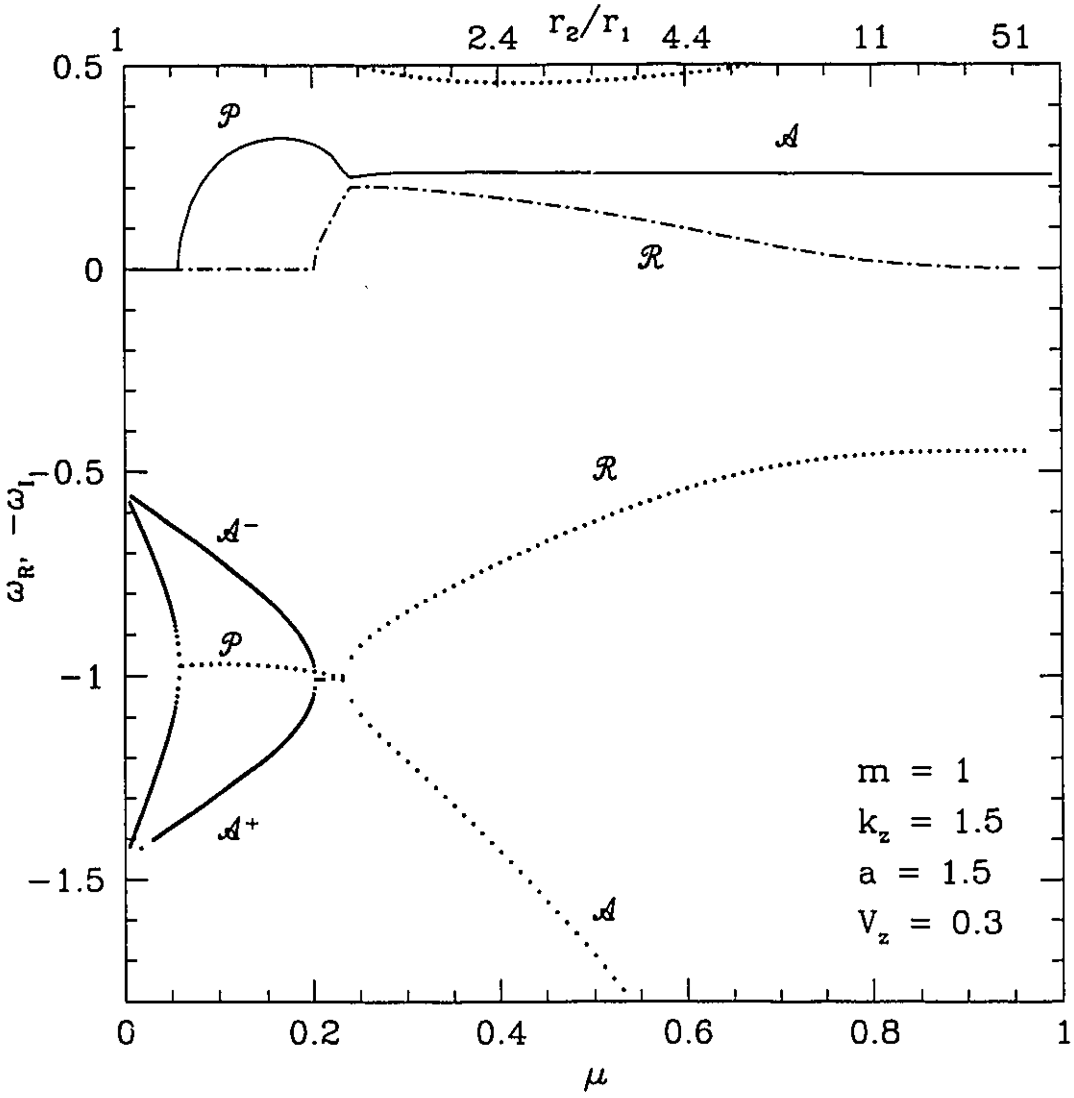

Figure 5.10: Mode Structure in the Keplerian case. Conventions are the same as in Figure 5.3.

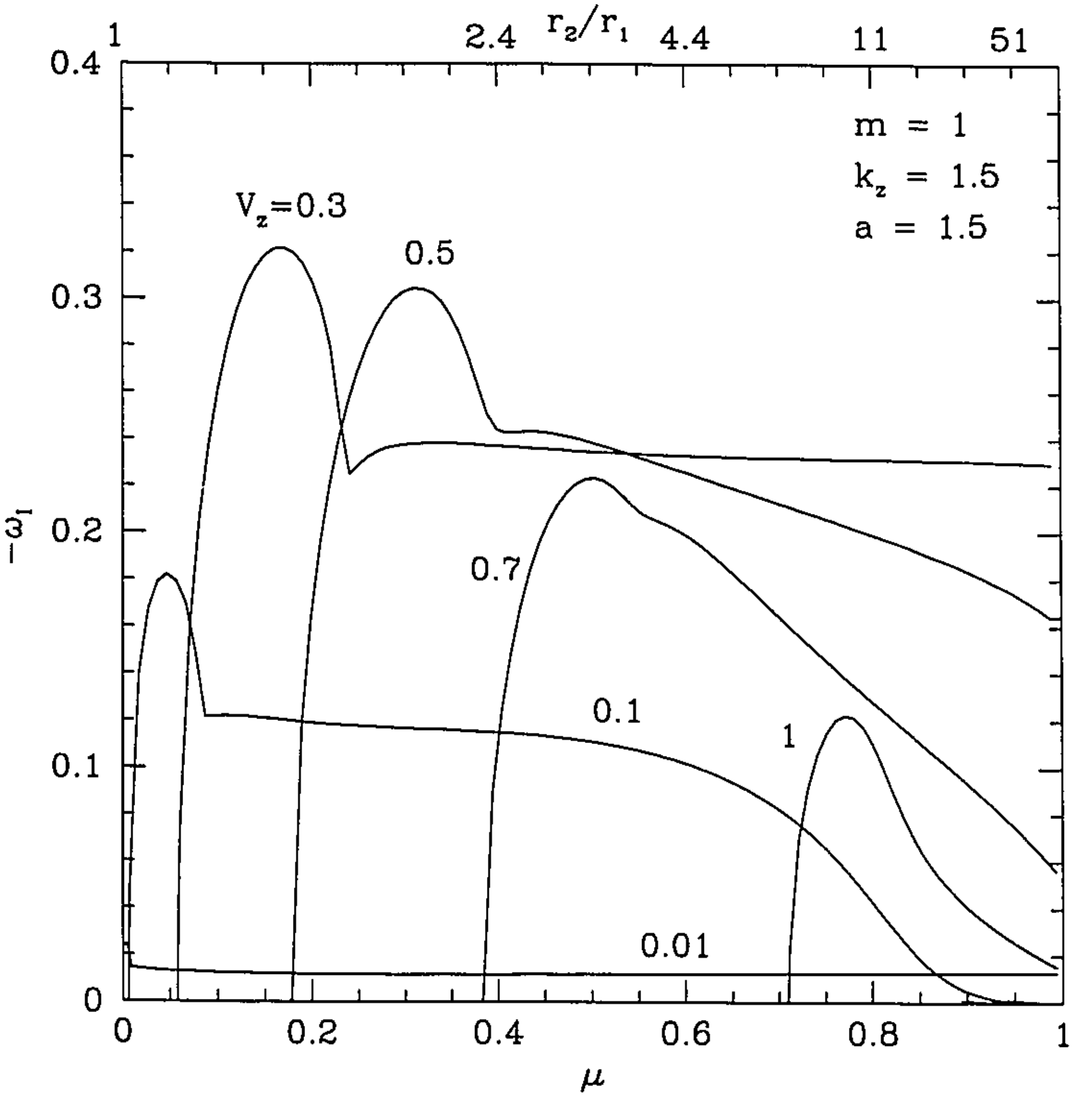

Figure 5.11: Growth rates for a range of V_z in the Keplerian case. This figure is the $a = 1.5$ counterpart of Figure 5.2.

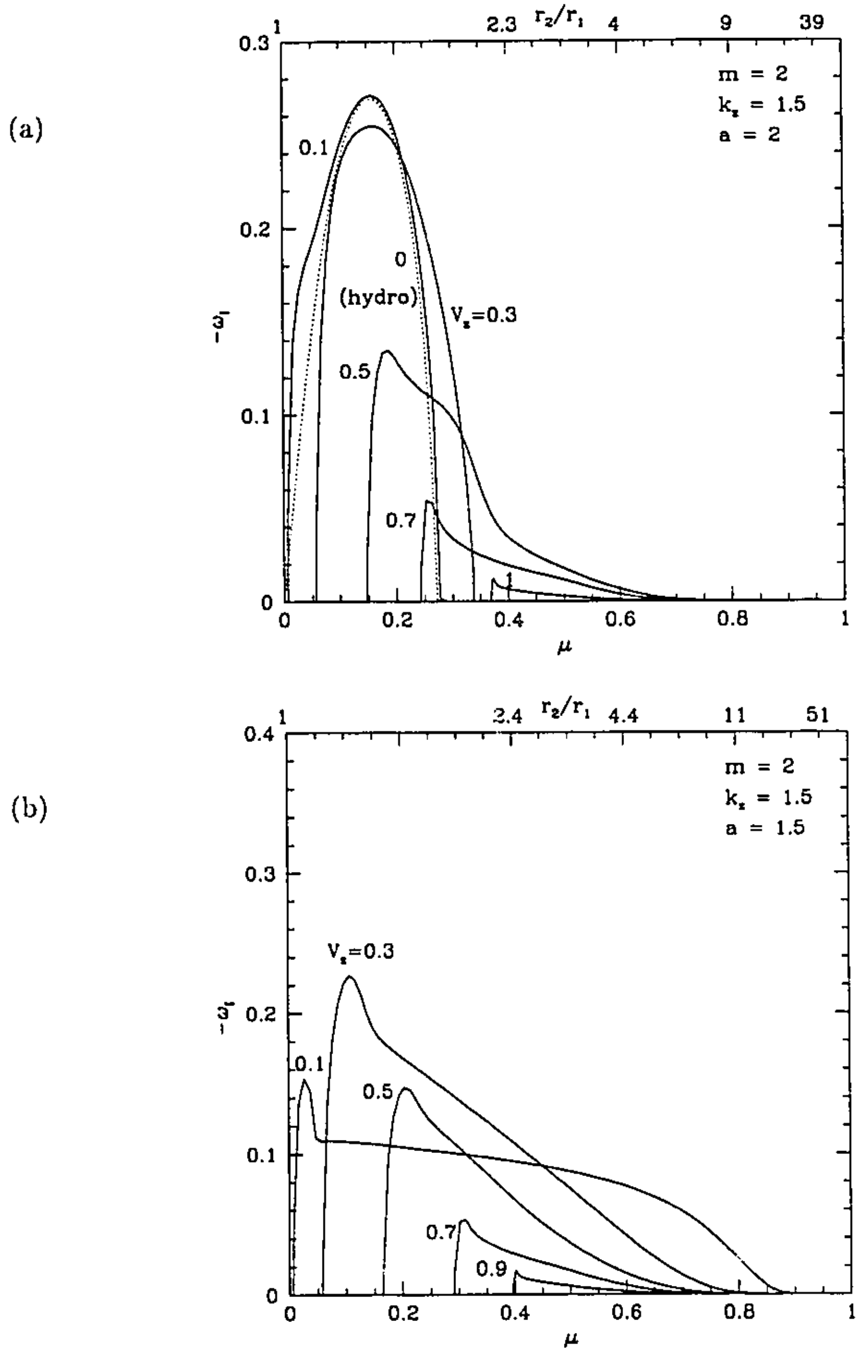

Figure 5.12: Growth rates for $m = 2$, a range of V_z, and (a) $a = 2$; (b) $a = 1.5$. Dotted line in (a) is the hydro ($V_z = 0$) case.

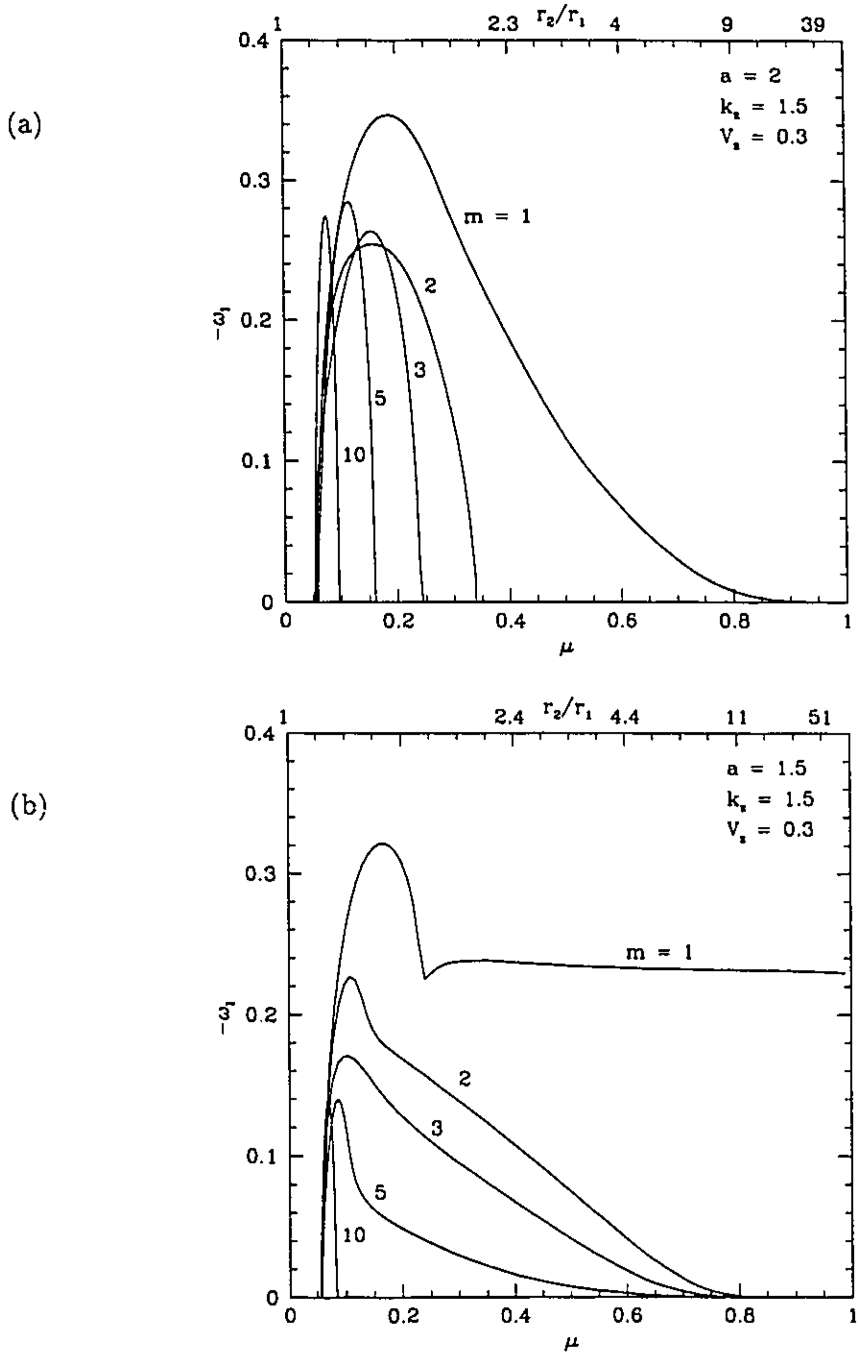

Figure 5.13: Growth rates for higher m, $V_z = 0.3$, and (a) $a = 2$; (b) $a = 1.5$; (c) $a = 2$, hydro case (next page).

Fig. 13(c)

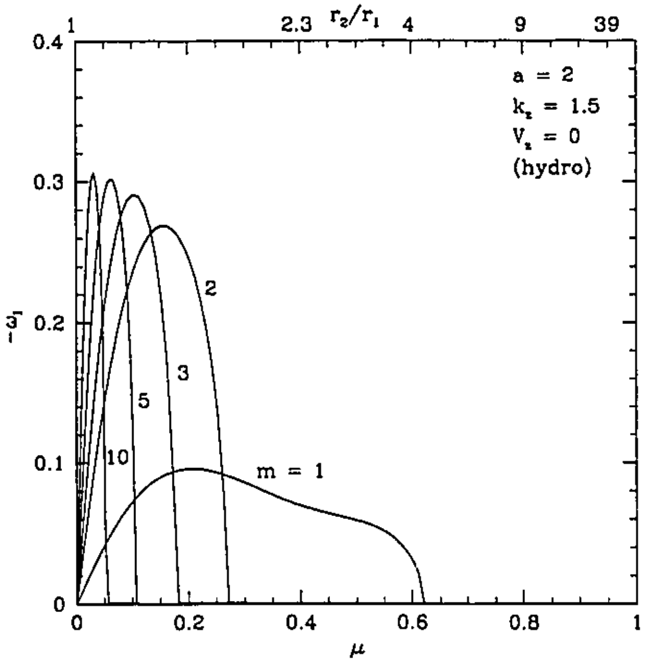
1
2.3
r₂/r₁
4
9
39
0.4
0.3
0.2
0.1
0
−ω_I
a = 2
k_z = 1.5
V_z = 0
(hydro)
2
3
5
10
m = 1
0
0.2
0.4
0.6
0.8
1
μ

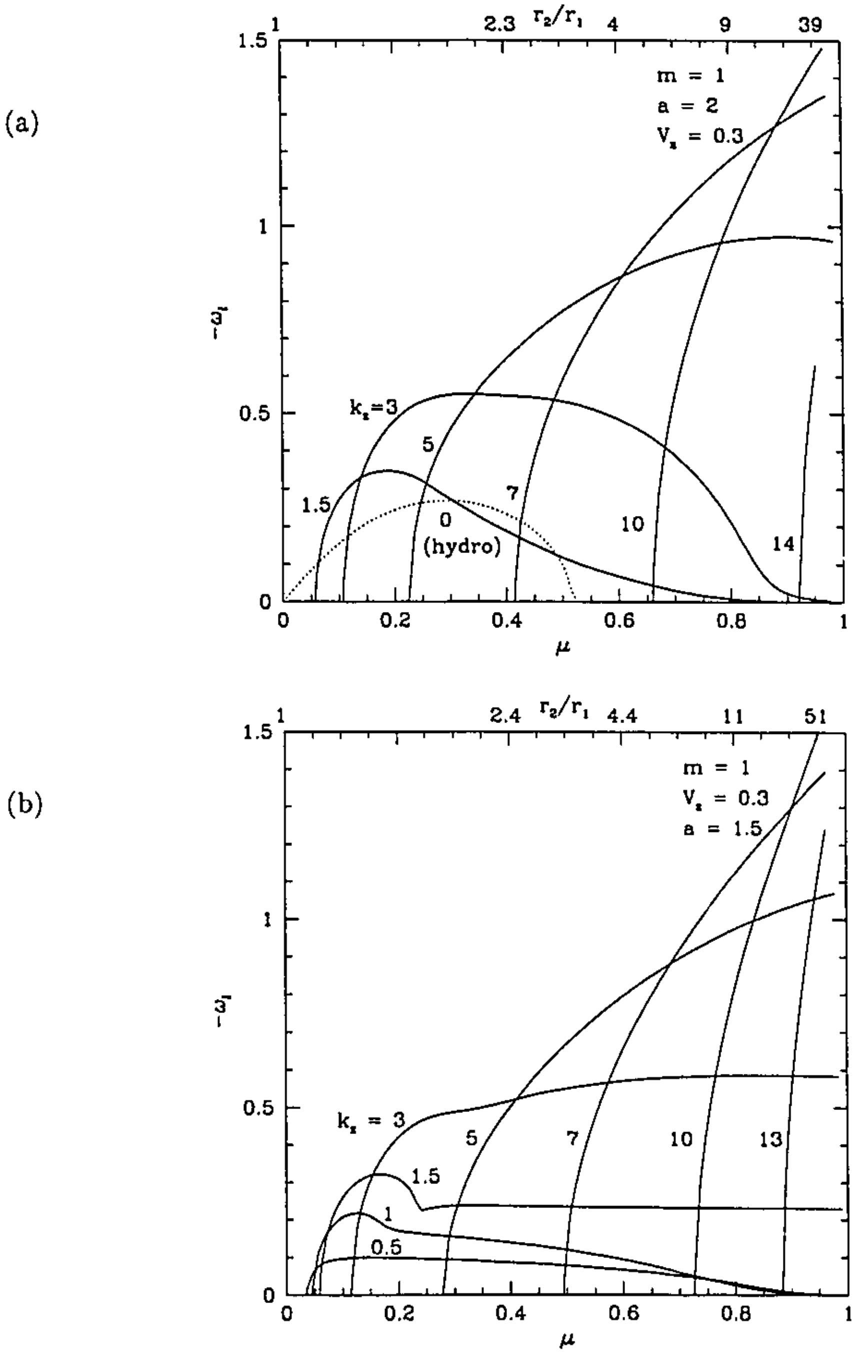

Figure 5.14: Growth rates for higher k_z, $V_z = 0.3$, and (a) $a = 2$; (b) $a = 1.5$.

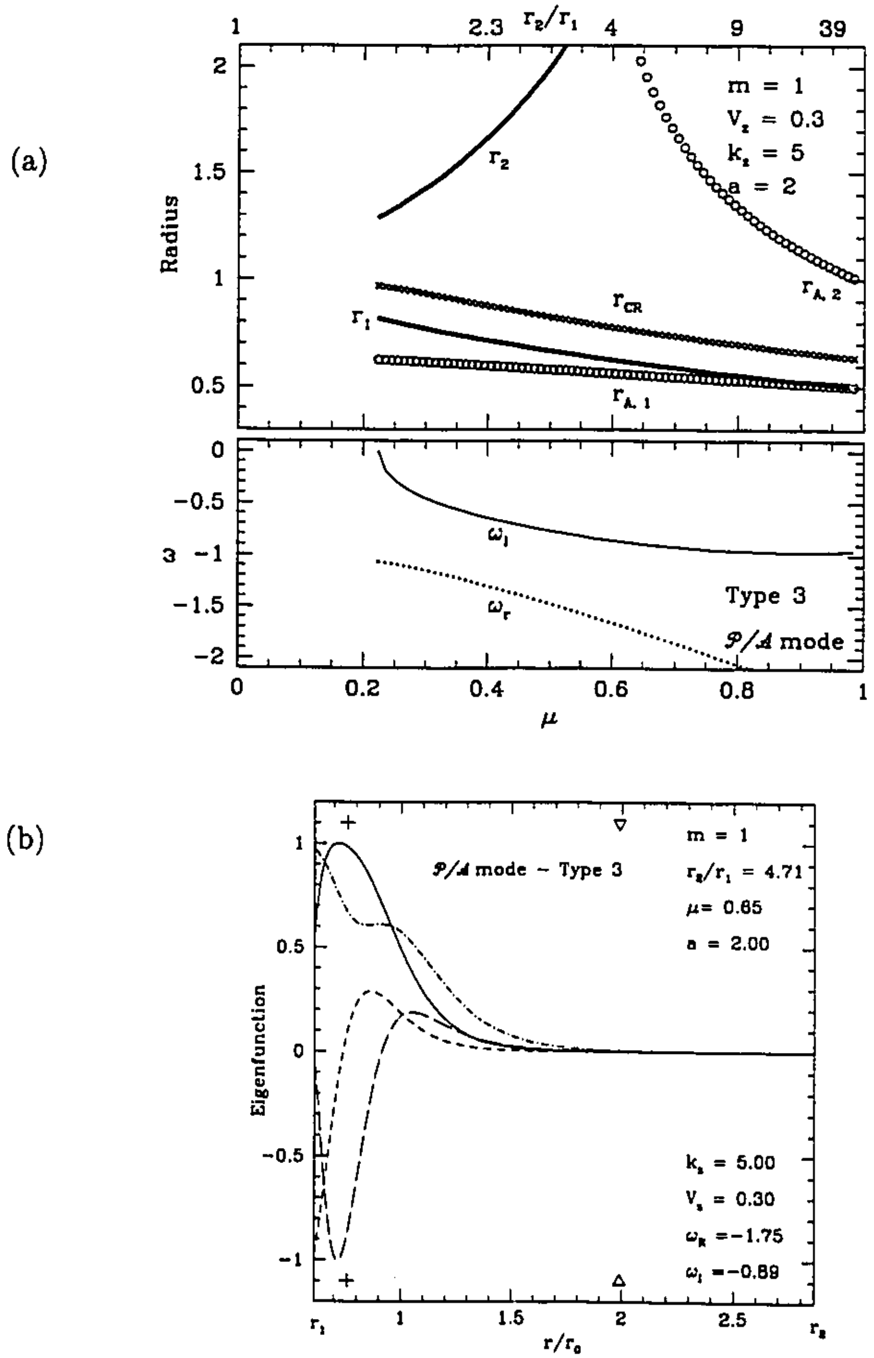

Figure 5.15: (a) Characteristic radii, and (b) eigenfunctions for $a = 2$ and $k_z = 5$. Note that this mode is of Type 3.

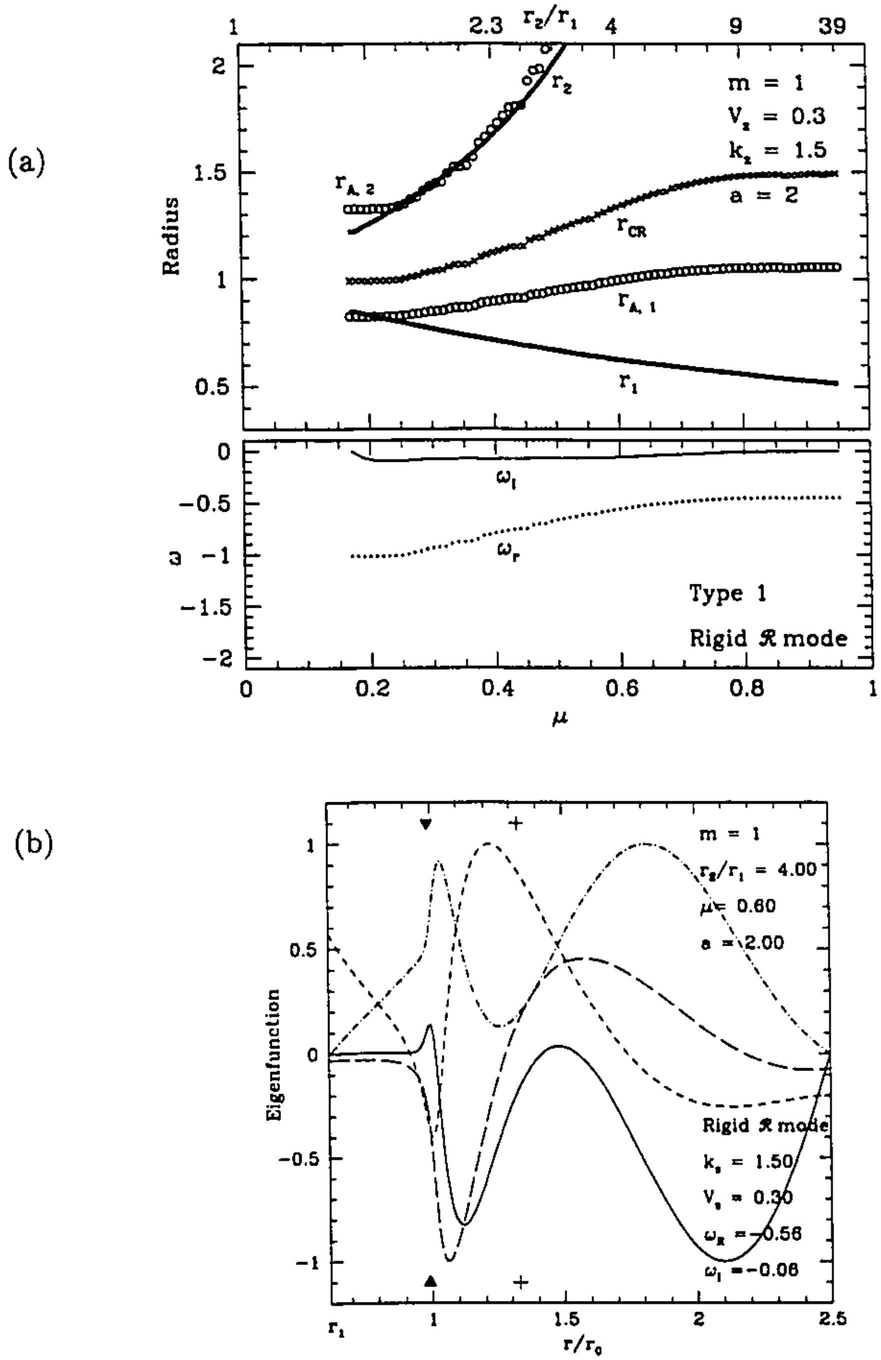

Figure 5.16: (a) Characteristic radii, and (b) eigenfunctions for $a = 2$, $k_z = 5$, and rigid boundary conditions. Note that this mode is of Type 1.

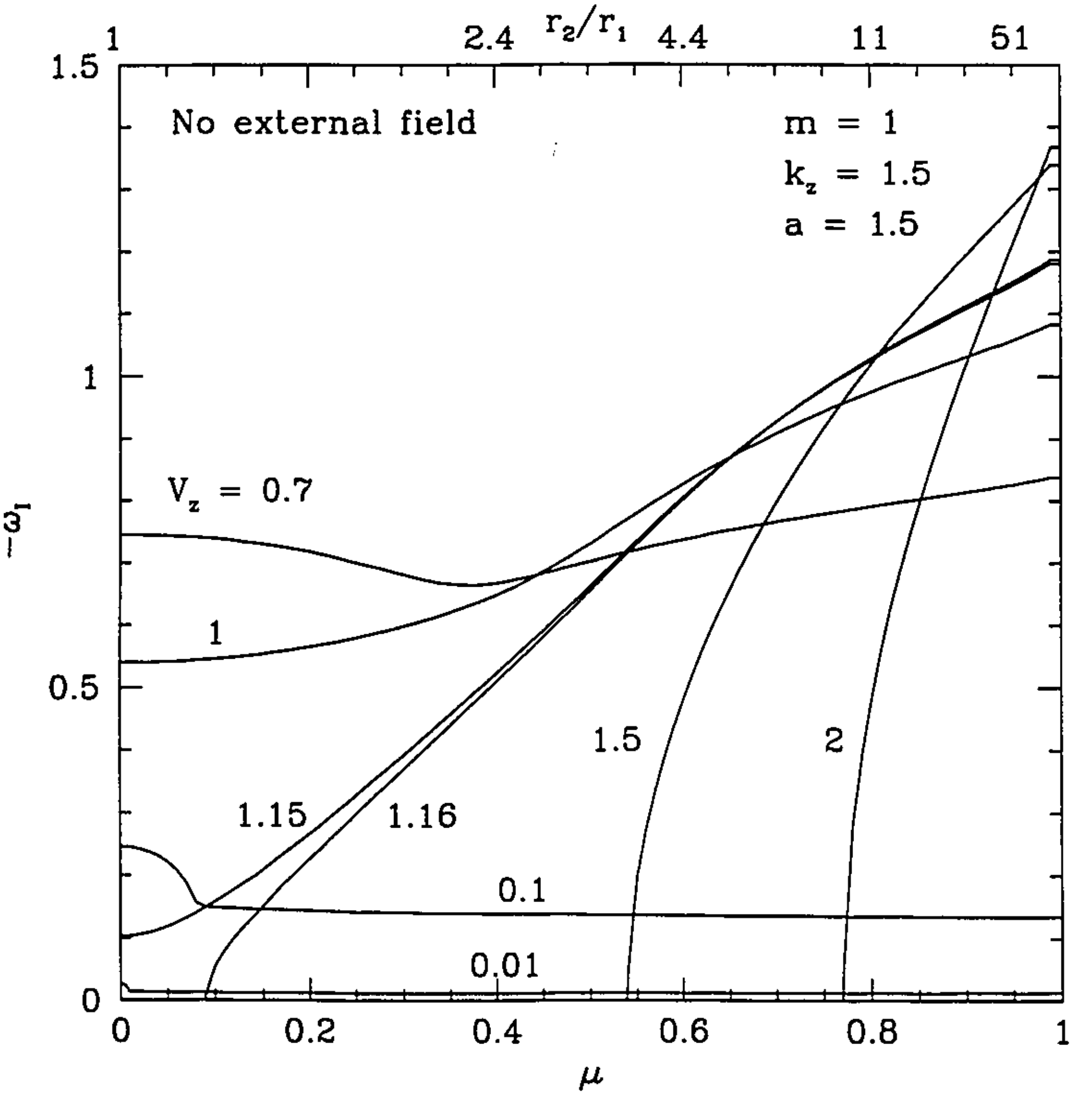

Figure 5.17: Keplerian growth rates for free boundaries with vanishing external field. Curves are labelled with different values of V_z.

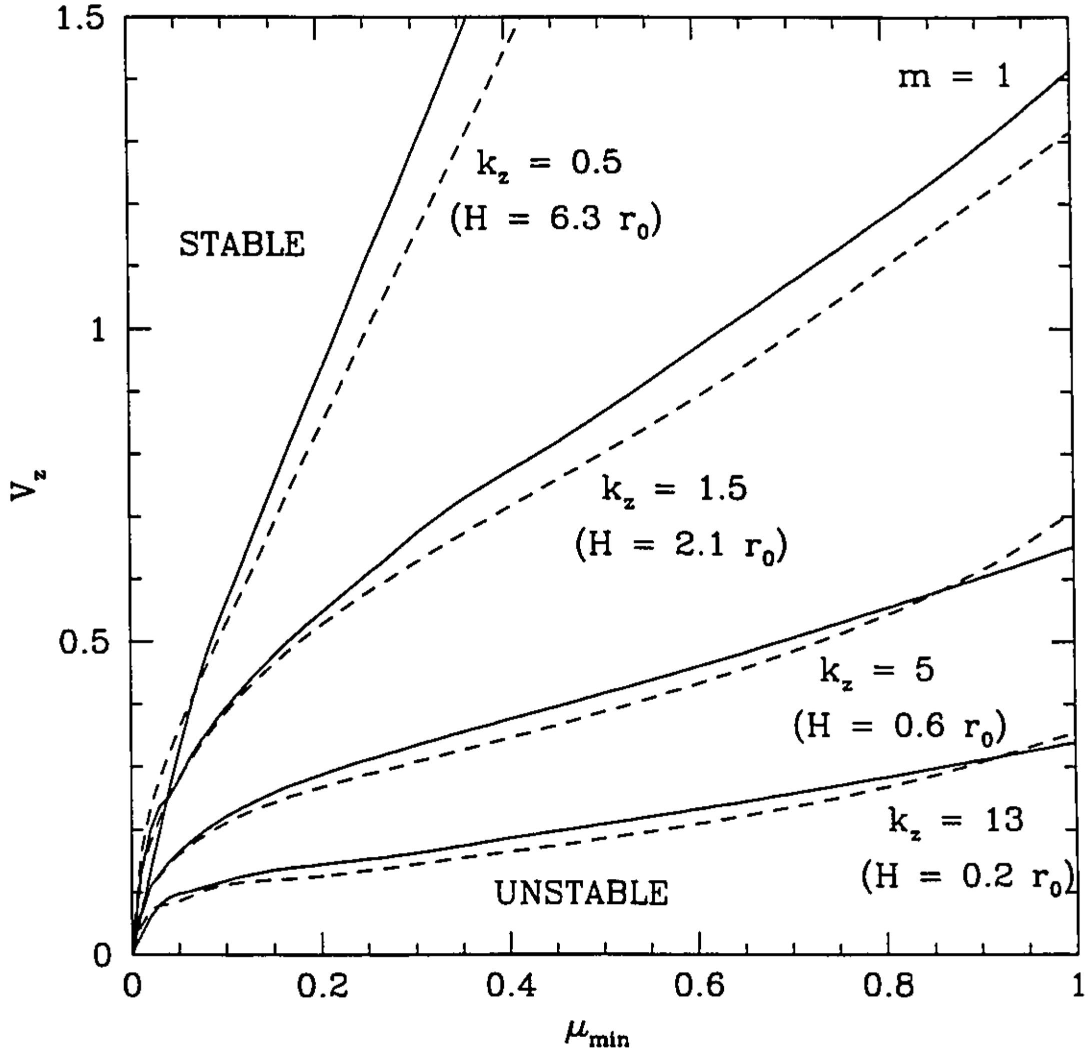

Figure 5.18: Critical Alfvén speed, V_z, as a function of μ_{min} for $m = 1$. Curves are labelled by k_z and the corresponding H (see text for details). Solid curve is for $a = 2$; dashed curve for $a = 1.5$.

Chapter 6

EPILOGUE

> Although much can be learned from linear perturbation theory, a linear instability is simply a signal that one has to do more work! Once the instability grows into the non-linear regime, it may provide to be relatively harmless, or to produce only small changes in the background flow.
>
> *Schutz (1983), quoted in Abramowicz, Blaes, & Lu (1986)*

As a summary of results has been included in each of the last three chapters, there is little need for restatement here. Instead I close with some remarks on possible implications of the thesis work and likely directions of future progress. These are organized into the general categories appearing below.

Radial Angular Momentum Transport

Much of the work to date on magnetic instabilities in accretion disks has focussed on their possible role as a source of anomalous viscosity (§1.2). A magnetically-induced viscosity may transport angular momentum more effectively than its hydrodynamic counterpart, due to the addition of the Maxwell stress term in the angular momentum transport equation (§1.5). In the absence of an equilibrium radial magnetic field, the lowest-order radial flux of angular momentum at a given radius r is given by the sum of the Reynolds and Maxwell stresses (Chapter 1; Hawley & Balbus 1992; Coleman, Kley, & Kumar 1995)

$$\mathcal{F}_{\mathcal{L}}(r) = \rho r \left\{ \Re(\delta u_\phi)\Re(\delta u_r) - \frac{1}{4\pi\rho}\Re(\delta B_\phi)\Re(\delta B_r) \right\} = \omega_I |\delta u_r|^2 f(r), \tag{6.1}$$

where $f(r)$ is a function of ω, Ω_A, and the equilibrium quantities (see Coleman et al. 1995 for its detailed form), and $\Re$ denotes the real part of the perturbation. Note that $\mathcal{F}_{\mathcal{L}} = 0$ if the growth rate of the instability, $\omega_I = 0$. Thus, $m = 0$ hydromagnetic modes can effect the radial transport of angular momentum; the same is *not* true of $m = 0$ hydro*dynamic* modes. An intriguing result, especially given the robustness of the VC instability.

Equation (6.1) is readily applied to the results of the three preceeding chapters, so the radial angular momentum transport could be calculated as a natural next stage of the work. Such a calculation has been initiated by Coleman, Kley, & Kumar (1995), but only for a very limited range of models and questionable boundary conditions (Chp. 5). Two interesting points to address in the calculations would be: (1) Is angular momentum transported outward? One of the more surprising results of recent years is that of Ryu & Goodman (1992), who found that transport due to linear, convective instabilities occurred principally *inwards.* This is a concern since it shows that the mere existence of an instability is not enough to ensure "viscosity." (2) Assuming that the transport due to global magnetic instabilities *is* outward, which of the $m = 0$ or $m \neq 0$ varieties dominates? The growth rate of the former is larger, but the latter appears to act over larger portions of the disk. Limitations of time and space have prohibited the author from exploring these issues here.

Vertical Angular Momentum Transport

A disk threaded by a vertical magnetic field can transport angular momentum *vertically,* as well as radially. This additional channel for angular momentum could account for a large fraction of the total disk transport if the field is sufficiently strong and optimally oriented (Blandford & Payne 1982). It also leads to compelling models of outflows and winds from both protostars and AGN (Pudritz & Norman 1986; Uchida & Shibata 1985; Pelletier & Pudritz 1992). However, the vertical gradient of the Maxwell stress, $\partial\Pi_{\phi z}/\partial z$, that gives rise to this transport is identically zero in the model of Chps. 3, 4, and 5, since the vertical structure of the disk is not treated explicitly.

It would clearly be desirable to modify the above model so that these effects could be investigated. The approach of Gammie & Balbus (1994), which treats the vertical structure at the expense of the radial, might be a good starting point for such a calculation. The optimal model, in my view, is the MHD torus, which would allow the *simultaneous* consideration of transport in both r and z. However, the discussion of Chp. 2 shows that a reasonable equilibrium model of the MHD torus needs considerably more work (especially with regard to matching onto an exterior field).

Many models of magnetically-driven winds have not treated the underlying accretion disk explicitly; i.e., *complete* disk plus wind solutions are relatively rare. Models of the latter type are important, since they not only offer an explanation of the observed winds and outflows, but may also obviate the need for the Shakura-Sunyaev α through the idea of wind-driven accretion. In the latter, the removal of angular momentum *vertically* via the wind can lead directly to *radial* inflow of matter onto the star. As more disk plus wind solutions become known, it becomes necessary to consider the global stability of the combined system. It is even possible that time-dependent models of accretion disks with extensive coronal structure might generate winds spontaneously as a result of instabilities in the disks. There is in fact some evidence that observed variations in outflows can be traced to properties of the underlying disk, rather than being produced in the outflows themselves (Andre et al. 1990). An heuristic approach to the stability of the Blandford & Payne (1982) solution has recently been presented by Lubow, Papaloizou, & Pringle (1994), but it is fair to say that the subject is wide open for the application of the stability techniques used in this thesis.

Large-Scale Magnetic Field Generation

There has long been a pressing need to explain how large-scale, ordered magnetic fields might be generated in disks. As expected, dynamo enthusiasts have advanced a host of mechanisms to generate global fields from the local dynamo-producing mechanism outlined in §1.5.4, but these rely on poorly-understood details of turbulence theory as input (Moffatt 1978; Parker 1979). The results of Chapters 3, 4 and 5, however, explicitly demonstrate the existence of finite-amplitude growing δu_r, and so δB_r, showing that *a large-scale field is a natural outcome of infinitesimal perturbations to a well-understood equilibrium.* It is simply not known at this time whether the ultimate nonlinear resolution of these instabilities is "turbulent" (as in the local regime; §1.5.3) or ordered, but in any case the magnetic energy seems likely to be quite large. Following the calculations of this thesis into the nonlinear regime would help clarify the situation.

While the $m = 0$ global modes are the most rapidly growing ones for most reasonable disk sizes, the radial eigenmodes presented in Ch. 3 suggest that they are largely confined to the extreme inner regions of the disk. The $m \neq 0$ modes, on the other hand, are not similarly restricted; they can often extend over almost the entire disk (cf. the $\mathcal{P}$ and $\mathcal{R}$ modes of Chp. 5). This difference might have observable consequences if globally-ordered fields of significant strength develop from such instabilities. For example, MHD models of protostellar outflows (see above for references) can depend sensitively on the field distribution across the disk.

Applications to the Interstellar Medium

A topic of mounting interest is the role of MHD waves in the interstellar medium (ISM), in particular the possibility that such waves are responsible for molecular cloud support. Several mechanisms have been proposed for the generation of the waves (Falgarone & Puget 1988), and the results of this thesis suggest yet another.

As discussed in Chp. 4, the simultaneous presence of rotation and magnetic fields in clouds, though perhaps rare, offers a natural mechanism for the generation of MHD waves through the BH instability.[1] Moreover, in the incompressible model with a purely axial field an exact, time-dependent (and so nonlinear), local solution of the perturbation equations is known (Goodman & Xu 1994). It is this solution that can and should be utilized for the calculation of MHD wave spectra, since it is sensitive to all-important nonlinear processes such as wave steepening and wave-wave coupling. While the incompressible assumption would seem an even poorer one to make in the ISM than in disks, it is nevertheless fre-

---

[1] I refer to the local BH, not the global VC instability here, since "boundaries" in the ISM are notoriously ill-defined. A local model is also preferable for other reasons, discussed below.

quently used; e.g., in the ISM turbulence model of Sridhar & Goldreich (1994). This is more a reflection of profound difficulties in turbulence theory than ignorance of ISM conditions, as the few known exact solutions in the subject are incompressible ones (e.g. Kolmogorov 1941). What is most interesting is the finding of Sridhar & Goldreich that 3- and 4-wave resonant couplings can occur between shear Alfvén waves in the ISM. The intimation of similar interactions in Ch. 5 of this thesis seems to hint at a certain convergence of microphysics taking place here, despite the fact that the two contexts (accretion disks and clouds) are so different.

Finally, it is clear that the model on which the stability analyses of Chapters 3, 4, and 5 is based can be improved and extended in myriad ways. For example, a fully three-dimensional model such as the MHD torus could be constructed, relativistic effects might be explored by introducing a pseudo-Newtonian potential (especially important for AGN; Blaes 1986), and magnetic diffusivity and separate ion and neutral components might be introduced. While all these would facilitate a valuable confirmation of the results, and the generation of a few new ones, I feel that perhaps it is better still to heed the tone (if not the precise content) of Schutz's comment which opens this chapter. In fact, it is hoped that this thesis has succeeded in shifting the focus somewhat from local processes to effects that might tell us something more about disks and their environments as a whole. While observations cannot yet be confronted head-on, further studies along these lines may continue to reveal fundamental properties of disks never before suspected.

Chapter 7

APPENDIX: COMPUTER CODE

This partial FORTRAN program was used for all the numerical stability calculations in this thesis. It employs a standard shooting method as applied to eigenvalue problems (Press et al. 1992). Only the user-supplied portions (written by the author) are given below; the remaining portions may be imported directly from Press et al. As presented here, the program is set up for the calculations of Chapter 5.

```
c
c-----------------------------------------------------------------------
c     Program naxi.f calculates eigenvalues and eigenfunctions, given
c     the governing differential equations, boundary conditions, and
c     relevant input parameters.
c
c     AUTHOR: Charles Curry
c-----------------------------------------------------------------------
c
      program naxi
      implicit double precision (a-h,o-z)
      parameter (n2=2,nmax=50,kmaxx=200)
      dimension v(n2)
      complex*16 y1,y2,yu,yh,yw,y(3)
      character*16 bcs
```

```
      logical check
      external fff
      common /integ/ m,ifree
      common /caller/ x1,x2,nvar
      common /vals/ a,alf,beta,vk,vz
      common /path/ kmax,kount,dxsav,xp(kmaxx),yp(nmax,kmaxx)
      open(3,file="ev")
      open(10,file="ef")
      nvar=6
      binc=0.01d0
c
c     Input of data
c
      write(*,*) 'beta ?'
      read(*,*) beta
      write(*,*) 'eigr,eigi ?'
      read(*,*) eigr,eigi
      ifree=1
      a=2.d0
      m=1
      vk=1.5d0
      vz=0.3d0
      alf=vk*vz
      ri=1.d0
      if (ifree.eq.0) then
        bcs='Rigid BCs'
      else
        bcs='Free BCs'
      endif
      dxsav=.001d0
      v1last=0.d0
      v2last=0.d0
      nefn=0
c
c     Calculate inner radius for given a, r2/r1
c
      rmin=0.1d0
      do 70 i=1,1000
        ro=1.d0/(1.d0-beta)
        x2=1.d0/(1.d0-beta)
        call hyp(x1,fff,rmin,1.d0,1.d-10,iflag)
        v(1)=eigr
        v(2)=eigi
        call newt(v,n2,check)
        if (check) then
```

```
          write(*,*) 'shoot failed -- bad initial guess'
          stop
        endif
        rc=(abs(v(1))/m)**(-1.d0/a)
        racin=((abs(v(1))+alf)/m)**(-1.d0/a)
        racout=((abs(v(1))-alf)/m)**(-1.d0/a)
        write(*,100) x1,x2,beta,v(1),v(2),rc,racin,racout
        write(3,100) x1,x2,beta,v(1),abs(v(2)),rc,racin,racout
c       * Normalize eigenfunctions *
c       * yp(3,j) is Re(eigenfn. y); yp(4,j) is Im part *
c       * yp(5,j) is Re(eigenfn. y)'; yp(6,j) is Im part *
c       * yu prefaces del ur, yh del h *
c       * eigenfn. automatically written at max. growth *
        nefn=1
        write(10,150) m,x1,x2,x2/x1,beta,a,vk,vz,v(1),v(2),rc,
     %                racin,racout,bcs
        yurmax=0.d0
        yuimax=0.d0
        yhrmax=0.d0
        yhimax=0.d0
        do 40 j = 1,kmaxx
          if (xp(j).eq.0.d0)goto 40
          do ii=1,3
            jj=2*ii-1
            y(ii)=dcmplx(yp(jj,j),yp(jj+1,j))
          enddo
          omeg=xp(j)**(-a)
          vreal=v(1)+m*omeg
          y1=dcmplx(vreal,v(2))
          y2=y1*y1-alf*alf
          yu=y(2)*(0.d0,1.d0)*y1
          yh=(y2*y(3)+(y2 - 2.d0*m*y1*omeg)*y(2)/xp(j))/(m*m/xp(j)**2
     %       + vk*vk)
          yur=dreal(yu)
          yui=dimag(yu)
          yhr=dreal(yh)
          yhi=dimag(yh)
          if (abs(yur).le.yurmax)goto 15
          yurmax=abs(yur)
 15       if (abs(yui).le.yuimax)goto 20
          yuimax=abs(yui)
 20       if (abs(yhr).le.yhrmax)goto 30
          yhrmax=abs(yhr)
 30       if (abs(yhi).le.yhimax)goto 40
          yhimax=abs(yhi)
```

```
 40     continue
        do 50 j = 1,kmaxx
          if (xp(j).eq.0.d0)goto 50
          do ii=1,3
            jj=2*ii-1
            y(ii)=dcmplx(yp(jj,j),yp(jj+1,j))
          enddo
          omeg=xp(j)**(-a)
          vreal=v(1)+m*omeg
          y1=dcmplx(vreal,v(2))
          y2=y1*y1-alf*alf
          yu=y(2)*(0.d0,1.d0)*y1
          yh=(y2*y(3)+(y2 - 2.d0*m*y1*omeg)*y(2)/xp(j))/(m*m/xp(j)**2
     %        + vk*vk)
          yur=dreal(yu)
          yui=dimag(yu)
          yhr=dreal(yh)
          yhi=dimag(yh)
          yurnorm=yur/yurmax
          yuinorm=yui/yuimax
          yhrnorm=yhr/yhrmax
          yhinorm=yhi/yhimax
          write(10,100) xp(j),yurnorm,yuinorm,yhrnorm,yhinorm
 50     continue
 60     beta=beta+binc
        eigr=v(1)+.2d0*binc
        eigi=v(2)
        v1last=abs(v(1))
        v2last=abs(v(2))
 70   continue
100   format(1x,1g10.4,1x,1g10.4,1x,1g10.4,1x,1g10.4,1x,1g10.4,
     %       1x,1g10.4,1x,1g10.4,1x,1g10.4)
150   format(1i2/1f5.2/1f5.2/1f5.2/1f5.2/1f5.2/1f5.2/1f5.2/1f5.2/
     %       1f5.2/1f5.2/1f5.2/1f5.2/1f5.2/a9)
      end
c
      subroutine load(x1,v,y)
c
      implicit double precision (a-h,o-z)
      dimension v(2),y(6)
      complex*16 s,y1,y2,yl(3)
      common /integ/ m,ifree
      common /vals/ a,alf,beta,vk,vz
c
c     ** Input starting values for COMPLEX fns. yl(i) **
```

```
c
      yl(1)=dcmplx(v(1),v(2))
      omeg=x1**(-a)
      y1=yl(1) + m*omeg
      y2=y1*y1 - alf*alf
      s=2.d0*y1*y1/y2 - a
      rkm=vk*vk*x1*x1+m*m
      g1=-1.d0/x1/x1 + x1**(1.d0-2.d0*a)
      if (vk.eq.0.d0) then
        chii=0.d0
        goto 10
      endif
      xi=abs(vk)*x1
      chii=BESSI0(xi)/(abs(vk)*BESSI1(xi))
 10   g1n=g1+alf*alf*chii
      if (ifree.eq.1) then
c     * Free BCs for xi*
        yl(2)=1.d0
        yl(3)=-(1.d0-2.d0*m*omeg*y1/y2 + rkm*g1n
     %           /y2/x1)*yl(2)/x1
c     * Rigid BCs *
      else
        yl(2)=0.d0
        yl(3)=1.d0
      endif
c
c     ** Break into real and imag parts **
c
      do i=1,3
        j=2*i-1
        y(j)=dreal(yl(i))
        y(j+1)=dimag(yl(i))
      enddo
      return
      end
c
      subroutine score(x2,y,f)
c
      implicit double precision (a-h,o-z)
      dimension f(2),y(6)
      complex*16 s,yk,y1,y2,yr(3)
      common /integ/ m,ifree
      common /vals/ a,alf,beta,vk,vz
      g2=-1.d0/x2/x2 + x2**(1.d0-2.d0*a)
      omeg=x2**(-a)
```

```
      rkm=vk*vk*x2*x2+m*m
      if (vk.eq.0.d0) then
         chio=0.d0
         goto 10
      endif
      xo=abs(vk)*x2
      chio=-BESSK0(xo)/(abs(vk)*BESSK1(xo))
 10   g2n=g2+alf*alf*chio
      do i=1,3
        j=2*i-1
        yr(i)=dcmplx(y(j),y(j+1))
      enddo
      y1=yr(1) + m*omeg
      y2=y1*y1 - alf*alf
      s=2.d0*y1*y1/y2 - a
      if (ifree.eq.1) then
c     * Free BCs for xi*
        yk=-(1.d0-2.d0*m*omeg*y1/y2 + rkm*g2n
     %  /y2/x2)*yr(2)/x2
        f(1)=dreal(yr(3)-yk)
        f(2)=dimag(yr(3)-yk)
      else
c     * Rigid BCs *
        f(1)=dreal(yr(2))
        f(2)=dimag(yr(2))
      endif
      return
      end
c
      subroutine derivs(x,y,dydx)
c
      implicit double precision (a-h,o-z)
      dimension y(6),dydx(6)
      complex*16 aa,bb,p,s,y1,y2,yy(3),dyydx(3)
      common /integ/ m,ifree
      common /vals/ a,alf,beta,vk,vz
      do i=1,3
        j=2*i-1
        yy(i)=dcmplx(y(j),y(j+1))
      enddo
      omeg=x**(-a)
      y1=yy(1) + m*omeg
      y2=y1*y1 - alf*alf
      s=2.d0*y1*y1/y2 - a
      rkm=vk*vk*x*x+m*m
```

```
c     * Coeffs. for xi perturbation eqns. *
      aa=(vk*vk*x*x+3.d0*m*m)/rkm/x - 2.d0*a*m*y1*omeg/x/y2
      bb=vk*vk*(2.d0*omeg*omeg*s+4.d0*m*y1*omeg/rkm
     %    - (y2/rkm)*(x*x*vk*vk+1.d0+2.d0*m*m))
     %    - (y2/rkm)*m*m*(m*m-1.d0)/x/x
      dyydx(1)=0.d0
      dyydx(2)=yy(3)
      dyydx(3)=-aa*yy(3)-bb*yy(2)/y2
      dydx(1)=0.d0
      dydx(2)=0.d0
      dydx(3)=dreal(dyydx(2))
      dydx(4)=dimag(dyydx(2))
      dydx(5)=dreal(dyydx(3))
      dydx(6)=dimag(dyydx(3))
      return
      end
C *************************
C THE EQUIPOTENTIAL FUNCTION
C *************************
      FUNCTION FFF(r)
      implicit double precision(a-h,o-z)
      common /integ/ m,ifree
      common /vals/ a,alf,beta,vk,vz
      common/caller/ x1,x2,nvar
      cpp=(x2**(2.d0*(1.d0-a)))/(2.d0*(a-1.d0))-1.d0/x2
      FFF=(1.d0/r+(r**(2.d0*(1.d0-a)))
     %/(2.d0*(1.d0-a))+cpp)
      RETURN
      END
c
C     NONLINEAR EQUATION SOLVER
c
c     Kindly provided by Omer Blaes
c
      SUBROUTINE HYP(XHYP,FC,X1,X2,EPS,NZERI)
      implicit double precision(a-h,o-z)
      INTEGER AP,BP,P
      double precision N
      DIMENSION Z(3),FSMALL(3)
      EXTERNAL FC
      NZERI=0
      Z(1)=X1
      FSMALL(1)=FC(X1)
      Z(3)=X2
      FSMALL(3)=FC(X2)
```

```
      IF((FSMALL(3)*FSMALL(1)).GT.0.d0) GO TO 777
      AP=0
      P=0
      BP=1
      GO TO 21
 10   T=0.d0
      N=0.d0
      DO 100 J=1,3
      XHYP=Z(J)
      IF(FSMALL(J).EQ.0.d0) GO TO 99
      G=(J-2)*(Z(4-J)-Z(2))/FSMALL(J)
      IF(J.EQ.2) G=(Z(3)-Z(1))/FSMALL(2)
      T=T+G*(Z(J)-Z(-AP-BP+2))
      N=N+G
100   CONTINUE
      IF((N.NE.0.d0).AND.(ABS(FSMALL(AP+2)).GT.ABS(FSMALL(-AP-BP
     %   +2)))) GO TO 20
      GO TO 21
 20   XHYP=Z(-AP-BP+2)+T/N
      IF(ABS(XHYP-Z(-AP-BP+2)).LE.ABS(Z(BP+2)-Z(-AP-BP+2))/2.d0)
     %   GO TO 22
 21   XHYP=(Z(BP+2)+Z(-AP-BP+2))/2.d0
 22   Z(AP+2)=XHYP
      FSMALL(AP+2)=FC(XHYP)
      IF(FSMALL(AP+2)*FSMALL(BP+2))30,30,40
 30   P=P+1
      GO TO 50
 40   BP=-AP-BP
      IF(P.LT.6) P=0
 50   AP=-AP-BP
      IF((ABS(Z(AP+2)-Z(BP+2)).GT.EPS).AND.(ABS(Z(AP+2)-Z(-AP-BP
     %   +2)).GT.EPS)) GOTO 60
      GO TO 99
 60   CONTINUE
      IF(P-6)70,80,80
 70   M=1
      GOTO 90
 80   M=2
 90   GOTO(10,21),M
777   NZERI=1
      PRINT  1000
1000  FORMAT(//'     NO ZERO FOUND'//)
      PRINT*,FSMALL(1),FSMALL(3)
      XHYP=0.d0
      RETURN
```

```
  99  CONTINUE
      RETURN
      END
c
c-------------------------------------------------------------------
c     Below are the names of a number of required subroutines, which
c     may be taken directly from Press et al. (1992).
c-------------------------------------------------------------------
c
      SUBROUTINE newt(x,n,check)
      subroutine funcv(n2,v,f)
      SUBROUTINE fdjac(n,x,fvec,np,df)
      FUNCTION fmin(x)
      SUBROUTINE lnsrch(n,xold,fold,g,p,x,f,stpmax,check,func)
      SUBROUTINE lubksb(a,n,np,indx,b)
      SUBROUTINE odeint(ystart,nvar,x1,x2,eps,h1,hmin,nok,nbad,derivs,
     *rkqs)
      SUBROUTINE rkqs(y,dydx,n,x,htry,eps,yscal,hdid,hnext,derivs)
      SUBROUTINE rkck(y,dydx,n,x,h,yout,yerr,derivs)
      SUBROUTINE ludcmp(a,n,np,indx,d)
      FUNCTION bessi0(x)
      FUNCTION bessi1(x)
      FUNCTION bessk0(x)
      FUNCTION bessk1(x)
c-----------------------------------------------------------------------
```

Chapter 8

REFERENCES

Abramowicz, M. A., Blaes, O. M., & Lu, J. 1986, in Structure and Evolution of Active Galactic Nuclei, ed. S. Giuricin (Dordrecht: Reidel), 113

Abramowicz, M. A., Curir, A., Schwarzenberg-Czerny, A., & Wilson, R. E. 1984a, MNRAS, 208, 279

Abramowicz, M. A., Livio, M., Piran, T., & Wiita, P. J. 1984b, ApJ, 279, 367

Acheson, D. J. 1973, J. Fluid Mech., 61, 609

Acton, F. S. 1970, Numerical Methods That Work (New York: Harper & Row), 148

Adams, F. C., & Shu, F. H. 1986, ApJ, 308, 836

Adams, F. C., Lada, C. J., & Shu, F. H. 1987, ApJ, 312, 788

Adams, F. C., Lada, C. J., & Shu, F. H. 1988, ApJ, 326, 865

Adams, F. C., Ruden, S. P., & Shu, F. H. 1989, ApJ, 347, 959 (ARS)

Adams, F. C., Emerson, J. P., & Fuller, G. A. 1990, ApJ, 357, 606

Aitken, D.K., Wright, C.M., Smith, C.H., & Roche, P.F. 1993, MNRAS, 262, 456

Aizenman, M., Smeyers, P., & Weigert, A. 1977, A & A, 58, 41

André, Ph., Martin-Pintado, J., Despois, D., & Montmerle, T. 1990, A & A, 236, 180

Antonucci, R. 1993, ARAA, 31, 473

Balbus, S. A., & Hawley, J. F. 1991, ApJ, 376, 214 (BH)

Balbus, S. A., & Hawley, J. F. 1992, ApJ, 400, 610

Bally, J. 1989, in ESO Workshop on Low Mass Star Formation and Pre-Main Sequence Objects, ed. B. Reipurth (Garching: European Southern Obs.), 1

Bateman, G. 1978, MHD Instabilities (Cambridge: MIT Press), 113

Bath, G. T., & Pringle, J. E. 1985, in Interacting Binary Stars, ed. J. E. Pringle & R. A. Wade (Cambridge: Cambridge Univ. Press), 177

Beckwith, S. V. W. 1994, in Theory of Accretion Disks - 2, ed. W. J. Duschl, J. Frank, F. Meyer, E. Meyer-Hofmeister, & W. M. Tscharnuter (Dordrecht: Kluwer), 1

Beckwith, S. V. W., Sargent, A. I., Chini, R. S., & Güsten, R. 1990, AJ, 99, 924

Bell, K. R., & Lin, D. N. C. 1994, ApJ, 427, 987

Bender, C. M., & Orszag, S. A. 1978, Advanced Mathematical Methods for Scientists and Engineers (New York: McGraw-Hill), 504

Bernstein, I., Frieman, E. A., Kruskal, M. D., & Kulsrud, R. M. 1958, Proc. Roy. Soc. Lond. A, 244, 17

Birkhoff, G., & Rota, G.-C. 1989, Ordinary Differential Equations (New York: Wiley), 317

Blaes, O. 1985, MNRAS, 212, 37P

Blaes, O. 1986, Ph. D. thesis, Intl. School for Adv. Studies, Trieste

Blaes, O. 1987, MNRAS, 227, 975

Blaes, O., & Glatzel, W. 1986, MNRAS, 220, 253 (BG)

Blaes, O., & Balbus, S. A. 1994, ApJ, 421, 163

Blandford, R. D. 1989, in Theory of Accretion Disks, ed. F. Meyer, W. J. Duschl, J. Frank, & E. Meyer-Hofmeister (Dordrecht: Kluwer), 35

Blandford, R. D. 1990, in Active Galactic Nuclei, Saas-Fee Advanced Course Lecture Notes 1990, ed. T. J.-L. Courvoisier & M. Mayor (Berlin: Springer-Verlag), 161

Blandford, R. D., & Payne, D. G. 1982, MNRAS, 199, 883

Blitz, L. 1993, in Protostars and Planets III, ed. E.H. Levy & J.I. Lunine (Tucson, Univ. of Arizona Press), 125

Bondi, H. 1952, MNRAS, 112, 195

Brandenburg, A., Nordlund, A., Stein, R. F., & Torkelsson, U. 1995, ApJ, 446, 741

Cairns, R. A. 1979, J. Fluid Mech., 92, 1

Camenzind, M. 1990, Reviews in Modern Astronomy, Vol. 3, ed. G. Klare (Heidelberg: Springer), 234

Cameron, A. G. W. 1978, Moon & Planets, 18, 5

Cap, F. F. 1976, Handbook on Plasma Instabilities (New York: Academic Press)

Case, K. M. 1960, Phys. Fluids, 3, 143

Chandrasekhar, S. 1960, Proc. Natl. Acad. Sci., 46, 253

Chandrasekhar, S. 1961, Hydrodynamic and Hydromagnetic Stability (Oxford: Clarendon), 384

Chandrasekhar, S. 1964, ApJ, 139, 664

Channugam, G. 1979, MNRAS, 187, 769

Christodoulou, D. M. 1993, ApJ, 412, 696

Christodoulou, D. M., & Narayan, R. 1992, ApJ, 388, 451

Clement, M. J. 1964, ApJ, 140, 1045

Coleman, C. S., Kley, W., & Kumar, S. 1995, MNRAS, 274, 171

Coroniti, F. V. 1981, ApJ, 244, 587

Cox, J. P. 1980, Theory of Stellar Pulsation (Princeton: Princeton Univ. Press), Chp. 17

Craik, A. D. D. 1985, Wave Interactions and Fluid Flows (Cambridge: Cambridge Univ. Press)

Cross, R. 1988, An Introduction to Alfvén Waves (Bristol: Hilger). Chp. 8

Curry, C., & Pudritz, R.E. 1995, ApJ, 453, in press

Curry, C., Pudritz, R.E., & Sutherland, P.G. 1994, ApJ, 434, 206 (CPS)

Drazin, P. G., & Reid, W. H. 1981, Hydrodynamic Stability (Cambridge: Cambridge Univ. Press)

Drury, L. O'C. 1985, MNRAS, 217, 821

Dubrulle, B., & Knobloch, E. 1992, A & A, 256, 673

Dubrulle, B., & Knobloch, E. 1993, A & A, 274, 667

Dyson, J., & Schutz, B. F. 1979, Proc. Roy. Soc. Lond. A, 368, 389

Edwards, S., Cabrit, S., Strom, S. E., Heyer, I., Strom, K. M., & Anderson, E. 1987, ApJ, 321, 473

Elmegreen, B. G. 1982, ApJ, 253, 634

Elmegreen, B. G. 1987, ApJ, 312, 626

Falgarone, E., & Puget, J. L. 1988, in Galactic and Extragalactic Star Formation, ed. R. E. Pudritz & M. Fich (Dordrecht: Kluwer), 195

Ferraro, V. C. A. 1937, MNRAS, 97, 458

Foglizzo, T., & Tagger, M. 1994, A & A, 287, 297

Frank, J., King, A. R., & Raine, D. J. 1985, Accretion Power in Astrophysics (Cambridge: Cambridge Univ. Press) (FKR)

Fricke, K. 1969, A & A, 1, 388

Fridman, A. M., & Polyachenko, V. L. 1984, Physics of Gravitating Systems. 2 vols. (New York: Springer)

Friedjung, M. 1985, A & A, 146, 336

Frieman, E., & Rotenberg, M. 1960, Rev. Mod. Phys., 32, 898 (FR)

Galeev, A. A., Rosner, R., & Vaiana, G. S. 1979, ApJ, 229, 318

Galli, D., & Shu, F. H. 1993, ApJ, 417, 220

Gammie, C. F., & Balbus, S. A. 1994, MNRAS, 270, 138 (GB)

Gat, O., & Livio, M. 1992, ApJ, 396, 542

Genzel, R. 1989, in IAU Symposium 136, The Center of the Galaxy, ed. M. Morris (Dordrecht: Kluwer), 393

Genzel, R., & Stutzki, J. 1989, ARAA, 27, 41

Glatzel, W. 1987a, MNRAS, 225, 227

Glatzel, W. 1987b, MNRAS, 228, 77

Glatzel, W. 1988, MNRAS, 231, 795

Goldreich, P., & Lynden-Bell, D. 1965, MNRAS, 130, 126

Goldreich, P., & Narayan, R. 1985, MNRAS, 213, 7P

Goldreich, P., Goodman, J., & Narayan, R. 1986, MNRAS, 221, 339 (GGN)

Goldsmith, P.F., & Arquilla, R. 1985, in Protostars & Planets II, ed. D.C. Black & M.S. Matthews (Tucson, Univ. of Arizona Press), 137

Goodman, J., & Narayan, R. 1988, MNRAS, 231, 97

Goodman, J., & Xu, G. 1994, ApJ, 432, 213

Goossens, M., Smeyers, P., & Denis, J. 1976, Astrophys. Sp. Sci. 39, 257

Hartmann, L. 1994, in Theory of Accretion Disks - 2, ed. W. J. Duschl, J. Frank, F. Meyer, E. Meyer-Hofmeister, & W. M. Tscharnuter (Dordrecht: Kluwer), 19

Hartmann, L., & Kenyon, S. J. 1987, ApJ, 312, 243

Hawley, J. F. 1987, MNRAS, 225, 677

Hawley, J. F. 1991, ApJ, 381, 496

Hawley, J. F., & Balbus, S. A. 1991, ApJ, 376, 223

Hawley, J. F., & Balbus, S. A. 1992, ApJ, 400, 595

Hawley, J.F., Gammie, C.F., & Balbus, S.A. 1995, ApJ, 440, 742

Hayashi, C. 1981, Prog. Theor. Phys. Suppl., 70, 35

Heiles, C. 1987, in Interstellar Processes, ed. D.J. Hollenbach & H.A. Thronson, Jr. (Dordrecht, D. Reidel), 171

Heiles, C., Goodman, A.A., McKee, C.F., & Zweibel, E.G. 1993, in Protostars and Planets III, ed. E.H. Levy & J.I. Lunine (Tucson, Univ. of Arizona Press), 279

Hildebrand, R. H. 1983, QJRAS, 24, 267

Hildebrand, R. H., et al. 1990, ApJ, 362, 114

Hoiland, E. 1941, Avhandliger Norske Videnskaps-Akademi i Oslo, I, Math.-Naturv. Klass., No 11, 1

Horne, K. 1994, in Theory of Accretion Disks - 2, ed. W. J. Duschl, J. Frank, F. Meyer, E. Meyer-Hofmeister, & W. M. Tscharnuter (Dordrecht: Kluwer), 77

Horne, K. 1995, A & A, in press

Howard, L.N., & Gupta, A.S. 1962, J. Fluid Mech. 14, 463

Hoyle, F., & Lyttleton, R. A. 1939, Proc. Camb. Phil. Soc., 35, 405

Jackson, J. D. 1975, Classical Electrodynamics (New York: Wiley), Ch. 10

Jaffe, W., Ford, H., Ferraresse, L., van den Bosch, F., & O'Connell, R. 1993, Nature, 364, 213

Jaroszyński, M. 1988, Acta Astron., 38, 289

Jaroszyński, M., Abramowicz, M. A., & Paczyński, B. 1980, Acta Astron., 30, 1

Jin, L. 1993, unpublished preprint

Kaisig, M., Tajima, T., & Lovelace, R.V.E. 1992, ApJ, 386, 83

Kenyon, S. J., & Hartmann, L. 1987, ApJ, 323, 714

Knobloch, E. 1992, MNRAS, 255, 25P

Kolmogorov, A. N. 1941, Compt. Rend. Acad. Sci. URSS, 30, 301

Königl, A. 1991, ApJ, 370, L39

Kovetz, A. 1966, ApJ, 146, 462

Krolik, J., & Begelman, M. 1988, ApJ, 329, 702

Kruskal, M., & Schwarzschild, M. 1954, Proc. Roy. Soc. Lond. A, 223, 348

Kumar, S., & Coleman, C. S. 1993, MNRAS, 260, 323

Kumar, S., Coleman, C. S., & Kley, W. 1994, MNRAS, 266, 379

Kutner, M.L., Tucker, K.D., Chin, G., & Thaddeus, P. 1977, ApJ, 215, 521

Lada, C. J. 1991, in The Physics of Star Formation and Early Stellar Evolution, ed. C. J. Lada & N. D. Kylafis (Dordrecht: Kluwer), 329

Landau, L. D., & Lifshitz, E. M. 1959, Fluid Mechanics (London: Pergamon)

Laplace, P. S. 1802, Celestial Mechanics, trans. N. Bowditch (New York: Chelsea)

Lightman, A. P. 1974, ApJ, 194, 429

Lightman, A. P., & Eardley, D. M. 1974, ApJ, 187, L1

Lin, D. N. C., & Papaloizou, J. 1980, MNRAS, 191, 37

Livio, M., & Shaviv, G. 1977, A & A, 55, 95

Lubow, S.H., Papaloizou, J.C.B., & Pringle, J.E. 1994, MNRAS, 268, 1010

Lubow, S.H., & Spruit, H C. 1995, ApJ, 445, 337

Lynden-Bell, D., & Ostriker, J. P. 1967, MNRAS, 136, 293

Lynden-Bell, D., & Pringle, J. E. 1974, MNRAS, 168, 603

Madau, P. 1988, ApJ, 327, 116

Mark, J. W.-K. 1976, ApJ, 256, 363

Malkan, M. A., & Sargent, W. L. W. 1982, ApJ, 254, 22

Matsumoto, T., & Tajima, T. 1995, ApJ, 445, 767 (MT)

Matsumoto, T., Nakamura, F., & Hanawa, T. 1994, PASJ, 46, 243

McCaugrean, M. J., Rayner, J. T., Zinnecker, H., & Stauffer, J. R. 1995, in Disks and Outflows Around Young Stars, ed. S. Beckwith & J. Staude (in press)

Michael, D. H. 1954, Mathematika, 1, 45

Moffatt, H. K. 1978, Magnetic Field Generation in Electrically Conducting Fluids (Cambridge: Cambridge Univ. Press)

Moncrief, V. 1980, ApJ, 235, 1038

Moss, D. L., & Tayler, R. J. 1969, MNRAS, 145, 217

Myers, P. C., & Goodman, A. A. 1988, ApJ, 326, L27

Narayan, R., & Goodman, J. 1989, in Theory of Accretion Disks, ed. F. Meyer, W. J. Duschl, J. Frank, & E. Meyer-Hofmeister (Dordrecht: Kluwer), 231 (NG)

Narayan, R., Goldreich, P., & Goodman, J. 1987, MNRAS, 228, 1

Natta, A. 1993, ApJ, 412, 761

Netzer, H. 1990, in Active Galactic Nuclei, Saas-Fee Advanced Course Lecture Notes 1990, ed. T. J.-L. Courvoisier & M. Mayor (Berlin: Springer-Verlag), 57

Osterloh, M., & Beckwith, S. V. W. 1995, in Disks and Outflows Around Young Stars, ed. S. Beckwith & J. Staude (in press)

Paczyńsky, B., & Wiita, P. J. 1980, A & A, 88, 23

Papaloizou, J. C. B., & Pringle, J. E. 1984, MNRAS, 208, 721 (PP 1984)

Papaloizou, J. C. B., & Pringle, J. E. 1985, MNRAS, 213, 799 (PP 1985)

Papaloizou, J., & Szuszkiewicz, E. 1992, Geophys. Astrophys. Fluid Dynamics, 66, 223

Parker, E. N. 1966, ApJ, 145, 811

Parker, E. N. 1979, Cosmical Magnetic Fields (Oxford: Clarendon)

Pelletier, G., & Pudritz, R.E. 1992, ApJ, 394, 117

Pier, E., & Krolik, J. 1992, 399, L23

Piran, T. 1978, ApJ, 221, 652

Pitts, E., & Tayler, R.J. 1985, MNRAS, 216, 139

Pudritz, R. E., & Norman, C. 1986. ApJ, 301, 571

Press, W. H., Flannery, B. P., Teukolsky, S. A., & Vetterling, W. T. 1992, Numerical Recipes in FORTRAN (2nd Edition) (Cambridge: Cambridge Univ. Press), 749

Pringle, J. E. 1981, ARAA, 19, 137

Pringle, J. E., Rees, M. J., & Pacholczyk, A. G. 1973, A & A, 29, 179

Rayleigh, Lord. 1916, Proc. Roy. Soc. Lond. A, 93, 148

Rees, M. J., Begelman, M. C., Blandford, R. D., & Phinney, E. S. 1982, Nature, 295, 17

Ross, D. W., Chen, G. L., & Mahajan, S. M. 1982, Phys. Fluids, 25, 652

Rowan-Robinson, M., Lock, T. D., Walker, D. W., & Harris, S. 1986, MNRAS 222, 611

Ruden, S. P., & Lin, D. N. C. 1986, ApJ, 308, 883

Ryu, D., & Goodman, J. 1992, ApJ, 388, 438

Sargent, A. I., & Beckwith, S. V. W. 1991, ApJ, 382, L31

Schmidt, G. 1966, Physics of High Temperature Plasmas (New York: Academic Press), Chp. 5

Schramkowski, G. P. 1994, Ph. D. thesis, Universiteit Utrecht

Schwarzschild, K. 1906, Göttingen Nachr., 41

Schwarzschild, M. 1958, Structure and Evolution of the Stars (Princeton: Princeton Univ. Press), §II.7

Sekiya, M., & Miyama, S. M. 1988, MNRAS, 234, 107

Shakura, N. I., & Sunyaev, R. A. 1973, A & A, 24, 337

Shakura, N. I., & Sunyaev, R. A. 1976, MNRAS, 175, 613

Shields, G. A. 1978, Nature, 272, 706

Shu, F. H. 1974, A & A, 33, 55

Shu, F. H. 1991, in The Physics of Star Formation and Early Stellar Evolution, ed. C. J. Lada & N. D. Kylafis (Dordrecht: Kluwer), 365

Shu, F. H. 1992, The Physics of Astrophysics, Vol. II (Mill Valley: University Science Books)

Shu, F. H., Tremaine, S., Adams, F. C., & Ruden, S. P. 1990, ApJ, 358, 495

Sikora, M., & Wilson, D. B. 1981, MNRAS, 197, 529

Simon, R. 1958, ApJ, 128, 375

Smith, B. A., & Terrile, R. J. 1984, Science, 226, 1421

Solberg, H. 1936, Procès-Verbaux Ass. Météor., U.G.G.I., 6^e Assemblée Générale (Edinburgh), Mém. et Disc. 2, 66

Spitzer, L. 1962, Physics of Fully Ionized Gases (New York: Wiley)

Spruit, H. C., Stehle, R., & Papaloizou, J. C. B. 1995, MNRAS, in press

Sridhar, S., & Goldreich, P. 1994, ApJ, 432, 612

Stella, L., & Rosner, R. 1984, ApJ, 277, 312

Stepinski, T. F., Reyes-Ruiz, M., & Vanhala, H. A. T. 1993, Icarus, 106, 77

Stone, J. M., & Norman, M. L. 1994, ApJ, 433, 746

Strom, K. M., Strom, S. E., Edwards, S., Cabrit, S., & Skrutskie, M. F. 1989, AJ, 97, 1451

Tagger, M., Pellat, R., & Coroniti, F. C. 1992, ApJ, 393, 708

Tassoul, J.-L. 1978, Theory of Rotating Stars (Princeton: Princeton Univ. Press)

Tayler, R. J. 1957, Proc. Phys. Soc. (London), B70, 1049

Tayler, R. J. 1973, MNRAS, 161, 365

Tayler, R. J. 1980, MNRAS, 191, 135

Tout, C. A., & Pringle, J. E. 1992, MNRAS, 259, 604 (TP)

Treves, A., Maraschi, L., & Abramowicz, M. 1988, PASP, 100, 427

Tscharnuter, W. M., & Boss, A. P. 1993, in Protostars and Planets III, ed. E.H. Levy & J.I. Lunine (Tucson, Univ. of Arizona Press), 921

Uchida, Y., & Shibata, K. 1985, PASJ, 37, 515

Velikhov, E. 1959, Sov. Phys. JETP, 36, 1398 (p. 995 in English translation)

Wade, R. A., & Ward, M. J. 1985, in Interacting Binary Stars, ed. J. E. Pringle & R. A. Wade (Cambridge: Cambridge Univ. Press), 129

Wardle, M., & Königl, A. 1990, ApJ, 362, 120

Woltjer, L. 1990, in Active Galactic Nuclei, Saas-Fee Advanced Course Lecture Notes 1990, ed. T. J.-L. Courvoisier & M. Mayor (Berlin: Springer-Verlag), 1

Zahn, J.-P. 1990, in Structure and Emission Properties of Accretion Disks, ed. J.-P. L. C. Bethout, S. Collin-Souffrin, & J. T. T. Van (Editions Frontières), 87

Zhang, W., Diamond, P. H., & Vishniac, E. T. 1994, ApJ, 420, 705

Zurek, W. H., & Benz, W. 1986, ApJ, 308, 123